

**Investigation of Bi-Metallic Oxide Composites for
Electrochemical and Photoelectrochemical Splitting of
Water**

By

Sriram Kumar

CHEM01201404025

Bhabha Atomic Research Centre

A thesis submitted to the

Board of Studies in Chemical Sciences

In partial fulfillment of requirements

for the Degree of

DOCTOR OF PHILOSOPHY

of

HOMI BHABHA NATIONAL INSTITUTE



October 2020

CERTIFICATION ON ACADEMIC INTEGRITY

1. I *Sriram Kumar* HBNI Enrollment No. *CHEM01201404025* hereby undertake that, the Thesis titled "*Investigation of Bi-metallic Oxide Composites for Electrochemical and Photoelectrochemical Splitting of Water*" is prepared by me and is the original work undertaken by me and free of any plagiarism. That the document has been duly checked through a plagiarism detection tool and the document is plagiarism free.

2. I am aware and undertake that if plagiarism is detected in my thesis at any stage in future, suitable penalty will be imposed as per the applicable guidelines of the institute/UGC.

Sriram Kumar
20/10/2020

Signature of the student
(with date)

Endorsed by PhD Supervisor



Signature (with date) 20/10/2020

Name: Dr. A. K. Satpati

Designation: SO/G, and Head, Electrochemical Methods Section

Department/Centre: Analytical Chemistry Division

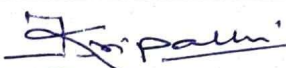
Name of the CI/OCC: Bhabha Atomic Research Centre

Homi Bhabha National Institute¹

Recommendations of the viva voce committee

As members of the Viva Voce Committee, we certify that we have read the dissertation prepared by Sriram Kumar entitled "Investigation of Bi-Metallic Oxide Composites for Electrochemical and Photoelectrochemical Splitting of Water" and recommend that it may be accepted as fulfilling the thesis requirement for the award of Degree of Doctor of Philosophy.

Chairman – Dr. A. K. Tripathi

 17/10/2020

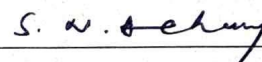
Guide / Convener – Dr. A. K. Satpati

 17-10-2020

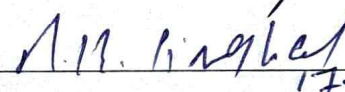
Examiner - Prof. Amartya Mukhopadhyay



Member 1- Dr. S. N. Achary



Member 2- Dr. R. K. Singhal

 17.10.2020

Final approval and acceptance of this thesis is contingent upon the candidate's submission of the final copies of the thesis to HBNI.

I/We hereby certify that I/we have read this thesis prepared under my/our direction and recommend that it may be accepted as fulfilling the thesis requirement.

Date: 17.10.2020

Place: Trombay


Signature

Guide Dr. A.K. Satpati

¹ This page is to be included only for final submission after successful completion of viva voce.

STATEMENT BY AUTHOR

This dissertation has been submitted in partial fulfillment of requirements for an advanced degree at Homi Bhabha National Institute (HBNI) and is deposited in the Library to be made available to borrowers under rules of the HBNI.

Brief quotations from this dissertation are allowable without special permission, provided that accurate acknowledgement of source is made. Requests for permission for extended quotation from or reproduction of this manuscript in whole or in part may be granted by the Competent Authority of HBNI when in his or her judgment the proposed use of the material is in the interests of scholarship. In all other instances, however, permission must be obtained from the author.

Sriram Kumar
20/10/2020
Sriram Kumar

DECLARATION

I, hereby declare that the investigation presented in the thesis has been carried out by me. The work is original and has not been submitted earlier as a whole or in part for a degree / diploma at this or any other Institution / University.

Sriram Kumar
20/10/2020
Sriram Kumar


20/10/2020
Dr. A. K. Satpati
(PhD Guide)

List of Publications arising from the thesis

Journal

1. “Electrochemical and SECM Investigation of MoS₂/GO and MoS₂/rGO Nanocomposite Materials for HER Electrocatalysis”, Sriram Kumar, Prashant Sahoo and A. K. Satpati, ACS Omega, 2 (2017), 7532-7545.
 2. “Insight into the PEC and interfacial charge transfer kinetics at the Mo doped BiVO₄ photoanodes”, Sriram Kumar, Satyaprakash Ahirwar and Ashis Kumar Satpati, RSC Adv., 9 (2019), 41368-41382
 3. “Insight into the catalytic performance of HER catalysis of noble metal/3D-G nanocomposites”, Sriram Kumar, Prasanta Kumar Sahoo and Ashis Kumar Satpati, Electrochimica Acta, 333 (2020), 135467
 4. “Investigation of Interfacial Charge Transfer Kinetics of Photocharged Co-Bi Modified BiVO₄ Using Scanning Electrochemical Microscopy (SECM)”, Sriram Kumar and Ashis Kumar Satpati, Electrochimica Acta (under revision).
 5. “Effect of the gamma radiation on the PEC efficiency of BiVO₄ and Co-Bi modified BiVO₄ photoanodes”, Sriram Kumar and Ashis Kumar Satpati, (to be communicated shortly).
-
6. “Study of electrical double layer of three-dimensional graphene based composite material for HER using impedance spectroscopy” Sriram Kumar and Ashis Kumar Satpati (to be communicated shortly)

7. * “Probing adsorption/desorption redox processes and detection of cysteine: A Voltammetry and Scanning Electrochemical Microscopy study”, Milan Kumar Dey, Sriram Kumar and Ashis Kumar Satpati, Journal of Electroanalytical Chemistry, 807 (2017), 119-127.
8. * “Evaluation of novel PVC-based efficient potentiometric sensor containing a tripodal diglycolamide (TREN-DGA) ionophores for europium (III) estimation”, Bholanath Mahanty, Ashis Kumar Satpati, Sriram Kumar, Andrea Leoncini, Jurriaan Huskens, Willem Verboom, Prasanta K. Mohapatra, Sensor & Actuators B: Chemical, 272 (2018), 534-542.
9. * “Development of polyvinyl chloride (PVC)-based highly efficient potentiometric sensors containing two benzene-centered tripodal diglycolamides as ionophores” Bholanath Mahanty, Ashis Kumar Satpati, Sriram Kumar, Andrea Leoncini, Jurriaan Huskens, Willem Verboom, Prasanta K. Mohapatra, , Sensor & Actuators B: Chemical 320 (2020), 127961
10. * “An Electrochemical Bisphenol F Sensor based on ZnO/G nano composite and CTAB surface modified carbon paste electrode architecture” G. Manasa, Ronald J. Mascarenhas, Ashis Kumar Satpati, Basavanakote M. Basavaraja, Sriram Kumar, Colloids and Surfaces B: Biointerfaces, 170 (2018), 144-151.
11. * “High sensitive determination of dopamine through catalytic oxidation and preconcentration over gold-multiwall carbon nanotubes composite modified electrode”, Durgasha C. Poudyal, A. K. Satpati, Sriram Kumar and Santosh K. Haram, Materials Science and Engineering C, 103 (2019), 109788.

12. * “Electrochemical synthesis of carbon nano spheres and its application for detection of ciprofloxacin”, Priyanka R. Ipte, Sriram Kumar and Ashis Kumar Satpati, Journal of Environmental Science and Health, 55:2 (2020), 142-150.

* **Not included in the thesis**

Conference Papers

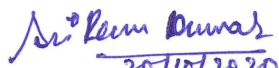
1. “Electrochemical Investigation of MoS₂/GO nanocomposite for HER Electrocatalysis”, Sriram Kumar and A. K. Satpati, iSEAST-2016, 8-10 December-2016, Chennai (Poster presentation).
2. * “A Mechanistic Study Approach towards Supercapacitor based Material” Srikant Sahoo, M. K. Dey, Sriram Kumar and A. K. Satpati, ICONEST-2017, 10-12 August-2017, IISc-Bangalore (Poster presentation).*

[Awarded best poster presentation award].

3. Kinetic Study of MoS₂/GO nanocomposite Catalyzed HER: A SECM Investigation” Sriram Kumar and A. K. Satpati, ICONEST-2017, 10-12 August-2017, IISc-Bangalore (Oral Presentation).
4. “Investigation of Bi-metallic oxide composite for the Electrochemical and Photoelectrochemical Splitting of Water”, Sriram Kumar and A. K. Satpati, RSM-2018, 9-10 February-2018 (Oral presentation).
5. “Cu₂O/MoS₂ Heterojunction Photocathode for Enhanced Charge Separation for Water Splitting”, Sriram Kumar and A. K. Satpati, CEAMCR-2018, 15-17 February-2018, BARC-Mumbai (poster presentation).

6. “SnO₂/BiVO₄ Heterojunction Photoanode for Enhanced Charge Separation for Water Splitting”, Sriram Kumar and A. K. Satpati., CEAMCR-2018, 15-17 February, BARC-Mumbai (Oral presentation).
[Awarded ACS best oral presentation award]
7. “Investigation of transport kinetics on Gradient doped of Mo in BiVO₄ using Scanning Electrochemical Microscopy (SECM)”, Sriram Kumar and A. K. Satpati, NSEMD-2018, 28-29 September-2018, CSIR-CSMCRI, Bhavnagar. (Poster presentation).
[Awarded best poster presentation award]
8. “Study of interfacial charge transfer kinetics at electrode-electrolyte interface of BiVO₄: A SECM approach” Sriram Kumar and A. K. Satpati, ICMST-2018, 10-13 October-2018, IIST-Thiruvananthapuram (poster presentation).
9. . “Kinetic study of the photocharged Co-B_i modified BiVO₄ for PEC water oxidation”
Sriram Kumar and A. K. Satpati, **MEHC-2020**, 1-3rd May, TIFR

* Not included in the thesis


20/10/2020
Sriram Kumar

DEDICATIONS

This thesis is dedicated to

My family

&

to my beloved teachers

ACKNOWLEDGEMENTS

First and foremost, I express my deepest gratitude to my guide **Dr. A. K. Satpati**, Head, Electrochemical Methods Section, Analytical Chemistry Division for his invaluable guidance, continuous support, motivation and encouragements throughout the tenure of my research work. His profound knowledge and logical way of thinking always inspires me. My sincere thanks to all the doctoral committee members for their critical review of my work and their valuable comments and suggestions during the progress reviews and pre-synopsis viva-voce. I sincerely thank Prof. A. K. Tyagi, Associate Director, Chemistry Group, Prof. P. D. Naik, former Associate Director, Chemistry Group and Prof. H. Pal, former Associate Director, Chemistry Group (A), for their encouragement and support. I thank the members of our laboratory Shri Prem Kumar Mishra, Dr. Milan Kumar Dey, Shri Srikant Sahoo, Ms. Priyanka R. Ipte, Abhishek Sharma and Sudipa Manna for their supports. I sincerely thank all the colleagues of Analytical Chemistry Division for their friendly and cooperative behavior which made the journey smooth and comfortable. I specially thank to the electronics group, ACD for their support. I express my heartfelt gratitude to some special persons, my teachers, Prof. D. N. Thakur, Shri Niteshwar Mishra, Shri Mukul Ranjan Prasad, Shri Chhotelal Baitha who made a great impact in my early academic carrier. I convey the deepest gratitude to the all my friends Mrs. Rakhee Yadav, Shri Rahul Kumar, Bharat Bhushan, Vivekananda Sinha, Tinku Kumar, Pankaj Kumar (maths), Pankaj Kumar (stat), Ajit Kumar, Joshi Sharma, Shivanand Giri, Mukesh, Raj Pandey, Gaurav Mishra and all friends who helped me. Without the support of my friends it would not be possible to come at this stage. Words fail to express my deepest gratitude to my best friend Ms. Anjali Vanapariya for her constant support and encouragements. Finally, I owe my heartfelt gratitude and indebtedness to my parents whose endless love, blessings, moral support and continuous faith in me made me overcome many obstacles in my life and to achieve this goal successful.

Table of Contents

1	Chapter 1: Introduction of the thesis.....	30
1.1	Introduction	30
1.2	Principle of water splitting reaction	31
1.3	Hydrogen evolution reaction.....	32
1.4	Oxygen evolution reaction	38
1.5	Photoelectrochemical water splitting	40
1.6	Scanning Electron Microscopy (SECM).....	43
1.7	Hydrogen evolution catalysis	47
1.8	Oxygen evolution catalysts	49
2	Chapter 2: Experimental Procedures	53
2.1	Electrochemical and photoelectrochemical techniques.....	53
2.1.1	Cyclic Voltammetry (CV).....	53
2.1.2	Linear sweep voltammetry	56
2.1.3	Chronoamperometry	57
2.1.4	Chronopotentiometry	58
2.1.5	Rotating disk electrode (RDE).....	58
2.1.6	Ultraviolet-visible (UV-Vis) Spectroscopy	60

2.1.7	Incident photon to current efficiency (IPCE).....	62
2.1.8	Absorption photon to current efficiency (APCE)	65
2.1.9	Faradaic efficiency	65
2.1.10	Solar to hydrogen efficiency (STH).....	66
2.1.11	Charge transport efficiency ($\eta_{\text{transport}}$)	67
2.1.12	Charge transfer efficiency	68
2.1.13	Transient time	68
2.1.14	Mott-Schottky analysis	69
2.1.15	Electrochemical Impedance Spectroscopy (EIS).....	70
2.1.16	Scanning Electrochemical Microscopy (SECM).....	72
2.2	Material Characterization	78
2.2.1	X-ray diffraction (XRD)	78
2.2.2	Fourier Transform Infrared Spectroscopy (FT-IR).....	80
2.2.3	Raman spectroscopy	81
2.2.4	Scanning electron microscopy (SEM)	83
2.2.5	Energy dispersive spectroscopy (EDS).....	83
2.2.6	Atomic force microscopy (AFM)	84
2.2.7	X-ray photoelectron spectroscopy (XPS)	85
2.2.8	High resolution transmission electron microscopy (HR-TEM).....	85

3	Chapter 3: Development of the noble metal and three dimensional graphene (3D-G) composite materials for the hydrogen evolution reaction.....	87
3.1	Introduction	87
3.2	Experimental Section	90
3.2.1	Chemicals.....	90
3.2.2	Preparation of noble metals (Ag, Au, Pd and Pt)/3D-G nanocomposites.....	90
3.2.3	Instrumentation	91
3.2.4	Procedure for Electrochemical Measurements	91
3.3	Results and discussion.....	93
3.3.1	Characterization of materials	93
3.3.2	Electrochemical investigation and evaluation of the performance of the catalysts	98
3.3.3	Hydrogen evolution kinetics study under hydrodynamic conditions	105
3.3.4	Investigation of Hydrogen evolution reaction kinetics with varying temperature	108
3.3.5	Electrochemical Impedance Measurements.....	118
3.4	Conclusion.....	123
4	Chapter 4: Development of the MoS ₂ graphene composite as cathode materials for the hydrogen evolution reaction	124
4.1	Introduction	124
4.2	Experimental procedures	126
4.2.1	Preparation of MoS ₂ nanoparticle:.....	126

4.2.2	Synthesis of graphene oxide	127
4.2.3	Procedure of electrochemical Studies and instrumentation	127
4.3	Results and discussion.....	129
4.3.1	Characterization of the materials	129
4.3.2	Electrocatalytic HER activity	133
4.3.3	Electrochemical impedance measurements	144
4.3.4	Scanning electrochemical microscopy measurements.....	146
4.4	Conclusion.....	153
5	Chapter 5: Development of BiVO ₄ based photoanode material for photoelectrochemical splitting of water	154
5.1	Introduction	154
5.2	Experimental Section	157
5.2.1	Materials	157
5.2.2	Fabrication of Photoanode	157
5.2.3	Photoelectrochemical measurements	158
5.2.4	Characterization of the materials	160
5.3	Result and discussion	160
5.3.1	Structure analysis by XRD and Raman spectroscopy.....	160
5.3.2	XPS analysis of the materials	164
5.3.3	SEM and EDS analysis	166

5.3.4	UV-vis spectral measurements	169
5.3.5	Photoelectrochemical investigation	171
5.3.6	Electrochemical Impedance measurements	177
5.3.7	Testing of stability of the photoanodes	179
5.3.8	Interfacial charge transfer kinetics using SECM	181
5.4	Conclusion.....	191
6	Chapter 6. Insight into the PEC and interfacial charge transfer kinetics at the Co-Bi modified BiVO ₄	192
6.1	Introduction	192
6.2	Experimental Section	196
6.2.1	Materials	196
6.2.2	Fabrication of Photoanode	196
6.2.3	Photoelectrochemical (PEC) measurements	197
6.3	Result and discussion	200
6.3.1	Material characterization	200
6.3.2	UV-Vis spectroscopy	206
6.3.3	Photoelectrochemical study	207
6.3.4	Electrochemical Impedance Measurements.....	213
6.3.5	Photocharging of the Photoanode	216
6.3.6	Investigation of charge transfer by scanning electrochemical microscopy	223

6.4	Conclusion.....	230
7	Chapter 7 Improvements in the photo-electrocatalysis of BiVO ₄ by gamma irradiation and plasma treatment	232
7.1	Introduction	232
7.2	Experimental Section	233
7.2.1	Materials	233
7.2.2	Fabrication of Photoanode	234
7.2.3	Photoelectrochemical (PEC) measurements	235
7.2.4	Characterization	235
7.3	Result and discussion	236
7.3.1	Material characterization	236
7.3.2	UV-Vis spectroscopy	242
7.3.3	Photoelectrochemical investigation	244
7.3.4	Mott-Schottky analysis	247
7.3.5	Impedance spectroscopy study	249
7.4	Conclusion.....	252
8	Chapter 8: Conclusions and Future Scope	254
9	References.....	261

Abstract

The objective of the research is utilization of solar energy to generate renewable energy in the form of solar hydrogen for supply of energy demand for sustainable growth. This research is focused on the improvement of hydrogen evolution reaction and oxygen evolution reaction. Latter one limits overall water splitting efficiency because of sluggish kinetics. The Fundamental study of water splitting has been done to understand the mechanism of the process. Considering the objectives of the present research, the thesis has been divided into two parts. In the first part, graphene and three-dimensional graphene (3D-G) have been synthesized. The major accomplishment here is the synthesis of highly porous and spongy graphene via environmental friendly freeze drying method. Noble metal/3D-G nanocomposite materials have been synthesized by low cost and environmental friendly freeze drying method. Then, MoS₂ and graphene based cathodic materials have been synthesized to replace the noble metals. The thermodynamic and kinetic studies have been extensively carried out for the investigation of the mechanism of the HER. The Effect of enthalpy and entropy on the mechanism of HER have been studied and correlated with the kinetics of the process. The internal energy and potential of zero charge (PZC) have been used to explain the HER mechanism. Further, the kinetic investigations (rate constant and the number of electrons transferred) of the HER has been investigated using the Koutechy-Levich analysis. The interfacial charge transfer kinetics and localized electrocatalytic activity have been investigated by using SECM technique.

In the second part, the developments of the BiVO₄ photoanodes have been carried out for the oxygen evolution reaction (OER). The major challenges of the BiVO₄ photoanodes have been taken as research motivation. Mo doping and SnO₂ heterojunction formation enhance the

charge transfer efficiency, charge transport efficiency and suppress the charge recombination process. Further, the PEC efficiency is improved by the incorporation of the oxygen evolution catalyst (OEC) as Co-Bi on the BiVO₄ surface. The details kinetic study of the Co-Bi modified BiVO₄ have been investigated. The improved photoelectrochemical (PEC) performance of the photoanodes has been correlated with the improvements of the surface and bulk properties of the photoanodes. The decrease of the charge transfer resistance (R_{ct}) upon Co-Bi incorporation shows improvements of the conductivity of the photoanodes. The Warburg impedance in the Co-Bi modified BiVO₄ suggests the diffusion control OER process. Mott-Schottky analysis shows the improvements in the donor density and the flat band potential upon cocatalyst incorporation. The photocharging technique as a tool is used to enhance the PEC efficiency of BiVO₄ and the Co-Bi modified BiVO₄. Photocharging leads to enhance the redox active state and conductivity of the photoanodes. Scanning electrochemical microscopy (SECM) technique study reveals the improvement of the interfacial hole transfer kinetics of the photoanodes upon the photocharging. Plasma treatment and gamma irradiation have been used as tool for further improvements in the photocurrent and efficiency of the photoanodes. The crystallinity of the photoanodes has been improved upon the gamma irradiation. SEM images suggest the incorporation of the micro-porosity in the photoanodes.

List of Figures

Figure 1.1 Schematic of the photoelectrochemical splitting of water for (A) photoanode, (B) photocathode and (C) Z-scheme for the complete cell.	41
Figure 1.2 Schematic representation of photogenerated electrons and holes in the (A) BiVO ₄ photoanode, (B) effect of heterojunction of SnO ₂ on BiVO ₄ electron-hole mobility and (C) effect of the cocatalyst on the hole transfer of BiVO ₄ photoanode.	43
Figure 1.3 Schematic representation of the measurements of interfacial charge transfer of BiVO ₄ photoanode in illumination.	46
Figure 2.1 (A) Potential time functions for the excitation signal in cyclic voltammetry and (B) typical cyclic voltammogram for the reversible electrochemical reaction.	54
Figure 2.2 (A) Potential time functions for the excitation signal in linear sweep voltammetry and (B) typical linear sweep voltammogram for electrochemical reaction	57
Figure 2.3 Schematic diagram of the experimental set up for IPCE measurement.	64
Figure 2.4 Typical transient photocurrent.	69
Figure 2.5. Schematic of scanning electrochemical microscopy system	74
Figure 2.6 Schematic of feedback mode of approach of the tip to the substrate. (A) diffusion hindrance process, (B) feedback of electroactive species on the conductive substrate and (C) blockage of regeneration of electroactive species on the insulating substrate.....	75
Figure 2.7 Schematic of typical X-ray powder diffractometer	79
Figure 2.8 Schematic of a typical FT-IR spectrometer	80
Figure 2.9 Energy level diagram of the Raman scattering	81
Figure 2.10 shows the schematic of the typical Raman spectrometer in which Laser light is used as the source. Laser light interacts with the molecular vibrations, phonons or other excitation.	

The scattered light from the sample typically Raman scattered light can pass from the filter. The Raman scattered light falls on the detector and produces the spectrum which is utilized in the characterization of the materials. 82

Figure 2.11 Schematic of atomic force microscopy (AFM) 84

Figure 2.12 Schematic of high-resolution transmission electron microscope. 86

Figure 3.1 Linear sweep voltammetry at a rate of 1 mVs^{-1} for calibration of the Ag/AgCl reference electrode with RHE potential 93

Figure 3.2 (i) XRD patterns of (a) GO, (b) bare 3D-G, (c) Ag/3D-G, (d) Au/3D-G, (e) Pd/3D-G, and (f) Pt/3D-G nanocomposites; (ii) Raman spectra of (a) GO, (b) bare 3D-G, (c) Ag/3D-G, (d) Au/3D-G, (e) Pd/3D-G, and (f) Pt/3D-G nanocomposites. 94

Figure 3.3 C1s XPS spectra of (a) GO, (b) Pt/3D-G nanocomposite; (c) Ag 3d (d) Au 4f (e) Pd 3d and (f) Pt 4f XPS peaks of Ag/3D-G, Au/3D-G, Pd/3D-G, and Pt/3D-G nanocomposites respectively. 95

Figure 3.4 FEG-SEM images of (a) Ag/3D-G, (b) Au/3D-G, (c) Pd/3D-G, and (d) Pt/3D-G nanocomposites..... 96

Figure 3.5 HRTEM images of (a) Ag/3D-G, (b) Au/3D-G, (c) Pd/3D-G, and (d) Pt/3D-G nanocomposites..... 97

Figure 3.6 (A) Polarization curve of different catalysts at a scan rate of 5 mVs^{-1} for comparison on HER catalytic activity. Potential due to iR loss was compensated for each catalyst and compared with the measured current. (B) Current vs scan rate plot of different catalysts for double-layer capacitance (C_{dl}) measurements. (C) Tafel plots for catalysts in comparison with Pt/C catalyst Potential due to iR loss were compensated for correct measurement of Tafel plot for

each catalyst. Extra lines were drawn for measurements of the Tafel slope. (D) Effect of hydrodynamic study of different catalysts on HER activity.	100
Figure 3.7 Koutechy-Levich plots for (A) Pt/3D-G, (B) Pd/3D-G, (C) Au/3D-G and (D) Ag/3D-G catalysts. Extended lines were used to measure the linear portion of plots having maximum no. of points.	107
Figure 3.8 Effect of temperature on HER process was studied for catalyst (A) Pt/3D-G, (B) Pd/3D-G, (C) Au/3D-G and (D) Ag/3D-G. Temperatures were varied from room temperature to 70°C to 75°C.	109
Figure 3.9 Plots of $\ln(i)$ vs $1/T$ for HER process for different catalysts (A) Pt/3D-G, (B) Pd/3D-G, (C) Au/3D-G and (D) Ag/3D-G at six different potentials in 0.5 M H_2SO_4 solution.	111
Figure 3.10 Capacitance measurements for catalysts throughout potential windows. The potential of zero charges is calculated from the potential of corresponding minimum capacitance.	114
Figure 3.11 The temperature dependent symmetry coefficient is measured by the plot of $1/b$ vs $1/T$ for (A) Pt/3D-G, (B) Pd/3D-G, (C) Au/3D-G and (D) Ag/3D-G.	116
Figure 3.12 (A) Nyquist plot, (B) Bode plot and (C) equivalent circuit of fitted impedance data	119
Figure 3.13 Stability test of various catalysts by chronopotentiometry and Chronoamperometry.	122
Figure 4.1 XRD pattern of (A) MoS_2/GO and (B) MoS_2/rGO . Raman spectra of different vibrational modes of (C) MoS_2/GO and MoS_2/rGO . SEM images, TEM and SAED patterns of (D,E, F) pristine MoS_2 and (G, H, I)).	130

Figure 4.2 (A), (B) and (C) are HRTEM images and (D) is SAED pattern of the MoS ₂ /GO nano composite materials.	132
Figure 4.3 AFM images of MoS ₂ /GO (A) before electrochemical test using chronopotentiometry and (D) after chronopotentiometry at 10mA/cm ² current density for 4 hours. EDS images of (B, C) pristine MoS ₂ and (E, F) MoS ₂ /rGO.	132
Figure 4.4 (A)Polarization curve of various catalysts. Magnified image at lower current density is shown as inset. (B) Polarization curve of catalysts with and without hydrodynamic effect. Magnified image at lower current density is shown as inset. (C) Effects of scan rate on current density. (D) Effect of hydrodynamic conditions on the catalytic activity.	135
Figure 4.5 Koutechy-Levich plot of (A) MoS ₂ /GO and (B) MoS ₂ /rGO.....	137
Figure 4.6 Temperature dependent polarization curve for (A) MoS ₂ /GO and (B) MoS ₂ /rGO. Inset Figure is Arrhenius plot for activation energy calculation.....	139
Figure 4.7 . (A) Tafel plot of two catalyst system in comparison with the standard Pt/C catalyst (B) stability test using chronopotentiometry and (C) stability test using chronoamperometry of MoS ₂ /GO catalyst. (D) Nyquist plot of MoS ₂ /GO and MoS ₂ /rGO Inset: zoomed portion of the Nyquist plot at high frequency region and corresponding Bode plot at the entire frequency range.	143
Figure 4.8 Proposed mechanism of the proton exchange in the HER kinetics.	144
Figure 4.9 Equivalent circuit of the impedance spectroscopy measurement.....	145
Figure 4.10 Probe approach curve (PAC) for MoS ₂ /GO catalyst at different substrate potentials keeping constant probe potential -0.075V.	149

Figure 4.11 Scanning electrochemical microscopy (SECM) images of MoS ₂ /GO catalyst at different substrate potentials (A) 0.225 V, (B) 0.125V, (C) 0.025V, (D) -0.075V, (E) -0.125V and (F) -0.175V.....	151
Figure 4.12 Scanning electrochemical microscopy (SECM) images of MoS ₂ /rGO catalyst at different substrate potentials (A) 0.2246V, (B) 0.125V, (C) 0.025V, (D) -0.075V, (E) -0.175V and (F) -0.225V.....	152
Figure 5.1 (A) XRD patterns of all BiVO ₄ and Mo doped photoanodes and (B) Raman spectra of all BiVO ₄ based photoanodes.	162
Figure 5.2 XPS spectra of (A) Bi 4f, (B) O 1s, V 2p and Sn 3d and (C) Mo 3d in BiVO ₄	165
Figure 5.3 FE-SEM images all porous BiVO ₄ based photoanodes thin films on ITO substrate. (A) SBM0, (B) SBM1, (C) SBM3, (D) SBM5 and (E) SBM7.....	166
Figure 5.4 EDS analysis of different catalysts for calculation of Bi, V, O and Mo in the photoanodes (A) SBM0, (B) SBM1, (C) SBM3, (D) SBM5 and (E) SBM7.	167
Figure 5.5 Cross-sectional view of photoanodes for thickness measurements (A) SBM0, (B) SBM3 and (C) SBM7. Total thickness of film is 440 nm.	168
Figure 5.6 (A) UV-vis diffuse reflectance spectra and (B) Tauc plot for direct band for calculation of bandgap of all BiVO ₄ based photoanodes (C) Photoelectrochemical performances of the all BiVO ₄ based photoanodes were measured by chopped light voltammetry in 0.5 M Na ₂ SO ₄ in 0.1 M PBS buffer solution at scan rate 10 mVs ⁻¹ under the 1 Sun illuminations. (D) IPCE spectra at 1.0V vs Ag/AgCl of all photoanodes.	170
Figure 5.7 (A) Mott-Schottky analysis for calculation of donor density and flat band potential, (B) OCPV calculation by measuring the difference in potential in dark and illumination, (C) Nyquist plot and (D) Bode plots of the BiVO ₄ based photoanodes.....	173

Figure 5.8 Band diagram of BiVO₄ and Mo doped BiVO₄. The band diagram is constructed using UV-vis spectroscopy, OCPV and flat band potential measurements (not on scale). 175

Figure 5.9 All BiVO₄ based photoanode was characterized for stability test by chopped light voltammetry at 0.8V vs. Ag/AgCl for 1800sec (A) SBM0, (B) SBM1, (C) SBM3, (D) SBM5 and (E) SBM7. 180

Figure 5.10 Stability test of (A) SBM1 and (B) SBM5 in 0.5M Na₂SO₄ in 0.1M PBS at 1.44V. 181

Figure 5.11 (A)The proposed mechanism of feedback mode of analysis of BiVO₄/electrolyte interface by SECM analysis. In this technique, a 2mM ferricyanide solution was used as the redox mediator. In illumination, photo-generated holes oxidizes the [Fe(CN)₆]⁴⁻ to [Fe(CN)₆]³⁻ at the interface and the cathodic potential applied at Probe reduces the photo-oxidized [Fe(CN)₆]³⁻ to [Fe(CN)₆]⁴⁻. This redox close loop gives positive feedback in illumination and negative feedback in dark conditions. SECM imaging of the surface is characterized by the measuring o probe current to measure the hole transfer from the interface to the [Fe(CN)₆]⁴⁻. Normalized SECM feedback approach curve of the BiVO₄ based photoanodes (B) SBM0, (C) SBM1, (D) SBM3, (E) SBM5 and (F) SBM7 in 2mM [Fe(CN)₆]³⁻ solution at different applied bias potential at substrate under illumination using Pt ultra-microelectrode having r_T value 4.5μm. 183

Figure 5.12 (A) CV of Pt ultra-microelectrode (UME) in 2 mM [Fe(CN)₆]³⁻ at 10mVs⁻¹ scan rate and (B) probe approach curve (PAC) of Pt UME in 2mM [Fe(CN)₆]³⁻ solution at SBM0 photoanode in dark..... 184

Figure 5.13 Normalized SECM feedback approach curve of the SBM5 at (A) 0.94V, (B)1.04V, (C) 1.14V, (D) 1.24V, (E) 1.34V and (F) 1.44V in 2mM [Fe(CN)₆]³⁻ solution at different applied potential at substrate under illumination using Pt ultra-microelectrode having r_Tvalue 4.8μm. 187

Figure 5.14 Scanning electrochemical microscopy (SECM) imaging of photoanodes SBM0 at (A) 0.94V and (B) 1.14V and SBM1 at (C) 0.94V and (D) 1.14V substrate potential in 2mM $[\text{Fe}(\text{CN})_6]^{3-}$ at constant height mode using Pt UME as probe and photoanodes as substrate.	188
Figure 5.15 Scanning electrochemical microscopy (SECM) imaging of photoanodes SBM3 at (A) 0.94V and (B) 1.14V and SBM5 at (C) 0.94V and (D) 1.14V substrate potential in 2mM $[\text{Fe}(\text{CN})_6]^{3-}$ at constant height mode using Pt UME as probe and photoanodes as substrate.	190
Figure 5.16 Scanning electrochemical microscopy (SECM) imaging of photoanodes SBM7 at (A) 0.94V and (B) 1.14V substrate potential in 2mM $[\text{Fe}(\text{CN})_6]^{3-}$ at constant height mode using Pt UME as probe and photoanodes as substrate.	190
Figure 6.1 (A) XRD pattern of BV and Co-B _i modified BV, (B) Raman analysis of photoanodes. SEM images of (C) BV, (D) BV/Co-B _{i-1} , (E) BV/Co-B _{i-2} , (F) BV/Co-B _{i-3} and (G) BV/Co-B _{i-4}	202
Figure 6.2 EDS elemental analysis of photoanodes (A) BV, (B) BV/Co-B _{i-1} , (C) BV/Co-B _{i-2} , (D) BV/Co-B _{i-3} and (E) BV/Co-B _{i-4}	203
Figure 6.3 Cross-sectional thickness of photoanodes (A) BV, (B) BV/Co-B _{i-1} , (C) BV/Co-B _{i-2} and (D) BV/Co-B _{i-3}	204
Figure 6.4 XPS analysis of (A) Bi 4f, (B) V 2p, (C) Mo 3d, (D) O 1s (E) Co 2p and (F) B 1s.	204
Figure 6.5 (A) Absorption spectra and (B) Tauc plot of photoanodes. (C) is transient time calculation of BV and BV/Co-B _{i-3}	207
Figure 6.6 (A) Copped light voltammetry of photoanodes, (B) IPCE measurements, (C) Mott-Schottky plot, (D) open-circuit photovoltage, (E) Nyquist plot and (F) Bode plot.	210
Figure 6.7 Stability test of the photoanodes (A) BV, (B) BV/Co-B _{i-1} , (C) BV/Co-B _{i-2} , (D) BV/Co-B _{i-3} and (E) BV/Co-B _{i-4} at 0.8V for 2 h.	216

Figure 6.8 The effect of photocharging is characterized by chopped light voltammetry and LSV of (A) BV, (B) BV/Co-B _i -1, (C) BV/Co-B _i -2, (D) BV/Co-B _i -3 and (E) BV/Co-B _i -4. Chopped light voltammetry is shown in a solid line, and LSV is shown in the dotted line.....	218
Figure 6.9 (A) CV of BV and BV/Co-B _i -3 before and after PC in the dark. (B) Multiple CV cycles of BV/Co-B _i -3 in the dark after PC	219
Figure 6.10 Electronic properties of the photoanodes are characterized by the measuring impedance at 0.8V under illumination in the frequency range from 10 ⁵ to 10 ⁻¹ Hz of (A) BV (B) BV/Co-B _i -1, (C) BV/Co-B _i -2, (D) BV/Co-B _i -3 and (E) BV/Co-B _i -4.....	221
Figure 6.11 Mott-Schottky analysis of photoanodes (A) BV, (B) BV/Co-B _i -1, (C) BV/Co-B _i -2 , (D) BV/Co-B _i -3 and (E) BV/Co-B _i -4 at 100Hz.....	222
Figure 6.12 (A) CV of Pt UME in 2 mM [Fe(CN) ₆] ³⁻ solution at 50 mV s ⁻¹ and (B) approach curve of Pt UME in 2 mM [Fe(CN) ₆] ³⁻ a solution towards BV/Co-B _i -3 in the dark.....	226
Figure. 6.13 Normalized feedback approach curves for Pt ultramicroelectrode (UME) towards BV/Co-B _i -3 under illumination using 2mM [Fe(CN) ₆] ³⁻ redox probe at various substrate potential with approach rate is 0.1 μm s ⁻¹	226
Figure 6.14 Plots of ln(k _{eff}) vs. η of photoanodes (A) BV, (C) BV/Co-B _i -3 before photocharging, and (B) and (D) are after photocharging.....	227
Figure 6.15 SECM imaging of photoanodes by measuring probe current in feedback mode at constant height using Pt UME in 2mM [Fe(CN) ₆] ³⁻ at various substrate potentials. SECM images of BV/Co-B _i -3 at (A) 0.4V, (B) 0.6V and (C) 0.8 V and BV/Co-B _i -3 after PC at (D) 0.4 V, (E) 0.6 V and (F) 0.8 V.	229
Figure 7.1 (A) XRD pattern and (B) Raman spectra of BV and Co-B _i modified BV with gamma irradiation.....	237

Figure 7.2 SEM images of (A) BV, (B) BV_50 kGy, (C) BV_100 kGy, (D) BV/Co-Bi, (E) BV/Co-Bi_50kGy and (F) BV/Co-Bi_100 kGy	239
Figure 7.3 AFM images of (A) BV, (B) BV-50 kGy, (C) BV-100 kGy, (D) BV/Co-Bi, (E) BV/Co-Bi-50kGy and (F) BV/Co-Bi-100 kGy	240
Figure 7.4 EDS images of (A) BV, (B) BV-50 kGy, (C) BV-100 kGy, (D) BV/Co-Bi, (E) BV/Co-Bi-50kGy and (F) BV/Co-Bi-100 kGy.	241
Figure 7.5 Cross-sectional view of the photoanodes (A) BV and (B) BV/Co-Bi.....	242
Figure 7.6 (A) UV-Vis spectroscopy measurements, (B) Tauc plot for bandgap measurement, (C) chopped light voltammetry of photoanodes and (D) IPCE measurements.	243
Figure 7.7 (A) Mott-Schottky plot, (B) open circuit photovoltage, (C) Nyquist plot and (D) Bode plot.	248
Figure 7.8 Stability test of the photoanodes (A) BV, (B) BV_50 kGy, (C) BV_100 kGy, (D) BV/Co-Bi (E) BV/Co-Bi_50 kGy and (F) BV/Co-Bi_100 kGy at 0.8V for 2 h.	252

List of Table

Table 3.1 Electrochemical parameters are obtained from CV and LSV measurements	102
Table 3.2 Activation energy of HER of catalysts is compared at the different applied potential.	110
Table 3.3 Temperature dependent Tafel slopes are measured for the further insight of the HER for the catalysts.	113
Table 3.4 Enthalpy and entropy dependent transfer coefficient are calculated and equation for Temperature dependent transfer coefficient was tabulated.	117
Table 3.5 Temperature dependent transfer coefficient is calculated for understanding of the thermodynamics of HER.....	117
Table 3.6 Randle-Sevik equivalent circuit parameters calculated from simulation of EIS data to this equivalent circuit	120
Table 4.1 . Electrochemical parameters as obtained from the cyclic voltammetry measurements at different scan rates.	136
Table 4.2 Analysis results from the hydrodynamic voltammetric measurements using the Koutechy-Levich analysis. The final values of n and k are rounded off to 2 decimal places. ...	138
Table 4.3 Activation energies obtained on two catalytic systems at different applied potentials	140
Table 5.1 Analysis of Raman spectroscopy of all BiVO ₄ based photoanodes. All stretching and bending modes of vibrational of BiVO ₄ are listed here. The bond length of V-O is calculated based on the symmetric stretching of V-O mode.....	163
Table 5.2 XPS analysis of Bi 4f, O 1s, V 2p and Mo 3d binding energy.	164
Table 5.3 Elemental analysis of Bi, V, O, Mo and Sn in BiVO ₄ photoanodes	168

Table 5.4 PEC activity of the photoanodes were characterized by the following parameters. . .	174
Table 5.5 Impedance spectroscopy analysis of photoanodes for measurements of bulk and surface characterization.	178
Table 5.6 The k_{eff} of hole transfer from the $\text{BiVO}_4/\text{electrolyte}$ interface to $[\text{Fe}(\text{CN})_6]^{3-}$	187
Table 6.1 Summary of characterization of PEC of photoanodes and impedance spectroscopy.	212
Table 6.2 Summary of characterization of PEC of photoanodes after photocharging treatment.	219
Table 7.1 summery of the PEC study of photoanodes.	249

Thesis highlights

- Three-dimensional graphene (3D-G) has been synthesized by green, cost effective and one pot synthesis.
- Pt/3D-G shows the better HER catalytic activity than Pt/C catalyst.
- HER catalytic activity on Pt/3D-G and Pd/3D-G are enthalpy dependent and on Au/3D-G and Ag//3D-G are entropy dependent
- 1T phase of MoS₂ is more HER active than 2H phase.
- MoS₂/GO composite shows better HER catalytic activity than MoS₂/rGO due to better mass transfer.
- Mo doping improves bulk and surface charge separation efficiency.
- SnO₂/BiVO₄ heterojunction improves charge separation and suppress charge recombination
- Cobalt borate (Co-B_i) improves surface catalytic activity of BiVO₄ and improves PEC efficiency
- Photocharging improves the stability of BiVO₄ and Co-B_i modified BiVO₄
- Gamma irradiation decreases the particle size of BiVO₄ and Co-B_i modified BiVO₄
- Gamma treatment improves PEC efficiency of BiVO₄ and BiVO₄/Co-B_i.

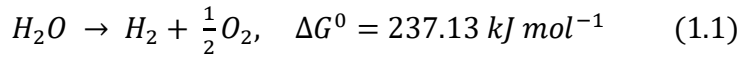
Chapter 1: Introduction of the thesis

1.1 Introduction

The solar energy reaching to the earth surface an hourly is more than the annual global energy consumption [1, 2]. Therefore, solar energy is one of the most promising alternatives to nonrenewable energy. An efficient utilization of solar energy requires conversion and storage of solar energy in the cost-effective and environmentally friendly fashion for the fulfillment of energy demand for sustainable development of mankind [3-5]. Hydrogen is the potential energy carrier due to high energy density [5]. The production of solar hydrogen is the most sought research to store solar energy in the form of chemical energy. The challenge however is the production of solar hydrogen in a cost-effective and efficient manner as compared to the current industrial hydrogen generation [5, 6]. The development of efficient and cost-effective electrocatalysts and photo-electrocatalysts enable the cost-effective solar hydrogen generation. Solar to hydrogen (STH) energy conversion efficiency in the range of 5-10% enables the production of hydrogen on a commercial scale [6]. However, for overall water splitting the STH is in the range of 1% on laboratory scale [5]. For scalability of the hydrogen production based on STH efficiency, development of the efficient electrocatalysts and photo-electrocatalysts are vital. For efficient photo-electrocatalysts, materials must have suitable bandgap and band position, sufficient separation of photogenerated electrons and holes, less photo-corrosion and fast catalytic activity of the materials.

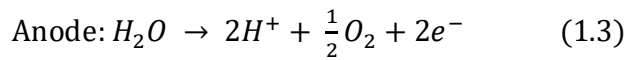
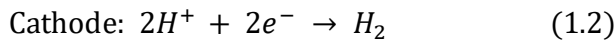
1.2 Principle of water splitting reaction

Water splitting reaction is a thermodynamically unfavorable chemical reaction requires the energy input to overcome the energy barrier as follows

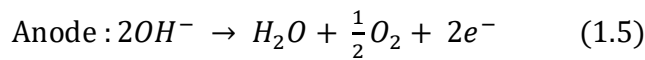
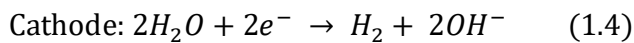


Electrochemical splitting of water consists of the anode, cathode and electrolytes. When an external potential is applied greater than the thermodynamic potential, hydrogen evolution reaction (HER) and oxygen evolution reaction (OER) takes place at cathode and anode respectively. Water splitting reaction depends on the nature of the electrolyte used as follows [7]

In acidic solution



In alkaline solution or neutral solution



The thermodynamic voltage 1.23 V is required for the water-splitting irrespective of the electrolyte is used [8]. For practical application of water splitting, an extra potential is applied to overcome the different polarization. The overall operation voltage for water splitting can be described as follows [9]

$$V_{OP} = 1.23 V + \eta + iR \quad (1.6)$$

Where η , overpotential, is required to overcome the intrinsic energy barrier. The intrinsic energy barrier can be minimized by using highly active HER or OER catalysts. iR is the ohmic potential drop due to solution resistance.

1.3 Hydrogen evolution reaction

The kinetics of hydrogen evolution reaction is complex and strongly dependent on the electrochemical potential as given by Butler-Volmer equation [10]

$$j = j_0 \left[e^{-\alpha n F \eta / RT} + e^{(1-\alpha) n F \eta / RT} \right] \quad (1.7)$$

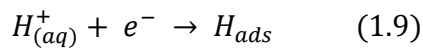
Where j is current density, j_0 is exchange current density, α is charge transfer coefficient, n is the number of electrons transferred, F is the Faraday constant, R is the ideal gas constant and T is the absolute temperature. The exchange current density is the measurement of current density at equilibrium potential. When the overpotential is high ($\eta > 50$ mV), the Butler-Volmer equation is simplified in the form as

$$\eta = a + b \log j = \frac{-2.3RT}{\alpha n F} \log j_0 - \frac{2.3R}{\alpha n F} \log j \quad (1.8)$$

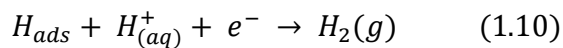
There is a linear relationship between η and $\log j$ with Tafel slope, $b = \frac{2.3RT}{\alpha n F}$. Tafel slope is used to determine the mechanism associated with the HER. The Tafel analysis gives kinetic information such as exchange current density and rate constant.

For efficient electrocatalysis, electrocatalyst should have low overpotential, low Tafel slope and high exchange current density. Overpotential is required to achieve 10 mAcm^{-2} , which is used as benchmark to measure the performance of catalysts. The HER kinetics is strongly influenced by

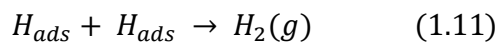
the reaction pathway, which is catalyst dependent and potential dependent. In acidic medium, HER kinetics consists of two steps [11]. The first step is proton discharge at the electrode surface is called Volmer reaction or discharge reaction



Hydrogen desorption process may follow two pathways. The adsorbed hydrogen reacts with the proton of the solution followed by the desorption process. This process is called electrochemical desorption or Heyrovsky mechanism.



Hydrogen desorption process can proceed with the combination of two adsorbed hydrogen. This step is called recombination process or Tafel mechanism.



Tafel slope gives the insight of the rate-determining step and plausible reaction pathway for the hydrogen evolution reaction [10, 11]. The Tafel slope of discharge reaction, electrochemical desorption reaction and recombination reaction are 120 mV per decade, 40 mV per decade and 30 mV per decade respectively. The fast discharging step is followed by either electrochemical desorption step or combination step. If the fast discharging step is followed by slow electrochemical desorption step, Tafel slope will be ~ 40 mV/decade and HER mechanism would be Volmer-Heyrovsky mechanism. If the fast discharging step is followed by the rate-limiting combination step, Tafel slope will be ~ 30 mV/decade and the overall mechanism of the process would be Volmer-Tafel mechanism. When the electrochemical discharging step is the rate-limiting step, the Tafel plot will be ~ 120 mV/decade, and rate-determining follows the Volmer

reaction [12]. It is observed that at low overpotential for Pt in acidic solution, the Tafel slope is ~ 30 mV/decade suggesting that the recombination reaction is the rate-determining step. When overpotential is increased, the coverage of the adsorbed hydrogen atoms approaches the saturation as a result of that, recombination step becomes very fast. Therefore, the discharge step becomes the rate determining step and hence Tafel slope is increased from 30 mV per decade to the ~ 120 mV per decade [13].

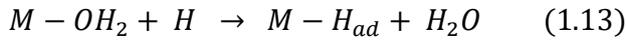
The hydrogen adsorption and desorption processes are successive however; they compete for the overall reaction. When the bonding of hydrogen with the catalyst is too weak, it is very difficult to absorb the hydrogen atom to initiate the HER. When bonding of catalysts with hydrogen is too strong, desorption of hydrogen after completion of reaction will be difficult. For ideal electrocatalyst of HER, hydrogen binding energy and releasing should be balanced. Sabatier principle states that 'in heterogeneous catalysis and electrocatalysis, the optimal catalytic activity can be achieved on the catalytic surface having intermediate energies with reactive intermediates [14]. The maximum current density is obtained when hydrogen adsorption free energy is close to the zero (i.e. $\Delta G_H \sim 0$) [15]. The hydrogen adsorption free energy is an intrinsic property of electrocatalyst.

The temperature-dependent HER kinetics is used to calculate the activation energy of the process and investigate the process as enthalpy or entropy controlled [16]. The improvement of the onset potential of all the catalysts with the increase in temperature can be due to the (1) temperature coefficient of variation of the solution, (2) increased in the mobility of charge in solution, and (3) the endothermic process of water splitting. Quantitative investigation of the dependency of temperature on the electrocatalytic activity can be measured using Arrhenius analysis of the

catalysis process. The apparent energy of activation (E_a^{app}) can be calculated [17, 18] using the following equation.

$$\frac{\partial \ln i}{\partial \left(\frac{1}{T}\right)} = -\frac{E_a^{app}}{R} \quad (1.12)$$

Where T is absolute temperature, R is Universal gas constant, and i is measured current. The activation energy can be calculated from the slope of $\ln i$ vs. $1/T$ plot. In HER kinetics, it is assumed that the proton containing complex to be discharged at the outer Helmholtz layer and discharged transition state is close to the electrode surface. During the discharge step, hydrated protons move from the outer Helmholtz layer to the electrode surface and get discharged closer to the electrode surface and replace the adsorbed water molecule from the electrode surface and get adsorbed as H_{ad} [19-23].



E_a^{app} depends on the binding energy of $M - OH_2$ and $M - H_{ad}$. If binding energy of $M - OH_2$ is greater than the $M - H_{ad}$, activation energy will be more and if the reverse is there, there is very little activation energy is needed. E_a^{app} depends on internal energy, transfer coefficient and overpotential.

$$E_a^{app} = U^\ddagger - U^R + \beta F \eta \quad (1.14)$$

There is a decrease in activation energy for applying electrode potential in the negative direction. Therefore, an increase in the value of $U^\ddagger - U^R$ overcompensates the decrease in activation energy induced by the potential energy of the electron.

Temperature-dependency HER can be further explained based on temperature-dependent variation of transfer coefficients. The catalytic HER would follow the Arrhenius equation as,

$$k_{rds} = A' \exp\left[-\frac{E_a}{RT}\right] \quad (1.15)$$

The transition state theory as a function of applied potentials can be written as,

$$k_{rds} = A \exp\left[-\frac{U^\ddagger - U^R + \beta F \eta}{RT}\right] \quad (1.16)$$

The rate constant thus has the dependency on the energy of the transition state as noted by the transition state theory; it has also got the dependency on the applied potentials. Contribution from both two factors leads to the temperature dependence of the observed current. The contribution of the transfer coefficient plays an import role in determining the observed current with varying temperatures. Further, the temperature dependent Tafel analysis is used to calculate the transfer coefficient. Conway et al. have correlated the transfer coefficient with temperature by the relation [24]

$$\beta = \beta_H + T\beta_S. \quad (1.17)$$

Where β_H and β_S are enthalpy and entropy dependent transfer coefficient, β is total transfer coefficient and T is the absolute temperature. From the linear correlation of the $1/b$ vs. $1/T$ plot, β_H and β_S can be calculated from the slope and intercept of the following equation

$$\frac{1}{b} = \frac{F\beta_H}{2.3RT} + \frac{F\beta_S}{2.3R} \quad (1.18)$$

Where b is Tafel slope for HER. The dependency of β_H and β_S with temperature can be measured and hence the overall process of HER can be identified as enthalpy or entropy dependent process.

Koutechy-Levich Analysis

The reaction at the static electrode depends on the various factors such as; mass transfer, electron transfer, chemical reaction and adsorption and desorption. Typically, in the hydrodynamic method, the rate of mass transfer at the electrode is larger than the rate of diffusion. Therefore, mass transfer is no longer the limiting parameter to the electron-transfer kinetics [10]. Using hydrodynamic effect, double layer charging is avoided, and hence only kinetic limiting current is measured as the function of the rotation rate. The steady-state current is used to determine the diffusion coefficient. A rotating disk electrode is rotated in the solution under study and the current depends on the solution flow rate. The rate of mass transport at the rotating disk electrode is varied by altering the disk rotation speed. The rotating electrode is mounted vertically to a controllable-speed motor and rotated with constant angular velocity. The components of the fluid velocity depend on this angular velocity of the disk, which is given by $\omega = 2\pi f$, where f is the rotation speed in revolutions per minutes (rpm) or rotation frequency in hertz. It depends on other factors such as the radial distance from the center of the disk (r), the coefficient of kinematic viscosity of the fluid (ν) and on the axial distance from the surface of the disk. The kinetic investigation about the contribution from the charge transfer and mass transfer kinetics can be investigated by the Koutechy-Levich analysis using the following equation [25]

$$\frac{1}{i} = \frac{1}{i_k} + \frac{1}{i_l} \quad (1.19)$$

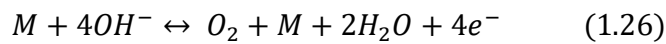
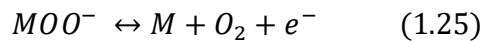
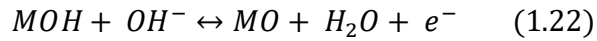
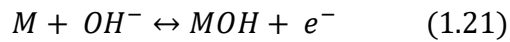
$$\frac{1}{i} = \frac{1}{i_k} + \frac{1}{B\omega^{1/2}} \quad (1.20)$$

Where $i_k = nFAkC_0$ and $B = 0.2nFC_0D^{2/3}\nu^{-1/6}$. i , i_k and i_l are measured current, kinetic current and limiting current, respectively. ω is the rotation rate of the electrode in rpm. k is electron-transfer rate constant, n is number of electron transfer, $F = 96500 \text{ C mol}^{-1}$, A is surface

area of rotating disk electrode in cm^2 , C_0 is concentration of H^+ in bulk solution in mol cm^{-3} , D is diffusion coefficient of proton in 0.5 M H_2SO_4 and value corresponds to $9.3 \times 10^{-5} \text{ cm}^2 \text{ s}^{-1}$, ν is the kinematic viscosity of 0.5 M H_2SO_4 and value is $0.01 \text{ cm}^2 \text{ s}^{-1}$ [26]. The kinetic parameters as the number of electrons transferred, transfer coefficient, rate constant and exchange current density can be determined. The intercept of i^{-1} vs. $\omega^{-1/2}$ plot is inversely proportional to the kinetic limiting current. The rate constant is determined by using the kinetic current measurements. The slope of the plot is inversely proportional to the diffusion limiting current and the number of electrons transferred can be calculated. Koutechy-Levich analysis method has limitation for multi-electron transferred reaction. For multi-step reaction, Koutechy-Levich analysis is applied to one step at a time. For multi-step reaction, rate constant determination is for the rate-determining step of the overall multi-step reaction. Tafel slope is used for rate constant calculation for the rate-determining step of multi-step reaction.

1.4 Oxygen evolution reaction

Oxygen evolution reaction (OER) mechanism and pathways are more complex as compared to HER mechanism. In the overall water splitting reaction, OER is the rate limiting because of sluggish kinetics as compared to the HER. The OER catalysts are mainly of metal oxide-based catalysts and mechanism associated with the different catalysts are different. The different electro-kinetic of the catalysts is due to the various factors such as morphology, conductivity, thickness, preparation method. The general mechanism of OER in alkaline medium is proposed as, [27]



The performance of OER is compared in terms of overpotential, Tafel slop, exchange current density, Faradaic efficiency, and turnover frequency.

Overpotential (η)

For the real system, the extra driving force is required than the thermodynamic potential for the water splitting is called overpotential. For both the HER and OER, overpotential is needed to compensate for the activation polarization, concentration polarization and iR loss. The activation polarization is the intrinsic property of the material and can be minimized by choosing the efficient catalysts. The concentration polarization is due to concentration drop near the interface and can be minimized by stirring the solution. Potential drop due to iR loss can be subtracted from the experimental potential. The onset potential is calculated from the plot of polarization vs. current density. Calculation of overpotential for OER is more complex than the HER. The OER mechanism as given above proceed through the first elementary step of water coordination in an acidic solution or hydroxide ion coordination in alkaline solution is followed by other elementary steps. The activation energy associated with each of these steps will

contribute to the overall activation overpotential of the OER catalyst. The theoretical OER overpotential (η_{OER}) for ideal conditions i.e. $U=0$ vs. RHE, can be calculated as follows [28]

$$\eta_{OER} = (\Delta G_{max}/e) - 1.23 \text{ V} \quad (1.27)$$

The kinetic hindrance is not considered in the thermodynamic consideration of the onset potential. The overpotential at 10 mA cm^{-2} is widely used to compare the performance of the electrocatalysts [29].

Tafel slope and exchange current density

The Tafel slope is inversely proportional to the charge transfer coefficient as given in equation 1.28.

$$\frac{d \log j}{d \eta} = \frac{2.3 RT}{\alpha n F} \quad (1.28)$$

The number of electrons transferred (n) is equal to 2 for HER and 4 for the OER. This shows that catalysts having high charge transferability will show small Tafel slope. Therefore, Tafel slope is used as the primary parameter in determining the catalytic activity.

The exchange current density is another important parameter to characterize the performance of electrocatalysts. The exchange current density is directly correlated to the onset potential for HER and OER. Therefore, Tafel slope, onset potential and exchange current density are activity parameters.

1.5 Photoelectrochemical water splitting

In photoelectrochemical (PEC) water splitting, there is formation of electron and holes in the presence of illumination. Photo-excited electrons are moved from valance band to the

conduction band and the photogenerated holes are in the valence band of the semiconductor. The photogenerated electrons and holes reduce water to hydrogen and oxidize water to oxygen respectively depending on the band position of the semiconductor as shown in Figure 1.1.

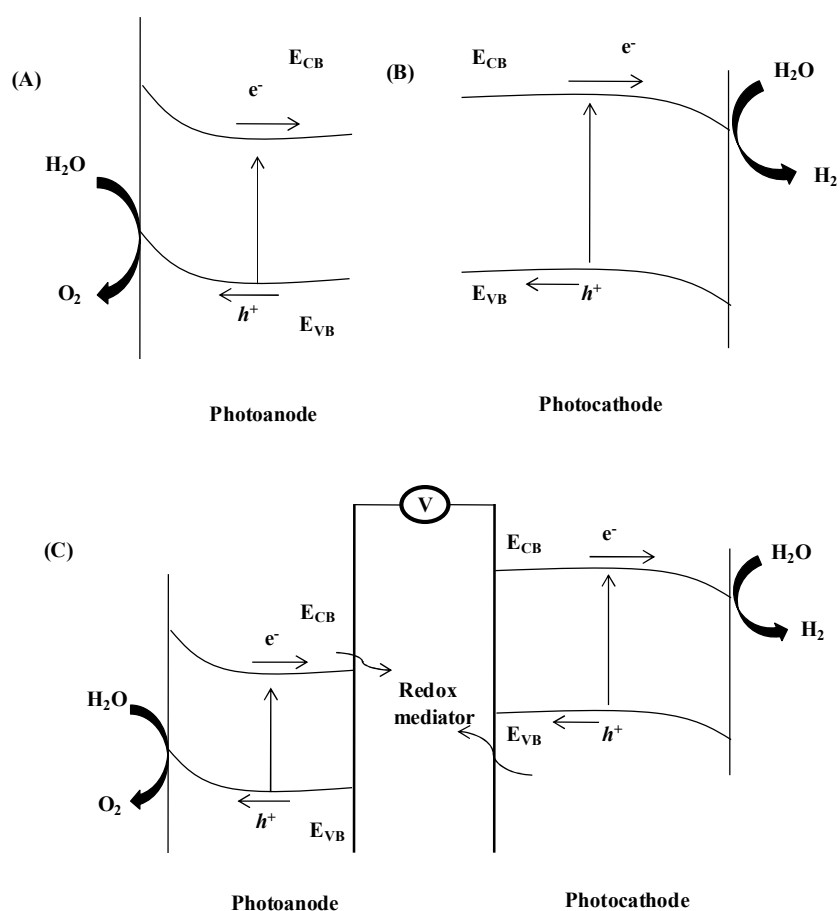


Figure 1.1 Schematic of the photoelectrochemical splitting of water for (A) photoanode, (B) photocathode and (C) Z-scheme for the complete cell.

When the bottom of the conduction band is more negative to the proton reduction potential, reduction of proton takes place. When the top of the valence band is more positive to the water oxidation potential, oxidation of water takes place. The semiconductor having bandgap larger

than the thermodynamic required energy 1.23 eV and suitable band position is the prerequisite of PEC water splitting. The narrow bandgap of semiconductor improves the STH efficiency; however, narrowing the bandgap decreases the driving force to compensate the activation energy barrier. Water is oxidized to oxygen by the photogenerated holes in the valence band and oxidized redox mediator is reduced by photogenerated electrons in the conduction band. The overall water splitting reaction is completed with the redox mediator [5]. In Z-scheme, the application of a wide range of narrow bandgap semiconductor can have conduction band negative to the hydrogen evolution potential or valence band is positive to the water oxidation potential. Therefore, the maximum solar energy can be harvested using the Z-scheme cell setup.

In two-step excitation steps, hydrogen evolution photocatalyst and oxygen evolution photoelectrocatalyst mediated with the redox mediator as shown in Figure 1.1 (C). In a typical method, proton reduction takes place by the photogenerated electrons of the conduction band and the redox mediator is oxidized by the photogenerated holes in the valence band on the In pure BiVO_4 photoanode, photogenerated electrons get transferred to the conduction band and the photogenerated holes are in the valence band, which are transferred to the water molecule for the oxidation process of water. The trapped holes at the interface of the photoanode may get transferred to the defect state of the FTO/ITO. The photogenerated holes and electrons get recombine to the interface or at the defect state. The heterojunction of $\text{SnO}_2/\text{BiVO}_4$ is used to suppress the recombination process of the photogenerated electrons and holes as illustrated in Figure 1.2. The back electron-hole recombination process can be completely blocked by heterojunction modification. The interfacial kinetics of water oxidation reaction (WOR) can be improved by incorporation of electrocatalysts as Co-Bi on the BiVO_4 . Co-Bi collects hole at interface and facilitates the efficient hole transfer to the water molecule for WOR. Therefore,

photogenerated charge recombination suppress and as a result of overall PEC efficiency increased.

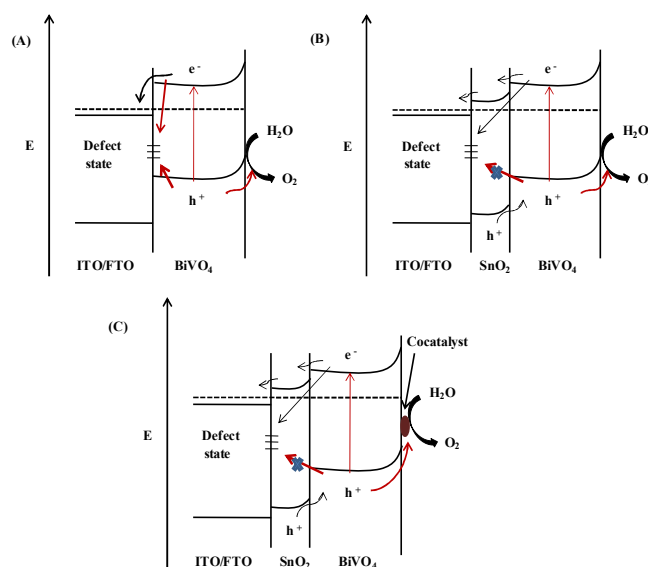
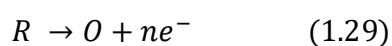


Figure 1.2 Schematic representation of photogenerated electrons and holes in the (A) BiVO₄ photoanode, (B) effect of heterojunction of SnO₂ on BiVO₄ electron-hole mobility and (C) effect of the cocatalyst on the hole transfer of BiVO₄ photoanode.

1.6 Scanning Electron Microscopy (SECM)

Scanning electrochemical microscopy (SECM) is a scanning probe microscopy technique, capable of imaging substrate (insulating, semi-conductive or conductive) topography and local activity with high temporal and spatial resolution [10]. An ultra-microelectrode of diameter 10 μm or less is used as the tip/probe in the close proximity to a surface of interest. The electrochemical response of the tip of the substrate in the response of tip provides the qualitative and quantitative information of the interfacial region. This technique is widely used in the variety

of research area as kinetics, research on energy materials, corrosion, biology (i.e. molecular transport across the membrane, adsorption/desorption process, the activity of living biological cells), instrumental development and surface modification. SECM technique is mainly applied in the different mode of operation such as feedback mode, generation/collection mode and redox completion mode. In the feedback mode, the tip current is measured as the function of the approaching distance to the substrate.



The faradaic current of the tip depends on the topography and electrochemical activity of the substrate. For probe of disk geometry, the steady-state current is defined as $i_{T,\infty} = 4nFDCa\beta$ where n is the number of electrons transferred, F is Faraday constant, D is diffusion coefficient of the redox mediator, C is the concentration of redox mediator, a is the tip area and β is the geometric co-efficient [30]. When the tip approaches the substrate, the tip current is perturbed by the presence of the substrate either by regeneration of R at the substrate (positive feedback, ($i_T > i_{T,\infty}$)) or by blockage of the diffusion of redox mediator R to the tip (negative feedback, ($i_T < i_{T,\infty}$)). The tip to substrate distance can be calculated using the feedback approach curve. The topographical information of the substrate can be obtained from the feedback current measurements as the feedback response is highly depended on the tip to substrate distance. The approach curve is used to determine the heterogeneous rate constant at the interface [10, 31]. For the disk-shaped tip, the normalized approach curve can be fitted using the following equations; [10]

For the insulator substrate

$$I_T(L) = 0.292 + \frac{1.5151}{L} + 0.6553 \exp\left(\frac{-0.2035}{L}\right) \quad (1.30)$$

For the conductive substrate

$$I_T(L) = 0.68 + \frac{0.78377}{L} + 0.3315 \exp\left(\frac{-1.0672}{L}\right) \quad (1.31)$$

Cornut et.al have given the more comprehensive theoretical mode for the fitting of the approach curve [32]

$$I_T^{ins}(L, RG) = \frac{\frac{2.08}{RG^{0.358}} \left(L - \frac{0.145}{RG}\right) + 1.585}{\frac{2.08}{RG^{0.358}} (L + 0.0023RG) + 1.57 + \frac{LnRG}{L} + \frac{2}{\pi RG} Ln\left(1 + \frac{\pi RG}{2L}\right)} \quad (1.32)$$

$$I_T^{cond}(L + \kappa^{-1}, RG) = \alpha(RG) + \frac{\pi}{4\beta(RG) \arctan(L + \kappa^{-1})} + \left(1 - \alpha(RG) - \frac{1}{2\beta(RG)}\right) \frac{2}{\pi} \arctan(L + \kappa^{-1}) \quad (1.33)$$

$$I_T(L, \kappa, RG) = I_T^{cond}\left(L + \frac{1}{\kappa}, RG\right) + \frac{I_T^{ins}(L, RG) - 1}{(1 + 2.47RG^{0.31}L\kappa)(1 + L^{0.006RG+0.113\kappa^{-0.023RG+0.91}})} \quad (1.34)$$

$$I_T = I_s \left(1 - \frac{I_T^{ins}}{I_T^{cond}}\right) + I_T^{ins} \quad (1.35)$$

$$\alpha(RG) = \text{Ln}2 + \text{Ln}2 \left(1 - \frac{2}{\pi} \text{arcCos} \left(\frac{1}{RG} \right) \right) - \text{Ln}2 \left(1 - \left(\frac{2}{\pi} \text{arcCos} \left(\frac{1}{RG} \right) \right)^2 \right) \quad (1.36)$$

$$\beta(RG) = 1 + 0.639 \left(1 - \frac{2}{\pi} \text{arcCos} \left(\frac{1}{RG} \right) \right) - 0.186 \left(1 - \left(\frac{2}{\pi} \text{arcCos} \left(\frac{1}{RG} \right) \right)^2 \right) \quad (1.37)$$

Where $RG = r_{\text{glass}}/r_T$ is the ratio of the radius of glass sheath (r_{glass}) to the radius of the active area of Pt UME (r_T), I_T^{cond} is diffusion control current for conducting substrate i.e. positive feedback, I_T^{ins} is diffusion control current for insulating substrate i.e. negative feedback.

The details reaction mechanism of PEC regeneration has been developed under the steady-state SECM using $[\text{Fe}(\text{CN})_6]^{4-} / [\text{Fe}(\text{CN})_6]^{3-}$ redox probe on the photoanode [33, 34].

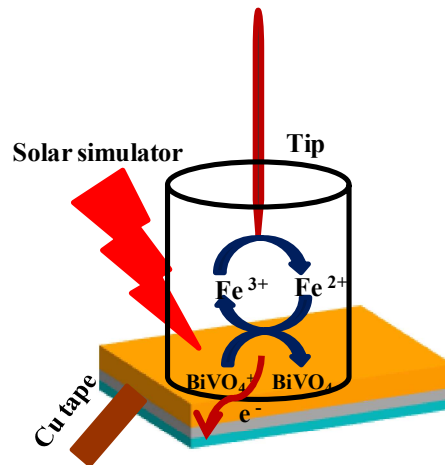
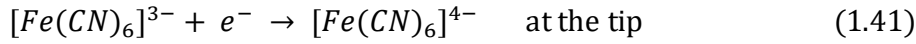
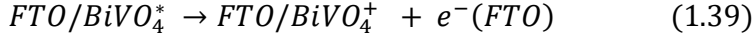


Figure 1.3 Schematic representation of the measurements of interfacial charge transfer of BiVO₄ photoanode in illumination.

The mechanism of the hole transfer at the interface



For steady-state approximation, the above equations can be solved as

$$\frac{1}{I_s} = \frac{1}{I_{T,cond}} + \frac{4D_{diffusion}[Fe^{3+}]^*}{\pi r_T l [BiVO_4^0] \phi_{hv} J_{hv}} + \frac{4D_{diffusion}}{\pi r_T l [BiVO_4^0] k'_{ox}} \quad (1.42)$$

For the first-order reaction, the following expression is in correlation with the feedback approach curve [30, 35].

$$\frac{1}{I_s} = \frac{1}{I_{T,cond}} + \frac{1}{\pi \kappa} \quad (1.43)$$

$$k_{eff} = \kappa \frac{D_{diffusion}}{r_T} \quad (1.44)$$

Normalized probe approach curves are fitted using the above equations at different κ and the interfacial effective rate constant (k_{eff}) is calculated using equation 1.44.

1.7 Hydrogen evolution catalysis

In acidic solution, Pt group metals are the most effective catalyst for the hydrogen generation [36-41]. The recent advancement in the noble metal-based catalysis has been achieved by the bimetallic and trimetallic materials such as PtPd, PtCu, AuPd@Pd, and PtRhCo for the HER, oxygen reduction reaction (ORR) and alcohol oxidation reaction [42-45], but due to

the high cost of the Pt group metal elements, large scale application using these elements is not economically viable [46-49]. Thus, there is a trust for the development of multifunctional materials in the scientific community. It was demonstrated that three-dimensional graphene (3D-G) composites with PtPdCu and Pd₂/PtFe show good catalytic activity for alcohol oxidation reaction [50, 51]. Feng and coworkers have synthesized AuPd@Pd and 3D-G composite for the alcohol oxidation reaction [44]. Noble metal (3D-G) composite materials have been synthesized by freeze casting method for the applications such as catalysis, supercapacitor, antibacterial activity and electromagnetic interference shielding [52-54]. However, the HER kinetics of the noble metal (Pt, Pd, Au and Ag) and 3D-G composite is not much investigated. For the development of knowledge in the field, the kinetic and thermodynamic investigation needs to be done.

Different transition metal alloys, carbides, polymeric carbon nitride, and transition metal chalcogenides are a better choice as HER catalyst, due to their earth abundant nature and comparable efficiency [55-61]. Thus, there is a trust for the development of multifunctional materials for this research. Among the electrocatalyst, molybdenum disulfide (MoS₂) has attracted much attention due to the low cost and high catalytic activity, high chemical stability, large in-plane carrier mobility and good mechanical properties [57, 58, 62, 63]. It has been reported that the monolayer MoS₂ has higher electrocatalytic activity for HER; however, there are some shortcoming as lower intrinsic catalytic activity, poor interlayer conductivity and the limited number of active sites. The catalytic activity of 2H phase is mostly through the edges of the catalytic system [64, 65] and is improved by the increase in the percentage of active edge sites [66-73]. The basal plane of the 1T-MoS₂ is electrochemically active for the HER catalytic activity [74-76] which improves the electrical conductivity as compared to the 2H-MoS₂. 1T-

MoS₂ with highly conducting basal plane and graphene composites will improve the HER catalytic activity [77].

It has been focused on the synthesis of three-dimensional graphene (3D-G) by the environmentally friendly freeze-drying method and utilize the high porosity and surface area for the HER kinetics. Noble metal –3D-G composites have been synthesized to reduce the loading of the noble metal. These composite materials have been used for the understanding of the molecular level kinetics of the HER on noble metal/(3D-G) composite materials. Then, transition metal-based catalysts MoS₂ has been investigated to reduce the loading of the noble metal in HER. The electrochemical investigation has been carried out to determine the forward rate constant, the number of electrons transferred, exchange current density and transferred coefficient. The Tafel analysis has been performed to compare the performance of the electrocatalyst. To understand the kinetics of the HER, temperature dependent Tafel analysis has been performed and enthalpy and entropy dependency of HER is evaluated.

1.8 Oxygen evolution catalysts

The photoanode materials such as TiO₂, α -Fe₂O₃, WO₃ and BiVO₄ have been used for the OER [78-86]. Among these materials, BiVO₄ is the most researched photoanode due to its suitable band position, bandgap and high theoretical efficiency ($\sim 7.5 \text{ mAcm}^{-2}$) and high solar to hydrogen (STH) conversion efficiency ($\sim 9\%$) [87-90]. However, the slow surface catalytic activity, short hole diffusion length, fast electron-hole recombination are major challenges with the BiVO₄ [78, 91-94]. To overcome these challenges, a number of the strategies have been widely investigated such as; nanostructure control [95-98], band engineering [89, 99-106], heteroatom doping [107-113], generation of oxygen vacancy [94, 114-116] and the oxygen

evolution catalyst (OEC) incorporation [90, 117-125]. SnO_2 has been used for the heterojunction formation in the BiVO_4 system which suppresses the back electron-hole recombination process [89]. Additionally, the SnO_2 underneath of BiVO_4 blocks the surface state of the ITO/FTO. These modifications improve the injection of the photogenerated holes to the electrode-electrolyte interface; however, the sluggish kinetics of BiVO_4 interface limits the performance. Therefore, oxygen evolution co-catalyst (OEC) is used for the surface modification to accelerate the OER kinetics and suppress the surface charge recombination. A number of the OEC such as CoPi [90, 94, 108, 110, 117, 120, 126], Co-B_i [83, 127-129], Ni-Bi [130], NiOOH/Ni-borate [130, 131], FeOOH [132, 133], Ni(Fe)OOH [134] and FeOOH/NiOOH [87] have been investigated to improve the onset potential and suppress the charge recombination for the PEC water oxidation. Among all, Co-based cocatalyst, especially CoPi has been extensively investigated because of low cost and excellent catalytic activity in PEC water oxidation [90, 94, 108, 110, 117, 119-121, 126]. CoPi is stabilized in the phosphate buffer, but the phosphate buffer solution is corrosive to the BiVO_4 photoanode [135]. The borate buffer solution is recently found relatively less corrosive to the BiVO_4 for the PEC water oxidation reaction [83, 134, 136]. Therefore, Co-B_i would be the promising materials for the PEC water oxidation reaction. Previous reports shown the improved catalytic activity of the Co-B_i modified BiVO_4 [129].

The gamma radiation has been used to alter the physical and chemical properties of materials such as optical, electrical, electronic and structural properties of the materials [137, 138]. The alteration of chemical bonds due to the irradiation may improve the performance of materials. Gamma radiation strongly affects the metal-based oxide materials for the biosensor and gas sensor application [139-141]. The grain size and bandgap of the ZnO thin film have been decreased upon the gamma irradiation [137]. The electron mobility of the In-ZnO based

transistor has been improved upon exposure to the radiation [142]. The enhancement of the gas sensing sensitivity is due to the defect generation of the nanoparticles. The sensitivity of the SnO₂ based gas sensor for CO is improved upon the gamma irradiation [143]. There is red-shift of absorption of the InVO₄ with the increase in the dose of gamma irradiation [144]. The sensitivity of InVO₄ based sensor for ammonia is improved significantly and is due to the defect introduction. The performance of TeO₂ has been linearly improved with the increase of γ radiation dose. The gamma effect on the absorption spectra and energy bandgap of SeO₂ were reported to significantly increase the optical absorption due to the change of chemical structure. The structural and optical properties of CdS, PbS, Fe_{3-x}O₄ thin film, were also reported to improve the bandgap [145]. Gamma radiation has changed the bonding structure of g-C₃N₄ which reduces the optical bandgap energy. The PEC efficiency of irradiated g-C₃N₄ is enhanced two folds as compared to the non-irradiated g-C₃N₄. The performance of irradiated g-C₃N₄ in the g-C₃N₄/BiVO₄ heterojunction has been improved by two folds [146].

Considering the shortcoming of BiVO₄, our focus of work is to improve the catalytic efficiency of the BiVO₄ photoanodes with SnO₂ as the interlayer. BiVO₄ was doped with Mo to further improvement of the catalytic activity. The SnO₂ coating over the ITO plate was carried out for suppressing the charge recombination process through the generation of heterojunction of SnO₂ and BiVO₄. Further, the PEC efficiency of the BiVO₄ is improved by the incorporation of the Co-Bi as a cocatalyst for the OER. We have investigated the PEC, optical, structural, chemical, and electronic properties of the Co-Bi modified BiVO₄ upon the photocharging for further insight into the physical and chemical mechanism behind the photocharging. In this study, first, we have optimized the thickness of the Co-Bi loading on the BiVO₄ photoanode and studied the PEC, optical, structural, and electronic properties of the catalysts. After that, photocharging of the

photoanodes under the applied bias has been performed. Secondly, we have used the impedance spectroscopy technique and Mott-Schottky analysis to investigate the effect of photocharging on the electronic properties of the photoanodes. Finally, scanning electrochemical microscopy (SECM) study has been employed to study the interfacial charge transfer kinetics at the interface before and after the photocharging [147]. We have demonstrated the photocharging as a noble approach to improve the PEC efficiency of the Co-Bi modified BiVO₄ photoanodes. Gamma irradiation and plasma treatment as a tool are used for the improvements of the PEC efficiency of BiVO₄.

Chapter 2: Experimental Procedures

In this chapter the brief description of the electrochemical and photoelectrochemical techniques have been discussed. Among different techniques the frequently used techniques like; Cyclic voltammetry (CV), Linear sweep voltammetry (LSV), Chronoamperometry (CA), Chronopotentiometry (CP), Rotatory disk electrode (RDE), UV-Vis Spectroscopy, Incident photon to current efficiency (IPCE), Absorbance photon to current efficiency (APCE), Faradic efficiency, Solar to hydrogen efficiency (STH), Charge transfer efficiency, Charge transport efficiency, Mott-Schottky plot, Transient time Electrochemical impedance spectroscopy (EIS), Scanning electrochemical microscopy (SECM), X-ray diffraction (XRD), FTIR Raman spectroscopy), Scanning electron microscopy (SEM), Atomic force microscopy (AFM), X-ray photoelectron spectroscopy (XPS), High resolution transmission electron microscopy (HR-TEM), energy dispersive spectroscopy (EDS) are briefly in this chapter.

2.1 Electrochemical and photoelectrochemical techniques

2.1.1 Cyclic Voltammetry (CV)

The cyclic voltammetry technique is the most widely used voltammetry technique for the ability to provide thermodynamics and kinetics information of the electroactive species [10, 148]. The potential of the working electrode (WE) is ramped in the triangular V-t wave form for the excitation signal as shown in Figure 1 (A). Typically, the potential of working electrode is linearly varied from the initial potential (let say V_i) to the terminal potential (V_f) and the direction of the potential is reversed to the initial potential (E_i). The rate at which the potential of

the working electrode is varied with time is called scan rate. The current of the working electrode is plotted against the applied potential is called the cyclic voltammogram. Figure 1 (A) shows the typical cyclic voltammogram of the reversible redox system for the heterogeneous catalysis system.

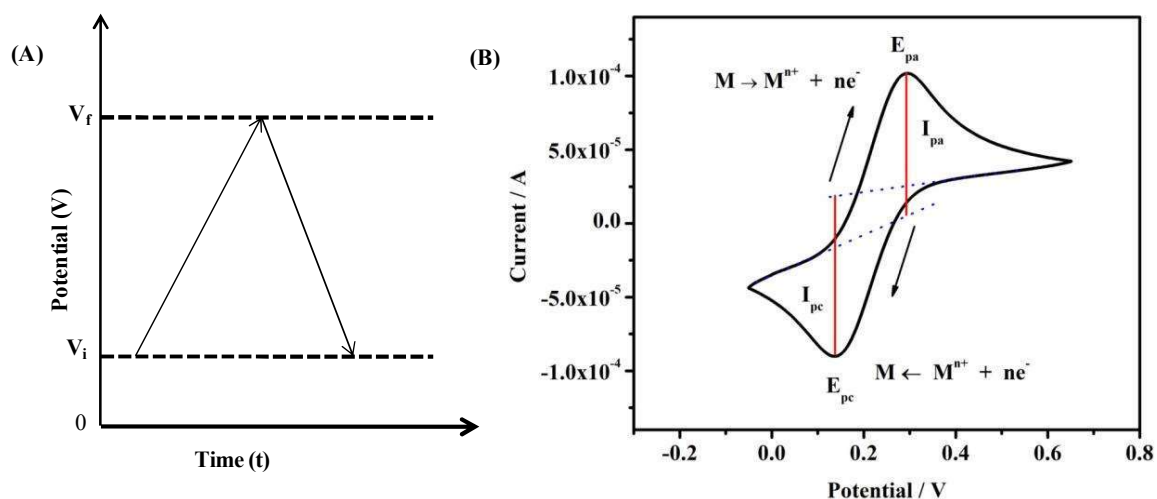


Figure 2.1 (A) Potential time functions for the excitation signal in cyclic voltammetry and (B) typical cyclic voltammogram for the reversible electrochemical reaction.

Reversible process

A reversible process is one in which the electron transfer process is rapid and the electroactive oxidized (or reduced) species in the forward scan is in equilibrium with the electroactive reduced (or oxidized) species in the reverse scan as shown below:



In reversible reactions, the magnitudes of I_{pc} and I_{pa} are equal and proportional to the concentrations of active species. In reversible reactions, ΔE_p ($E_{pa} - E_{pc}$) is independent of the scan rate (v) but in practice ΔE_p slightly increases with increase in v value. This is due to the

solution resistance (R_s) between the reference and working electrodes [10]. Theoretically, for reversible electrochemical reactions, the potential difference, ΔE_p between the oxidation and reduction peaks is ~ 59 mV. However, in practice, ΔE_p is sometimes found to vary slightly. Reversibility is a direct and straight forward means of probing the stability of an electroactive species. An unstable species reacts as it is formed and hence produces no current wave in the reverse scan whereas a stable species remains in the vicinity of the electrodes surface and produces a current wave that is opposite to the forward scan. Larger differences or asymmetric reduction and oxidation peaks are an indication of quasi reversible or irreversible reactions. The peak current for reversible process is given by the Randle-Sevcik equation as shown below [10]

$$I_p = (2.69 \times 10^5) n^{3/2} A D^{1/2} C v^{1/2} \quad (2.2)$$

where I_p is the peak current (A), n is the number of electrons transferred, A is the electrode area (cm^2), C is the concentration of electroactive species (mol cm^{-3}), D is the diffusion coefficient ($\text{cm}^2 \text{ s}^{-1}$) and v is the scan rate (V s^{-1}). These parameters make CV suitable for the characterization and mechanistic studies of redox reactions at electrodes.

Irreversible process

In an irreversible process, the reaction occurs only in one direction-either oxidation or reduction. In this, E_p changes with v because the current takes more time to respond to the applied voltage than in reversible case. The Randle-Sevcik equation for the irreversible process is as follows [10]

$$I_p = (2.99 \times 10^5) \alpha n^{3/2} A D^{1/2} C v^{1/2} \quad (2.3)$$

Where α is charge transfer coefficient. The irreversible systems are characterized using the equation shown below [10]

$$E_p = E^{0'} + \frac{RT}{\alpha n F} \left[\ln \frac{(RT k_s)}{\alpha n F} - \ln v \right] \quad (2.4)$$

The values of k_s and αn are deduced from the intercept and slope of the linear plot of E_p vs. $\ln v$, when the value of $E^{0'}$ is known. The value of $E^{0'}$ is obtained from the intercept of the plot of E_p vs. v .

Quasi-reversible system

In this system, both the electron transfer and mass transport control the current. The shape of the cyclic voltammogram is a function of the ratio, $k_0/[\pi\gamma nFD/RT]^{1/2}$. As the ratio increases, the process approaches the reversible case. Overall, the voltammogram of quasi-reversible system exhibits a larger separation in peak potentials compared to that for a reversible system. For small values (i.e., at very fast v), the system exhibits an irreversible behavior [10].

2.1.2 Linear sweep voltammetry

LSV is a method where current at working electrode is measured with the linear sweep of electrode potential with time as shown in Figure 1.2 (A). Figure 1.2 (B) shows the measurement of the working electrode current with respect of potential applied. In LSV, only the first half-cycle of a cyclic voltammogram is executed. LSV is used to identify unknown species and determine the concentration of solution. $E_{1/2}$ is used for the identifying unknown species and limiting current is used to determine the concentration. LSV is used to compare the performance of catalysts for hydrogen evolution reaction (HER) and oxygen evolution reaction (OER).

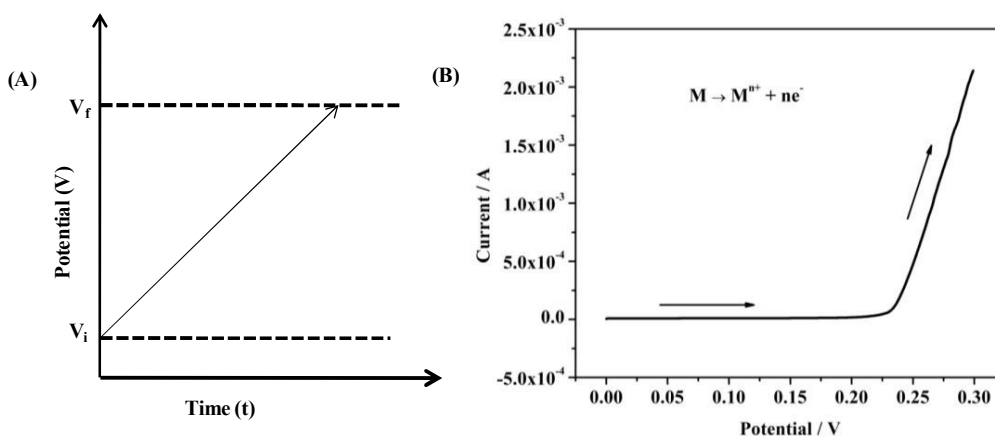


Figure 2.2 (A) Potential time functions for the excitation signal in linear sweep voltammetry and (B) typical linear sweep voltammogram for electrochemical reaction

2.1.3 Chronoamperometry

In chronoamperometry, current of the electrolytic cell is measured with respect to the time at constant applied potential. In this measurement, a stationary working electrode and unstirred solution are being usually used. Under these conditions, the mass transport is solely by diffusion, current-time curve reflects the change in the concentration gradient in the vicinity of the electrode surface. This involves gradual expansion of the diffusion layer associated with the depletion of analyte species and hence decreased the slope of the concentration profile as time progress [10]. Accordingly, the current decays with time, as given by the Cottrell equation indicated below:

$$I_p(t) = nFACD^{1/2}\pi^{-1/2}t^{-1/2} \quad (2.5)$$

where n , F , A , C , D and t are the number of electrons, Faraday's constant, the surface area of electrode, the concentration of the analyte, the diffusion coefficient and time, respectively. This technique is often used for measuring the diffusion coefficient of electroactive species and surface area of the working electrode. In addition, some analytical applications of this method

rely on pulsing of the potential of the working electrode repetitively at fixed time intervals. This technique is being used for the determination of a wide range of bioactive compounds at bare and modified electrodes [10] and stability test of the electrocatalysts and photo-electrocatalysts. The double layer potential step method is used to measure the rate constant of chemical reaction and adsorption process. Chronoamperometry measurements under the hydrodynamic condition enhance the mass transport of electroactive species and hence the sensitivity of the detection enhanced.

2.1.4 Chronopotentiometry

Chronopotentiometry is widely used technique, where current is applied to the electrode and the potential changes are monitored as the function of time. At certain interval of time, the flux of redox species to the surface cannot sustain this current and the potential changes rapidly to a new value at which another species is reduced or oxidized. This time interval is termed as transition time τ , follows the Sand equation

$$\tau^{1/2} = \pi^{1/2} n F D^{1/2} C^* / 2i_0 \quad (2.6)$$

where i_0 is the current density (i/A). Diffusion coefficients can be calculated using above equation. The advantage of chronopotentiometry is that the τ value is directly proportional to D, and that τ is the same regardless of heterogeneous electrode kinetics.

2.1.5 Rotating disk electrode (RDE)

The reaction at the static electrode depends on the various factors as mass transfer, electron transfer, chemical reaction and adsorption and desorption. Typically, in hydrodynamic method, the rate of mass transfer at the electrode is larger than the rate of diffusion. Therefore, mass transfer is no longer the limiting parameter to the electron-transfer kinetics. Using

hydrodynamics effect, double layer charging is avoided, and hence only kinetic limiting current is measured as the function of the rotation rate. The steady state current is used to determine the diffusion coefficient. A rotating disk electrode is rotated in the solution under study and the current depends on the solution flow rate. The rate of mass transport at the rotating disk electrode is varied by altering the disk rotation speed. The rotating electrode is mounted vertically to a controllable-speed motor and rotated with constant angular velocity. The components of the fluid velocity depend on this angular velocity of the disk, which is given by $\omega = 2\pi f$, where f is the rotation speed in revolutions per minutes (rpm) or rotation frequency in hertz. It depends on other factors such as the radial distance from the center of the disk (r), the coefficient of kinematic viscosity of the fluid (ν) and on the axial distance from the surface of the disk.

In RDE experiment, linear sweep voltammetry is recorded at the different rotation at low scan rate. The detail kinetic investigation about the contribution from the charge transfer and mass transfer kinetics can be investigated by the Koutechy-Levich analysis using following equation

$$\frac{1}{i} = \frac{1}{i_k} + \frac{1}{i_l} \quad (2.7)$$

$$\frac{1}{i} = \frac{1}{i_k} + \frac{1}{B\omega^{1/2}} \quad (2.8)$$

Where $i_k = nFAkC_0$ and $B = 0.2nFC_0D^{2/3}\nu^{-1/6}$. i , i_k and i_l are measured current, kinetic current and limiting current, respectively. ω is rotation rate of electrode in rpm. k is electron-transfer rate constant, n is number of electron transfer, $F = 96500$ C/mol, A is surface area of RDE in cm^2 , C_0 is concentration of H^+ in bulk solution in mol cm^{-3} , D is diffusion coefficient of proton in 0.5 M H_2SO_4 and value corresponds to $9.3 \times 10^{-5} \text{ cm}^2\text{s}^{-1}$, ν is the kinematic viscosity of 0.5 M H_2SO_4 and value is $0.01 \text{ cm}^2 \text{ s}^{-1}$ [26]. The kinetic parameters as number of electrons transferred, transfer coefficient, rate constant and exchange current density can be determined.

The intercept of i^{-1} vs. $\omega^{-1/2}$ plot is inversely proportional to the kinetic limiting current. The rate constant is determined by using the kinetic current measurements. The slope of the plot is inversely proportional to the diffusion limiting current and number of electrons transferred can be calculated. Koutechy-Levich analysis method has limitation for multi-electron transferred reaction. For multi-step reaction, Koutechy-Levich analysis is applied to one step at a time. For multi-step reaction, rate constant determination is calculated for the rate determining step (RDE).

2.1.6 Ultraviolet-visible (UV-Vis) Spectroscopy

In UV-Vis spectroscopy, absorption of light as the function of wavelength provides the electronic transition in the material. Beer-Lambert law states that the fraction of light (transmittance or reflected) measured after interaction with the sample is function of the path length (l) of light through the sample, the absorption cross-section (σ) of the transition, and the difference in the population in the initial state (N_1) and final state (N_2) of initial (E_1) and final (E_2) electronic energy levels.

$$\frac{I}{I_0} = e^{-\sigma(N_1-N_2)l} \quad (2.9)$$

In the simple format the Beer's law can be written as

$$A = \epsilon cl = -\log_{10}\left(\frac{I}{I_0}\right) \quad (2.10)$$

Where A is absorbance, ϵ is the molar absorptivity coefficient of the material, c is the concentration of the absorbing species, and l is the path length of the light.

The absorption coefficient α can be determined by using following equation

$$\alpha (cm^{-1}) = \frac{\ln(10) \times A}{l(cm)} \quad (2.11)$$

The optical Bandgap of the semiconductor is determined by using UV-Vis spectroscopy as it measures the electronic transition from the valance band (VB) to the conduction band (CB). The exciton binding energies, phonon absorptions and emission, d-d transitions, and excitations to or from defect bands and color centre can complicate the interpretation of the UV-Vis spectra [149]. UV-Vis spectroscopy allows the characterization of the electronic transition as either direct or indirect. It further characterizes the allowed or forbidden transition. The direct transition is modeled as the two particles interaction between an electron and a proton and indirect transition is modeled as three particles interaction among photon, electron and phonon to ensure momentum conservation [149]. A transition is allowed or forbidden depending on the dipole selection rules associated with the system. The shape of the UV-Vis spectra can reveal the types of the transitions by analyzing the Tauc plots.

The photon absorption efficiency can be written as the following

$$A_{\%} = n_{e^{-}/h^{+}} = 1 - \frac{I}{I_0} = 1 - 10^{-A} \quad (2.12)$$

Where $A_{\%}$ is the absorptance, defined as the fraction of photons absorbed per photons impinging of the sample.

The UV-Vis spectroscopy experiments can be performed in the following modes (a) Transmission UV-Vis (b) Diffuse reflectance UV-Vis and (c) Absorption UV-Vis

Analysis of the Bandgap

The bandgap in the absorption spectrum corresponds to the point at which absorbance begins to increase from the baseline, as this indicates the minimum amount of energy required for a photon to excite an electron across the Bandgap. In real spectra, absorption is nonlinear, which reflects the local density of states at the valance band maxima and conduction band minima and defects states as well.

The detail analysis of Bandgap involves the plotting and fitting of the absorbance data to the Tauc plot. Ideally, Absorbance (A) is normalized to the path length of the light (l) to produce the absorbance coefficient (α) using above equation. For $\alpha > 10^4 \text{ cm}^{-1}$ the Tauc et al. have given following relation for the calculation of the bandgap and nature of band transition [150, 151].

$$\alpha hv = \alpha (hv - E_g)^{1/n} \quad (2.13)$$

Where n can be 3, 2, 3/2 or 1/2 corresponding to the indirect (forbidden), indirect (allowed), direct (forbidden), and direct (allowed) transitions respectively [149]. The bandgap is calculated from the extrapolated to the baseline of the $(\alpha hv)^n$ vs. hv plot [152, 153].

2.1.7 Incident photon to current efficiency (IPCE)

Incident photon to the current efficiency (IPCE) is the measure of the ratio of photocurrent to the incident photon as a function of the wavelength of the illumination [154, 155].

$$IPCE \% = \left(\frac{J_{ph} \left(\frac{A}{cm^2} \right)}{P_{in} \left(\frac{W}{cm^2} \right)} \times \frac{1240}{\lambda(nm)} \right) \times 100 \% \quad (2.14)$$

Where P_{in} is power of incident monochromatic light measured with a power meter equipped with the standard silicon photodiode, J_{ph} is photocurrent obtained from the chronoamperometry

experiment as steady state value over a period of time and λ is wavelength of the monochromatic light in nm. The number of photogenerated electrons can be calculated from photocurrent using following equation

$$electron/s = j_{ph}(mC/s) \times 6.241506 \times 10^{15} \text{ electrons/mC} \quad (2.15)$$

Where j_{ph} is the steady state photocurrent (in mA or mC/s).

The energy of photon is given by following equation

$$E(\lambda) = \frac{hc}{\lambda} = \frac{1.988 \times 10^{-1} (mJ \times nm)}{\lambda(nm)} \text{ per photon} \quad (2.16)$$

The number of photons at each wavelength is determined by measuring the power of the monochromatic light using following equation

$$P_{mono}(mW) = \Phi(\text{photos/s}) \times \frac{1.988 \times 10^{-13} (mJ \times nm)}{\lambda(nm)} \quad (2.17)$$

$$\Phi(\text{photos/s}) = 5.03 \times 10^{12} (mj^{-1} \times nm^{-1}) \times \lambda(nm) \times P_{mono}(mW) \quad (2.18)$$

The analysis of the IPCE plot can reveal the most important fundamental properties that limit the performance of the photo-electrode. IPCE is determined by the efficiencies of the three fundamental processes in the PEC water splitting reaction: light absorption efficiency, charge transport efficiency from electrode to the electrode-electrolyte interface and the charge transport efficiency at the electrode-electrolyte interface [156].

$$IPCE(\lambda) = \eta_{e^-/h^+} \times \eta_{transfer} \times \eta_{transport} \quad (2.19)$$

IPCE measurements give combined information to all efficiencies. These efficiencies can be calculated from the strategic experimental plan. Light absorption efficiency can be calculated

from the UV-Vis measurements. When the IPCE and charge generation efficiency are known, charge transfer and transport efficiency can be calculated. If IPCE is low and charge generation efficiency is high, $\eta_{transfer}$ and $\eta_{transport}$ will be the limiting parameters.

The IPCE (λ) value measured for the monochromatic illumination can be used for the calculation of the total photocurrent density, by integrating them over the AM 1.5 G Solar spectrums [155].

$$J_{ph} = \int IPCE(\lambda) \times E(\lambda) / \frac{hc}{\lambda} \times e d\lambda \quad (2.20)$$

Where J_{ph} is the total photocurrent density, $E(\lambda)$ is spectral irradiation of light source used. Generally, integrated J_{ph} value should be consistent with the photocurrent measured under AM 1.5 G illumination.

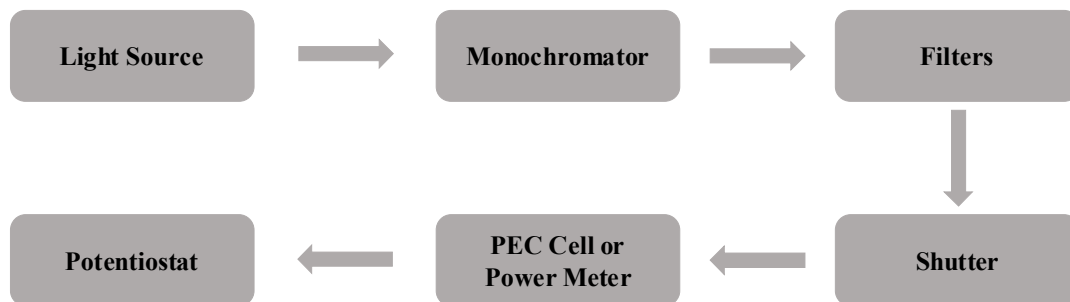


Figure 2.3 Schematic diagram of the experimental set up for IPCE measurement.

Bandgap of the semiconductor as measured from the IPCE may be higher than that of the optical absorption techniques because onset potential of the photocurrent may be limited by slow transfer and transport kinetics. The IPCE measured at the constant bias often increase the photocurrent which is due to either a shift of the Fermi level of the counter electrode or the increase in the carrier collection at the working electrode.

2.1.8 Absorption photon to current efficiency (APCE)

Absorption photon to current efficiency (APCE) is measurement of the percentage of the absorbed incident photon that is converted into the electrons by the PEC cell as a function of the wavelength of illuminated light [154, 155].

$$APCE(\lambda) = \frac{IPCE(\lambda)}{\eta_{e^-/h^+}} \quad (2.21)$$

Where η_{e^-/h^+} is the light absorption (charge generation) efficiency, which is defined as the percentage of the incident light absorbed to generate the electron-hole pair e^-/h^+ [156].

$$APCE(\lambda) = \frac{IPCE(\lambda)}{\eta_{e^-/h^+}} = \eta_{transfer} \times \eta_{transport} \quad (2.22)$$

2.1.9 Faradaic efficiency

In the PEC cell, faradaic efficiency is the ratio of the charged used for the hydrogen/oxygen evolution and overall charge flow in the cell.

$$\eta_F = \frac{N_F}{N_T} \times 100 \% \quad (2.23)$$

Where N_F is the charge used for the Faradaic process i.e. HER or OER and N_T is the total charge flow in the cell. N_T can be calculated by the measuring the photocurrent as function of time in time Δt . Then total current is calculated by integration the photocurrent over the time from 0 to Δt . The number of electrons used for the hydrogen or oxygen generation can be calculated by measuring amount of the hydrogen or oxygen by gas chromatography (GC). The faradaic efficiency less than the 100% in the practical cell is due to the side reaction occurring at the working electrode and inhibition of the proton reduction.

2.1.10 Solar to hydrogen efficiency (STH)

Solar to hydrogen efficiency (STH) is defined as the ratio of chemical energy stored to hydrogen gas to the solar energy input [155]. The mathematical expression for the STH calculation is given as follows

$$STH = \left[\frac{(mmol H_2 s^{-1}) \times (237000 J mol^{-1})}{P_{total}(mWcm^{-2}) \times area (cm^2)} \right] \quad (2.24)$$

The chemical energy stored in the form of hydrogen can be calculated by the multiplication of the rate of the hydrogen production and the change of Gibbs free energy per mole of H₂ for the generation from water splitting. The solar energy input can be calculated from the multiplication of the power of the incident illumination and illuminated electrode area. The above equation is only valid for the STH calculation without any bias potential.

The alternative method for the calculation of the STH is as follows [155]

$$STH = \left[\frac{J_{sc}(mAcm^{-2}) \times 1.229(V) \times \eta_F}{P_{Total}(mWcm^{-2})} \right] \quad (2.25)$$

Where $J_{sc}(mAcm^{-2})$ is short circuit photocurrent density measured in the two electrodes configurations, 1.229 V is the thermodynamic reversible potential for the water splitting reaction, η_F is the faradaic efficiency for the hydrogen evolution and P_{Total} is the incident power density.

In actual experiment, an external bias is applied for working PEC cell. In this case, applied bias photon to current efficiency (ABPE) is defined as the analogous to the STH efficiency with no bias [155]. ABPE is calculated by the following equation [157]

$$ABPE = \left[\frac{J(mAcm^{-2}) \times (1.229 - |V_{app}|)(V) \times \eta_F}{P_{Total}(mWcm^{-2})} \right] \quad (2.26)$$

Where J is the photocurrent obtained at the applied bias, V_{app} is the applied bias between WE and CE in two electrode configurations.

2.1.11 Charge transport efficiency ($\eta_{transport}$)

The charge transport efficiency ($\eta_{transport}$) is the percentage of the charge carriers among the photogenerated electrons and holes that can be separated and transported to the photoelectrode/electrolyte interface without charge recombination [158]. The efficient photo-induced charge generation should be followed by efficient charge transport process. The charge transport process is influenced by the physical properties of the photoelectrode materials such as Fermi energy level, carrier diffusion length, charge carrier concentration, doping concentration, film thickness, morphology. The measurement of the charge transport efficiency is based on the assumption that the oxidation kinetics of the hole scavenger such H_2O_2 or Na_2SO_3 is fast and charge transfer efficiency is considered as 100% [126]. The charge transport efficiency ($\eta_{transport}$) is calculated by the dividing the photocurrent density for hole scavenger, $J_{scavenger}$ by photon absorption rate, J_{abs} as

$$\eta_{transport} = J_{scavenger} / J_{abs} \quad (2.27)$$

The value of J_{abs} is obtained from the measurements of light absorption and integration of light absorption over the AM 1.5 G solar spectrum. Analysis of charge transport efficiency provides the information about performance loss due to the bulk recombination within the photoelectrodes [126].

2.1.12 Charge transfer efficiency

Charge transfer efficiency ($\eta_{transfer}$) is the measurement of the interfacial charge transfer from the photoelectrode surface to the water molecule at the photoelectrode-electrolyte interface. The measurement of the charge transfer efficiency is based on the assumption that the oxidation kinetics of the hole scavenger such H_2O_2 or Na_2SO_3 is very fast and 100% efficient. The charge transfer efficiency ($\eta_{transport}$) is calculated by the dividing the photocurrent density for water oxidation, J_{H_2O} by hole scavenger $J_{scavenger}$ as follows [126]

$$\eta_{transfer} = J_{H_2O} / J_{scavenger} \quad (2.28)$$

Analysis of charge transfer efficiency insights the performance loss due to the surface recombination or slow kinetics at the photoelectrode/electrolyte interface [126].

2.1.13 Transient time

Transient time is the ability of the photogenerated charge to transport before recombination. When photoelectrode is illuminated, there is initial photocurrent (I_i) is observed and then there is decay of photocurrent is due to the photogenerated holes recombine at the electrode surface with the photogenerated electrons from the conduction band [159] as shown in the Figure 2.4

The transient time is calculated from the following equation

$$\ln D = -\tau/t \quad (2.29)$$

$$D = \frac{(I_t - I_s)}{(I_i - I_s)} \quad (2.30)$$

Where t is the time, τ is the transient time constant at which $\ln D = -1$, I_i is current at time t , I_i and I_s are the initial and steady state photocurrent respectively. The time at which $\ln D = -1$ in the $\ln D$ vs. t plot gives the τ value [160]. The typical values of τ varies from the several tenths of second to the several seconds depending on the nature of the materials.

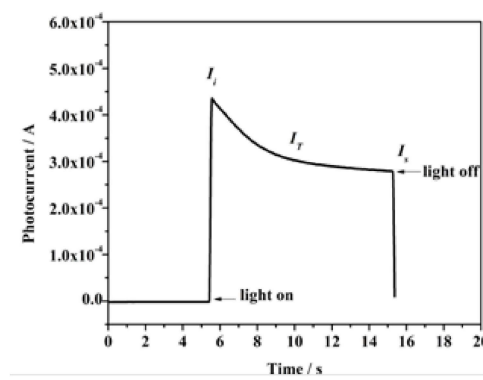


Figure 2.4 Typical transient photocurrent.

2.1.14 Mott-Schottky analysis

Mott-Schottky analysis is the qualitative investigation of the charge transport properties and the band bending of the semiconductor at semiconductor-electrolyte interface [161, 162]. It provides the insight the donor density and flat band potential of the semiconductor. The flat band potential is the potential at which potential drops across the bulk of the electrode and the surface is zero. It provides the qualitative information of the semiconductor energy bands with respect to the redox potentials of the electroactive species in the electrolyte. The flat band potential and donor density can be obtained from the Mott-Schottky plot [162].

$$\frac{1}{C^2} = \frac{2}{q\epsilon\epsilon_0 A^2 N_D} \left(V - V_{FB} - \frac{k_B T}{q} \right) \quad (2.31)$$

Where C is the interfacial capacitance; q is electronic charge; ϵ is the dielectric constant of semiconductor; ϵ_0 is permittivity of free space; A is the area of electrode exposed to the electrolyte; N_D is the charge-carrier density/donor density; V is applied potential; V_{FB} is flat band potential of the semiconductor; k_B is Boltzmann constant; T is absolute temperature.

The charge carrier density (N_D) can be calculated by taking derivative of equation 1.32 as

$$N_D = \frac{2}{q\epsilon\epsilon_0 A^2} \left(\frac{d(1/C^2)}{dE} \right)^{-1} \quad (2.32)$$

Where $\frac{d(1/C^2)}{dE}$ is the slope of the straight line of tangent of Mott-Schottky plot. N_D can be calculated by measuring the slope of tangent line during the fitting of the plot. V_{FB} can be calculated by intercept on the X-axis of the Mott-Schottky plot. The type of semiconductor (n or p-type) can be determined from the slope of straight tangent line. The positive slope indicates n-type and negative slope indicates p-type nature of the semiconductor [162].

2.1.15 Electrochemical Impedance Spectroscopy (EIS)

The electrochemistry of faradaic process involves (a) double-layer rearrangement at the interface, (b) diffusion of analyte from bulk to the interface, (c) charge transfer resistance across the interface and (d) movements of the ions in solution. These processes are strongly coupled and occur at different time scales. The individual contribution to the overall faradaic process is not identified in the voltammetry, chronopotentiometry and chronoamperometry technique because of large current/potential perturbation is applied to drive the reaction on the working electrode. The contribution of individual four processes can be determined by monitoring the relaxation frequency of all these processes using the electrochemical impedance spectroscopy (EIS) technique. Oliver Heaviside defined the impedance as the complex ratio of voltage and current in an ac circuit as [163]

$$Z(j\omega) = \frac{E(j\omega)}{I(j\omega)} \quad (2.33)$$

Where Z is the impedance, E is the potential, and I is the current, j is the imaginary component and ω is the angular frequency of the alternating potential. The impedance Z is measured by applying a sinusoidal potential of small perturbation (5-10 mV) in the variable frequency range (i.e. 100 kHz to 0.01 Hz). The sinusoidal potential (E_t) can be represented as

$$E_t = E_0 \sin(\omega t) \quad (2.34)$$

Where E_0 is the amplitude of sinusoidal potential, ω is the angular frequency ($\omega = 2\pi f$, f is frequency in Hz). The resultant sinusoidal current (I_t) is in same frequency and different phase is obtained as

$$I_t = I_0 \sin(\omega t + \phi) \quad (2.35)$$

Where I_0 is amplitude of sinusoidal current and ϕ is the phase angle of the current. The impedance is calculated as

$$Z(\omega) = \frac{E_t(j\omega)}{I_t(j\omega)} = \frac{E_0 \sin(\omega t)}{I_0 \sin(\omega t + \phi)} = Z_0 \frac{\sin(\omega t)}{\sin(\omega t + \phi)} \quad (2.36)$$

$$Z(\omega) = Z_0 (\cos \theta - j \sin \theta) \quad (2.37)$$

$$Z(\omega) = Z_{real} - j Z_{im} \quad (2.38)$$

Where Z_{real} and Z_{im} are the real and imaginary components of the impedance. The magnitude of Z can be obtained as $Z = \sqrt{Z_{real}^2 + Z_{im}^2}$ and phase angle ϕ can be written as $\tan \phi = Z_{im}/Z_{real}$.

The impedance measurement is represented in the two ways as the Nyquist plot and the Bode plot. In Nyquist plot, Z_{real} is plotted against Z_{im} for different value of ω . Each point of the Nyquist plot is at frequency. Frequency dependent Z reveals the interfacial phenomenon. In the Bode plot, $\ln(\text{frequency})$ vs. $\ln(Z)$ and $\ln(\text{frequency})$ vs. phase angle are plotted. The electrochemical reaction is fitted using the equivalent electrical circuit using resistor, capacitor, inductor etc.

2.1.16 Scanning Electrochemical Microscopy (SECM)

Scanning electrochemical microscopy (SECM) is a scanning probe microscopy technique, capable of imaging substrate (insulating, semi-conductive or conductive) topography and local activity with high temporal and spatial resolution. An ultra-microelectrode of diameter 10 μm or less is used as the tip/probe in the close proximity to a surface of interest. The electrochemical response of the tip or the substrate in the response of tip provides the qualitative and quantitative information of the interfacial region. The SECM technique was reported by concurrently Allen J. Bard and Engstrom in 1989 [31, 164]. Since the inception of SECM in 1989, it has been utilized in the wide variety of research area as kinetics, energy, corrosion, biology (i.e. molecular transport across membrane, adsorption/desorption process, the activity of living biological cells), instrumental development and surface modification.

2.1.16.1 Instrumentation

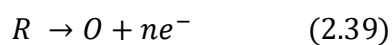
Scanning electrochemical microscope consists of four components as bipotentiostat, three-dimensional positing systems, tip/probe, and data acquisition system. The low current bipotentiostat is used for the precise measure and control of potential and current at probe and substrate simultaneous. A high-resolution three-dimensional positioning system is used for the accurate movements of the probe over the substrate using X, Y and Z stage using stepper and

piezoelectric motors for finer movements. The tip/probe is a small-scale probe with dimension micrometer (μm) to nanometer (nm) which defines the resolution of the SECM measurement. The fourth is data acquisition system i.e. computer which synchronize and coordinate each component to perform each of the measurements. The additional components can be added such as inverted optical microscope for biological measurements consists of live cells detection, fluorescence detection system. The careful considerations are needed for the designing of the SECM experiments such as redox mediator, substrate being investigated, solvent in which the electrochemical reaction will occur and the tip/probe. The right combination of all these parameters is required for the designing of the experiment.

2.1.16.2 Modes of SECM operation

The following are the modes of operation of SECM such as feedback mode, generation/collection mode, redox competition mode, direct mode, potentiostat mode and transient mode etc.

Feedback mode: Feedback mode consists of the measuring the tip current of a potentially biased tip. The tip current is generated due to the oxidation of the redox mediator (i.e. R as reduced species) as the following equation



The faradaic current of the tip is the electrochemical reaction of redox mediator and depends on the topography and electrochemical activity of the substrate. When a probe is positioned at tip to substrate distance (d) greater than 10 times the radius of the tip, the measured current is the diffusion limited current (steady state current). For probe of disk geometry, the steady state current is defined as $i_{T,\infty} = 4nFDC$ where n is the number of electron transferred, F is

Faraday constant, D is diffusion coefficient of redox mediator, C is the concentration of redox mediator, a is the tip area and β is the geometric co-efficient [30]. When tip approaches the substrate, the tip current is perturbed by the presence of the substrate either by regeneration of R at the substrate (positive feedback, $(i_T > i_{T,\infty})$) or by blockage of the diffusion of redox mediator R to the tip (negative feedback, $i_T < i_{T,\infty}$)

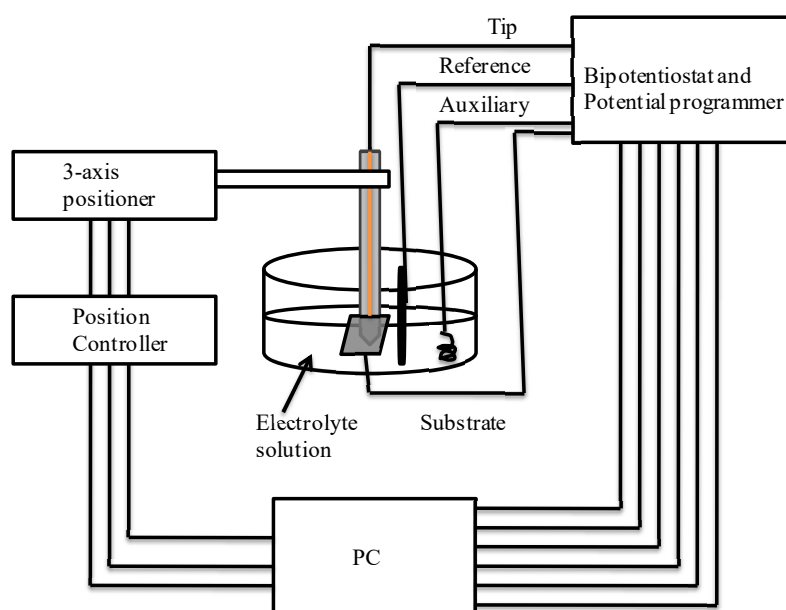


Figure 2.5. Schematic of scanning electrochemical microscopy system

The tip current-distance curve as shown in Figure 2.6 are known as positive and negative feedback approach curve where I_T is the normalized current is the ratio of the tip current (i_T) and tip current in the bulk ($i_{T,\infty}$). The tip to substrate distance can be calculated using the feedback approach curve. This mode is used to determine the heterogeneous rate constant at the interface [10, 31]. The topographical information of the substrate can be obtained from the feedback current measurements as the feedback response is significantly depended on the tip to substrate distance.

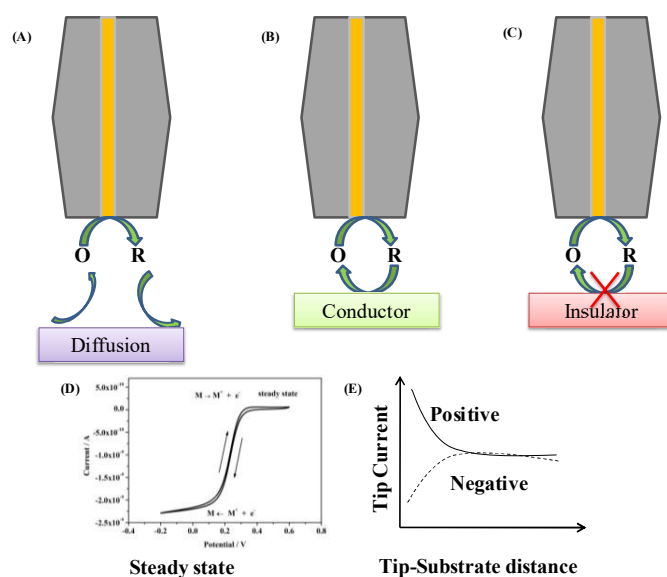


Figure 2.6 Schematic of feedback mode of approach of the tip to the substrate. (A) diffusion hindrance process, (B) feedback of electroactive species on the conductive substrate and (C) blockage of regeneration of electroactive species on the insulating substrate.

Generation/collection mode: In the generation (G) /collection (C) modes of SECM, the tip is generally located at distance of the order of ten tip radii or less from the substrate and tip and substrate current are monitored. There two types of G/C modes in which SECM operates. First is tip generation/substrate collection (TG/SC) mode and second is the substrate generation/tip collection (SG/TC) mode [10, 31, 165]. In TG/SC mode, tip is used to generate the reactant and substrate is used for the collection of generated reactants. For example, oxidation of the reactant at the tip occurs such that $R \rightarrow O + ne^-$ and the potential at the substrate is held such that the product O of the tip will react and collected according to the $O + ne^- \rightarrow R$ reaction. Generally the substrate area is considerably larger than the tip, therefore the collection efficiency (i_S/i_T) is 100 % for stable tip generated species, O, if tip is close to the substrate (order of two tip radii). If

O reacts in the transient from tip to the substrate, i_S/i_T becomes smaller and it changes with the separation distance d and hence it is used to determine the rate constant of the homogeneous reaction [10]. TG/SC mode is used for the measurements of reaction kinetics and study the modification of the substrate. In the substrate generation/tip collection (SG/TC) mode, substrate acts as the generator and the tip is the collector of the collector. Therefore, SG/TC mode is used for the measurements of concentration profiles or chemical flux from a substrate. The tip scanned at constant height mode to the substrate surface can probe the concentration profile and can identify the active spots where reaction occurs at a higher rate. The SG/TC suffers from several flaws such as low collection efficiency, lack of steady state at large substrate and interference between substrate and tip reaction. This mode of SECM is useful for the corrosion and enzymatic measurement.

Redox completion mode: The redox competition (RC) mode is first reported by Schuhmann and co-workers [166]. This mode of operation is used in the field of the surface catalytic activity and corrosion [166, 167]. In this typical mode, the SECM tip and the substrate are in close proximity to each other and compete for the same redox species. The potential is applied to the tip and the substrate for the oxidation of R as $R \rightarrow O + ne^-$ and measured the current at the tip only. To avoid the complete depletion of the concentration in the vicinity of the tip and substrate, the substrate is biased at the oxidation potential and oxidative potential pulse is applied to the SECM tip. The tip current is monitored throughout the imaging of the substrate interface; the oxidative current of tip is constant for the inactive substrate. Over the active region of the substrate where the oxidation reaction occurs, the redox species is consumed at substrate and tip which leads to the decrease the oxidation current of the SECM tip. The decrease in the tip current can be

correlated with the activity of the substrate. In addition to these normally used modes of operation of SECM there are some more modes of operation, which are mentioned as below.

Direct mode: Direct mode is the specific mode in which the electrochemical cell configuration is reversed such that the microelectrode tip is used as the counter electrode and the substrate electrode as the working electrode. When potential is applied, the electric field is localized between the substrate and the tip. This mode has been used for the surface modification such as semiconductor etching, micro-patterning and enzyme deposition.

Transient mode: In this mode, the tip current is measured with respect to time. This mode is used in the measurement of homogeneous kinetics, for systems that are changing with time and for the determining the diffusion coefficient of the species without knowing the solution concentration or the number of electrons transferred in the electrode reaction [168, 169].

Potentiometric mode: In this mode, potential of tip is measured. The advantages of this mode are high selectivity and measurement of non-electroactive species or electroactive species with standard reduction potential outside of the solvent window. The concentration and oxidation state of the analyte species is unchanged during the measurement. Ultramicroelectrode are used as potentiometric probe for the selective recognition of local concentration of ions/species. The different mediators are used for the different modes of operation depending upon the solvent used for the experiment and the nature of the study. The common mediators are used in aqueous medium are ferrocenemethanol, ascorbic acid/dehydroascorbic acid, hydroquinone, dopamine/dopamine-o-quinone, ferrocenecarboxylic acid, hexacyanoferrate (III), hydrogen peroxide, dihydrogen orthophosphate.

2.2 Material Characterization

2.2.1 X-ray diffraction (XRD)

Max Von Laue in 1912 discovered that the crystalline substance acts as the three-dimensional diffraction grating for X-ray wavelength. The XRD is used to characterize the crystallographic properties of the material. The beam of X-ray emitted from the X-ray tube interacts with electron density of the atoms of the crystal plan of the sample. The X-ray is diffracted by the crystal plan in the various directions resulting of constructive and destructive diffraction pattern. The constructive interference obtained thus follows the Bragg' diffraction as the follows

$$n\lambda = 2d \sin \theta \quad (2.40)$$

Where n presents the number of planes in the lattice, θ is the angle between the lattice planes and the incident beam and d is the distance of the lattice planes for which the constructive interference occurs. The diffraction patterns consist of the different peaks, each of the peak corresponds to the different interplanar spacing, d. X-ray diffraction is widely used for the identification of unknown crystalline materials. Figure 2.7 shows the schematic of typical diffractometer. It consists of source of X-ray beam, usually copper as anode, nickel filter for the monochromatic X-ray beam, called CuKa- 1.54 Å, sample holder and X-ray detector. Source of X-ray and detector both move around the sample for the different angle of measurements (usually 10-90°) [170].

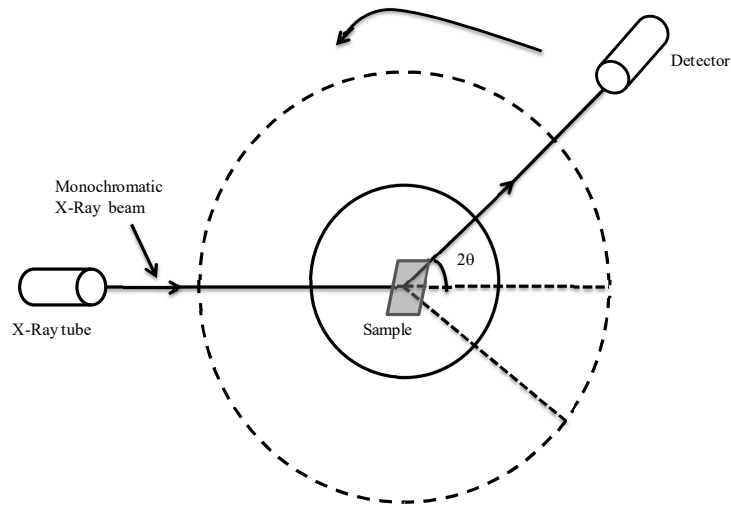


Figure 2.7 Schematic of typical X-ray powder diffractometer

Samples in the form of powder, thin films etc. are used to measure the diffracted X-ray beam and intensity of the diffracted beam is plotted as a function of angle 2θ to get diffraction pattern. The X-ray detector such as Geiger-Muller, proportional counter, scintillation counters etc. is used to measure the diffracted X-ray beam. For small angle diffraction measurement, different diffractometer is used, and that technique is called small-angle X-ray scattering (SAXS).

XRD is used for characterization of crystalline materials, determination of unit cell dimensions, measurement of the sample purity, determination of the lattice mismatch between film and substrate and to inferring stress and strain, determination of the dislocation density and quality of the film by rocking curve measurements, measurements of the super lattice in the multilayered epitaxial structures, determination of the thickness, roughness and density of the film using glancing incident X-ray reflectivity measurements, determination of the orientation of the grains in the polycrystalline samples.

2.2.2 Fourier Transform Infrared Spectroscopy (FT-IR)

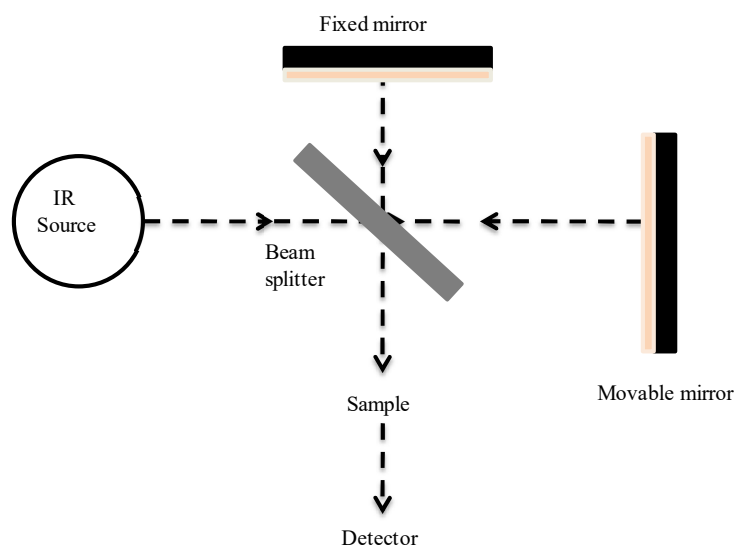


Figure 2.8 Schematic of a typical FT-IR spectrometer

Fourier-transform infrared spectroscopy (FTIR) is used to measure the infrared spectrum of absorption or emission of samples used for measurements. FT-IR spectrometer uses the Michelson interferometer for recording spectra. The source of IR is tungsten lamp, nichrome coil and high-pressure mercury-arc lamp depending upon NIR, mid IR or far IR region measurement. The IR detector as photoconductive cell, thermopiles, thermistors, Golay or pyroelectric is used depending on the interest of wavelength is to be detected. Figure 2.8 shows the schematic of FT-IR spectrometer [171]. The parallel beam of IR rays falls on the beam splitter and part of the beam falls on the fixed and movable mirror. The reflected beam from both of mirror falls on the sample and detector. The constructive and destructive interference occur depending on the path length of the beam. The recombined beam passing through sample produces characteristic absorption frequency of the molecules present in the sample. The detector records the signals

every millisecond and then Fourier transformed the collected signals and transformed into the output spectrum.

2.2.3 Raman spectroscopy

Raman spectroscopy is the non-destructive mode of analysis technique which provides the information about phase, crystallinity, chemical structure, and molecular interactions [172]. Raman spectroscopy is a light scattering technique in which high intensity incident laser light interacts with the samples and produces the Rayleigh and Raman scattering as shown in Figure 2.9.

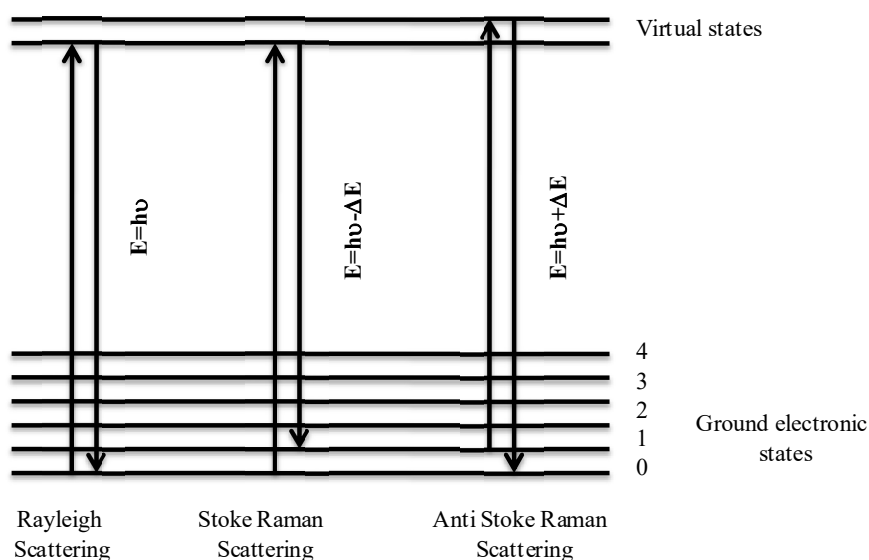


Figure 2.9 Energy level diagram of the Raman scattering

Raman spectrum consists of several peaks showing the intensity and wavelength position of the Raman scattering which corresponds to the molecular bond vibration. Raman spectrum is a chemical fingerprint for a molecule or material and used for the identification of the materials. The intensity of a spectrum is directly proportional to the concentration of the material. The

relative peak intensity provides the relative concentration of the components and the absolute intensity provides the absolute concentration of the components. Raman spectroscopy provides the information about chemical structures and identity, phase and polymorphism, intrinsic stress/strain, contamination and impurity of the samples.

Figure 2.10 shows the schematic of the typical Raman spectrometer in which Laser light is used as the source. Laser light interacts with the molecular vibrations, phonons or other excitation. The scattered light from the sample typically Raman scattered light can pass from the filter. The Raman scattered light falls on the detector and produces the spectrum which is utilized in the characterization of the materials.

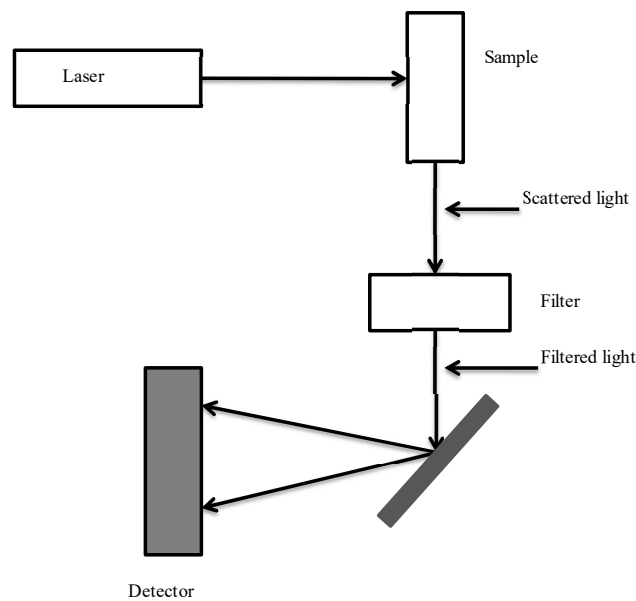


Figure 2.10 Schematic of a typical Raman spectrometer

2.2.4 Scanning electron microscopy (SEM)

Scanning electron microscopy is the electron microscopy in which a high energy beam of electron is used to scanning of the surface. The high energy electron interacts with the atom of the sample produces the different signals containing the information of sample topography and the composition of the sample. The secondary electrons emitted by the excited atoms by high energy beam electron mostly contain the topographic information of the sample. The resolution obtained in SEM depends on multiple factors such as size of the electron spot, wavelength of the electrons and the electron-optical system. The resolution of the SEM is 1-20 nm, SEM is used in characterization materials in various fields such as medical, biological, metals, semiconductors and ceramics, is broadening its application frontier.

2.2.5 Energy dispersive spectroscopy (EDS)

Energy-dispersive X-ray spectroscopy (EDS), sometimes called energy dispersive X-ray analysis (EDXA), is an analytical technique used for the elemental analysis or chemical characterization of a sample. The EDS analysis is used to determine the elemental composition of individual points or the lateral distribution of elements from the imaged area. It can also be used to obtain compositional information on quasi-bulk specimens. The EDS works mainly on Moseley's law. The EDS detector measures the relative abundance of emitted X-rays versus their energy. The detector is typically lithium-drifted silicon, solid-state device. When an incident X-ray strikes the detector, it creates a charge pulse that is proportional to the energy of the X-ray. The charge pulse is then converted to a voltage pulse by a charge-sensitive preamplifier. The signal is then sent to a multichannel analyzer where the pulses are sorted by voltage. The energy, as determined from the voltage measurement for each incident X-ray, is sent to a computer for

display and further data evaluation. The spectrum of X-ray energy versus counts is evaluated to determine the elemental composition of the sampled volume.

2.2.6 Atomic force microscopy (AFM)

Atomic force microscopy (AFM) is a highly sensitive scanning probe microscopy (SPM) with resolution of 1000 times of the optical diffraction limit. AFM is used to measure the force constant, topographic and manipulation of the sample properties by AFM tip. The force measurement is used to perform the force spectroscopy to measure the mechanical properties such as Young's Modulus and stiffness. For topographical measurements, the force acts on the probe by the sample is used for the three-dimensional measurements. In the manipulation, the force between the probe and sample is used to modify the sample properties. The schematic diagram of AFM is shown in Figure 2.11

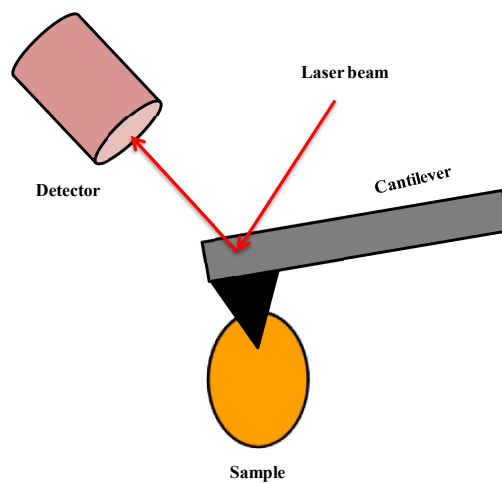


Figure 2.11 Schematic of atomic force microscopy (AFM)

The cantilever with a very sharp tip is used to scan over the sample. When tip approaches to the sample surface, the force between surface and tip deflects the tip towards the surface. When tip is too close to the surface, there is repulsive force acts on the tip and hence deflection of tip away

from the surface occurs. The incident beam of laser light falls on the backside of the cantilever. When cantilever deflects, reflected laser light also shifted, this shifting in the reflected laser light is the measure of topographical images of the samples.

2.2.7 X-ray photoelectron spectroscopy (XPS)

X-ray photoelectron spectroscopy (XPS), is a surface sensitive spectroscopy technique which determines elemental, chemical and electronic state information. The sample is irradiated with monochromatic X-rays of Al K α or Mg K α and kinetic energy and number of electrons emitted from the element from 1-10 nm depth are determined. The kinetic energy of these emitted electrons is characteristic of the element from which the photoelectron originated. The position and intensity of the peaks in an energy spectrum provide the desired chemical state and quantitative information. The chemical state of an atom alters the binding energy (BE) of a photoelectron which results in a change in the measured kinetic energy (KE). The BE is related to the measured photoelectron KE by the simple equation; $BE = hv - KE$ where hv is the photon (X-ray) energy. The chemical or bonding information of the element is derived from these chemical shifts.

2.2.8 High resolution transmission electron microscopy (HR-TEM)

High resolution transmission electron microscopy (HRTEM) is a powerful tool to study the properties of material at atomic scale [173]. HR-TEM provides direct images of the atomic structure of the samples; hence, it is possible to have direct information about the crystallographic structure of materials from images. Electrons of high energy (~ 200 keV) are used to pass through the series of magnetic lenses as shown in the Figure 2.12. Electron source, condenser lens, specimen, objective lens, and fluorescence screen are main component of the HR-TEM. The high vacuum chamber ($\sim 10^{-5}$ torr) is needed for the proper functioning of the HR-

TEM. The electromagnetic lenses, whose focal length is variable, are used. The high-resolution diffraction pattern obtained detailed crystal analysis of the sample. This technique is widely used in advanced characterization of materials, allowing the acquisition of information about punctual defects, stacking faults, precipitates, and grain boundaries.

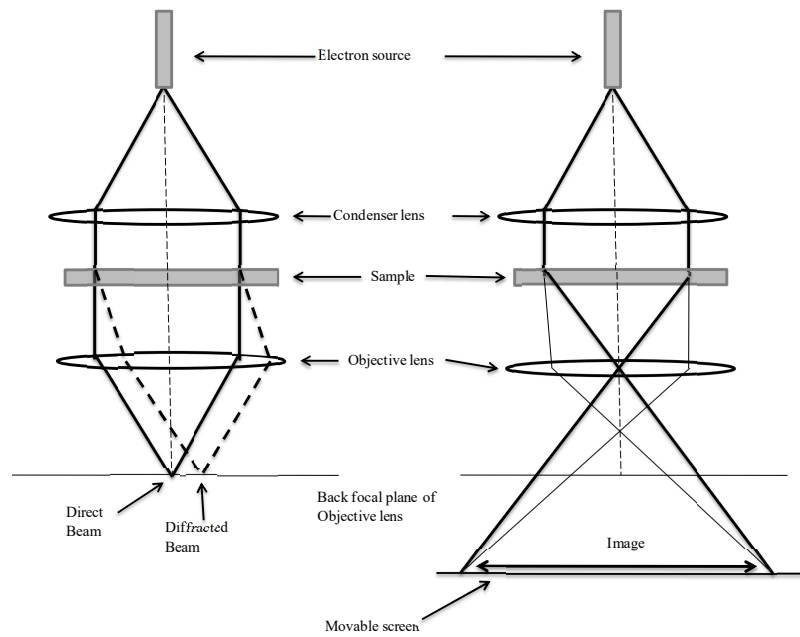


Figure 2.12 Schematic of high-resolution transmission electron microscope.

Chapter 3: Development of the noble metal and three dimensional graphene (3D-G) composite materials for the hydrogen evolution reaction

3.1 Introduction

The emission of carbon dioxide associated with the generation of energy from fossil fuel has been the issue of environmental pollution, most importantly, its detrimental role in global warming. In order to overcome the detrimental effect of carbon dioxide and to meet the energy demand, the scientific proposition is to generate hydrogen and oxygen from water using solar energy. The scientific and technologic challenge, however, to generate hydrogen and oxygen from water is gigantic. Two significant steps associated with the generation of hydrogen and oxygen from water are the hydrogen evolution reaction (HER) and oxygen evolution reaction (OER) [174-178]. Though the chemical reaction of the generation of hydrogen and oxygen from water looks simple, the processes are highly non-spontaneous and associated with complicated intermediate pathways, thus involves high overpotential to sustain the process. Various catalytic systems have been reported in the sustainable generation of hydrogen and oxygen from water; however, the issue remains unresolved; thus, keeping it one of the most important recent research topics.

The generation of hydrogen through the electrochemical and photo-electrochemical splitting of water is being considered as the favored route for the generation of hydrogen using solar energy. The primary requirements for suitable catalysts are efficiency, cost-effectiveness, environment

friendliness, and sustainability in long-time operation. In terms of the improvement of efficiency, the most important technical parameter is to decrease the overpotential of the splitting of water molecules [179].

In acidic solution, Pt group metals are the most effective catalyst for the generation of hydrogen [36-41]. The recent advancement in the noble metal based catalysis has been achieved by the bimetallic and trimetallic materials such as PtPd, PtCu, AuPd@Pd, and PtRhCo for the HER, oxygen reduction reaction (ORR) and alcohol oxidation reaction [42-45], but due to the high cost of the Pt group metal elements, large scale application using these elements is not economically viable [46-49]. Different transition metal alloys, carbides, polymeric carbon nitride, and transition metal chalcogenides are a better choice as HER catalyst, due to their earth abundant nature and comparable efficiency [55-61]. Thus, there is trust for the development of multifunctional materials in the scientific community. Graphene is a potential material because of its unique properties such as; electrical, mechanical and thermal characteristics, which have found its application in energy conversion, storage, sensor, and medicine. Among various graphene-based materials, 3D-G has attracted considerable research interest due to its unique structural advantage with connected pores in addition to properties like lightweight, high surface area, and suitable mechanical and excellent electrical properties [180-183]. Thus it is used in diverse fields such as energy storage and conversion, catalysis, sensors, adsorbents and antibacterial agents [184-194].

Performance of 3D-G is further improved via the formation of the nanocomposite materials and decorating with metal nanoparticles, metal oxide, and doping. This synergic effect of dopant in the 3D-G improves performances in diverse applications such as catalysis, water splitting, supercapacitor, Li-ion batteries, fuel cell, and sensors. Hu's group have demonstrated that 3D-G

composites with PtPdCu and Pd₂/PtFe show good catalytic activity for alcohol oxidation reaction [50, 51]. Feng and his coworkers have synthesized AuPd@Pd and 3D-G composite for the alcohol oxidation reaction [44]. Several methods of synthesis of 3D-G have also been reported [183-186, 195-197]. These methods of synthesis, however, are expensive and involve toxic, hazardous chemicals, which limit the synthesis in terms of economic viability, efficiency, and environmental friendliness. For the first time, Zhang H. F. et al. have synthesized three dimensional nanocomposites of graphene using the freeze casting method [198]. Afterward Ling Qiu et al. have exploited the freeze casting method further and cost-effective, efficient, and environmentally friendly method for the synthesis of 3D-G monoliths, which shows good electrical conductivity, super-elasticity, ultralow density and high energy absorption efficiency [199]. Noble metal 3D-G composite materials have been synthesized by freeze casting method for the applications such as catalysis, supercapacitor, antibacterial activity and electromagnetic interference shielding [52-54].

In the present investigation, 3D-G is synthesized through the state-of-the-art synthesis procedure by freeze casting method. The nanocomposites of 3D-G and noble metals Pt, Pd, Au, and Ag were synthesized and are named as Pt/3D-G, Pd/3D-G, Au/3D-G, and Ag/3D-G respectively. The motivation is to improve the catalytic performance of noble metal ions by incorporating them along with the 3D-G matrix, which eventually should lead to the decrease in the requirements of noble metals in the catalytic system. It is also aimed at improving the catalytic activity through the incorporation of 3D-G and application of noble metals down the order from Pt to Ag without significantly affecting the catalytic activity. The catalytic performances of the noble metal 3D-G composite for HER are investigated and compared across the four catalysts. Performance of the noble metal catalysts is observed to be increased significantly on the

incorporation of 3D-G matrices. The mechanism of the HER catalytic process has been evaluated by measurements through Tafel analysis, hydrodynamic conditions, the variation of temperatures, and carrying out detailed analysis of the results to describe the mechanism of the catalytic process. The role of the activation barrier on the overall catalytic current has been discussed. The use of catalytic system in the hydrogen evolution process involves the improvements of mass flow, the suitable orientation of water molecules, better kinetics of the discharge step, and efficient recombination and removal of hydrogen [19-23, 200-209]. In the present investigation, the variation of the performance of the four catalytic systems is explained through the evaluations of the electro-kinetics and thermodynamics parameters for a better understanding of the hydrogen evolution process.

3.2 Experimental Section

3.2.1 Chemicals

Graphite powder (particle size 45 μm , 99.99%), AgNO_3 , $\text{HAuCl}_4 \cdot 3\text{H}_2\text{O}$, Na_2PdCl_4 , and $\text{H}_2\text{PtCl}_6 \cdot 6\text{H}_2\text{O}$ were supplied from Sigma-Aldrich. All other chemicals were of analytical grade and were obtained from Merck Specialties Private Limited, India. All the compounds were used as received without any further purification. Ultrapure water from the Mill-Q system was used throughout the experiments for the solution preparation.

3.2.2 Preparation of noble metals (Ag, Au, Pd and Pt)/3D-G nanocomposites

Noble metals (NM)/3D-G nanocomposites were prepared according to the method reported previously from our group [52]. In a typical procedure for the preparation of NM/3D-G nanocomposites, different noble metal precursors ($\text{AgNO}_3 = 7.9 \text{ mg}$; $\text{HAuCl}_4 \cdot 3\text{H}_2\text{O} = 10 \text{ mg}$; $\text{Na}_2\text{PdCl}_4 = 13.8 \text{ mg}$; $\text{H}_2\text{PtCl}_6 \cdot 6\text{H}_2\text{O} = 13.2 \text{ mg}$) were mixed with GO solution (5 mg mL^{-1}) separately in a reaction glass vials of 4 mL capacity. Afterward, 15 mg of ascorbic acid was

added to each vial and heated to 100 °C for 30 min. After 30 min of heating, each vial was put in a dry ice bath for 30 min. After being thawed, each vial was heated for 4 h at 100 °C. Then, the un-reacted species present in the as-prepared samples were removed by dialysis followed by freeze-drying for 48 h. After freeze-drying, the as-prepared samples were dried for 24 h at 50 °C. The mechanism of preparation of noble metals (Ag, Au, Pd and Pt)/3D-G nanocomposites by the freeze-casting method has been discussed in our previous work [210].

3.2.3 Instrumentation

X-ray powder diffraction (XRD) measurements were performed on a Philips powder diffractometer (PW 3040/60) with a Cu K α radiation ($\lambda = 1.541 \text{ \AA}$) source. The Raman spectra were collected on a Lab RAM HR 800 Micro laser Raman system with a 519 nm Ar⁺ laser. The morphology was characterized by FEG-SEM (JEOL Model JSM-7600F) and HRTEM (Phillips-CM 200 electron microscope, operated at 200 kV). XPS measurements were conducted on MULTILAB (Thermo VG Scientific) using Al K α radiation as a monochromator. The compositional analysis of the as-prepared samples was carried out with an ICP-OES instrument (Prodigy, Teledyne Leeman Labs). The Brunauer-Emmett-Teller (BET) surface area was measured by using ASAP 2020 Micromeritics instrument. Electrochemical studies were performed by using the CH Instrument, model no. 920 D. Effect of hydrodynamics was studied by rotatory disk electrode (RDE) by using custom cell made by Pine Instruments in combination with the Autolab 100 potentiostat.

3.2.4 Procedure for Electrochemical Measurements

1 mg of each catalyst was put into 0.5 mL of ethanol-water solution (1:4 ratios) and sonicated for 10 minutes to homogeneously dispersing in the solution. Then 50 μL of 5% Nafion was added and again sonicated for another 10 minutes. An aliquot of 5 μL (0.01 mg)

homogeneously mixed catalyst ink thus prepared was drop casted on glassy carbon electrode (GCE, 3 mm diameter) and dried under an IR lamp. Electrochemical investigation for hydrogen evolution reaction was carried out in 0.5 M H₂SO₄ solution as electrolyte using three electrode systems. The catalyst modified GCE was used as a working electrode, glassy carbon rod as counter electrode and Ag/AgCl electrode was used as a reference electrode. Standard Pt/C catalyst (20 % Pt loading) was used for the comparative study of HER activity of catalysts. Prior to the electrochemical investigation, H₂SO₄ solution was purged with pure Ar gas to remove dissolved oxygen. Glassy carbon electrode was polished with 0.05 μm size alumina powder and ultrasonically cleaned in distilled water for 10 minutes. Prior to electrochemical measurements, catalysts were refreshed and activated using cyclic voltammetry (CV) for 50 cycles using a scan rate of 10 mVs⁻¹. All electrochemical measurements are reported with respect to the reference hydrogen electrode (RHE). For conversion of potential to RHE, 0.5 M H₂SO₄ solutions were saturated with Ar gas, Pt electrode was used as working electrode, glassy carbon rod as counter electrode and Ag/AgCl electrode was used as a reference electrode. Linear Sweep Voltammetry (LSV) was recorded at a scan rate of 1 mVs⁻¹ and potential was measured where the current was zero and reported as a reference potential for hydrogen electrode. The measured potential was -0.225 V. All electrochemical studies were carried out using reference Ag/AgCl electrode potential and potentials were converted and reported to the RHE potentials using following equation

$$E_{RHE} = E_{Ag/AgCl} + 0.225 V \quad (3.1)$$

Where, E_{Ag/AgCl} is electrode potential of reference Ag/AgCl electrode, -0.225 V is corrected potential. All electrochemical measurements were carried out at room temperature (25 ± 1°C).

The overpotential η for hydrogen evolution reaction was measured by using the following eq. (3.2).

$$\eta = E_{RHE} - 0V - 0.0591 pH \quad (3.2)$$

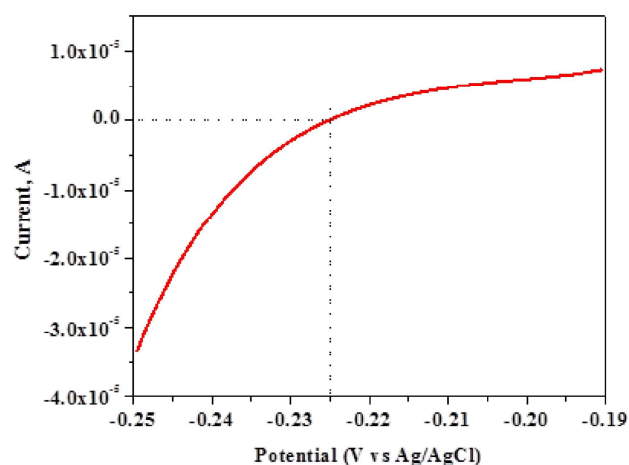


Figure 3.1 Linear sweep voltammetry at a rate of 1 mVs^{-1} for calibration of the Ag/AgCl reference electrode with RHE potential

3.3 Results and discussion

3.3.1 Characterization of materials

Figure 3.2 (i) represents the powder X-ray diffraction (XRD) pattern of GO, bare 3D-G, and 3D-G metal particle nanocomposites. XRD pattern of graphene oxide (GO) in Figure 3.2 (i)(a) shows peaks at 10.8° and 43° , which corresponds to the (001) plane of GO and the (100) plane of hcp structure of carbon [211]. On the other hand (Figure 3.2 (i) (b-f)), there is a reduction of (002) peak intensity in the XRD patterns of bare 3D-G and 3D-G metal particle nanocomposites, which indicates that GO is reduced in the reduction process. The sharp diffraction peaks at 40.1° , 39.7° , 38.3° and 38.2° in case of four different 3D-G metal particle

nanocomposites (Figure 3.2 (i) (c-f)) correspond to the (111) plane of cubic Ag (JCPDS no. 87-0720), Au (JCPDS no. 89-3697), Pd (JCPDS no. 89-4897) and Pt (JCPDS no. 87-0642) respectively. Using the Scherrer equation, the average crystallite size of Ag, Au, Pd, and Pt nanoparticles are obtained as 20, 17.5, 10.5, and 7 nm, respectively.

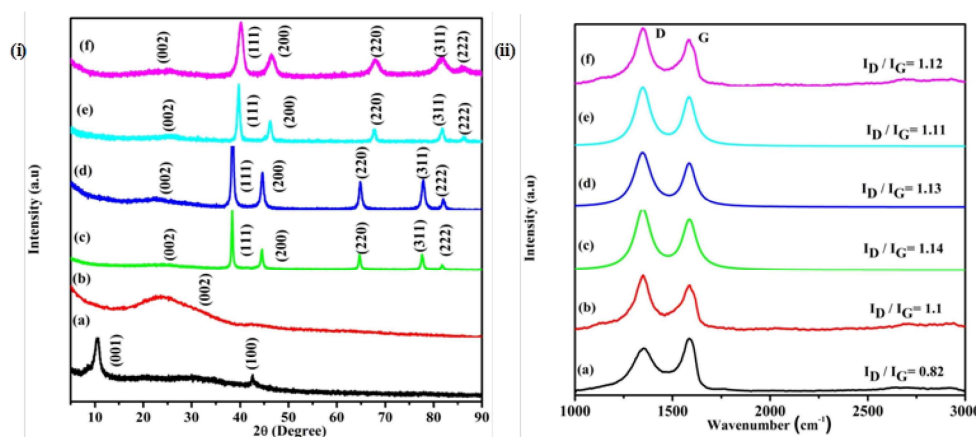


Figure 3.2 (i) XRD patterns of (a) GO, (b) bare 3D-G, (c) Ag/3D-G, (d) Au/3D-G, (e) Pd/3D-G, and (f) Pt/3D-G nanocomposites; (ii) Raman spectra of (a) GO, (b) bare 3D-G, (c) Ag/3D-G, (d) Au/3D-G, (e) Pd/3D-G, and (f) Pt/3D-G nanocomposites.

Raman spectroscopy was used to differentiate the surface and electronic structures of GO, bare 3D-G, and 3D-G metal particle nanocomposites. Figure 3.2 (ii) (a-f) shows the comparative Raman spectra of GO, bare 3D-G, and 3D-G metal particle nanocomposites. The two characteristic bands (D and G) corresponding to the defects in the curved graphene sheets and the stretching mode of crystal graphite are present at approximately 1345 and 1580 cm^{-1} in both the GO and 3D-G metal particle nanocomposites [212]. The intensity ratio (I_D/I_G) of the D band to the G band is the well-known signature of the average size of sp^2 domains [213]. Here, the I_D/I_G ratio increased from 0.82 (GO) to 1.1 (bare 3D-G), 1.14 (Ag/3D-G), 1.13 (Au/3D-G), 1.11 (Pd/3D-G) and 1.12 (Pt/3D-G) in bare 3D-G and different 3D-G metal particle nanocomposites

indicates reduction of GO and formation of new and isolated smaller graphitic domain in bare 3D-G and different 3D-G metal particle nanocomposites [213].

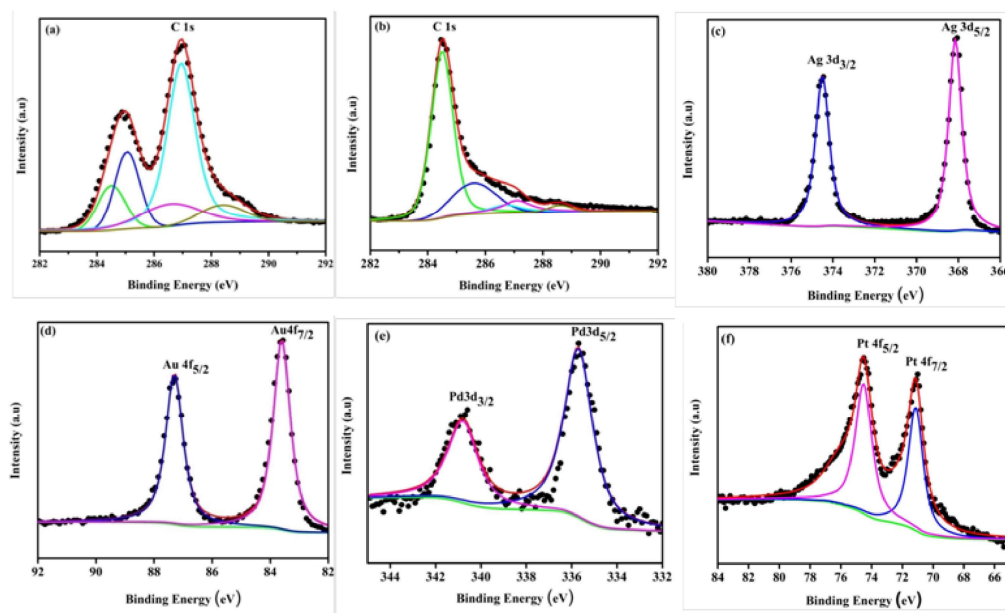


Figure 3.3 C1s XPS spectra of (a) GO, (b) Pt/3D-G nanocomposite; (c) Ag 3d (d) Au 4f (e) Pd 3d and (f) Pt 4f XPS peaks of Ag/3D-G, Au/3D-G, Pd/3D-G, and Pt/3D-G nanocomposites respectively.

X-ray photoelectron spectroscopy (XPS) is an important technique to investigate the surface chemistry of GO and 3D-G metal particle nanocomposites. Figure 3.3 (a, b) presents the C 1s XPS spectra of GO and 3D-G metal nanocomposites. The C1s spectrum of GO contains oxygenic functional groups (-COO at 288.4 eV, -C=O at 286.9 eV, and -C-O at 286.6 eV) in the range of 286-289 eV, which indicates that there is considerable oxidation of graphite in the oxidation process. In C1s XPS spectra of Pt/3D-G nanocomposites (Figure 3.3 (b)), a significant decrease of the peak intensities of various oxygenic functional groups indicated a high degree of reduction of GO to graphene in the reduction process [210]. Figure 3.3 (c-f) shows the high-resolution XPS spectra of different metal nanoparticles in 3D-G metal nanocomposites. The

peaks assigned at 374.4 and 368.1 eV are due to Ag3d_{3/2} and Ag3d_{5/2} while the peaks at 87.3 and 83.6 eV correspond to Au4f_{5/2} and Au4f_{7/2} respectively. The peaks located at 340.0 and 335.4 eV are from Pd3d_{3/2} and Pd3d_{5/2} while the peaks at 74.6 and 71.1 eV are from Pt4f_{5/2} and 4f_{7/2}, respectively. These observations clearly indicate from Figure 3.3 (c-f) that different noble metal nanoparticles (Ag, Au, Pd, and Pt) are successfully incorporated all over the 3D-G sheets.

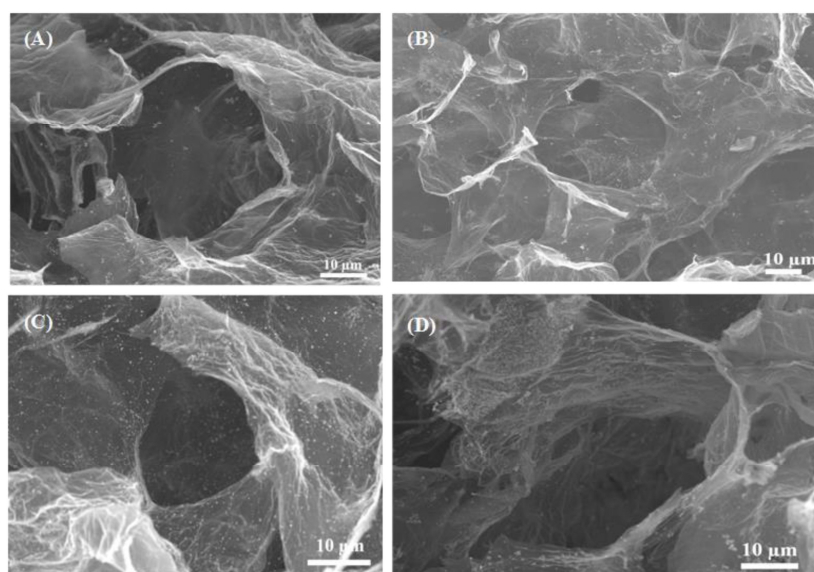


Figure 3.4 FEG-SEM images of (a) Ag/3D-G, (b) Au/3D-G, (c) Pd/3D-G, and (d) Pt/3D-G nanocomposites.

The morphology of the as-prepared metal/3D-G nanocomposites was examined by field emission scanning electron microscopy (FEG-SEM) and high-resolution transmission electron microscopy (HRTEM) measurements. Figure 3.4 (a-d) shows a well-defined and interconnected 3D porous arrangement of graphene framework with continuous open pores of an average size of 10-50 μm. Figure 3.5 (a-d) shows the HRTEM images of different metal/3D-G nanocomposites. The

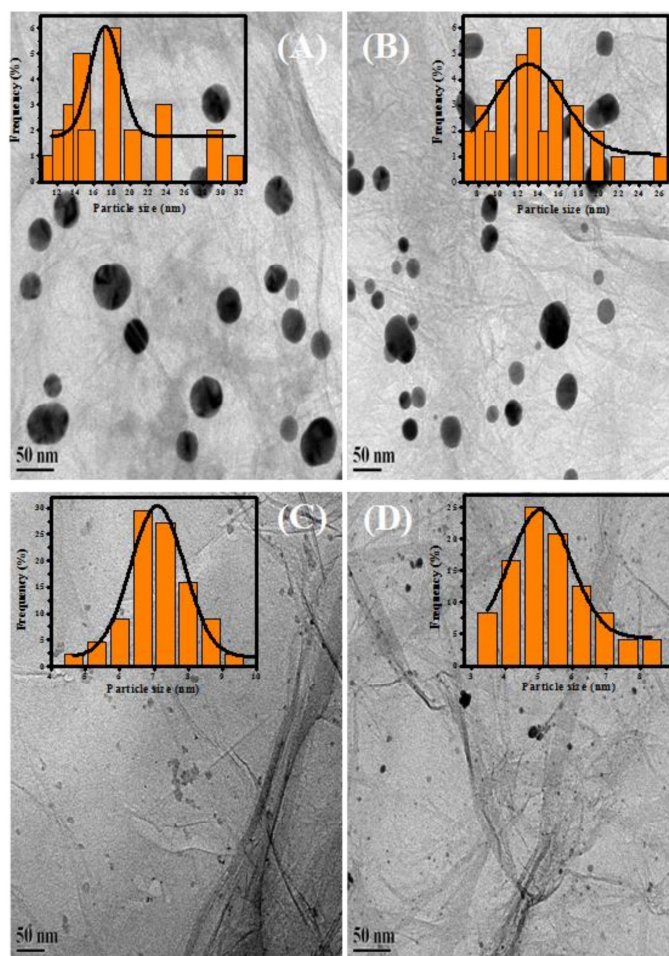


Figure 3.5 HRTEM images of (a) Ag/3D-G, (b) Au/3D-G, (c) Pd/3D-G, and (d) Pt/3D-G nanocomposites.

particle size distribution plots are shown in the inset of the Figure 3.5. The average particles size of Ag, Au, Pd, and Pt metal nanoparticles have been obtained as 18, 13, 7, and 5 nm respectively, were homogeneously distributed throughout the surface of 3D-G sheets and no free metal nanoparticles from the 3D-G sheet supports can be found. These results effectively demonstrate that graphene sheets effectively prevent the agglomeration of metal nanoparticles and strong anchoring of different metal nanoparticles over the surface of graphene sheets.

Present study focused on using nanoparticles synthesized through similar routes, though the particle sizes of the metal nanoparticles generated using similar synthesis routes are different. It is expected that a similar synthesis procedure would result in nanoparticles of different metals sizes based on their work function. It is essential to know that the metal loading due to the presence of different metal nanoparticles in the corresponding metal/3D-G nanocomposites, which has a direct influence on the morphology as well as the catalytic activity. Inductively coupled plasma optical emission spectrometry (ICP-OES) analysis was carried out for this purpose, and the metal loading of Ag, Au, Pd, and Pt metals on the corresponding metal/3D-G nanocomposites are 16, 19, 20, and 21 %, respectively. The Brunauer-Emmett-Teller (BET) surface area of Pt, Pd, Au and Ag containing catalytic systems obtained as 155, 160, 150, 165 m²/g respectively.

3.3.2 Electrochemical investigation and evaluation of the performance of the catalysts

Electrochemical investigations were carried out in 0.5 M H₂SO₄ solution using three electrodes system as previously described. For the measurements of hydrogen evolution reactions, linear sweep voltammetry (LSV) was carried out at the scan rate of 5 mVs⁻¹, as shown in Figure 3.6 (A). In acidic medium, concentration of H⁺ is very high, thus H⁺ can easily go to the surface of electrode, once it is reduced on the surface of electrode and generates hydrogen gas, its transfer rate from electrode surface to the bulk limits the kinetics of HER; thus, hydrogen evolution reaction in acidic medium is diffusion-controlled process. Before gas evolution, the supersaturation of H₂ near the electrode surface may be as high as 300 times relative to the saturation concentration of hydrogen at room temperature and pressure [214, 215]. The supersaturation of hydrogen leads to the increase in the resistance of the solution near the electrode surface; to overcome this issue, iR correction is carried out. The polarization curves of

different catalysts were compared with the iR corrected polarization curve to get the idea about the accurate kinetic current as shown in Figure 3.6 (A). At -0.05 V, the kinetic currents, i_k were found as -10.44 mAcm^{-2} , -28.41 mAcm^{-2} , -4.32 mAcm^{-2} , -0.192 mAcm^{-2} and -0.131 mAcm^{-2} for Pt/C, Pt/3D-G, Pd/3D-G, Au/3D-G and Ag/3D-G respectively. The kinetic current of Pt/3D-G catalyst was found to be almost three times better than the standard Pt/C catalyst. The onset potentials obtained for HER process were found to be the same for Pt/C and Pt/3D-G. However, the catalytic current was found to be significantly higher than the standard Pt/C catalyst. At 10 mAcm^{-2} current density, Pt/3D-G catalyst required 23 mV less potential than that of Pt/C catalyst, which shows superior catalytic activity for HER in Pt/3D-G catalyst. The Pd/3D-G catalyst (onset potential is -0.024 V) is less reactive towards HER than Pt/C as Pd has a very high affinity for the hydrogen adsorption. However, for the HER process, hydrogen desorption is the rate-determining step. Thus, high hydrogen adsorption hinders the catalytic activity for HER in the case of Pd/3D-G. For the hydrogen adsorption process; the onset potential of 0.055 V is obtained in the case of Pd/3D-G, which is more positive than Pt/C (0.050 V) and Pt/3D-G (0.029 V). In the case of Au/3D-G and Ag/3D-G, the hydrogen adsorption process is not strong, and the catalytic currents are significantly lower compared to the Pt and Pd based catalytic systems. The onset potentials for HER in Au/3D-G and Ag/3D-G were found as 0.031 V and 0.035 V, respectively. The catalytic activity of pure Au and Ag deposited glassy carbon electrode is applied for the HER catalytic process, and the plots are shown as an inset of Figure 3.6 (A). It is observed that with the incorporation of 3D-G, the catalytic activity of both Au and Ag is improved significantly.

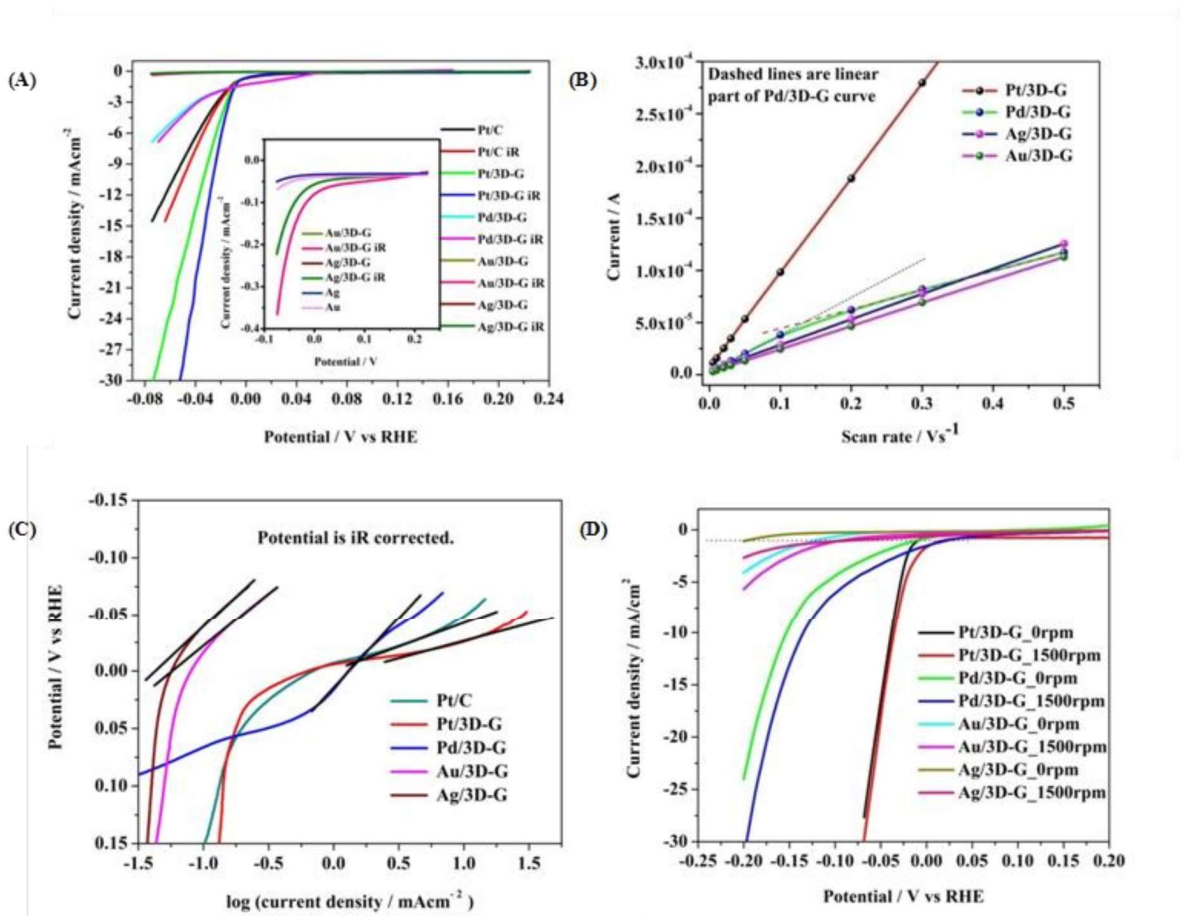


Figure 3.6 (A) Polarization curve of different catalysts at a scan rate of 5 mVs^{-1} for comparison on HER catalytic activity. Potential due to iR loss was compensated for each catalyst and compared with the measured current. (B) Current vs scan rate plot of different catalysts for double-layer capacitance (C_{dl}) measurements. (C) Tafel plots for catalysts in comparison with Pt/C catalyst Potential due to iR loss were compensated for correct measurement of Tafel plot for each catalyst. Extra lines were drawn for measurements of the Tafel slope. (D) Effect of hydrodynamic study of different catalysts on HER activity.

Double-layer capacitance (C_{dl}) was measured from cyclic voltammetry (CV) experiment in the non-faradic region, in the potential range of 0.164 V to 0.044 V for Pd/3D-G, Au/3D-G

and Ag/3D-G and from 0.22 V to 0.07 V for Pt/3D-G catalysts. At 0.125 V, the charging and discharging currents were measured for all the catalysts, and the average of these two currents is plotted against the scan rate to get double-layer capacitance, as shown in Figure 3.6 (B). C_{dl} calculated by this method contains contributions from double-layer charging and also the pseudo capacity of electrolyte ion adsorption process [216]. The C_{dl} values are summarized in Table 3.1. C_{dl} value of Pt/3D-G (9.07×10^{-4} F, 90.7 F/g) is significantly higher than the corresponding values in the case of Pd/3D-G (3.54×10^{-4} F, 35.4 F/g), Au/3D-G (2.22×10^{-4} F, 22.2 F/g) and Ag/3D-G (2.43×10^{-4} F, 24.3 F/g) catalysts. The electrochemical active surface area (ECSA) provides important information about the active surface site during the electrochemical process. ECSA accounts for the availability of active surface sites of catalyst for charge transfer and access of conducting path to transfer the electron to and from the electrode surface [217]. ECSA is calculated from the double layer capacitance measurements using the following equation

$$ECSA = \frac{\frac{C_{dl}}{cm^2}}{\text{amount of catalyst in } \frac{g}{cm^2} \times C_s} \quad (3.3)$$

Where, C_{dl} is double layer capacitance per unit geometrical surface area (0.07065 cm^2), amount of active catalyst per unit geometrical surface area (calculation is shown in supporting information), (amount of Pt, Pd, Au, and Ag only), C_s is the standard capacitance in acidic medium. C_s value for Pt and Pd was reported as $34 \mu\text{F cm}^{-2}$, and specific capacitance for Au and Ag was considered as $30 \mu\text{F cm}^{-2}$ in 0.5 M H_2SO_4 solution [218-221]. The ECSA results are reported in Table 3.1; the ECSA of Pt/3D-G catalyst was found to be over 2 times higher than Pd, Au and Ag based catalysts. Double-layer capacitance for the Pd/3D-G catalyst is 1.5 times higher than the Ag/3D-G catalyst, but ECSA is found to be

almost the same, which suggests that both catalysts are equally active for HER process. However, polarization curve Figure 3.6 (A)) suggested that Pd/3D-G catalyst is much better compared to the Ag/3D-G catalyst in the given potential window, observation thus indicates that Ag/3D-G catalyst is a potential material to function as an efficient catalytic system; however, its catalytic activity is not reflected well from the linear polarization measurements.

Table 3.1 Electrochemical parameters are obtained from CV and LSV measurements

Name of catalysts	Tafel slope mV/decade	Exchange current density(mA/cm ²)	C _{dl} (F) at 0.125V	ECSA (in cm ² /g) from DLC	R _f (in 10 ⁵ /g)	TOF from iR n at k (cms ⁻¹) at corrected 0V 0V at -0.05V
Pt/C	42	-1.05	-	-	-	-
Pt/3D-G	31	-1.63	9.07×10 ⁻⁴	105.5×10 ⁵	1493.30	0.807 2.82 19.00
Pd/3D-G	122	-1.31	3.54×10 ⁻⁴	47.4×10 ⁵	670.90	0.075 2.78 17.08
Au/3D-G	84	-0.06	2.22×10 ⁻⁴	36.9×10 ⁵	522.30	6.9×10 ⁻³ 1.60 7.90
Ag/3D-G	105	-0.04	2.44×10 ⁻⁴	49.8×10 ⁵	704.80	3.18×10 ⁻³ 1.74 9.63

Further, the roughness factor (R_f), which is an important parameter in the electrochemical process, is calculated by ECSA data and Tabulated in Table 3.1. R_f = ECSA/ geometrical surface area. R_f values are consistent with the polarization plots, which supports the activity order observed from LSV. Turnover frequency (TOF) is used for explaining the reaction mechanism of heterogeneous catalysis. Michel Boudart et al. insighted the importance of TOF in heterogeneous catalysis [222]. Turnover frequency is calculated by using the following equation

$$TOF = \frac{\text{Current density} \left(\frac{A}{cm^2} \right) \times \text{geometry surface area}}{2 \times F \times \text{no. of moles of active catalyst}} \quad (3.4)$$

Current density was sampled at -0.05 V from Figure 3.6 (A) of the polarization curve, which was iR corrected. Geometrical surface area of 3 mm diameter of GEC is 0.07065 cm². The number of moles of active catalysts was calculated from the drop casted sample. The TOF values thus obtained are tabulated in Table 3.1. The TOF value of Pt/3D-G catalyst was found as 0.807 s⁻¹, which is almost ten times higher than that of the Pd/3D-G catalyst. For industrial application, TOF value for heterogeneous catalysis are generally obtained in the range of 10⁻² to 10² s⁻¹; therefore, TOF for Pt/3D-G catalyst is reasonably high for consideration in the industrial process.

Tafel plot was used to evaluate the reaction mechanism of HER for catalytic systems investigated [208, 209, 223]. For linear fitting of the Tafel plot, LSV was recorded at scan rate of 5 mVs⁻¹ and fitted in Tafel equation $\eta = a + b \log j$, where, j is current density in mAcm⁻² and b is Tafel slope as shown in Figure 3.6 (C). Tafel slope is used to elucidate reaction mechanism of HER process. The possible reaction mechanism of HER in acidic medium consists of three steps [224]. The first step is the discharge step (Volmer reaction): $H_3O^+ + e^- \rightarrow H_{ads} + H_2O$, for the discharge step the Tafel slope, $b = 2.3 RT/\alpha F \approx 120$ mV/decade, where, R is Universal gas constant, T is absolute temperature, α (symmetry coefficient) = 0.5 and F is Faraday constant. The second step is re-combination step (Tafel reaction): $H_{ads} + H_{ads} \rightarrow H_2$. The Tafel slope, b for this step, is 30 mVdecade⁻¹. The third step is electrochemical desorption step (Heyrovsky reaction): $H_{ads} + H_3O^+ + e^- \rightarrow H_2 + H_2O$. The Tafel slope b , for this reaction, is $2.3RT / (1+\alpha) F \approx 40$ mVdecade⁻¹. The Tafel slope which has inherent properties of the reaction mechanism determines rate-determining step of reaction and hence the mechanism of the reaction. In acidic medium, HER process occurred by either two processes. One is the fast

discharge step, which is followed by rate-determining combination step, and hence Tafel slope for this process will be 30 mVdecade^{-1} , and overall, this process is called Volmer-Tafel mechanism. Another possible mechanism would be the fast discharge step is followed by rate-determining electrochemical desorption step, and hence Tafel slope for this process will be 40 mVdecade^{-1} and the overall reaction will be called Volmer-Heyrovsky mechanism.

Presently the standard Pt/C catalyst has generated 42 mVdecade^{-1} as the Tafel slope, and the Pt/3D-G catalyst has generated 31 mVdecade^{-1} ; thus the Tafel slope measurement indicates better catalytic activity of HER over Pt/3D-G catalyst compared to the commercially available Pt/C catalyst. The observed value of the Tafel slope thus indicates the HER to follow the Volmer-Tafel mechanism on Pt/3D-G catalyst. The Tafel slope of the Pd/3D-G catalyst is found to be $122 \text{ mVdecade}^{-1}$, which is closer to the required value of the Volmer reaction step. Pd has a very high hydrogen adsorption capacity, which limits the efficiency of HER reaction during the dynamic process like LSV. The Tafel slopes for Au/3D-G and Ag/3D-G catalysts are observed as 84 mV/decade and 105 mV/decade respectively, which indicates that the HER process over these two catalysts substrate follows the near Volmer reaction mechanism.

The exchange current density is an important parameter in evaluating the performance of the electrochemical process. It is a measure of the intrinsic electron transfer rate. It provides information about the structure and bonding of analyte and electrode, which are essential for heterogeneous catalysis. The exchange current densities are calculated and tabulated in Table 3.1. The exchange current density for Pt-based catalyst (-1.63 mAcm^{-2}) is found to be significantly higher than Pd based catalyst (-1.31 mAcm^{-2}), as shown in Figure 3.6 (C). These values show that there is a fast electron transfer process between the analyte and the electrode in the case of Pt-based catalyst. Exchange current density of Pt/3D-G catalyst is found to be higher

than that of Pt/C catalyst, which suggests a better electron transfer rate in Pt/3D-G catalyst compared to the commercially available Pt/C catalysts. The exchange current density of the catalytic system followed the order Pt/3D-G > Pd/3D-G > Au/3D-G > Ag/3D-G. This result is consistent with the results obtained from LSV and Tafel analysis.

3.3.3 Hydrogen evolution kinetics study under hydrodynamic conditions

Effects of hydrodynamics on HER catalysis were investigated; rotating disk electrode from Pine instruments was modified by the catalyst and used as the working electrode. LSV was recorded at 1500 rpm and compared with the stationary conditions, and the results are shown in Figure 3.6 (D). Applied potential is compared to achieve 1 mAcm⁻² of current density across different catalytic systems investigated. It is observed that potentials are shifted to anodic direction by 27 mV, 32 mV, 29 mV, and 113 mV for Pt/3D-G, Pd/3D-G, Au/3D-G, and Ag/3D-G catalysts respectively when hydrodynamics is applied as compared to the static conditions. The improvement in the potentials at 1 mAcm⁻² is similar for Pt/3D-G, Pd/3D-G, Au/3D-G catalysts upon hydrodynamics application. However, a significant improvement in overpotential is observed in the case of Ag/3D-G catalysts under hydrodynamic conditions. The significant improvements in the onset potential in the Ag/3D-G catalytic system under hydrodynamic condition implies that the catalysts are inherently very good at generating hydrogen and has high charge transfer efficiency. However, under static conditions, there might be the influence of concentration polarization which, leads to the retardation of the catalytic process. Removal of the concentration polarization under hydrodynamic conditions releases the overpotential significantly, which brings down the onset potential significantly in Ag/3D-G catalytic system to generate the current density of 1mAcm⁻².

Hydrodynamic study was further investigated for the measurement of kinetics parameters. Koutechy-Levich analysis was used to investigate mass flow and charge transfer to the HER process in the present conditions [200, 202-204, 206, 225, 226]. The Koutechy-Levich equation [25] was used to measure kinetics parameter as follows:

$$\frac{1}{i} = \frac{1}{i_k} + \frac{1}{i_l} \quad (3.5)$$

$$\frac{1}{i} = \frac{1}{i_k} + \frac{1}{B\omega^{1/2}} \quad (3.6)$$

Where, $i_k = nFkC_0$ and $B = 0.2nFC_0D^{2/3}\nu^{-1/6}$ i_k , i_l , and i are kinetic current, limiting current and measured current density respectively, n is the number of electron transfer, $F = 96500 \text{ C mol}^{-1}$ is Faraday constant, C_0 is the concentration of H^+ in bulk solution in mol cm^{-3} . D is the diffusion coefficient of proton in $0.5 \text{ M H}_2\text{SO}_4$, and the value corresponds to $9.3 \times 10^{-5} \text{ cm}^2 \text{ s}^{-1}$, and ν is the kinematic viscosity of $0.5 \text{ M H}_2\text{SO}_4$ and value is $0.01 \text{ cm}^2 \text{ s}^{-1}$ [26]. A is the surface area of RDE in cm^2 , and ω is the rotation rate of the electrode in rpm.

LSV plots of different catalysts at different rpm values have been recorded. The current is sampled at 0 V for all the catalysts in measuring the kinetic parameters. Inverse of current densities were plotted against the inverse of the square root of rpm using the above equation, as shown in Figure 3.7. Linear portions of the plot were used to obtain the slope of the plot, and the kinetic parameters were determined and tabulated in Table 3.1.

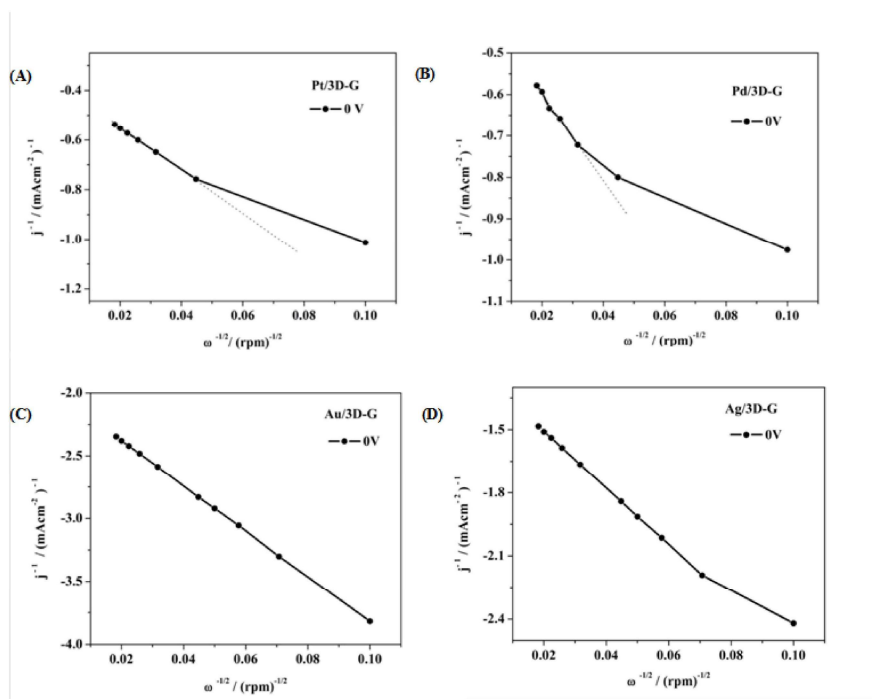


Figure 3.7 Koutechy-Levich plots for (A) Pt/3D-G, (B) Pd/3D-G, (C) Au/3D-G and (D) Ag/3D-G catalysts. Extended lines were used to measure the linear portion of plots having maximum no. of points.

The Pt/3D-G catalyst has shown the highest rate constant of the HER followed by the Pd/3D-G catalyst, the Au/3D-G, and Ag/3D-G based catalyst materials have similar rate constant values, and the absolute value of the rate constants in Au/3D-G and Ag/3D-G are around half as that for Pt/3D-G and Pd/3D-G catalysts. The number of electrons transferred in the process as obtained at the applied potential of 0 V and the values is obtained around 2.8 in the case of Pt and Pd based catalysts, and in the case of Au and Ag based catalysts, the values are around 1.7. The expected electron transfer number for the hydrogen evolution process is 2, the Au/3D-G and Ag/3D-G catalysts are showing the results as expected. The considerably higher value in the

electron transfer number in the case of Pt/3D-G and Pd/3D-G catalysts is due to the complication from the strong adsorption process.

3.3.4 Investigation of Hydrogen evolution reaction kinetics with varying temperature

Kinetics of HER process is further investigated at different temperatures. The polarization curves at different temperatures for the catalysts were measured using Ag/AgCl reference electrode and corrected to RHE reference electrode, as shown in Figure 3.8. The variation in the reference electrode potentials is measured using the following equation [227]

$$E^0(V)_{Ag/AgCl} = 0.23695 - 4.8564 \times 10^{-4} t - 3.4205 \times 10^{-6} t^2 \quad (3.7)$$

Where t is the temperature in °C. Ag/AgCl reference electrode potential was corrected using the above equation so that accurate potential could be measured. The onset potential of all catalysts is improved while the temperature of the measurement is increased, which shows good temperature dependency of HER process. For Pt/3D-G catalyst, onset potential is improved by 31 mV when the temperature is increased from 23°C to 70°C, as shown in Figure 3.8. Similar observations are obtained for other catalysts. The improvement of the onset potential of all the catalysts with the increase in temperature can be due to the (1) temperature coefficient of variation of the solution, (2) increased in the mobility of charge in solution, and (3) the endothermic process of water splitting.

In order to quantitatively investigate the dependency of temperature on the electrocatalytic activity, Arrhenius analysis of the catalysis process was carried out, and the apparent energy of activation (E_a^{app}) is calculated [17, 18] using the following equation.

$$\frac{\partial \ln i}{\partial \left(\frac{1}{T}\right)} = -\frac{E_a^{app}}{R} \quad (3.8)$$

Where T is absolute temperature, R is Universal gas constant, and i is measured current. Currents were sampled at six different potential ranges from Figure 3.8 and plotted the $\ln i$ against $1/T$ at six different applied potentials, as shown in Figure 3.9. The slopes of Pt/3D-G and Pd/3D-G catalysts are found to decrease when more cathodic potentials are applied, which indicates the strong positive dependency of the overall reaction rate on the apparent activation energy. However, the reverse trend is observed for Au/3D-G and Ag/3D-G catalysts. From Figure 3.9,

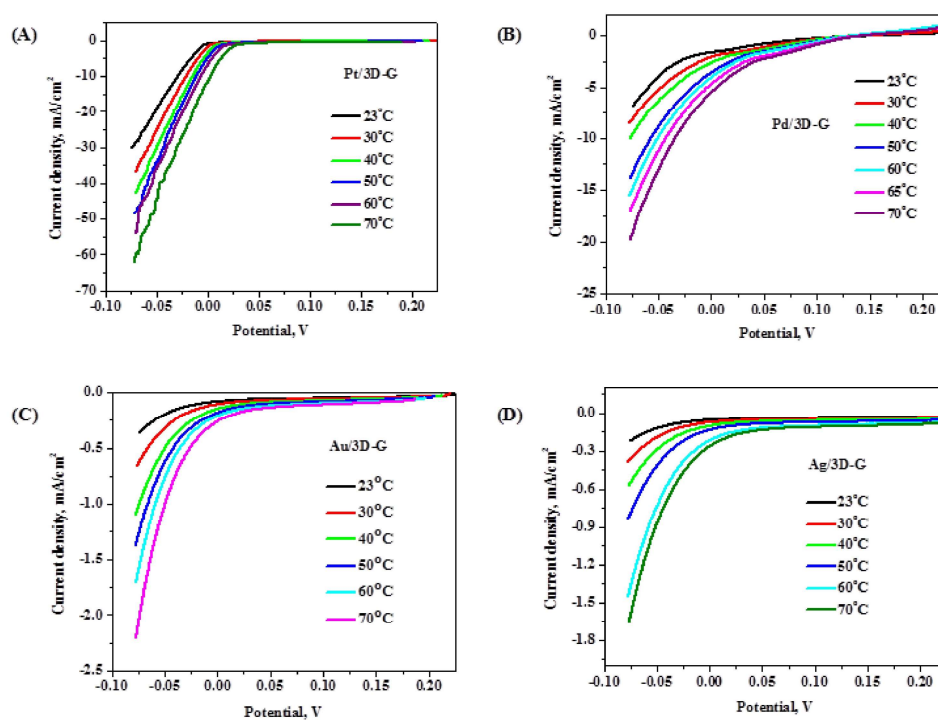


Figure 3.8 Effect of temperature on HER process was studied for catalyst (A) Pt/3D-G, (B) Pd/3D-G, (C) Au/3D-G and (D) Ag/3D-G. Temperatures were varied from room temperature to 70°C to 75°C.

slopes at different potentials of all catalysts are measured, and apparent activation energy is calculated and tabulated in Table 3.2. It is observed that the apparent activation energy is lower in the case of Pt/3D-G and Pd/3D-G catalysts compared to the Au/3D-G and Ag/3D-G catalysts. With the application of more cathodic potentials, the activation energy in case Pt/3d-G and Pd/3D-G decreased significantly, whereas in the case of Au/3D-G and Ag/3D-G catalytic systems increase in the activation energy is observed. This interesting observation is discussed in the following subsection while further analyzing the effect of temperature on the catalytic activity of the systems.

Table 3.2 Activation energy of HER of catalysts is compared at the different applied potential.

Potential, V	Apparent activation energy, E_a^{app} in kJ/mol			
	Pt/3D-G	Pd/3D-G	Au/3D-G	Ag/3D-G
0.03	25.37	32.36	16.14	24.82
0.01	29.10	28.18	17.08	26.87
0	41.57	21.29	19.37	29.03
-0.01	22.59	26.68	21.94	31.27
-0.027	13.91	27.47	26.14	34.85
-0.04	12.38	22.10	28.43	37.67

It is reported that the proton containing complex to be discharged at the outer Helmholtz layer and discharged transition state is close to the electrode surface. During the discharge step, hydrated protons move from the outer Helmholtz layer to the electrode surface and get discharged closer to the electrode surface and replace the adsorbed water molecule from the electrode surface and get adsorbed as H_{ad} [19-23].

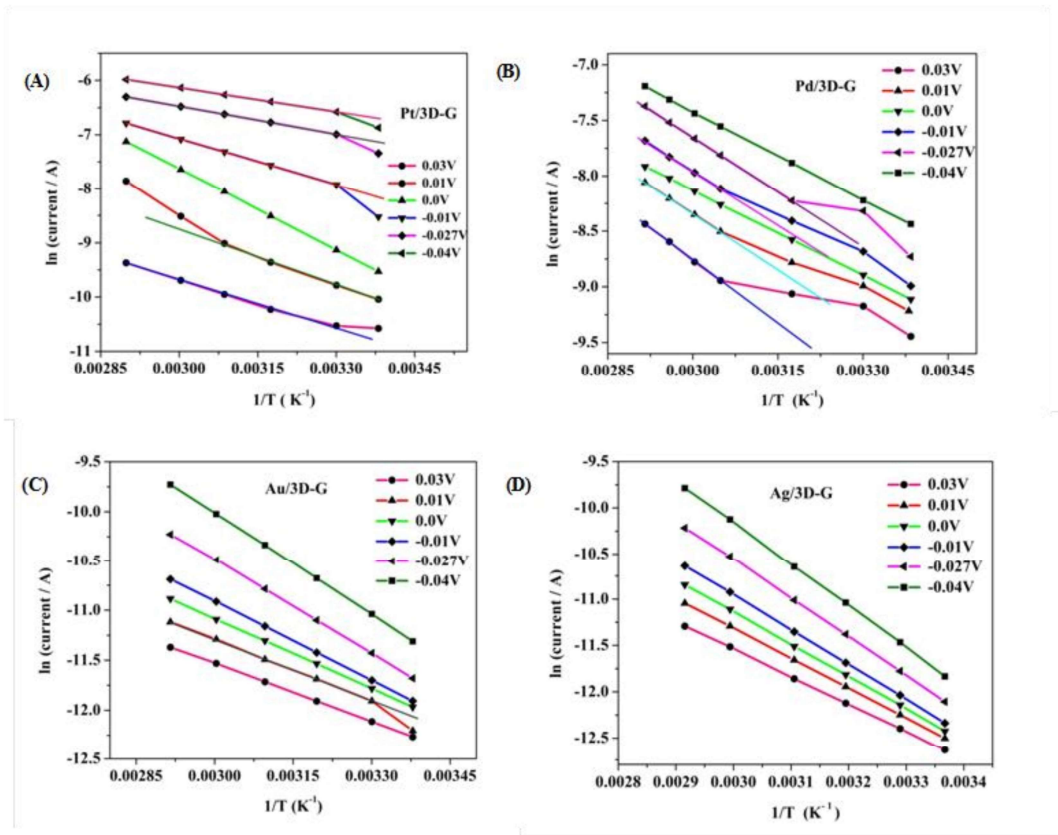
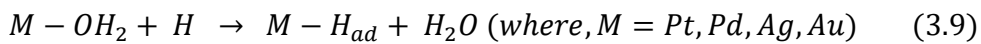


Figure 3.9 Plots of $\ln(i)$ vs $1/T$ for HER process for different catalysts (A) Pt/3D-G, (B) Pd/3D-G, (C) Au/3D-G and (D) Ag/3D-G at six different potentials in 0.5 M H_2SO_4 solution.

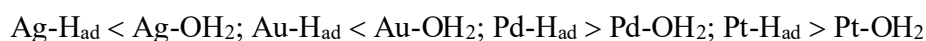


Since, overpotential η is negative for HER, the negative shift in electrode potential should lead to a decrease in activation energy

$$E_a^{app} = U^\ddagger - U^R + \beta F \eta \quad (3.10)$$

In our investigation, E_a^{app} varies with temperature differently for different catalysts. E_a^{app} of Ag/3D-G and Au/3D-G catalysts increases with potential in a negative direction, which implies

an increase in the value of $U^{\neq}-U^R$ should overcompensate the decrease in activation energy induced by the potential energy of the electron. The comparison of binding energies between the adsorption of hydrogen and water over the catalytic surface are as below [228].



Since binding energy of Ag-H_{ad} and Au-H_{ad} are lower than that for Ag-OH_2 and Au-OH_2 , a significant amount of activation energy is required to desorb water molecules from Au/3D-G and Ag/3D-G electrode surface to have the orientation required for the electron transfer process.

The potential of zero charges (PZC) of the catalyst modified electrode surface was measured from the potential dependent impedance measurements, and the plots are shown in Figure 3.10. The PZC values are obtained in four catalytic systems Pt/3D-G, Pd/3D-G, Au/3D-G, and Ag/3D-G are 0.075 V, 0.025V, -0.155V and -0.195 V, respectively. The PZC values can be utilized to explain the interaction of the water molecules and the catalyst surface across different applied potentials of the experiments. Since the PZC for Pt/3D-G catalyst is positive, the water molecule would adsorb through hydrogen atom even at the applied potential of 0.03 V, as the difference between the applied potential and PZC ($0.03 \text{ V} - 0.075 \text{ V} = -0.045 \text{ V}$) is negative, near similar observation is observed in case of Pd/3D-G catalyst. However, in the case of Au/3D-G and Ag/3D-G catalytic system due to the large negative PZC values, at the applied experimental potentials, water molecule will tend to adsorb over the catalysts surface through the negatively polarized oxygen atom. Since the binding energy of Ag-OH_2 and Au-OH_2 are higher compared to their corresponding binding with hydrogen atoms, the observed apparent activation energy of the HER is expected to be higher in the case of Au/3D-G and Ag/3D-G catalysts.

Temperature dependent HER can be further explained based on temperature dependent variation of transfer coefficients. The catalytic HER would follow the Arrhenius equation as,

$$k_{rds} = A' \exp \left[-\frac{Ea}{RT} \right] \quad (3.11)$$

The transition state theory as a function of applied potentials can be written as,

$$k_{rds} = A \exp \left[-\frac{U^\ddagger - U^R + \beta F \eta}{RT} \right] \quad (3.12)$$

The rate constant thus has the dependency on the energy of the transition state as noted by the transition state theory; it has also got the dependency on the applied potentials. Contribution

Table 3.3 Temperature dependent Tafel slopes are measured for the further insight of the HER for the catalysts.

Temperature	Tafel slope, mV/decade			
	Pt/3D-G	Pd/3D-G	Au/3D-G	Ag/3D-G
23°C	31.25	122	84.33	105.26
30°C	39.47	129	83.33	103.09
40°C	43.45	137	82.70	98.02
50°C	46.86	134	75.75	92.47
60°C	52.63	147	76.92	90.23
70°C	61.72	144	76.92	91.60

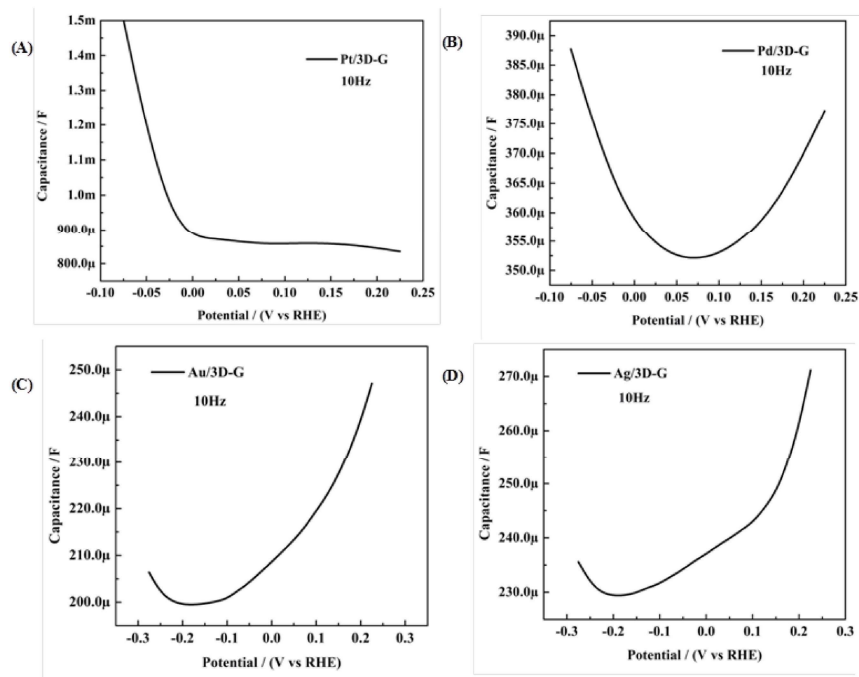


Figure 3.10 Capacitance measurements for catalysts throughout potential windows. The potential of zero charges is calculated from the potential of corresponding minimum capacitance.

from both two factors leads to the temperature dependence of the observed current. The contribution of the transfer coefficient plays an important role in determining the observed current with varying temperatures. In order to evaluate the process further, Tafel analysis was carried out at different temperatures and tabulated in Table 3.3.

Conway et al. have correlated the transfer coefficient with temperature by the relation $\beta = \beta_H + T\beta_S$ [24]. From the linear correlation of the $1/b$ vs. $1/T$ plot, β_H and β_S are calculated from the slope and intercept of the following equation and reported in Table 3.4.

$$\frac{1}{b} = \frac{F\beta_H}{2.3RT} + \frac{F\beta_S}{2.3R} \quad (3.13)$$

The correlation satisfying the total value of β using the values of β_H and β_S is shown in Table 3.5. Figure 3.11 has shown the positive slope in the case of Pt/3D-G and Pd/3D-G catalysts compared to the negative slope in case Au/3D-G and Ag/3D-G. The results indicate the HER kinetics decreases with an increase in temperature in the case of Pt/3D-G and Pd/3D-G, whereas in the case of Au/3D-G and Ag/3D-G, the HER kinetics improved with an increase in temperature of the solution. It would, therefore, be interesting to understand the relative contribution of β_H and β_S to the overall HER process in all the catalytic system. As seen from Table 3.4, β_H is very high in case of Pt/3D-G catalyst, indicates very high catalytic performance at room temperature; however it has got the negative temperature dependence, thus the catalytic performance should decrease slowly with increase in temperature due to the minor negative contribution of β_S . In the case of Pt/3D-G, the β value is significantly high even at room temperature, and its value decreases with an increase in temperature of the test solution. Pd/3D-G has β_H low positive and β_S is negative but its contribution is marginal therefore, with an increase in temperature the overall β remained positive and Pd/3D-G showed positive catalytic activity towards HER even at higher temperatures. In case of Au/3D-G and Ag/3D-G catalysts β_H is observed to be negative and have strong positive temperature dependency as β_S values are large positive, due to which the overall β is positive even at room temperature, and its magnitude increases with an increase in temperature of the measurements.

The parameter β_H is related to the change in enthalpy of the HER and as β_S is related to the change in entropy of the HER. The measurement of β_H and β_S and their temperature dependency in the investigated catalytic system thus indicates that HER on Pt/3D-G containing

catalysts is an enthalpy driven process. Pd/3D-G containing catalyst also driven by enthalpy change in the process; however, it has got weak dependency on temperature. Results indicate that the HER on Au/3D-G and Ag/3D-G containing the catalytic system are entropy driven process. At this juncture, it will be interesting to discuss the temperature dependency of the transfer coefficient to explain the variation of the activation energy at different applied potentials, as reported in the previous section. It is observed that with an increase in temperature, the transfer coefficients in the case of Au/3D-G and Ag/3D-G catalytic systems are increased, indicating better utilization of the applied potentials at higher temperatures.

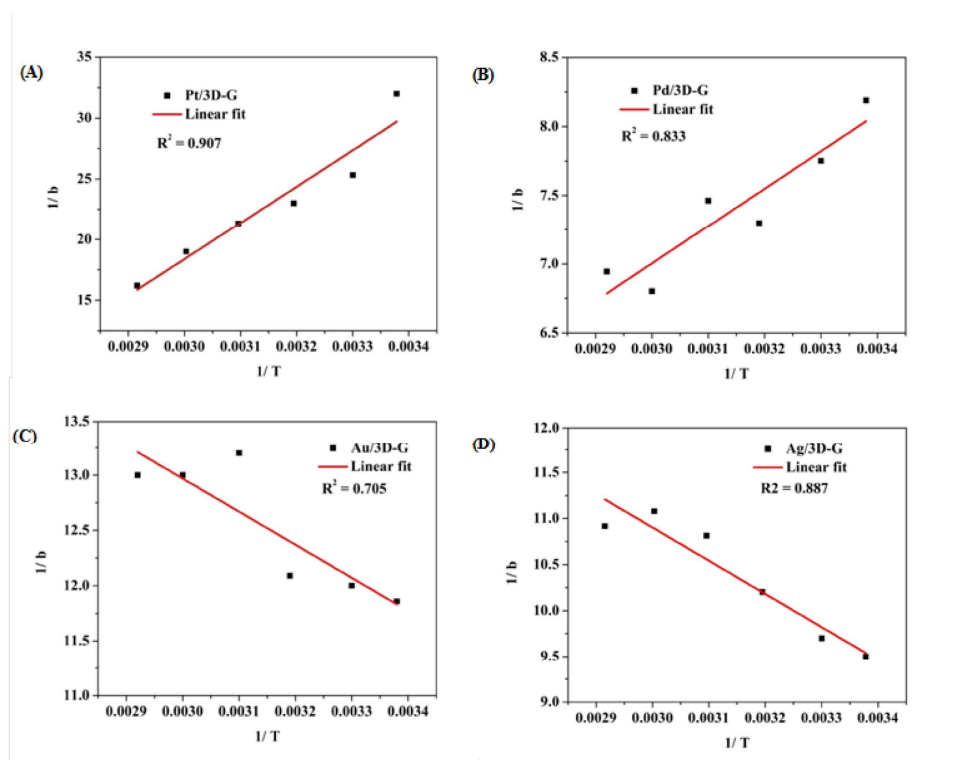


Figure 3.11 The temperature dependent symmetry coefficient is measured by the plot of $1/b$ vs $1/T$ for (A) Pt/3D-G, (B) Pd/3D-G, (C) Au/3D-G and (D) Ag/3D-G.

Table 3.4 Enthalpy and entropy dependent transfer coefficient are calculated and equation for Temperature dependent transfer coefficient was tabulated.

Catalyst	Slope	Intercept	β_H	β_S	Equation of temperature dependency of
Pt/3D-G	29925.69	-71.39	5.93	-14.14×10^{-3}	$5.93 - 14.14 \times 10^{-3}T$
Pd/3D-G	2723.22	-1.16	0.54	-2.31×10^{-4}	$0.54 - 4.76 \times 10^{-5}T$
Au/3D-G	-2995.54	21.95	-0.60	4.35×10^{-3}	$-0.60 + 4.35 \times 10^{-3}T$
Ag/3D-G	-3605.79	21.72	-0.71	4.30×10^{-3}	$-0.71 + 4.30 \times 10^{-3}T$

Table 3.5 Temperature dependent transfer coefficient is calculated for understanding of the thermodynamics of HER.

Temp., K	Pt, β	Pd, β	Au, β	Ag, β
296	1.74	0.47	0.69	0.56
303	1.64	0.47	0.72	0.59
313	1.50	0.46	0.76	0.64
323	1.36	0.46	0.81	0.68
333	1.22	0.46	0.85	0.72
343	1.08	0.46	0.89	0.76

Therefore, when the current is measured at higher temperatures, the catalytic current will be increased more significantly in the case of Au/3D-G and Ag/3D-G catalytic system compared to the Pt/3D-G and Pd/3D-G catalytic system, which will result in the higher apparent activation energy in Au/3D-G and Ag/3D-G. When the temperature dependent experiments are carried out at less negative applied potentials, where the overall electrochemical process occurs at slower

rates as the available energy to drive the reaction is low, the increment of transfer coefficient at a higher temperature will not make any significant change in the measured current. However, when temperature dependent experiments are carried out at more negative applied potentials, increment in the transfer coefficient will drive the HER at the forward direction significantly, which results in a considerable increase in the measured current. Thus, the apparent activation energy would increase at higher applied cathodic potentials in the case of Au/3D-G and Ag/3D-G catalytic systems.

The temperature dependent transfer coefficient measurements and the PZC measurements could through a light in the molecular-level understanding of the HER over different catalytic systems investigated. PZC values indicated the binding of the water molecule is through hydrogen atom in Pt/3D-G and Pd/3D-G catalysts since the enthalpy of such adsorption process is strong, the overall HER proceeds drive through enthalpy driven mechanism. Whereas in the case of Au/3D-G and Ag/3D-G catalysts, the binding is through an oxygen atom, thus during the electron transfer process, reorganization of the water molecule is required for efficient transfer of an electron from catalyst surface to the proton of water molecules. Such reorganization in the reaction system would increase the entropy of the process, which resulted in the entropy driven reaction kinetics in the case of Au/3D-G and Ag/3D-G catalytic systems.

3.3.5 Electrochemical Impedance Measurements

Further, the charge transfer efficiency of various electrocatalyst was characterized by Electrochemical Impedance spectroscopy (EIS) measurements using CH Instrument 920 D at -25 mV potential from 10^5 Hz to 10^{-1} Hz frequency range with 10 mV amplitude. EIS measurements were reported as Nyquist plot, Bode plot and corresponding equivalent Randle- Sevik circuit was drawn as shown in Figure 3.12 and observations are tabulated in **Table 3.6**. In the equivalent

circuit, R_s is solution resistance, R_{ct} is charge transfer resistance, R_{ad} is adsorption resistance, C_{dl} is double layer resistance, CPE is a constant phase element. R_s is found in the range of 10 to 15 Ω . R_{ct} values of Pt/3D-G and Pd/3D-G catalysts are found to be 210 Ω and 2681 Ω respectively, however; R_{ct} values of Au/3D-G and Ag/3D-G catalysts are $23 \times 10^3 \Omega$ and $20.91 \times 10^3 \Omega$ as shown in **Table 3.6**.

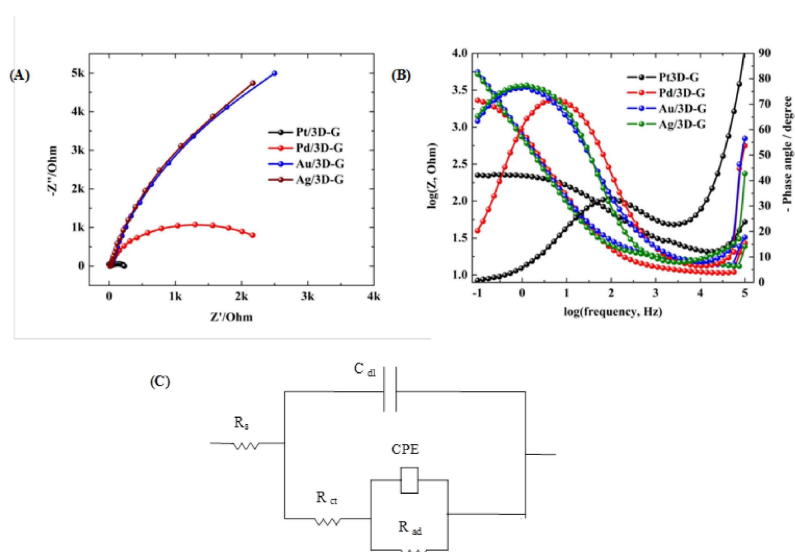


Figure 3.12 (A) Nyquist plot, (B) Bode plot and (C) equivalent circuit of fitted impedance data

Significantly lower charge transfer resistance values indicated a fast charge transfer process in the case of Pt/3D-G catalyst. The charge transfer resistance in the case of Pd/3D-G catalysts is also found to be lower, which is suitable for the fast charge transfer process. The higher charge transfer resistances in the case of Au/3D-G and Ag/3D-G catalysts indicate the lower catalytic current, which was discussed in previous sections.

The impedance characteristics of the catalysts were characterized by the Bode plot, and the results are shown in Figure 3.12 (B). The relaxation process of the electrical double layer was calculated from the phase angle maxima of the Bode plot. Relaxation frequency and relaxation

time constant are two measuring parameters of the relaxation process. Higher relaxation frequency and lower relaxation time constant lead to the faster charge transfer kinetics. The relaxation frequency of Pt/3D-G, Pd/3D-G, Au/3D-G and Ag/3D-G catalysts is 91.20 Hz, 5.66 Hz, 1.05 Hz, and 1.05 Hz respectively. The higher frequency of Pt/D-G suggests the faster charge transfer process. These results are consistent with the LSV measurements. The relaxation time constants were calculated from equation $\tau = 1/2\pi f$, where τ is the relaxation time constant, and f is relaxation frequency, which is measured from the Bode plot. The relaxation time constants are obtained as 1.7 ms, 28 ms, 151 ms, and 151 ms for Pt/3D-G, Pd/3D-G, Au/3D-G, and Ag/3D-G respectively. Faster relaxation time indicates a fast-electrochemical process, which has resulted in the higher catalytic current as revealed from the linear polarization measurements. Capacitance was also calculated from EIS, supports the data obtained from CV as shown in **Table 3.6**.

Table 3.6 Randle-Sevik equivalent circuit parameters calculated from simulation of EIS data to this equivalent circuit

Catalyst	R_s	R_{ct} (in Ω)	C_T (in F)	Relaxation frequency (Hz)	Relaxation time constant (ms)
Pt/3D-G	10 Ω	210	2.24×10^{-4}	91	1.8
Pd/3D-G	10 Ω	2681	2.10×10^{-4}	5.7	28
Au/3D-G	10 Ω	23×10^3	3.33×10^{-4}	1.05	151
Ag/3D-G	10 Ω	21×10^3	3.34×10^{-4}	1.05	151

After electrochemical measurements, stability tests of 3D-G based catalysts were performed by chronopotentiometry and chronoamperometry methods, as shown in Figure 3.13. Prior to the stability test, dissolved oxygen gas was removed by purging Ar gas for 30 minutes and maintained an inert atmosphere in the electrochemical cell. Figure 3.13 (A) shows that all catalysts are quite stable for 10000 s. For Pt/3D-G catalyst, potential is found to be quite stable at the measurement current density of 10 mAcm^{-2} . In the case of Pd/3D-G catalyst, after initial fluctuations, the potential is gradually stabilized towards more anodic potential. On chronopotentiometry measurements, Ag/3D-G catalyst showed better characteristics than Au/3D-G catalyst. Further, the stability test was conducted by the chronoamperometry method, as shown in Figure 3.13 (B). The scans were recorded by application of potential stabilized after 10000 s of chronopotentiometry measurements; the observed current response was recorded for further 10000 s. Thus, the combination of both the measurements resulted in stability testing of the catalysts for 20000 s. Pt/3D-G and Au/3D-G catalysts have shown a stable current of 10 mAcm^{-2} , as expected from their respective applied potentials. However, Pd/3D-G catalyst behaved differently; its current density is improved significantly with time; the current density in Ag/3D-G system also improved. This is indeed an interesting observation; the required bias potential of the Pd/3D-G catalyst is higher compared to the Pt/3D-G catalyst, which can be seen from LSV and chronopotentiometry measurements. However, when a relatively higher biased potential is applied to the Pd/3D-G catalyst (-0.075V) than in Pt/3D-G catalyst (-0.035 V), the chronoamperometric current improved significantly in Pd/3D-G catalyst.

The Pt/3D-G catalyst has shown the best catalytic performance as the highest catalytic current is obtained during the linear polarization measurements. The Pd/3D-G catalyst, however, has shown significant improvements in the catalytic activity with the electrolysis time while testing

the stability of the catalytic system. In a dynamic potential scan, as seen in the linear sweep measurement, the Pd/3D-G catalyst has shown inferior performance compared to the Pt/3D-G catalyst, owing to the slower dynamics in the Pd/3D-G catalysts. Under the stability test, the experiments are carried out at a constant potential, and the catalytic interface gets enough time for activation of the surface, which has resulted in the improvement of the catalytic activity in Pd/3D-G catalysts at the application of sufficient applied potential. The significant increase in the catalytic current in the case of Pd/3D-G catalyst and the improvement in the catalytic activity than Pt/3D-G catalyst is an interesting observation. The improvement in the catalytic activity in the case of Ag/3D-G catalysts is also an important observation, indicating the possibility of sustainable production of hydrogen through the evolution of hydrogen from water using the catalyst. The performance is expected to improve further in hydrodynamic conditions.

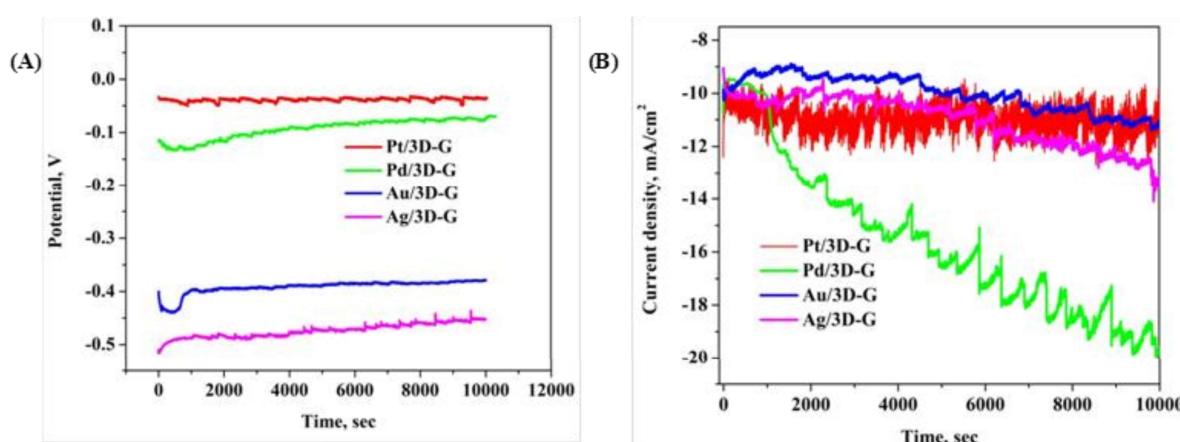


Figure 3.13 Stability test of various catalysts by chronopotentiometry and Chronoamperometry.

(A) Chronopotentiometry at 10 mAcm^{-2} current density for 10,000 s, (B) Chronoamperometry after performing chronopotentiometry for 10,000 s.

3.4 Conclusion

We have synthesized 3D-G and noble metal 3D-G nanocomposite materials by exploiting one step freeze casting method. High conducting and porous network of graphene sponge provides the excellent charge transfer and diffusion of ions through highly porous materials and improves the HER catalytic activity and stability as well. Pt/3D-G shows the better catalytic activity of HER than the commercially available Pt/C catalysts. Koutechy-Levich analysis was performed to calculate the kinetic parameters such as the number of electron transfer and rate constant of HER process. The activation energy and temperature dependent transfer coefficient were calculated for HER process. Temperature dependent transfer coefficient has explained the dominance of enthalpy and entropy on the overall mechanism of the catalytic process. It was found that HER on Pt/3D-G and Pd/3D-G catalysts are enthalpy driven process and on Au/3D-G and Ag/3D-G is entropy driven process at the given potential window. The fast relaxation process as revealed from the electrochemical impedance measurements, explains the highest catalytic activity in Pt/3D-G and Pd/3D-G catalysts. Significant improvement in the catalytic performance has been observed with the incorporation of 3D-G. Such improvements are expected to decrease in the use of expensive noble metals in the HER catalysis. Improvement in the catalytic activity through the incorporation of 3D-G generated positive indication in the utilization of less expensive Ag based catalysts without sacrificing the catalytic performance. Insight into the catalytic activity of the catalysts has been evaluated in the line to explain the variation in the performance across the catalysts and under experimental conditions.

Chapter 4: Development of the MoS₂ graphene composite as cathode materials for the hydrogen evolution reaction

4.1 Introduction

Traditional ways of production of hydrogen involves release of greenhouse gas, CO₂ and high temperature reaction and the production of hydrogen through such processes are being phased out [229]. As an electrocatalyst its most important aspect is to decrease the overpotential of splitting water [179]. In acidic solution Pt group metals are most effective catalyst for the generation of hydrogen but due to the high cost of the Pt group metal elements large scale application using these elements is not feasible [46-49]. After discussion about the noble metal-based hydrogen evolution catalysts in chapter 3, present chapter has focused on the non-noble metal-based catalyst systems for the generation of hydrogen. Due to the earth abundant nature, different transition metal alloys, carbides, polymeric carbon nitride and transition metal chalcogenides have been investigated for the HER catalysis [55, 230, 231]. Molybdenum disulfide has been preferred as catalyst for HER due to the low cost and high chemical stability [57, 58, 62, 63]. HER catalytic activity of MoS₂ has been discussed comparing its activity of the 1T and 2H phases. The catalytic activity of 2H phase is mostly through the edges of the catalytic system and this has been supported using experimental and theoretical studies [64, 65] and the basal plane was found to have no significant catalytic activity. Therefore, to improve the

catalytic activity using 2H-MoS₂ it is essential to have higher percentage of active edge sites and there have been some report about the catalytic HER reaction using 2H-MoS₂ phase [66-73]. The activity of the MoS₂ has also been investigated to improve the catalytic activity by making nano phase-based materials. Electrical conductivity of the material has been improved by incorporating Co, Ni or Fe to nano scaled MoS₂ [232]. Incorporation of Au [233], activated carbon [234], carbon paper [235] or graphite [236] has also been reported to have improved catalytic activity.

There has been tremendous improvement in the electrical conductivity of 1T-MoS₂ compared to 2H-MoS₂ and this has been reflected in the improvement of the HER activity [74-76]. Even the basal plane of the 1T-MoS₂ is quite electrochemically active for the HER catalytic activity [74-76]. Therefore, if 1T phase of MoS₂ is formed there should not have any limitation of its use only through the edge planes. Conductivity of graphene is well understood and accepted for the fabrication nano phase composite materials of high conductivity [237, 238]. The growth of the catalyst nano phases all over the graphene substrate has further improved the charge transport property of the catalysts and hence enhanced the HER activity [230].

In previous report good charge transfer property between the adjacent layers of MoS₂ and graphene has been reported [77] which has been the key point in making MoS₂ graphene composites as HER catalysts. Therefore, 1T-MoS₂ with highly conducting basal plane when make composite with graphene would have the favorable combination for the effective transformation into HER catalyst. In this chapter 1T phase of MoS₂ has been synthesized through hydrothermal route and the improvement in the catalytic activity of the 1T phase when in composite with GO and rGO has been investigated. Since the entanglement of MoS₂ between GO and rGO substrate would have some differences, it would be interesting to observe the

possible differences in their catalytic activities. Scanning probe electrochemical technique and scanning electrochemical microscopy experiments have been employed to map the catalysts substrate using redox completion mode and this has reflected the difference in the catalytic behavior between the two composite materials. Probe approach plots at different applied potentials and their transformation from the positive feedback to the negative feedback due to the introduction of redox competition mode between the tip and the substrate has been investigated.

4.2 Experimental procedures

4.2.1 Preparation of MoS₂ nanoparticle:

MoS₂ was synthesized by hydrothermal method. Ammonium molybdate ((NH₄)₆Mo₇O₂₄·4H₂O, 0.44 gm) was dissolved in 5 mL of deionized water and then hydrazine hydrate (N₂H₄·H₂O, 86%, 4 mL) as reducing agent was added drop wise under stirring condition. Reaction mixture was stirred for 0.5 h and then sodium sulfide (Na₂S, 1.32g) dissolved in 5 mL de-ionized water was added into it, then the mixture was left for 10 minutes for incubation, 5mL of 2 M HCl was added drop wise to that mixture. Then the reaction mixture was left for 10 minutes again for incubation. After that the reaction mixture was transferred into a 50 mL Teflon lined stainless steel autoclave and heated at 180°C for 24 hours. After 24 h, autoclave was allowed to cool at room temperature, and then black product was washed with distilled water several times and then with ethanol. The product as obtained was dried at 60°C for 12 h in the vacuum oven. The mole ratio of the reactants was kept at Mo: N₂H₄:Na₂S of 1:357:48 during the synthesis process.

4.2.2 Synthesis of graphene oxide

Graphene oxide was synthesized using the modified Hummer's method [239, 240]. Concentrated H₂SO₄ (300ml) and H₃PO₄ (40 mL) were taken in a round bottomed (RB) flask of 1 L capacity. The RB flask was kept in an ice-bath at 0-5 °C. The whole setup was kept in magnetic stirrer then graphite (2g) powder was placed into RB flask slowly and the mixture was kept for stirring for 2 h. Then KMnO₄ (12g) was added slowly to this mixture under stirring condition, this reaction mixture was stirred for 3 days at room temperature. After that the reaction mixture was kept in ice-bath, H₂O₂ (20 mL) was added slowly to terminate the reaction followed by washing with HCl (10%) and then distilled water several times to achieve the neutral pH. The graphene oxide thus obtained was dried in vacuum oven and used for further experiments. Graphene oxide was reduced by treating GO suspended aqueous solution using hydrazine monohydrate by stirring for 1 h and then the solution mixture was kept under hydrothermal conditions at 180°C for 12 h. The rGO thus obtained was washed and dried for further use.

4.2.3 Procedure of electrochemical Studies and instrumentation

MoS₂ and GO or rGO were mixed in mortar (in 1:4 ratios). Then 1 mg sample mixture was suspended in ethanol and water solution (in 1:1 ratios) and kept in stirring conditions for 24 h. The suspension was sonicated for 1 h and then 100 µL nafion (5 wt %) was added and again sonicated for 30 min. After sonication a homogeneous mixture was formed and then 5 µL catalyst ink was drop casted onto the glassy carbon (GC) electrode which then dried under IR lamp. Electrochemical measurement for hydrogen evolution catalysis process was carried out using CH Instrument model 920d. Electrochemical studies were performed in 0.5 M H₂SO₄

solution using a typical three electrode setup using the catalyst modified electrode as the working electrode, Pt wire as counter electrode and Ag/AgCl electrode as reference electrode. Linear sweep Voltammetry (LSV) and cyclic Voltammetry (CV) were performed to evaluate HER performance. The glassy carbon electrode was polished to mirror finish using alumina powder of 0.05 microns size and ultrasonically cleaned in distilled water for 10 minutes followed by drying in IR lamp. Electrolyte solution was purged with N₂ gas for 30 minutes prior to the electrochemical measurements to remove dissolved oxygen. Before measurements, the samples were cycled at a scan rate of 10 mVs⁻¹ for 50 times to refresh the catalytic surface. All the electrochemical measurements are reported against the potential vs. reversible hydrogen electrode (RHE) as the reference electrode. The Ag/AgCl reference electrode was calibrated in three electrodes system using cleaned Pt electrode as working electrode and Pt wire as counter electrode. 0.5M H₂SO₄ solution was used as electrolyte which is purged using high purity H₂ gas before and during measurements. LSVs were recorded at the scan rate of 1mVs⁻¹ and the potential where the current was zero is taken as the reference potential of hydrogen electrode and was found to be -0.2246V. All the electrochemical potentials applied and measured using Ag/AgCl reference electrode were converted to RHE using following equation, in addition to conversion of the potential with respect to RHE, potentials were also corrected for the *iR_s* drop.

$$E_{corrected} = E_{Ag/AgCl} + 0.2246 V - iR_s \quad (4.1)$$

Where, $E_{Ag/AgCl}$ is Ag/AgCl electrode potential, 0.2246 V is corrected potential, R_s is resistance of solution, iR_s is potential drop due to solution resistance which is measured using electrochemical impedance measurements reported later section of this chapter.

All the measurements were iR_s compensated in the present study and value of R_s was found by conducting impedance measurement in 0.5 M H_2SO_4 and values of R_s was in the range of 6 to 7 Ω for both MoS_2/GO and MoS_2/rGO composite materials. The temperature during electrochemical measurements was $25\pm 1^\circ C$. The overpotential ' η ' for hydrogen evolution was calculated using following equation

$$\eta = E_{RHE} - 0 V - 0.0591 pH - iR_s \quad (4.2)$$

Atomic absorption spectrometry (AAS) was used for the chemical quantification of the catalyst, the Mo content was determined using AAS instrument model Contra AA-300 from Analytic Jena, Germany. The Mo content in both the samples were quantified at 20% (wt %). The presence of GO and rGO in the composite was determined by measuring total carbon content in the sample using carbon sulfur analyzer from Eltra. The GO and the rGO content of the sample were kept the same and the percentage composition of GO and rGO in the catalyst samples were determined at ~60%.

4.3 Results and discussion

4.3.1 Characterization of the materials

MoS_2/GO and MoS_2/rGO samples were characterized by X-ray diffraction (XRD) and the diffraction patterns are shown in **Figure 4.1** (A) and (B) respectively. Three diffraction peaks $2\theta = 12^\circ$, 43° and 57.5° correspond to (002), (006) and (110) plane of MoS_2 respectively [powder diffraction file (PDF no. 37-1492)], which are due to the metallic 1T structure of MoS_2 [241, 242]. XRD peak at (002) plane of MoS_2/GO and MoS_2/rGO , are at higher 2θ value than pristine MoS_2 suggests that the lower stacking height along Z-axis and more exposure of its active sites. The 1T phase of MoS_2 with trigonal crystal structure and octahedral orientation has

shown to have significant difference in the electronic property compared to the hexagonal 2H phase [243-245]. Raman spectroscopy was used for further characterization of phases of MoS₂. The three peaks at 283 cm⁻¹, 365 cm⁻¹ and 414 cm⁻¹ correspond to the hexagonal vibration modes E_{1g}, E_{2g}¹ and A_{1g} of MoS₂ respectively.

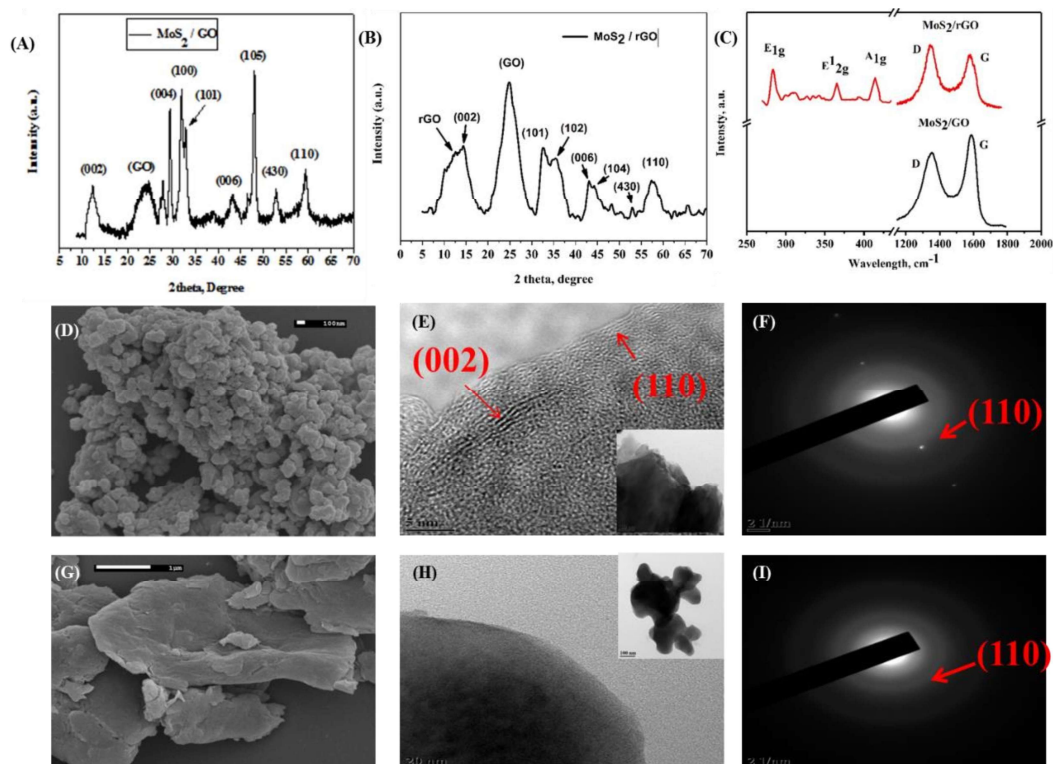


Figure 4.1 XRD pattern of (A) MoS₂/GO and (B) MoS₂/rGO. Raman spectra of different vibrational modes of (C) MoS₂/GO and MoS₂/rGO. SEM images, TEM and SAED patterns of (D,E, F) pristine MoS₂ and (G, H, I).MoS₂/GO.

The in-plane E_{2g}¹ and out of plane A_{1g} vibrational mode resulted from the opposite vibration of S atom with respect to Mo atom and out of plane vibration of only S atom to Mo atom [246], suggests the formation of pure MoS₂ phase. Two bands at 1357 cm⁻¹ and 1577 cm⁻¹ correspond to D and G band are clear evidence of graphene sheets in the nanocomposite. As shown in

Figure 4.1 (C), the I_D/I_G ratio of graphene oxide and reduced graphene oxide composite were calculated as 0.92 and 1.07 respectively, which confirmed that GO is reduced to rGO [247]. No significant change in the vibrational mode was observed with the MoS_2 phase during the reduction of GO to rGO. The surface area measured using Brunauer–Emmett–Teller (BET) method and the values for MoS_2/GO and MoS_2/rGO were obtained as 65 and 79 m^2/g respectively.

The morphology and lattice parameters were characterized by SEM and TEM images. **Figure 4.1** (D) and (G) are showing the SEM micrograph of the pristine MoS_2 and the MoS_2/rGO composite materials. Granular nature of the composite for the MoS_2 and sheet type composite for the MoS_2/rGO composite were observed. TEM images of pristine MoS_2 and MoS_2/rGO are shown in **Figure 4.1** (E) and (H) respectively and The TEM images of MoS_2/GO are shown in **Figure 4.2** both the composite materials have shown the layer type of structure. The selected area electron diffraction (SAED) of MoS_2 has shown the (002) plane and the (110) plane of MoS_2 . Random interconnection between the GO or rGO to MoS_2 network and random stacking of the (002) plane is vulnerable in MoS_2 for the decrease in the catalytic activity [248]. The clear observation of the (002) plane from the XRD and TEM measurements rule out the random stacking of the MoS_2 network. The TEM and SAED of the MoS_2/GO nano composite materials are shown in **Figure 4.2**; showed similar nano structural characteristics as that of the MoS_2/rGO . The SEM with EDS results of both the materials are shown in **Figure 4.3**. Presence of Mo, S along with C and O are observed. The surface morphology of the catalysts modified substrate was examined using AFM measurements using the MoS_2/GO modified substrate. The morphology has shown regular granular pattern of the catalyst embedded all over the GO substrate. The average particle size (diameter) for MoS_2/GO was obtained as 60 nm.

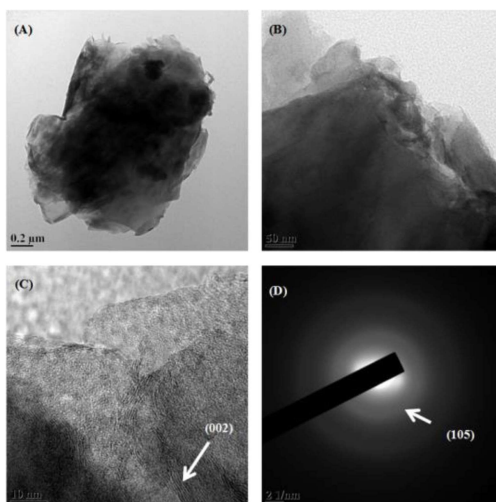


Figure 4.2 (A), (B) and (C) are HRTEM images and (D) is SAED pattern of the MoS₂/GO nano composite materials.

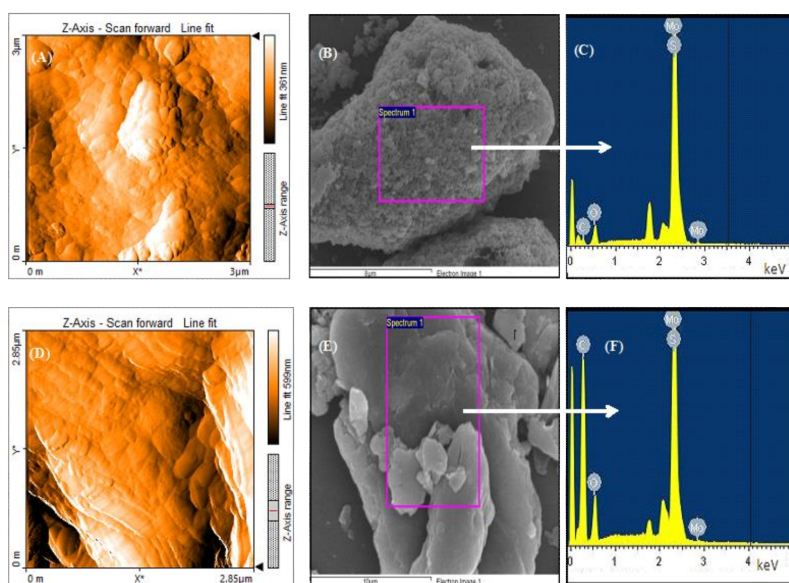


Figure 4.3 AFM images of MoS₂/GO (A) before electrochemical test using chronopotentiometry and (D) after chronopotentiometry at 10mA/cm² current density for 4 hours. EDS images of (B, C) pristine MoS₂ and (E, F) MoS₂/rGO.

4.3.2 *Electrocatalytic HER activity*

Electrochemical HER activity of the catalyst was investigated in 0.5 M H₂SO₄ solution by depositing catalyst ink on glassy carbon electrode using three electrode system as discussed in the experimental section. In polarization curve, potential is corrected with *iR* drop and with the potential with respect to the reversible hydrogen electrode (RHE). The LSV and CV plots for both the catalysts along with the commercially available Pt/C catalyst are shown in **Figure 4.4**. The LSV plot of both the composite materials have shown sharp increase in the catalytic hydrogen evolution current after the onset potential. The onset potential for the MoS₂/GO is lower by ~ 0.13 V than MoS₂/rGO, however when compared with the Pt/C catalyst, both the materials have shown good electrocatalytic properties and the onset potential is not so inferior to the commercially available Pt/C catalyst materials. As seen from **Figure 4.4** (A) the catalytic activity of the only GO and only rGO modified electrode has shown no reduction current due to the reduction of proton. Therefore the GO and rGO played only a synergistic role in catalysing the hydrogen evolution process along with MoS₂. The onset position of the LSV plots was zoomed and shown as inset of **Figure 4.4** (A) and (B), the reduction current in both the composite materials started increasing at 0.2 V and separated from the base line current of GO and rGO composite modified substrate. A peak shape was generated at -0.027 V, just before the onset potential for the hydrogen evolution process. This reduction peak is the partial reduction of MoS₂ at the Mo⁴⁺ centre, later it was oxidised back to its original oxidation state [249].

The LSV plots were further recorded under hydrodynamic conditions and corresponding results in comparison with the data under static condition is shown in **Figure 4.4** (B). At 1500 RPM, the onset potential was improved in both the composite materials compared to the static condition. However, the catalytic current at higher applied potential, beyond -0.15 V remained

the same at static and hydrodynamic conditions. Interestingly, the peak current for the peak observed just before the onset potential was increased under hydrodynamic conditions. LSVs were also compared at two different rotation speeds, as shown in **Figure 4.4 (C)**, the onset potential of the hydrogen evolution process was improved in both the materials when the rotation speed was increased from 500 rpm to 3000 rpm. The improvement in the catalytic activity at the low current region due to the hydrodynamic conditions is due to the enhanced mass transfer attained by the hydrodynamic mass flow.

From the LSV measurements as discussed in the previous section the MoS₂/GO has shown better catalytic activity for the hydrogen evolution process in terms of the better onset potential and the high catalytic current density. To delineate the better catalytic activity of the MoS₂/GO composite, the electrochemical surface area of the catalyst surface was measured from the double layer capacitance (C_{dl}) measurements. CV experiments were carried out at different scan rates and the current sampled at three potentials 0.1, 0.15 and 0.2 V, where no significant redox process observed, was plotted with respect to the applied scan rates. The results are shown in **Figure 4.4 (C)**, from the slope of the linear plot the double layer capacitance was determined and tabulated in **Table 4.1**. The “ C_{dl} ” value was calculated from the slope of the current density and scan rate plot [250].

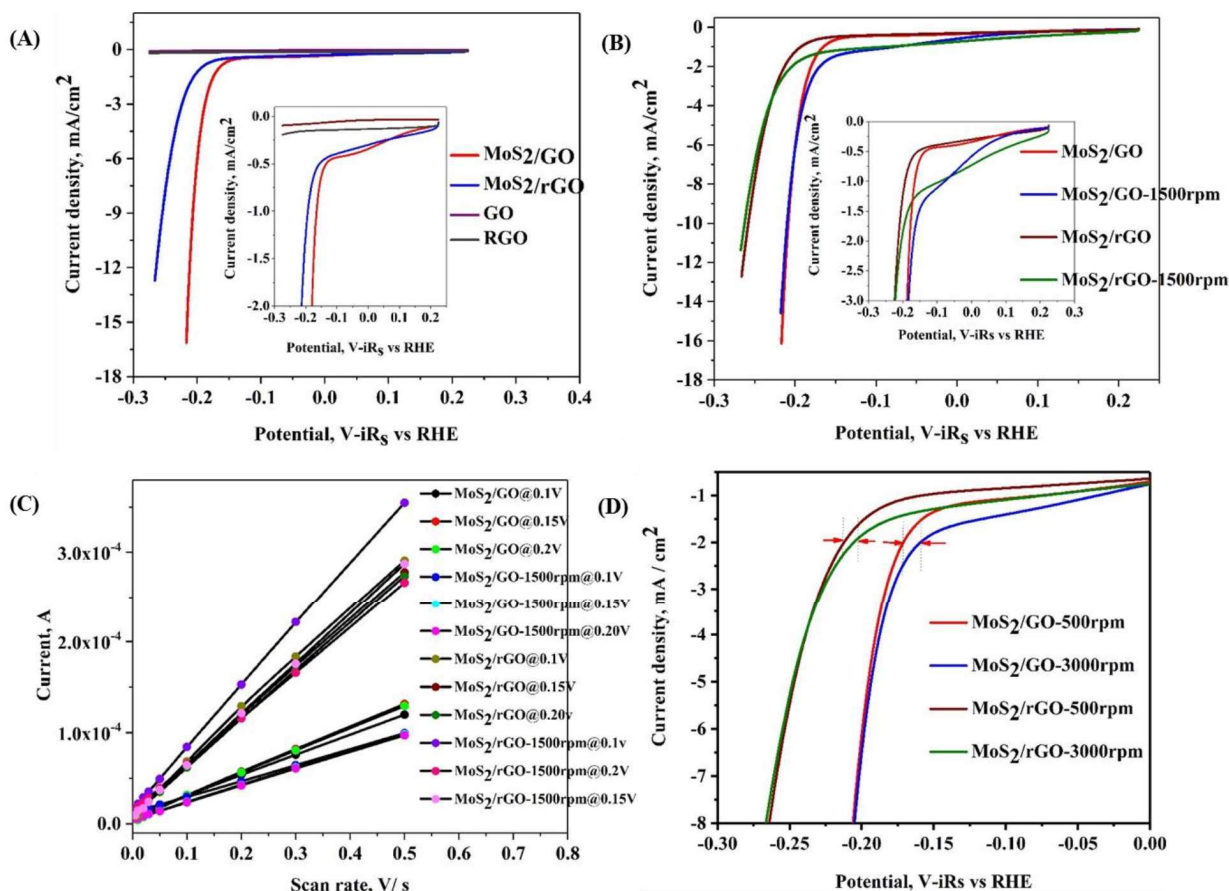


Figure 4.4 (A) Polarization curve of various catalysts. Magnified image at lower current density is shown as inset. (B) Polarization curve of catalysts with and without hydrodynamic effect. Magnified image at lower current density is shown as inset. (C) Effects of scan rate on current density. (D) Effect of hydrodynamic conditions on the catalytic activity.

The “ C_{dl} ” values of MoS₂/GO and MoS₂/rGO are obtained as 0.34 mF (~ 75 F/g) and 0.72 mF (~ 158 F/g) respectively. Effect of hydrodynamics on C_{dl} value shows that C_{dl} value increases for MoS₂/rGO from 0.72 to 0.87 mF (~ 158 to 192 F/g); however, C_{dl} value decreases for MoS₂/GO from 0.34 to 0.27 mF (~ 75 to 60 F/g). The roughness factor was calculated from the double layer capacitance using the following equation

$$R_f = C_{dl}/60 \quad (4.3)$$

Where, the value '60' represents the specific capacitance of a smooth surface in $\mu\text{F cm}^{-2}$ [251].

Table 4.1 . Electrochemical parameters as obtained from the cyclic voltammetry measurements at different scan rates.

Name of catalysts	Potentials	C_{dl} / F	$R_f = C_{dl}/60\mu\text{Fcm}^{-2}$
MoS ₂ /GO	0.20V	2.53×10^{-4}	4.21
	0.15V	2.55×10^{-4}	4.25
	0.10V	2.27×10^{-4}	3.78
MoS ₂ /GO-1500rpm	0.20V	1.85×10^{-4}	3.08
	0.15V	1.85×10^{-4}	3.08
	0.10V	1.72×10^{-4}	2.87
MoS ₂ /rGO	0.20V	5.3×10^{-4}	8.83
	0.15V	5.31×10^{-4}	8.85
	0.10V	5.76×10^{-4}	9.6
MoS ₂ /rGO-1500rpm	0.20V	5.06×10^{-4}	8.43
	0.15V	5.58×10^{-4}	9.3
	0.10V	6.81×10^{-4}	11.35

As seen from **Table 4.1**, the R_f value for MoS₂/rGO is higher than MoS₂/GO, so its HER activity should have been higher than MoS₂/GO, however polarization curve shows that MoS₂/GO is having better catalytic activity. This contradicts the above observation. Therefore, observation of higher catalytic activity in the case of MoS₂/GO compared to MoS₂/rGO indicates that higher catalytic current in the case of MoS₂/GO is not related to the surface area of the materials and something to do with the inherent characteristics of the HER process over the catalysts substrate.

Improvement of the onset potential due to the introduction of the hydrodynamic conditions has been mentioned while discussion with the results in Figure 4.4 (D). Hydrodynamic conditions were further discussed by determining the kinetic parameters. As shown in **Figure 4.4** (D) no significant effect of rotation on catalytic activity was observed at higher overpotential range, but at lower overpotential the catalytic current is modified significantly. At 2 mA/cm² current density, the applied potential was improved by 13.1 mV in the case of MoS₂/GO and improved by 7.4 mV in the case of MoS₂/rGO when the rotation speed was increased from 500 rpm to 3000 rpm. A detail kinetic information about the contribution from the mass flow and the charge transfer

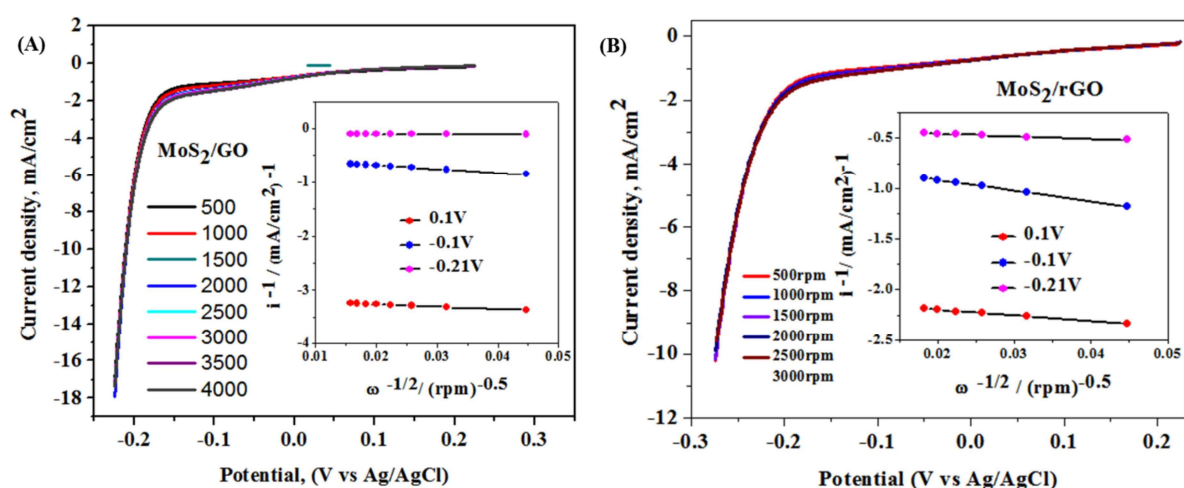


Figure 4.5 Koutechy-Levich plot of (A) MoS₂/GO and (B) MoS₂/rGO.

Currents were sampled at different applied potentials of the LSV plot (Figure 4.5) during the Koutechy-Levich analysis and corresponding kinetic parameters for both the composite materials are shown in Table 4.2. At lower applied potential, below the onset potential the number of electrons transferred was obtained close to one, at higher applied potential (at -0.21 V) the number of electrons transferred was increased significantly. Such unreasonably high value of the

number of electrons transferred for the HER process is accounted for the enhanced mass flow which resulted in the increased surface concentration of the H⁺ compared to its bulk concentration. The electron transfer rate constant of the HER process in MoS₂/rGO catalyst was marginally higher than that for MoS₂/GO catalytic system.

Table 4.2 Analysis results from the hydrodynamic voltammetric measurements using the Koutechy-Levich analysis. The final values of n and k are rounded off to 2 decimal places.

Name of catalyst	Potential	Slope	Intercept	1/intercept, i _k in mA/cm ²	n	k, cm/s
MoS ₂ /GO	0.10V	-4.41	-3.57	-0.28	1.15	5.06×10 ⁻³
MoS ₂ /GO	-0.10V	-6.66	-0.55	-1.81	0.76	49.45×10 ⁻³
MoS ₂ /GO	-0.21V	-0.18	-0.10	-10.32	27.91	7.66×10 ⁻³
MoS ₂ /rGO	0.10V	-5.72	-2.08	-0.48	0.88	11.26×10 ⁻³
MoS ₂ /rGO	-0.10V	-10.58	-0.71	-1.42	0.47	61.41×10 ⁻³
MoS ₂ /rGO	-0.21V	-2.43	-0.41	-2.45	2.08	24.44×10 ⁻³

Temperature dependent electrochemical measurements were carried out in a custom made cell in which water can be filled in outer jacket for temperature control, corresponding result for the MoS₂/GO and MoS₂/rGO materials are shown in Figure 4.6. Reference electrode was corrected for temperature using the following equation [227].

$$E^0(V)_{Ag/AgCl} = 0.23695 - 4.8564 \times 10^{-4}t - 3.4205 \times 10^{-6}t^2 \quad (4.4)$$

LSVs at different temperatures varying from 5°C to 70°C were recorded. The Ag/AgCl reference electrode was calibrated for different temperatures using above equation. Figure 4.6 shows the temperature dependent LSV for the MoS₂/GO and MoS₂/rGO catalyst and the results indicated the improvement of the onset potential for the HER process with rise in temperature.

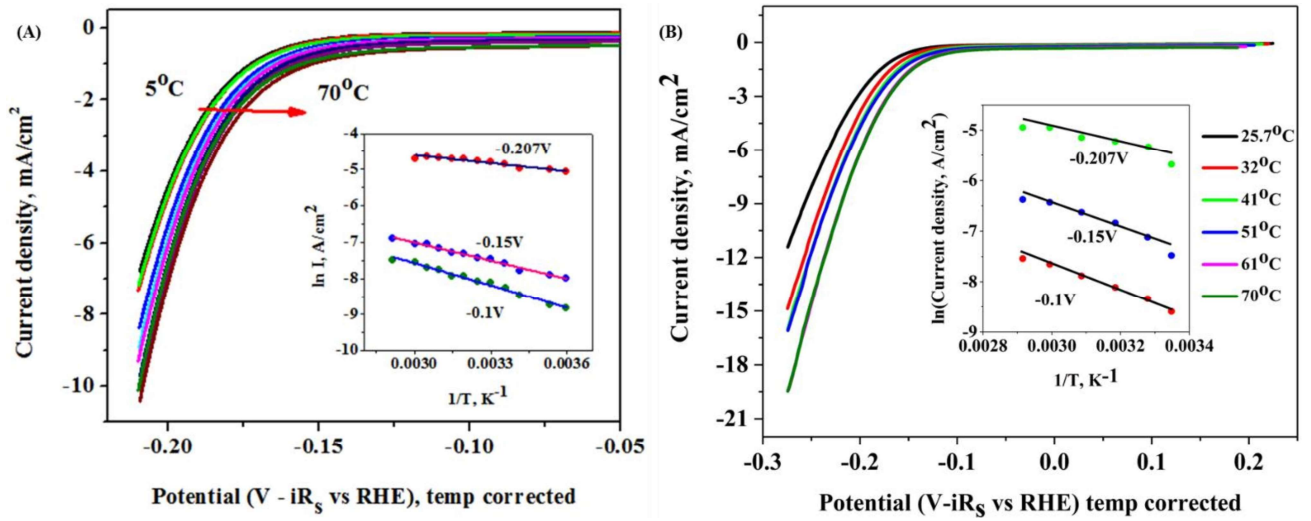


Figure 4.6 Temperature dependent polarization curve for (A) MoS₂/GO and (B) MoS₂/rGO. Inset Figure is Arrhenius plot for activation energy calculation.

In order to evaluate and extract the activity of the electro catalysts, apparent activation energy for hydrogen evolution (E_a^{app}) is estimated using the following equation [17, 18].

$$\frac{\partial \ln i}{\partial \left(\frac{1}{T}\right)} = - \frac{E_a^{app}}{R} \quad (4.5)$$

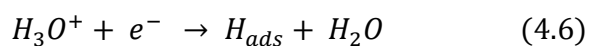
Where, E_a^{app} is evaluated at different applied potentials, i is the current density at a given applied potential, T is the absolute temperature and R is the universal gas constant. After recording the LSVs at different temperatures the observed currents were sampled at three different applied potentials and $\ln(i)$ vs $1/T$ plots at three different applied potentials are shown in inset of Figure 4.6. It was observed that the slopes of the plots were decreased with the application of more cathodic potential, indicating potential dependent apparent activation energy for the overall process. The apparent activation energy for MoS₂/GO composite material is relatively lower than that of the MoS₂/rGO at all applied potentials as given in **Table 4.3**. Since the activation energy

is calculated from the change in the overall current with the change in temperature of the process (mass transfer and charge transfer) affected by the change in temperature will be reflected in the activation energy calculation. Therefore, the relatively low activation energy in MoS₂/GO material might be due to the enhanced mass transfer compared to MoS₂/rGO.

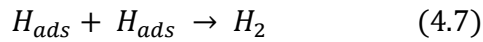
Table 4.3 Activation energies obtained on two catalytic systems at different applied potentials

$\ln i = \ln i_0 - E_a^{app} / RT$		
Overpotential, V	E_a^{app} of MoS ₂ /GO, kJ/mol	E_a^{app} of MoS ₂ /rGO, kJ/mol
0.10V	17	20
0.15 V	14	19
0.21 V	6	10

Tafel treatment was applied to the LSV plot and the linear portion of the Tafel plot in **Figure 4.7 (A)** was fitted using the Tafel equation, $\eta = a + b \log j$, where j is the current density and b is the Tafel slope. The Tafel slopes for the corresponding catalyst materials MoS₂/GO and MoS₂/rGO are obtained as ≈ 40.6 and ≈ 71.8 mV/decade respectively. Overpotential is iR_s corrected and in the scale of RHE value. The Tafel slope is used to elucidate the mechanisms involved in HER process. There are three possible reaction steps in acidic aqueous medium for the HER process [224]. First, the discharge step (Volmer reaction):

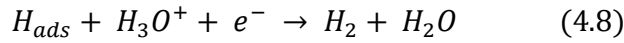


Where the Tafel slope, $b = 2.3RT/\alpha F \approx 120$ mV/decade, R is the universal gas constant, T is the absolute temperature, $\alpha = 0.5$ is the symmetry coefficient and F is the Faraday constant. Second step is the combination step (Tafel reaction):



$$b = 2.3RT/2F \approx 30 \text{ mV/decade}$$

Third step is the electrochemical desorption step (Heyrovsky reaction):



$$b = 2.3RT/(1 + \alpha)F \approx 40 \text{ mV/decade}$$

Tafel slope is an inherent property of the catalyst that is determined by the rate-limiting step of the HER process. Generally, fast discharging step (5) is followed by either combination step (6) or electrochemical desorption step (7). If, fast discharging step (5) is followed by rate limiting combination step (6), Tafel slope will be $\sim 30\text{mV/decade}$ in this case the overall mechanism of the process would be Volmer-Tafel mechanism. If, fast discharging step (5) is followed by slow electrochemical desorption step (7), Tafel slope will be $\sim 40\text{mV/decade}$ and in that case the HER mechanism would be Volmer-Heyrovsky mechanism. When the electrochemical discharging step is the rate limiting step Tafel plot will be $\sim 120\text{mV/decade}$ and the mechanism will be through the Volmer step as the rate determining step [224, 225, 252].

The observed Tafel slope of $\sim 40.6 \text{ mV/decade}$ in the present case as seen from **Figure 4.7 (A)** for MoS₂/GO hybrid catalyst suggests that electrochemical desorption step would be the rate limiting step of the present system. In the case of MoS₂/rGO hybrid catalyst the Tafel slope was observed as 71.8 mV/decade . The mechanism of the hydrogen evolution process over the MoS₂ catalytic system is such that the discharge step predominates over the Mo centre and S and graphene centers are responsible for the adsorption and further recombination process to liberate hydrogen gas out of the catalytic system. Mo centers are similar in both the catalytic systems and the major difference would arise due to the difference in the GO and rGO in the catalysts. The

significantly higher Tafel slope in the case of MoS₂/rGO hybrid catalyst system is indicative of mixed mechanism operating across the catalysts substrate. Part of catalyst substrate having Mo centers would have fast discharge process; whereas the rest of the surfaces are resulting in the slow discharge kinetics making the overall Tafel slope high [68, 253-256]. In the case of MoS₂/GO hybrid catalyst system, there are plenty of exchangeable H⁺ ions all over the matrix, due to such exchange of H⁺ ions between the solution and the -COOH and -OH groups present over the catalytic substrate the discharge step would be quite fast [257-260]. The electrochemical reduction of H⁺ has been consolidated and presented in Figure 4.8.

Furthermore, the stability of the catalyst was tested by chronopotentiometry and chronoamperometry method. Chronopotentiometry experiments were carried out at the current density of 10 mA/cm² for 4 h. As seen from the results in **Figure 4.7 (B)** the MoS₂/GO catalyst is quite stable at the experimental time period and the applied potential remained below -0.25 V for the chosen current density. Chronoamperometric experiments were carried out at applied potential of -0.20 V and it was observed that after an initial drop in current it remained stable for the experimental time period of 4 h. Even though the 1T phase of MoS₂ is said to be the metastable phase, composites of 1T MoS₂ has been stable even after long term testing [74]. GO and rGO might have important role in stabilizing the 1T MoS₂ phase on prolonged HER catalysis.

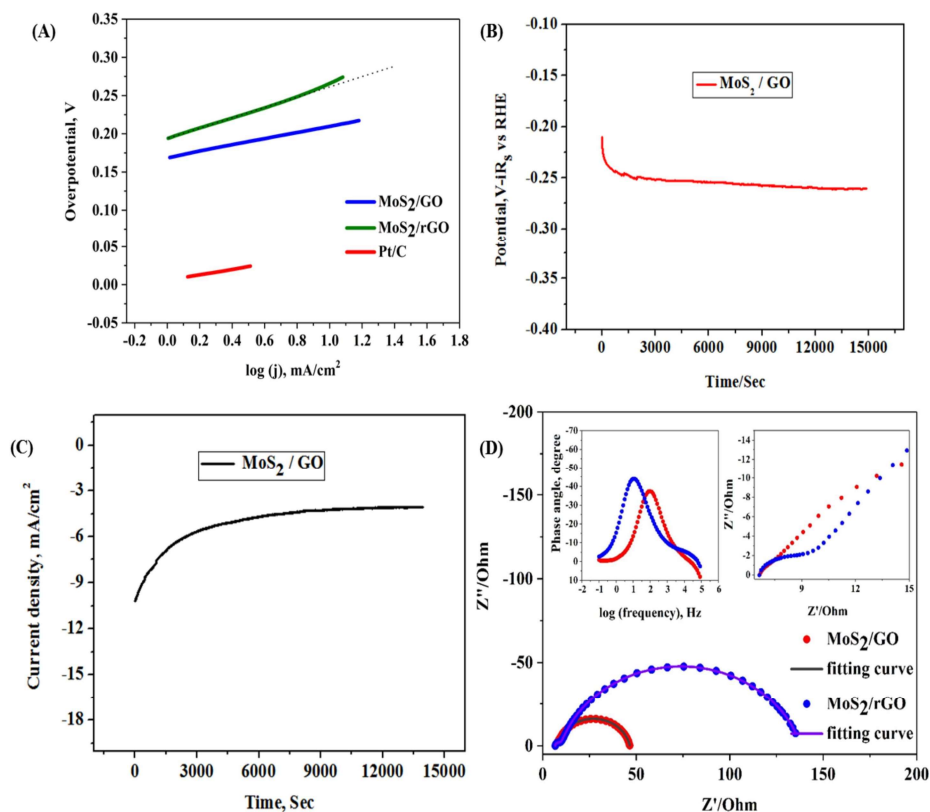


Figure 4.7 . (A) Tafel plot of two catalyst system in comparison with the standard Pt/C catalyst (B) stability test using chronopotentiometry and (C) stability test using chronoamperometry of MoS₂/GO catalyst. (D) Nyquist plot of MoS₂/GO and MoS₂/rGO Inset: zoomed portion of the Nyquist plot at high frequency region and corresponding Bode plot at the entire frequency range.

The catalyst modified electrode was examined using AFM measurements after the stability test i.e. the chronoamperometric experiments for 4 hrs. As seen from **Figure 4.3 (D)**, the general morphology of the materials remained similar as that of what was there before the electrochemical test. From the histogram and AFM micrograph the average particles size was decreased from 60 nm to 40 nm after the electrochemical test. The layer structure of the composite materials is well appeared after the electrochemical test. Due to the energetic changes during electrochemical test, the materials might have relaxed, which has resulted in the minor

modification in the morphology of the composite materials. Similar observation was reported previously on the Mo oxide materials where, on prolonged electrochemical cycles the size of the Mo oxide nano particles were decreased, such decrease in the size of the nano particles and the morphological change was described due to the redox activities at the catalytic centre on prolonged electrochemical cycles [261].

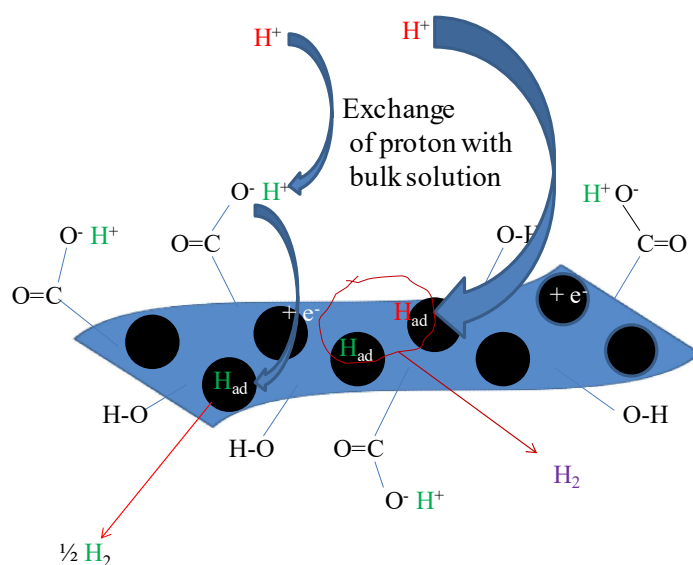


Figure 4.8 Proposed mechanism of the proton exchange in the HER kinetics.

4.3.3 Electrochemical impedance measurements

The charge transfer efficiency of the electrocatalyst was investigated using electrochemical impedance spectroscopy using CH Instrument by applying an AC voltage of 10 mV amplitude in a frequency range of 100000 Hz to 0.1 Hz. Corresponding results in the form of Nyquist plot and the circuit used for fitting the Nyquist plot are shown in **Figure 4.7 (D)**. The zoomed portion of the high frequency region of the Nyquist plot is shown as the inset of **Figure 4.7 (D)**. The

Nyquist plot was characterised with two semi circular regions one at high frequency and the other at the low frequency. The Nyquist plots were fitted with the equivalent circuit model as shown in Figure 4.9. Here R_s represents solution resistance, R_1 is charge transfer resistance, R_2 is the resistance incorporated to account for the second semicircle [253, 262-264]. The total resistance for faradaic process of HER is sum of R_1 and R_2 . From **Figure 4.7 (D)**, R_1 value for MoS_2/GO is 6Ω , which is lower than that value of MoS_2/rGO of 8Ω . The value of R_2 in the case of MoS_2/GO is 32Ω which is significantly lower than the value for MoS_2/rGO (120Ω). Corresponding to the mechanism of the overall process as discussed in Tafel analysis the resistance R_1 correspond to the Volmer step and the resistance at the low frequency region R_2 corresponds to the desorptive charge transfer process, the Heyrovsky step. Smaller value of R_1 in both the materials has suggested better charge transfer possibility. The semicircular loop at the low frequency region corresponds to the desorptive charge transfer process and this process has dominant role in the overall HER kinetics. Considerably low value of the this desorptive

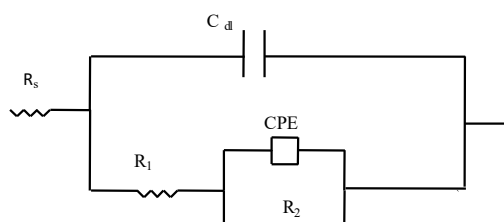


Figure 4.9 Equivalent circuit of the impedance spectroscopy measurement

phase angle maxima suggests improved faradaic process in the case of GO composite materials compared to the rGO composite materials [266, 267]. Similar to the CV measurements the roughness factor (R_f) was determined from the capacitance value obtained from the impedance measurements and the values are obtained as 4.33 and 11.5 for MoS_2/GO and MoS_2/rGO composite materials respectively.

Additionally, the phase angle maxima for the relaxation process associated with surface intermediates falls in the range of 10 to 100 Hz. Relaxation frequency for MoS₂/GO and MoS₂/rGO composites are 100 Hz and 20.89 Hz respectively. This relaxation process is due to the non-homogeneous charge transfer by the surface species. Above the onset potential of hydrogen evolution, the relaxation due to non-homogeneous charge distribution dominates with the minor contribution from double layer capacitance and the charge transfer components as shown in **Figure 4.7 (D)**. However, the phase angle maxima for GO composite is at higher frequency than that of rGO suggests that there is significant masking due to the double layer capacitance on the HER activity in the case of GO composite. This double layer masking effect should limit the performance of MoS₂/GO composite but performance of MoS₂/GO is better than that of rGO as shown on **Figure 4.7 (D)**. This anomalous property can be explained through the functionalised GO with hydroxyl and carboxylic acid groups which might increase the double layer masking at the same time increase the mass flow of proton through exchange mechanism from the acidic solution as shown in Figure 4.8.

4.3.4 Scanning electrochemical microscopy measurements

Scanning electrochemical microscopy (SECM) was employed to characterise the charge transport processes and to obtain the local electrochemical activity of the substrates. Pt ultramicro electrode (UME) of diameter 10 μ m was used as working electrode (probe or tip electrode), Pt wire was used as counter electrode, saturated Ag/AgCl electrode as reference electrode and glassy carbon electrode (GCE) modified by the catalyst was used as the substrate electrode. Approach of probe to the surface of the catalyst was performed by Probe Approach Curve (PAC) technique, in which a constant potential of -0.075V vs RHE was applied to the probe and different potentials in the range from 0.225 V to -0.175V were applied to the substrate.

Electrochemical signals were measured by measuring the current at UME tip as the function of precise tip position over substrate at the approach distance and the SECM imaging was obtained.

The steady state probe current is given by [31, 268]

$$I_d = 4nFDCa \quad (4.9)$$

where, I_d is diffusion limited current, number of electrons transferred at the electrode tip, F is Faraday's constant, C is concentration of H^+ ions in solution, D is diffusion coefficient and a is radius of UME disc. In bulk solution, H^+ ions got reduced at UME tip and produced steady state current limited by hemispherical diffusion. As tip approached the substrate the hydrogen atom formed after reduction of the H^+ ions at the tip oxidised at substrate when potential applied at substrate is more positive than tip potential and a positive feedback response was observed [31], though the catalyst substrate was not meant for the oxidation of hydrogen to proton, at an applied positive potential it should oxidise hydrogen to proton. Feedback responses at different substrate potentials are shown in Figure 4.10 where the normalized current, the tip current during approach (i_T) is divided by the steady state tip current when the tip was in the bulk solution ($i_{T,\infty}$) is plotted with respect to the normalized distance L (d/a), where d is the tip to substrate distance and 'a' is the radius of the tip electrode. Positive feedback response was obtained when substrate potential was more positive or equal to the tip potential and negative feedback responses were obtained when substrate potentials were more negative than tip potential. This is due to the enhanced mass flow of H^+ to the tip at a relatively positive applied potential at the substrate. The negative feedback response was due to the redox competition between the tip and the substrate. When potential at substrate was same or more negative, reduction of H^+ ions became prominent at substrate hence negative feedback responses were obtained.

Therefore at the same applied potential to the tip and the substrate, the substrate could impose negative feedback response to the tip due to the introduction of the redox competition mode into the system. This is essentially due to the higher surface area of the substrate and also to the good catalytic activity of the substrate. The feedback responses were fitted with standard models, as seen from the Figure 4.10, where most of the positive feedback responses could be fitted reasonably well, however the negative feedback responses could not be fitted due to the redox competition mode operating between the tip and the substrate.

After the probe approached to the substrate the catalysts modified substrate was scanned for the electrochemical imaging of the substrate using SECM using the steady state current response from the tip [268]. The SECM scanning was carried out in constant height mode where the distance between the probe and the substrate was kept constant at the approach distance of (1.1 μm) and the probe was scanned in X-Y plane. The SECM scans for the MoS_2/GO materials are shown in Figure 4.11. It was observed that at the relatively positive substrate potential overall probe current was high all over the substrate, there are some high current regions spread across

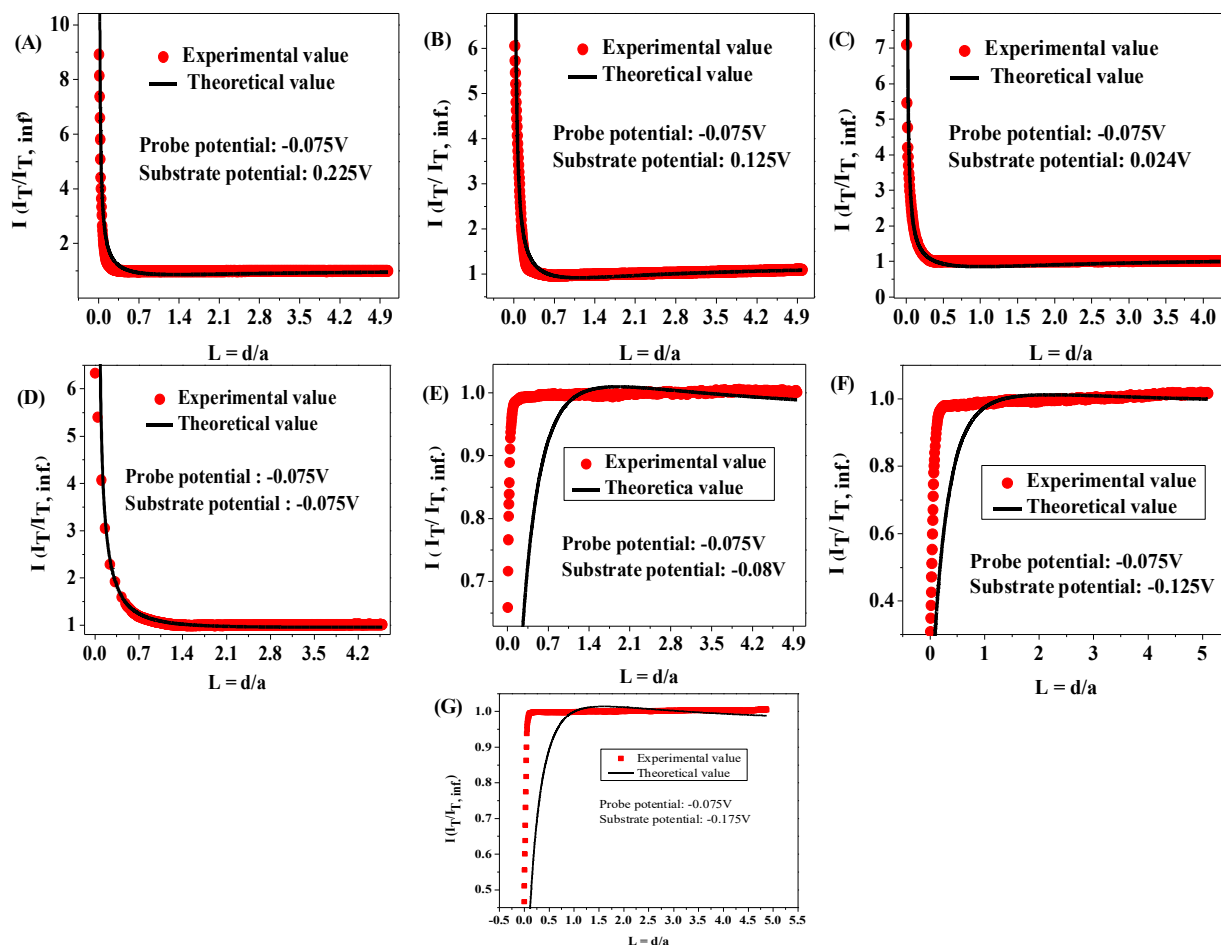


Figure 4.10 Probe approach curve (PAC) for MoS₂/GO catalyst at different substrate potentials keeping constant probe potential -0.075V.

the whole substrate. With shift in the applied potential towards more negative direction, the spread of the high current regions were decreased and only a few high current inlands were observed at the substrate potential of 0.025 V. At -0.075V, the transition potential between the positive and the negative feedback response, the entire substrate was covered with low current response. At further negative applied potential to the substrate the probe recorded very low negative currents across the substrate with some inlands of positive current as seen in Figure 4.11 (E). The positive current response from the probe was further increased at even more negative

applied potential to the substrate (*cf. Figure 4.11 (F)*). The probe approach plots and the SECM scans for the MoS₂/rGO materials are shown in FigureS7 of the supporting information. Near similar observation as that for the MoS₂/GO hybrid material was observed in the probe approach plot and SECM scan at different potentials. When the corresponding figures of Figure 4.11 (E) and (F) were compared with Figure 4.12 (E) & (F) it was observed that the positive current response from the tip was higher in the case of MoS₂/GO than MoS₂/rGO. Thus the more prominent positive current response at the substrate potentials of -0.125V and -0.175V in the case of MoS₂/GO hybrid material materials compared to the MoS₂/rGO hybrid material indicates better catalytic hydrogen evolution process over the MoS₂/GO. SECM was used previously for the investigation of HER processes and it was reported that the strained S vacancy of MoS₂ has much higher HER activity than an unstrained one[269]. Present result on SECM revealed that both the composite materials have imposed oxidation reaction at the Pt tip at the applied substrate potential of -0.075 V, however the oxidation process at the tip due to the redox competition process is induced predominantly by the MoS₂/GO composite materials than the MoS₂/rGO composite materials. Both the materials have shown good catalytic activity for the HER process with relatively higher activity for MoS₂/GO composite material has been revealed from the LSV measurements and supported by the impedance and hydrodynamic measurements. Previous investigation on SECM with surface interrogation has revealed the Mo-H bond formation during HER catalysis process using MoS₂ catalyst[270]. This Mo-H bond formation might be facilitated due to the presence of adjacent exchangeable proton in MoS₂/GO composite materials.

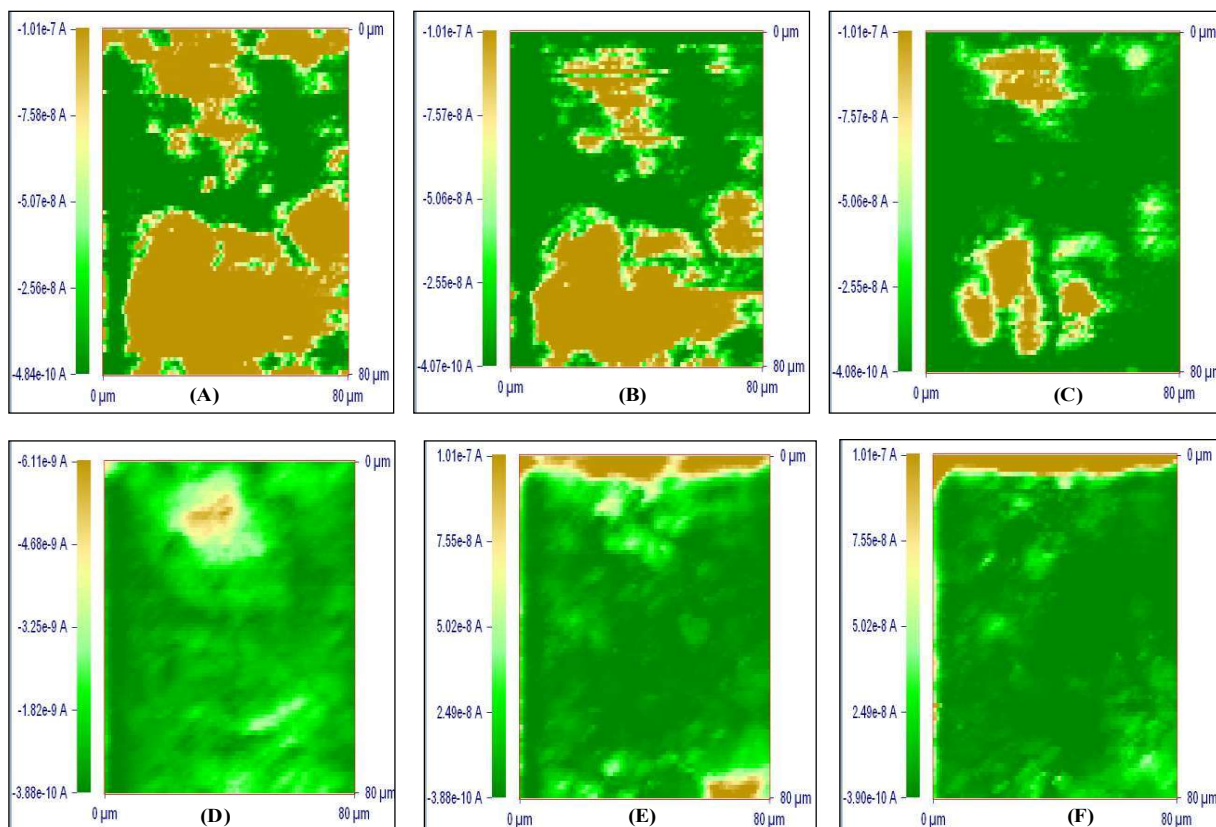


Figure 4.11 Scanning electrochemical microscopy (SECM) images of MoS₂/GO catalyst at different substrate potentials (A) 0.225 V, (B) 0.125V, (C) 0.025V, (D) -0.075V, (E) -0.125V and (F) -0.175V.

The difference in the work function between graphene and MoS₂ has been favorable for the electron to flow from MoS₂ towards graphene sheet, good coupling between the MoS₂ and the graphene sheet would always make this flow of electron fast for efficient HER process [77].

Present observation of the enhanced HER process in the case MoS₂/GO composite materials is explained from the direction of the electron flow from MoS₂ to the graphene sheets. Electron would transfer from the electrode to MoS₂, which will further be transferred to the graphene

sheet from which the electron will be transferred to H^+ ions and the charge transfer reaction will take place for the HER catalytic reaction. Since there are exchangeable proton already present in the graphene sheet of GO, the overall charge transfer process would always be favored in the case of MoS_2/GO composite materials compared to MoS_2/rGO [271, 272].

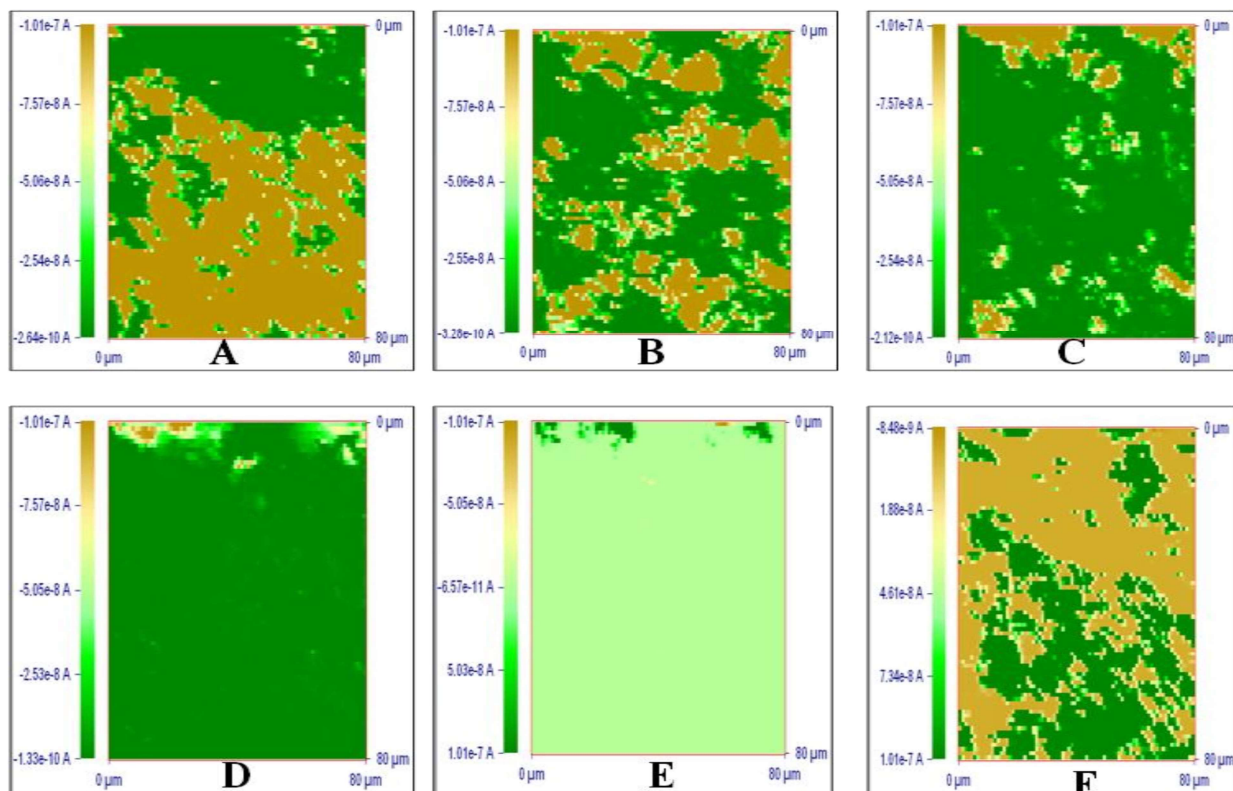


Figure 4.12 Scanning electrochemical microscopy (SECM) images of MoS_2/rGO catalyst at different substrate potentials (A) 0.2246V, (B) 0.125V, (C) 0.025V, (D) -0.075V, (E) -0.175V and (F) -0.225V

4.4 Conclusion

The composites of GO and rGO with the MoS₂ have been synthesized. Material characterization has revealed the 1T phase of MoS₂. Both the composite materials have shown very good catalytic activity for HER process and their catalytic activities are not so inferior to the commercially available Pt/C catalyst. Electrochemical investigations with Tafel analysis has indicated the Volmer-Heyrovsky mechanism for the HER process in MoS₂/GO catalytic system. LSV experiments were carried out in hydrodynamic mode and the results shown to have marginally higher electron transfer rate constant for MoS₂/rGO composite materials, where the current density and the onset potential for the HER process was comparatively favorable in the case of MoS₂/GO. Such anomaly in the observation has indicated the enhanced mass transfer process for MoS₂/GO; such enhanced mass transfer has been ascertained from the exchange of proton at the functional group over the GO matrix and the bulk acidic solution. Electrochemical impedance measurements have shown to have high desorptive charge transfer resistance for MoS₂/rGO composite material responsible for the comparatively low HER. SECM experiments were carried out using the catalyst modified substrate and the probe approach plot has shown the transformation of the composite modified electrode as the substrate from oxidation of proton to the efficient HER catalyst with the modulation of the applied potential. The SECM substrate scan has shown enhanced oxidation current from the tip electrode at a cathodic applied potential to the MoS₂/GO composite modified substrate compared to the MoS₂/rGO composite modified substrate.

Chapter 5: Development of BiVO₄ based photoanode material for photoelectrochemical splitting of water

5.1 Introduction

Photoelectrochemical (PEC) splitting of the water is one of the most promising methods for simultaneous conversion of hydrogen from water using solar energy as a sustainable and clean energy source and zero carbon footprints; the process has inherently high power and energy densities [179, 273-276]. PEC water splitting consists of photoanode and photocathode on which oxygen evolution reaction (OER) and hydrogen evolution reaction (HER) respectively are taking place. After having the discussion about the cathode materials in two previous chapters present chapter is focused on the development of anode materials, which important in terms of overall water splitting processes as it is limited by the sluggish OER kinetics; therefore, it is important to develop efficient photoanodes for the improvement in the overall water splitting process. Some of the important materials continued to discuss as photoanode materials for the OER are TiO₂, α -Fe₂O₃, WO₃ and BiVO₄ [78-86]. Among these materials, BiVO₄ is the most researched photoanode due to its suitable band position, bandgap and high theoretical efficiency ($\sim 7.5 \text{ mAcm}^{-2}$) and high solar to hydrogen (STH) conversion efficiency ($\sim 9\%$) [87-90]. However, the slow surface catalytic activity, short hole diffusion length, fast electron-hole recombination are major challenges with the BiVO₄ [78, 91-94]. To overcome these challenges, a number of the strategies have been widely investigated such as; nanostructure control [95-98], band engineering [89, 99-106], heteroatom doping [107-113], generation of oxygen vacancy [94, 114-116] and the oxygen evolution catalyst (OEC) incorporation [90, 117-125]. SnO₂ has been

used for the heterojunction formation in the BiVO₄ system which suppresses the back electron-hole recombination process [89]. Additionally, the SnO₂ underneath of BiVO₄ blocks the surface state of the ITO/FTO. These modifications improve the injection of the photogenerated holes to the electrode-electrolyte interface. During OER at the photoanode surface, photogenerated holes are expected to react with the OH⁻ to form OH° radical intermediate, which is converted to O₂ and very small part of them dimerize to H₂O₂ or OH⁻. Some of the OH° intermediate diffuse out into the electrolyte. The charge transfer kinetics at the electrode-electrolyte interface is in the range of nanosecond, which is very difficult to investigate by the conventional electrochemical method. Electrochemical impedance spectroscopy (EIS) [277] and the transient absorption spectroscopy (TAS) [93] are two important techniques implied to investigate the PEC processes and generate important parameters like photo-induced carrier lifetime and diffusion length.

Scanning electrochemical microscopy (SECM) is a powerful technique to investigate the charge transfer kinetics for in-situ measurements at the solid-liquid and liquid-liquid interfaces [278-280]. SECM is decisively applied for the investigation of the mechanism of interfacial charge transfer processes in OER, HER, oxygen reduction reaction (ORR) and hydrogen oxidation reaction (HOR) on the Pt, Pd, Au Hg, and the other electrodes [279, 281, 282]. Interfacial charge transfer kinetics at the semiconductor-electrolyte interface has been investigated for the photo-induced charge mediated reactions [283]. Bard group has demonstrated the detection, quantification, and evolution of decay kinetics of the photogenerated hydroxyl radicals in the PEC on the semiconductor interface [284, 285]. Surface interrogation SECM (SI-SECM) technique has been utilized to quantify photogenerated hydroxyl radicals (ads) and dimerization of the photogenerated radicals at the photoanode.

Considering the shortcoming of BiVO₄, this chapter is aimed to improve the catalytic efficiency by developing the BiVO₄ photoanodes with SnO₂ as interlayer, BiVO₄ was doped with Mo to further improvement of the catalytic activity. The SnO₂ coating over the ITO plate was carried out for suppressing the charge recombination process through the generation of heterojunction of SnO₂ and BiVO₄. The optical, chemical, and electronic properties of the materials have been investigated to understand the improvement in the PEC efficiency on Mo doping. The improvements in the photocurrent on Mo doping are analyzed based on the relative improvements in the bulk and surface properties as measured by the EIS and Mott-Schottky analysis. The decrease in the charge transfer resistance (R_{ct}) shows the improvements in the bulk property of the BiVO₄. The increase in the capacitance upon the Mo doping suggests better activity at the electrode-electrolyte interface due to the enhancement of the active surface sites, which leads to the enhancement in the PEC efficiency [92]. Strong correlation among the optical property of the material, the open circuit photovoltage (OCPV), and onset potential was discussed in relation with the improvement in the PEC efficiency on Mo doping. The increase in the flat band potential and OCPV suggests the improvements in the charge separation upon the Mo doping which resulted in the enhancement in PEC efficiency [162, 286-288]. SECM has been applied to investigate the photo-induced interfacial charge transfer kinetics in-situ at the electrode-electrolyte interface, the interfacial photo-generated hole transfer kinetics was correlated with the efficiency of PEC process across different catalysts investigated.

5.2 Experimental Section

5.2.1 Materials

Bismuth (III) Nitrate ($\text{Bi}(\text{NO}_3)_3 \cdot 5\text{H}_2\text{O}$, 98%), Ammonium Vanadate (NH_4VO_4 , > 99%), Stannic Chloride (SnCl_4 , 98%), and Sodium sulfite (Na_2SO_3 , 98%) were purchased from Sigma Aldrich. Ammonium tetrathiomolybdate ($(\text{NH}_4)_2 \text{MoS}_4$, 99.95%) was purchased from Alfa Aesar. Sodium Sulphate (Na_2SO_4), sodium monohydrogen phosphate (Na_2HPO_4), and sodium dihydrogen phosphate (NaH_2PO_4) were obtained from Sarabhai M Chemicals. Ethylene glycol and potassium ferricyanide were purchased from SDFCL and used as received.

5.2.2 Fabrication of Photoanode

$\text{SnO}_2/\text{BiVO}_4$ heterojunction was prepared by the spin coating technique. In this typical synthesis procedure, SnCl_4 (98%, 0.24 mL, 0.2 M) was dissolved in 10 mL of ethylene glycol and sonicated for 20 min and kept for stirring overnight prior to the spin coating. An aliquot of 100 μL as prepared precursor solution of SnO_2 was spin-coated on the ITO substrate at 2000 rpm for 1 min, followed by annealing at 250°C on the hot plate for 5 min. This process was repeated 8 times to get the optimum thickness of SnO_2 [289]. After spin coating; the modified electrodes were annealed at 450°C in a tube furnace for 2 h at 5°C per minute heating rate to form crystalline SnO_2 . After having the SnO_2 layer over the ITO substrate, the BiVO_4 film was formed on the ITO/ SnO_2 substrate by metal-organic decomposition method. In this typical synthesis method, $\text{Bi}(\text{NO}_3)_3 \cdot 5\text{H}_2\text{O}$ (0.2 mmol) was dissolved in 5 mL of ethylene glycol-water mixture (8:2, volume ratio) subsequently NH_4VO_3 (0.2 mmol) was added slowly, the mixture was sonicated for 30 min and kept on stirring for overnight at room temperature. The above solution was spin-coated over ITO (for control experiments) and ITO/ SnO_2 substrate at 2000 rpm for 1

min and then annealed at 350°C for 5 min on the hot plate. The coating was carried out for repeated 8 times to achieve the appropriate thickness for maximum efficiency [289], and after completion of the coating, the samples were heated at 450°C for 3 h at the heating rate of 5°C per minute in a tube furnace. Mo doping was achieved by adding ((NH₄)₂. MoS₄, 99.95%) at 1, 3, 5 and 7 atom percentage, resulting in a mixture containing Bi/(V+Mo) = 1:1 to replace V position in the crystal lattice of BiVO₄. The photoanodes thus fabricated using without Mo and at 1, 3, 5 and 7 atom percentage of Mo are designated as SBM0, SBM1, SBM3, SBM5, and SBM7 respectively.

5.2.3 Photoelectrochemical measurements

Photoelectrochemical measurements were performed using the CH Instrument (920 D model) using a three-electrode cell with an Ag/AgCl (3.0 M KCl) reference electrode, glassy carbon rod as counter and modified ITO coated with the catalyst material as the working electrode. 0.5 M Na₂SO₄ solution in 0.1 M potassium phosphate buffer solution (PBS, pH= 7) was used as electrolyte. All photoelectrochemical studies were carried out using Ag/AgCl (3 M KCl) reference electrode and potentials were converted and reported to reference hydrogen electrode (RHE) using the following

$$E_{(RHE)} = E_{Ag/AgCl} + 0.059 pH + E_{Ag/AgCl}^0 \quad (5.1)$$

Where, $E_{Ag/AgCl}$ is working potential and $E_{Ag/AgCl}^0$ is standard potential (i.e. 0.2243 V). To measure the charge transfer efficiency and the charge transport efficiency, 0.1 M Na₂SO₃ as hole scavenger was added in the electrolyte. All samples were front illuminated because of significantly higher photocurrent than that of back illumination. Solar Simulator having 1 sunlight fitted with AM 1.5 G filter was used as a light source. The xenon arc lamp is used as a

monochromatic light source; power of the monochromatic light is measured by digital power meter from Newport. The photocurrent was measured by linear sweep voltammetry (LSV) technique with 5 mVs^{-1} scan rate and chopped light voltammetry was recorded. Chronoamperometry was used for the stability test of the photoanode materials. Electrochemical Impedance Spectroscopy (EIS) was used to measure interfacial charge transfer resistance (R_{ct}) at 1.44 V by applying sinusoidal wave of amplitude 10 mV in the frequency range from 10^5 to 10^{-1} Hz under 1 sun illumination. Further, the relaxation frequency and time constant of the electrochemical process were measured from EIS data to quantify the efficiency of the photoanode materials. Mott-Schottky experiments were carried out at 100 Hz frequency for the measurements of donor density and flat band potential of photoanode material which inherently affects the PEC activity. Incident photon to current efficiency (IPCE) was measured with the setup similar to that of PEC measurement with monochromatic light from 350 to 650 nm with a 10 nm step. The incident light power was measurement at each wavelength with a calibrated photodiode. SECM study was performed on 920 D bi-potentiostat (CH Instrument) using four electrodes system. SECM Teflon cell was in-house fabricated for holding the substrate at the base with O-ring, reference and counter electrodes. Photoanode materials were used as the substrate, Ag/AgCl (3 M KCl) as a reference and glassy carbon rod as a counter electrode and results are reported in terms of RHE potential. Commercial Pt ultra-microelectrode (UME) having RG value of 5 and a diameter $10 \mu\text{m}$ was used as the probe. Pt microelectrode was polished with a micro polishing cloth with $0.05 \mu\text{m}$ alumina powder successively and then cleaned in 0.5 M H_2SO_4 solution for 20 cycles of cyclic voltammetry scans in the potential window of 1.44 V to 0.29 V vs RHE at the scan rate of 50 mVs^{-1} . Ferricyanide solution of 2 mM concentration was used as a redox couple in 0.1 M PBS of pH 7. The potential of the probe was

chosen at 0.64 V in the region of steady diffusion current after recording the CV in 2 mM ferricyanide solution with a scan rate of 50 mVs⁻¹. Samples were illuminated from the front side using the solar simulator as the light source. Probe Approach Curve (PAC) technique was used to record the approach curve to the substrate in dark and also under the illumination of light to measure the kinetic parameter using four electrodes system at different polarization potentials, from the fitting of the probe approach plots the interfacial charge transfer kinetics were obtained. The mapping of photoanodes was carried out by the SECM technique (constant height mode) under the illumination condition to map the catalytic activity of the catalyst substrate.

5.2.4 Characterization of the materials

XRD analysis of the prepared samples was performed by using a Rigaku powder diffractometer (9 kW Rotating Anode) with Cu K_α radiation ($\lambda = 1.5406\text{\AA}$). Raman spectra of photoanodes were recorded by using Lab RAM HR 800 Microlaser Raman system with an Ar⁺ laser of 516 nm. The morphology of the photoanodes was examined by field emission scanning electron microscopy (FE-SEM, JEOL model JSM-7600F). X-ray photoelectron spectroscopy (XPS, MULTILAB, VG Scientific, Al K_α radiation as monochromator) was used to investigate the binding energy of the components of Mo doped BiVO₄ photoanodes.

5.3 Result and discussion

5.3.1 Structure analysis by XRD and Raman spectroscopy

SnO₂/Mo-doped BiVO₄ was as synthesized by sol-gel spin coating method [289] are characterized by X-ray diffraction (XRD) technique, results are shown in Figure 5.1 (A). XRD peaks at 2 θ values of 18.59°, 28.61°, 30.01° and 34.96° correspond to (101), (112), (004) and

(020) planes respectively of monoclinic phase (JCPDS 75-1867) of BiVO₄. XRD peaks at 2 θ values of 26.48° and 50.46° correspond to (110) and (211) plane confirm the presence of inner layer tetragonal SnO₂ (JCPDS card 77-0450). The presence of these two layers indicates the successful formation of heterojunction. Upon an increase in the atomic percentage doping of Mo, a small shift of peak position towards the lower theta value indicates the expansion of crystal lattice. It has been reported that Mo preferentially substitutes V sites, which is a thermodynamically favorable process, as the impurity formation energy of Mo doping in V sites and Bi sites is 0.53 eV and 2.79 eV, respectively [290, 291]. Moreover, Mo is 6-fold coordinated in MoO₃, and V and Bi are having 4 folds and 8 folds coordination, respectively. Thus, when Mo atoms substitute V, all Mo-O bonds are expanded; however, Mo atoms keep the 4-folds coordination of V atoms. It has been reported that Mo doping in BiVO₄ causes deviation of the dipole moment of VO₄³⁻ tetrahedron from zero to non-zero dipole moment in the crystal lattice, thus making the crystal more polar. This enhanced dipole moment due to the distorted polyhedron are reported to promote the charge separation on photo-excitation, which would enhance the overall photocatalytic activity [291].

Raman spectroscopy is used to investigate the crystallization, local structure and electronic properties of the materials. Figure 5.1 (B) shows the characteristic Raman bands of the photoanode materials and tabulated in Table 5.1. The typical Raman bands of BiVO₄ are observed at 825.50, 713.80, 367.37 and 329.72 cm⁻¹. The strongest band near 825 cm⁻¹ is assigned to the ν_s (VO₄) (A_g) and weak shoulder like peak at 713.80 cm⁻¹ is assigned to the ν_{as} (VO₄) (B_g) mode. The Raman band near 367.37 and 329.72 cm⁻¹ are assigned to the δ_s (VO₄) (B_g) and δ_{as} (VO₄) (A_g) respectively. The external modes (rotational and translational) are at lower

frequencies than the internal modes of VO_4^{3-} units because they involve the heavier VO_4^{3-} unit and having weaker coupling interactions.

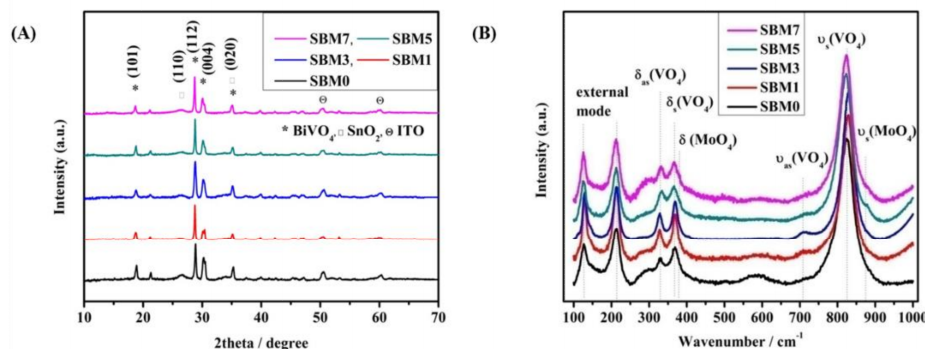


Figure 5.1 (A) XRD patterns of all BiVO_4 and Mo doped photoanodes and (B) Raman spectra of all BiVO_4 based photoanodes.

The modes at 213.23 cm^{-1} and 126.58 cm^{-1} are assigned as rotational and translational modes respectively [292-297]. The weak bands at 867.50 cm^{-1} and 374.70 cm^{-1} are assigned to the $\nu_s(\text{MoO}_4)$ and $\delta(\text{MoO}_4)$ respectively. The band corresponds to the $\nu_{as}(\text{MoO}_4)$ might be covered with 825.50 cm^{-1} peak. All these Raman band assignments for the present materials correspond well with the literature reports of similar materials [292-297]. It has been observed that there is a blue shift in the most intense peak from 825.50 cm^{-1} to 829.54 cm^{-1} in materials from SBM0 to SBM3 then red shifting is observed in SBM5 to SBM7. The change of vibrational frequency of V-O can be explained in terms of metal-oxygen bond length and strength. F. D. Hardcastle et. al have determined the V-O bond length and bond order from Raman stretching frequencies [297]. Calculations are made based on the correlation of diatomic approximation which assumes that each metal-oxygen bond vibrates independently in the crystal lattice. The empirical formula used for calculation of bond length is as follows [297]

$$\nu(\text{cm}^{-1}) = 21349 \exp(-1.9176R(\text{Å})) \quad (5.2)$$

Where ν is the Raman stretching frequency for V-O in cm^{-1} and R is the bond length in Å . The V-O bond varies from 1.696 Å to 1.698 Å upon doping of Mo in BiVO_4 lattice; thus, a marginal increase in the V-O bond length is observed at the 5% Mo content. The asymmetric stretching also has shown similar behavior to that of the symmetric stretching vibrations, where the V-O bond length is decreased initially on the addition of Mo, with further addition of Mo resulted in the increase in V-O bond length. The increase of the V-O bond causes distortion in the lattice, which has resulted in the shifting of XRD peaks towards lower theta values. However, the shifting is not significant in the modification of the crystal structure.

Table 5.1 Analysis of Raman spectroscopy of all BiVO_4 based photoanodes. All stretching and bending modes of vibrational of BiVO_4 are listed here. The bond length of V-O is calculated based on the symmetric stretching of V-O mode.

Catalysts	ν_s (V-O) cm^{-1}	V-O bond length Å	ν_{as} (V-O) cm^{-1}	δ_s (VO_4) cm^{-1}	δ_{as} (VO_4) cm^{-1}	Rotational cm^{-1}	Translational cm^{-1}	ν_s (MoO_4) cm^{-1}	δ (MoO_4) cm^{-1}
SBM0	825.50	1.696	713.80	367.37	329.72	213.23	126.58	-	-
SBM1	827.54	1.695	710.19	369.37	327.72	213.23	128.18	-	-
SBM3	829.54	1.694	708.19	369.37	327.72	213.23	129.12	867.50	-
SBM5	823.13	1.698	715.80	366.16	330.92	212.30	125.04	867.50	374.70
SBM7	823.94	1.697	716.21	367.37	330.92	212.90	125.64	867.50	374.70

5.3.2 XPS analysis of the materials

XPS was used to investigate the surface electronic properties of photoanodes. As shown in Figure 5.2, XPS spectra confirm the presence of elemental constituents of Bi, V, O, Mo and Sn of deposited films on ITO. Figure 5.2 (A) shows the spectra of the Bi 4f core level region. The Bi 4f region is characterized by the presence of the $4f_{5/2}$ and $4f_{7/2}$ components with a spin-orbit splitting of 5.22 eV. Likewise, V_{2p} is characterized by the $2p_{1/2}$ and $2p_{3/2}$ components with spin-orbit splitting of 7.64 eV as shown in Figure 5.2 (B).

Table 5.2 XPS analysis of Bi 4f, O 1s, V 2p and Mo 3d binding energy.

Catalysts	Bi $4f_{5/2}$ eV	Bi $4f_{7/2}$ eV	O 1s eV	V $2p_{1/2}$ eV	V $2p_{3/2}$ eV	Mo $3d_{3/2}$ eV	Mo $3d_{5/2}$ eV
SBM0	164.0	158.78	529.80	524.05	516.41	-	-
SBM1	164.34	159.07	529.94	524.21	516.84	233.94	230.87
SBM3	164.70	159.37	530.83	525.10	517.60	233.99	230.92
SBM5	164.94	159.60	531.34	525.36	518.11	234.10	230.93
SBM7	165.27	159.96	531.96	524.21	516.71	234.10	230.90

There are peaks corresponds to the Sn 3d confirm the presence of the inner layer of SnO_2 of $BiVO_4$. Doping of Mo with varying concentrations has been carried out in $BiVO_4$, and corresponding XPS spectra are shown in Figure 5.2 (C). Mo 3d is confirmed by the presence of Mo $3d_{3/2}$ and Mo $3d_{5/2}$ spectra with spin-orbit splitting of 3.06 eV, which confirms the doping of Mo in $BiVO_4$ lattice, which is in accordance with characterization by XRD and Raman measurements. The surface atomic composition of each sample is calculated using Bi $4f_{7/2}$, V

$2p_{3/2}$, Mo $3d_{5/2}$ spectral intensities, weighted by atomic sensitivity. The atomic composition is found to be in good agreement with EDS analysis.

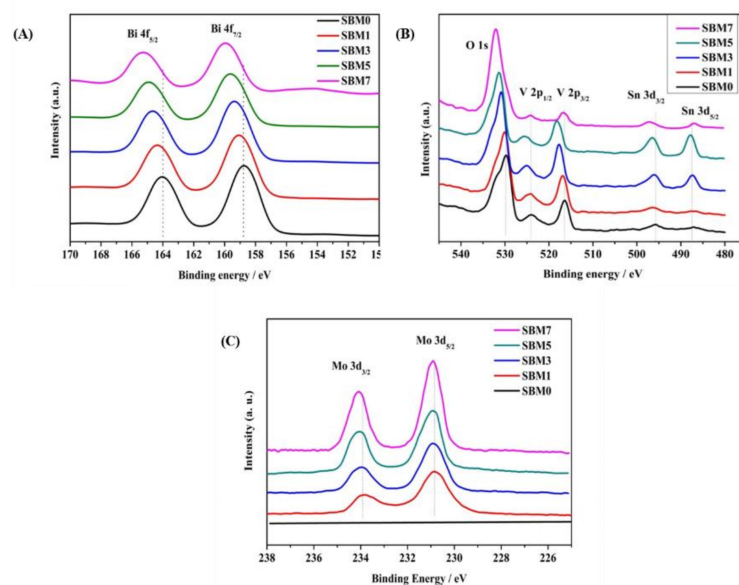


Figure 5.2 XPS spectra of (A) Bi 4f, (B) O 1s, V 2p and Sn 3d and (C) Mo 3d in BiVO₄.

Further, in addition to the chemical composition of constituent's elements, chemical states are determined from XPS measurements. Fitting of Bi 4f spectra reveals that each spin-orbit split corresponds to the single oxidation state in all samples. The binding energy positions of Bi 4f_{7/2} and Bi 4f_{5/2} in BiVO₄ are observed at 158.78 eV and 164.0 eV respectively, and the spin-orbit splitting energy of 5.22 eV suggests that Bi is in +3 oxidation state [298-301]. The binding energies of V 2p_{3/2} and V 2p_{1/2} are 516.41 eV and 524.05 eV, and spin-orbit split energy is 7.64 eV suggests that V is in +5 oxidation state [298-301]. All samples exhibit peaks at ~530 eV for O 1s orbital, which is due to the lattice oxygen. Hydroxyl O 1s peak is also observed near 532 eV suggests the hydroxylated surface of photoanodes, which might enhance the photoelectrocatalysis. Additionally, Mo dopant was characterized by Mo 3d peaks. The binding

energies of Mo 3d_{3/2} and Mo 3d_{5/2} are 233.94 eV and 230.88 eV, respectively having spin-orbit split energy 3.06 eV confirming Mo is in +6 oxidation state [301, 302]. The increase of binding energy of all ions (Bi³⁺, V⁵⁺, O²⁻), in Mo doped BiVO₄ is the result of doping of higher electronegative dopant (i.e. Mo⁶⁺: 2.16 > V⁵⁺: 1.63) [303].

5.3.3 SEM and EDS analysis

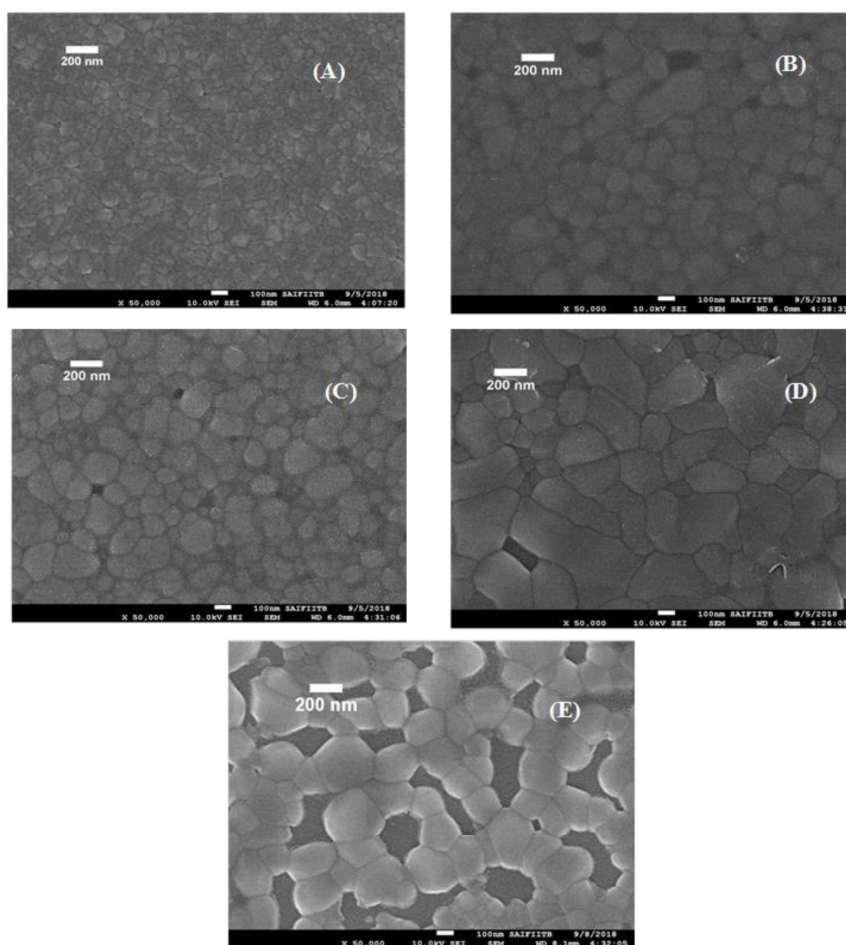


Figure 5.3 FE-SEM images all porous BiVO₄ based photoanodes thin films on ITO substrate.

(A) SBM0, (B) SBM1, (C) SBM3, (D) SBM5 and (E) SBM7.

Morphology of photoanode materials was characterized by scanning electron microscopy (SEM). BiVO_4 was uniformly coated on ITO/ SnO_2 as shown in Figure 5.3. The materials have shown the granular type of morphology, and the grain size is observed to be increased marginally with Mo doping. Similar observation has been reported in the literature [304-307]. On 7% Mo doping, the sample has shown chains of grains with vacant spaces in the matrix.

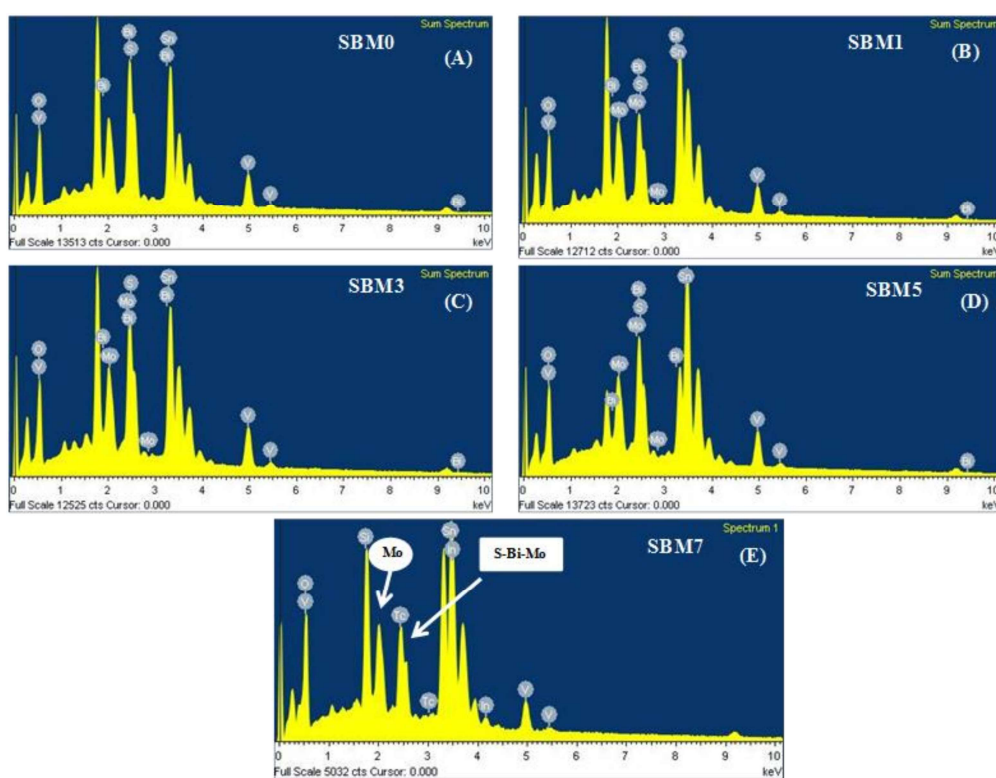


Figure 5.4 EDS analysis of different catalysts for calculation of Bi, V, O and Mo in the photoanodes (A) SBM0, (B) SBM1, (C) SBM3, (D) SBM5 and (E) SBM7.

Table 5.3 Elemental analysis of Bi, V, O, Mo and Sn in BiVO₄ photoanodes

Elements	SBM0	SBM1	SBM3	SBM5	SBM7
	Atomic %				
Bi M	11.20	10.51	11.14	11.34	10.47
V K	11.45	9.54	9.24	8.39	7.34
O K	72.06	71.31	69.63	64.49	66.02
Mo L	-	0.78	3.18	4.43	6.37
Sn L	5.10	6.53	5.57	5.90	9.80

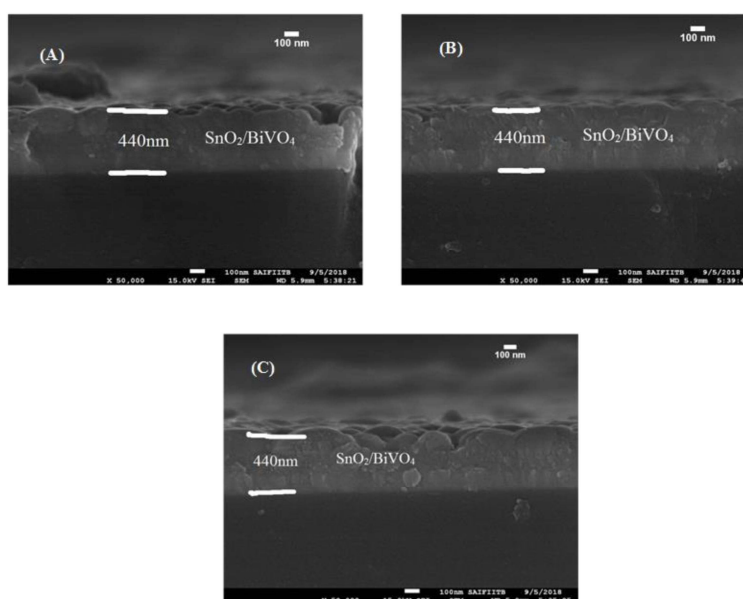


Figure 5.5 Cross-sectional view of photoanodes for thickness measurements (A) SBM0, (B) SBM3 and (C) SBM7. Total thickness of film is 440 nm.

Elemental analysis was carried out by Energy dispersive spectroscopy (EDS) as shown in Figure 5.4. In SBM0, the atomic ratio of Bi and V is 1:1 as shown in Table 5.3. The atomic percentage

of Bi, V, O, and Mo was found as these materials were taken during the synthesis procedure. Sn content corresponding to inner layer SnO₂ was observed. Further, the thickness of the coating was measured and shown in Figure 5.5. The thickness of the combined layers of SnO₂ and BiVO₄ was found to be around 440 nm.

5.3.4 UV-vis spectral measurements

The optical absorption property of a semiconductor reflecting the electronic property of the material is a key factor for determining the photo-electrocatalytic activity. All photoanodes materials are characterized by UV-vis diffuse reflectance spectra of as shown in Figure 5.6 (A). All samples show strong absorption in the visible region, having bandgap absorption edge in the region of 500-550 nm. The most intense absorption peak was observed at 447 nm for BiVO₄. The absorption bands correspond to the MoO₃ and SnO₂ are also observed at 418 nm and 358 nm respectively. A small red shift of absorption edge upon Mo doping is observed. Under the assumption of parabolic band dispersion, the energy dependence of optical transition strength can be explained by Tauc equation [152, 308].

$$(\alpha h\nu)^n = A(h\nu - E_g) \quad (5.3)$$

Where α is optical absorption coefficient, $h\nu$ is photon energy, E_g is the bandgap and A is a probability constant. The numerical values of n are $\frac{1}{2}$ and 2 for indirect and direct transition, respectively. Thus, the nature of the transition can be determined from the linearity of plots of $(\alpha h\nu)^{1/2}$ and $(\alpha h\nu)^2$ vs. $h\nu$ and bandgap can be determined from the X-axis intercept. Figure 5.6 (B) shows the Tauc plot for direct band transition. The bandgap of undoped BiVO₄ is obtained as 2.54 eV. Upon Mo doping, the bandgap is found to decrease marginally from 2.54 to 2.50 eV. On Mo substitution on V site, the band structure remained nearly the same as that of

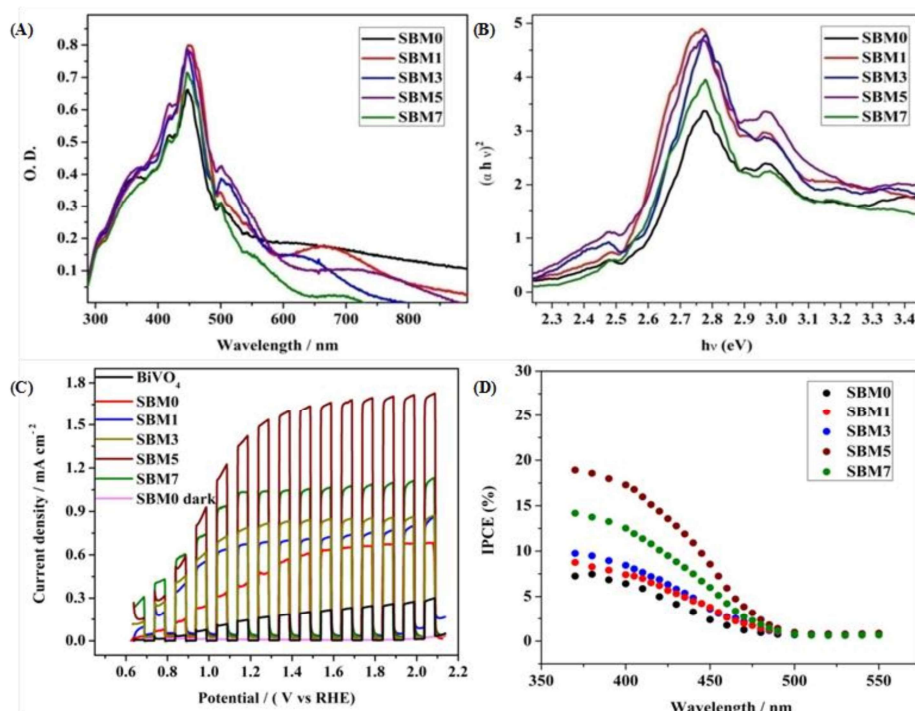


Figure 5.6 (A) UV-vis diffuse reflectance spectra and (B) Tauc plot for direct band for calculation of bandgap of all BiVO₄ based photoanodes (C) Photoelectrochemical performances of the all BiVO₄ based photoanodes were measured by chopped light voltammetry in 0.5 M Na₂SO₄ in 0.1 M PBS buffer solution at scan rate 10 mVs⁻¹ under the 1 Sun illuminations. (D) IPCE spectra at 1.0V vs Ag/AgCl of all photoanodes.

undoped BiVO₄. The marginal decrease in the bandgap, which means the optical absorption threshold, will not be affected by Mo doping in BiVO₄ [107, 290, 291, 309]. The Fermi level increases with the reduction of V⁵⁺ to V⁴⁺ which is explained in the photocharging section. The enhancement of the activity and modification of the band structure has significant role from the oxygen vacancy created due to the incorporation of Mo⁶⁺ into the V⁵⁺ site. Every oxygen vacancy pumps two electrons in the lattice and hence Fermi level and donor density of the photoanodes increased.

5.3.5 Photoelectrochemical investigation

All PEC experiments were carried out in 0.1 M PBS of pH 7 using 0.5 M Na₂SO₄ as supporting electrolyte using three electrodes systems in 1 Sunlight source using a Solar simulator. Photo-response of photoanode materials was performed by chopped light voltammetry technique, as shown in Figure 5.6 (C). At 1.64 V (vs RHE) the current densities of 0.65 mAcm⁻², 0.73 mAcm⁻², 0.84 mAcm⁻², 1.65 mAcm⁻² and 1.06 mAcm⁻² are obtained for SBM0, SBM1, SBM3, SBM5 and SBM7 respectively. The BiVO₄ without having the SnO₂ interlayer has shown the photocurrent of 0.22 mAcm⁻². The results thus indicate significant improvement in the photocurrent response due to the formation of the SnO₂ interlayer. The photocurrent is further increased by doping Mo in BiVO₄. SBM5 has shown the highest photo-electrocatalytic activity. There is ~154% improvement in the photocurrent from SBM0 upon 5% Mo doping observed in SBM5.

To understand the photo-electrocatalytic activity of BiVO₄ and Mo doped BiVO₄, further the incident photon to current efficiency (IPCE) was measured at 1.64 V (vs RHE) in 0.1 M PBS from 370 nm to 550 nm wavelength range, and the results are shown in Figure 5.6 (D). For IPCE measurements, LSV was recorded for the wavelength ranging from 370 nm to 550 nm, and photocurrents were sampled at 1.64 V, and then IPCE was measured by using the following equation [155]

$$IPCE \% = \left(\frac{J \left(\frac{A}{cm^2} \right)}{P_{in} \left(\frac{W}{cm^2} \right)} \times \frac{1240}{\lambda(nm)} \right) \times 100 \% \quad (5.4)$$

Where J is the photocurrent density, P_{in} is the power of incident photon (monochromatic light), λ is wavelength in nm. The onset wavelength of IPCE is 500 nm, which corresponds to the

bandgap of 2.48 eV, supports the bandgap calculation from the Tauc plot. On Mo doping IPCE is increased up to the Mo doping of 5%, thereafter on further doping of Mo, no increment is observed. At 5% Mo doping in sample SBM5, IPCE is observed to be at 17% which is about 166% improvements than that of SBM0 at 400 nm. For further insight into the charge transfer and separation process, Mott-Schottky analysis was carried out; the scans were recorded in the potential window from 0.64 V to 1.64 V (vs RHE) with an increment of 0.025 V at 100 Hz frequency as shown in **Figure 5.7 (A)**.

$$\frac{1}{C^2} = \frac{2}{qA^2\varepsilon\varepsilon_0N_D} \left(V - V_{FB} - \frac{k_B T}{q} \right) \quad (5.5)$$

Where C (F) is space charge capacitance, q is elementary charge, A is electrode surface area, ε is relative permittivity of BiVO₄ (68), [310] ε_0 vacuum permittivity (8.854×10^{-12} Fm⁻¹), N_D (cm⁻³) is donor density, V is applied potential, V_{FB} is flat band potential and k_B is Boltzmann constant (1.38×10^{-23} JK⁻¹) and T is absolute temperature. From the slope of a plot of $1/C^2$ vs V, donor density is measured, which is the inherent property of photoanode materials. Donor density was calculated from the slope of **Figure 5.7 (A)** and tabulated in **Table 5.4**. N_D of SBM0 is found as 5.23×10^{19} cm⁻³, the measured value is in accordance with the literature reports [290, 291, 309]. Upon doping of Mo, donor density is found to increase, and the values in samples SBM1, SBM3, SBM5, and SBM7 are obtained as 6.24×10^{19} , 9.66×10^{19} , 3.85×10^{20} and 8.82×10^{19} cm⁻³ respectively. This increase of donor density supports the increase of photocurrent with doping of Mo observed in chopped light voltammetry measurements [290, 309].

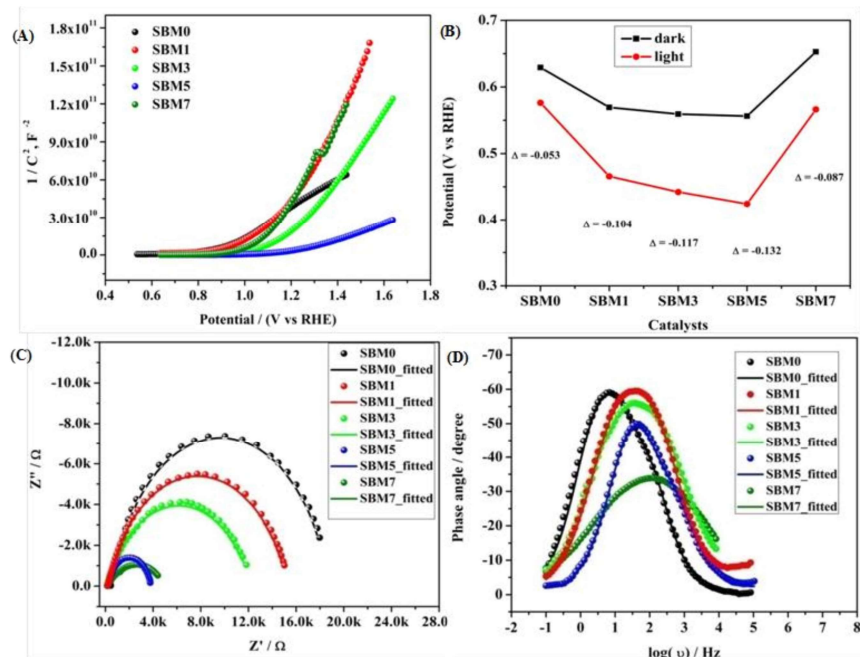


Figure 5.7 (A) Mott-Schottky analysis for calculation of donor density and flat band potential, (B) OCPV calculation by measuring the difference in potential in dark and illumination, (C) Nyquist plot and (D) Bode plots of the BiVO₄ based photoanodes.

Further, the flat band potential, which is also an important property of photoanode materials and qualitative measurement of the degree of band bending at the electrode-electrolyte interface,[161, 162, 286] was calculated from Mott-Schottky plot as shown in **Figure 5.7** (A). At higher band bending, the electron-hole recombination will be difficult at the interface, which will result in the improvements of PEC efficiency and stabilizes the photoanodes [161, 162, 286, 287]. The flat band potential of SBM0 is found as 0.94V, on Mo doping, the flat band potential is observed as, 1.09V, 1.16V, 1.20V and 1.05V for the samples SBM1, SBM3, SBM5, and SBM7 respectively. This observation suggests that the band bending is improved upon Mo doping up to the Mo doping of 5%, which resulted in the suppression of electron-hole recombination on the

interface. The suppression of charge recombination facilitates higher charge transfer property at the interface, and hence, overall PEC efficiency is improved. The increase in the flat band potential thus supports the observed enhancement of current in chopped light voltammetry and an increase in the IPCE values on Mo doping up to 5%.

Table 5.4 PEC activity of the photoanodes were characterized by the following parameters.

Catalysts	Band gap (eV)	% increase in photocurrent	Donor density (cm^{-3})	Flat band potential, V	OCPV	% of Charge transfer efficiency@1.64V	% of charge transport efficiency@1.64V
SBM0	2.54	-	5.23×10^{19}	0.94	-0.053	46.62	63.73
SBM1	2.52	12.30	6.42×10^{19}	1.09	-0.104	47.24	78.31
SBM3	2.54	29.23	9.66×10^{19}	1.16	-0.117	53.90	79.66
SBM5	2.50	153.84	3.85×10^{20}	1.20	-0.132	50.23	176.27
SBM7	2.53	63.08	8.82×10^{19}	1.05	-0.087	50.02	95.68

Band bending and charge separation efficiency were further investigated by open circuit photovoltage (OCPV, V_{ph}) measurements under AM 1.5 illumination. The extent of band bending is a qualitative measure of in-built potential and charge recombination [287, 288]. The OCPV was calculated from the difference in open circuit potential in dark and illumination as shown in **Figure 5.7** and tabulated in Table 5.4 for different samples investigated. OCPV of SBM0, SBM1, SBM3, SBM5 and SBM7 are obtained as -0.053 V, -0.104 V, -0.117 V, -0.132 V and -0.087 V respectively. The shifting of OCPV towards more cathodic side suggests a strong alternation of bands at the electrode-electrolyte interface with Mo doping. This change of OCPV, sourced from the higher band bending under photo-illumination, improves the overall catalytic

efficiency by suppressing of charge recombination and improvement of charge separation at the interface. The OCPV is basically the difference between the Fermi levels of the semiconductor when in dark and under illuminated conditions, which is improved on Mo doping. The Fermi level of the semiconductor under illumination, bends to lower its energy, due to which the open circuit voltage differs from that in the dark. The Fermi level bending and the enhancement of OCPV have been schematically shown in Figure 5.8 [287]. On Mo doping the Fermi level undergo enhanced bending, which enhances the OCPV up to the Mo content of 5%. The increase in the OCPV resulted in the improvement of photocurrent on doping of Mo in BiVO_4 .

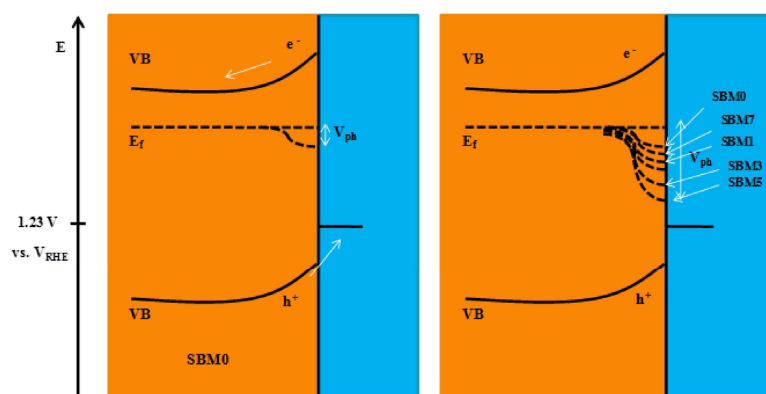


Figure 5.8 Band diagram of BiVO_4 and Mo doped BiVO_4 . The band diagram is constructed using UV-vis spectroscopy, OCPV and flat band potential measurements (not on scale).

The interfacial charge transfer efficiency and charge transport efficiency are two limiting parameters on which the overall efficiency of PEC depends. Charge transfer and transport efficiency measurements were performed using a hole scavenger method [311, 312]. LSV was

recorded in 0.1 M PBS for water splitting. Hole scavenger Na₂SO₃ (0.1 M solution) was used by assuming complete and fast oxidation of sulfite; the LSV plots. Then, current densities were sampled at 1.64 V and $\eta_{transfer}$ and $\eta_{transport}$ were calculated using following equations.

$$\eta_{transfer} = \frac{J_{H_2O}}{J_{Na_2SO_3}} \times 100 \% \quad (5.6)$$

$$\eta_{transport} = \frac{J_{Na_2SO_3}}{J_{max.}} \times 100 \% \quad (5.7)$$

$$J_{max.} = \frac{\text{integration of light absorption}}{\text{integration of solar light spectrum}} \quad (5.8)$$

Where, J_{max} was calculated from the photocurrent obtained from the silicon diode detector. J_{H_2O} is the current density for water oxidation; $J_{Na_2SO_3}$ is the current density for the oxidation of sulfite. Since the water oxidation process is sluggish, sodium sulfite was used as a hole scavenger. It is supposed that oxidation of sulfite is 100%; thus, the charge transfer efficiency was calculated with respect to 100% Faradaic efficient, i.e. how fast charge gets transferred from the electrode-electrolyte interface to water molecule for oxidation. The charge transfer efficiency was calculated and tabulated in Table 5.4. For SBM0, the charge transfer efficiency is calculated as 46.62 %. Doping of Mo in BiVO₄ resulted in the enhancement of charge transfer efficiency by 15 % from the SBM0 sample. The improvement of charge transfer efficiency at the interface is attributed from higher band bending upon Mo doping and increases in donor density as obtained from Mott-Schottky analysis and OCPV measurements. Charge transport efficiency is another factor that greatly affects the photocatalytic activity, it was calculated based on the charge generated inside the photoanode material, and the fraction of it gets transferred at the interface. The charge transport efficiency for SBM0 is obtained as 63.73 %. The charge transport

efficiency of other samples SBM1, SBM3, SBM5, and SBM7 are 78.31 %, 79.66 %, 176.27 %, and 95.27 %, respectively (*cf. Table 5.4*). These values suggest that band bending upon Mo doping improves charge transport and suppressed the recombination process, as suggested by Mott-Schottky analysis and OCPV values. Thus, the improvements of charge transfer and transport efficiencies are the factors responsible for enhancement in the PEC efficiency and support chopped light voltammetry results and IPCE measurements.

5.3.6 Electrochemical Impedance measurements

The conductivity and charge transfer resistance are measured from the analysis of Nyquist plot; it also provides the qualitative insight of the charge transfer processes in bulk as well as at the interface of the photoanode, corresponding results are shown in Figure 5.7 (C). Impedance results are fitted with the equivalent circuit and the fitting parameters are tabulated in Table 5.5. R_{ct} value of SBM0 is found as 16.8 k Ω . When Mo is doped, R_{ct} values decreased considerably. The decrease in R_{ct} value suggests faster charge transfer at the interface on Mo doping. This variation in R_{ct} values supports the PEC activity measurements. The photoanodes were further characterized for their charge relaxation processes from Bode plot analysis as shown in Figure 5.7 (D). Frequencies of phase maxima were sampled for different catalysts, which correspond to the relaxation frequency of photogenerated charge and the results are summarized in Table 5.5. The relaxation frequency of the SBM0 sample is 6.88 Hz, and the relaxation frequency is increased linearly with the Mo doping from SBM0 to SBM7. Further, the relaxation time constant (τ) of the electrochemical process was calculated using $\tau = 1/2\pi f$ where f is relaxation frequency. The decrease in τ indicates the faster electrochemical process on Mo doping, which supports the improvements in the PEC efficiency.

Table 5.5 Impedance spectroscopy analysis of photoanodes for measurements of bulk and surface characterization.

Catalysts	R_{ct} (Ω)	C_{total} (F)	Relaxation frequency (Hz)	Relaxation time constant (ms)	L_D (μm)
SBM0	16820	8.33×10^{-6}	6.88	23.12	340
SBM1	15060	4.43×10^{-6}	32.36	4.92	157
SBM3	12010	4.24×10^{-6}	32.36	4.92	157
SBM5	3610	1.18×10^{-5}	44.36	3.56	134
SBM7	4832	1.16×10^{-5}	91.20	1.75	94

Diffusion length is an important parameter in characterizing the interfacial processes, and the overall PEC efficiency depends heavily on the hole diffusion process. The measurement of the diffusion length from impedance measurements, however, includes the assumption that the relaxation time constant is the time taken by the hole to oxidize the water molecule, which contains the diffusion of the hole inside the films and also its diffusion at the electrolyte interface to oxidize water molecule. Diffusion length of the photo-generated holes is calculated by using the equation, $L_D = (D \times \tau)^2$ where L_D is diffusion length, D is the diffusion coefficient of the photogenerated hole, taken as $0.05 \text{ cm}^2 \text{ s}^{-1}$ [313], and τ is the relaxation time, the values as obtained are tabulated in Table 5.5. L_D of SBM0 is found to be 340 μm . The diffusion length thus obtained from the impedance measurements is decreased with the Mo doping in BiVO_4 . The measured diffusion process includes the diffusion inside the solid catalysts and at the interface since the observed diffusion length is significantly higher compared to the thickness of the films, the holes are expected to be transported outside the electrochemical interface. The thickness of the films has a negligible contribution to the overall measured diffusion length of the material.

The lower diffusion length at the electrochemical interface is associated with the fast charge transfer process at the interface, which is expected to have a higher PEC current.

As seen from Table 5.5 the capacitance of the SBM0 is significantly low (8.33×10^{-6} F) compared to the materials containing Mo. The observed capacitance improvement on the addition of Mo indicates the significant improvement in the surface charge density on the incorporation of Mo in BiVO₄. These results show that there are surface improvements as well with the improvements in the bulk property of the photoanode upon Mo doping in the BiVO₄, which enhances the overall PEC efficiency.

5.3.7 Testing of stability of the photoanodes

Stability of photoanode materials is important for prolonged application of the catalyst; it was performed using chronoamperometry technique at 1.44V vs RHE with chopped light voltammetry method, as shown in Figure 5.9, the photocurrent of SBM0 was decreased by 37% after initial excitation. On Mo doping, the recombination step has been reduced drastically, and in place of decay in current, growth in the photocurrent response is observed. The stability test was further performed for continuous illumination of light for 900 s, as shown in **Figure 5.10** for two catalyst samples. In both, the samples SBM1 and SBM5, the photocurrent is improved initially and then stabilized. The improvement of photocurrent is observed previously and explained on the basis of the charging effect of the photoanode [314, 315]. The photocharging effect has been discussed based on both the surface and bulk modifications in the materials. The redox reaction through the transformation of V (V) to V (IV) is discussed as one of the important

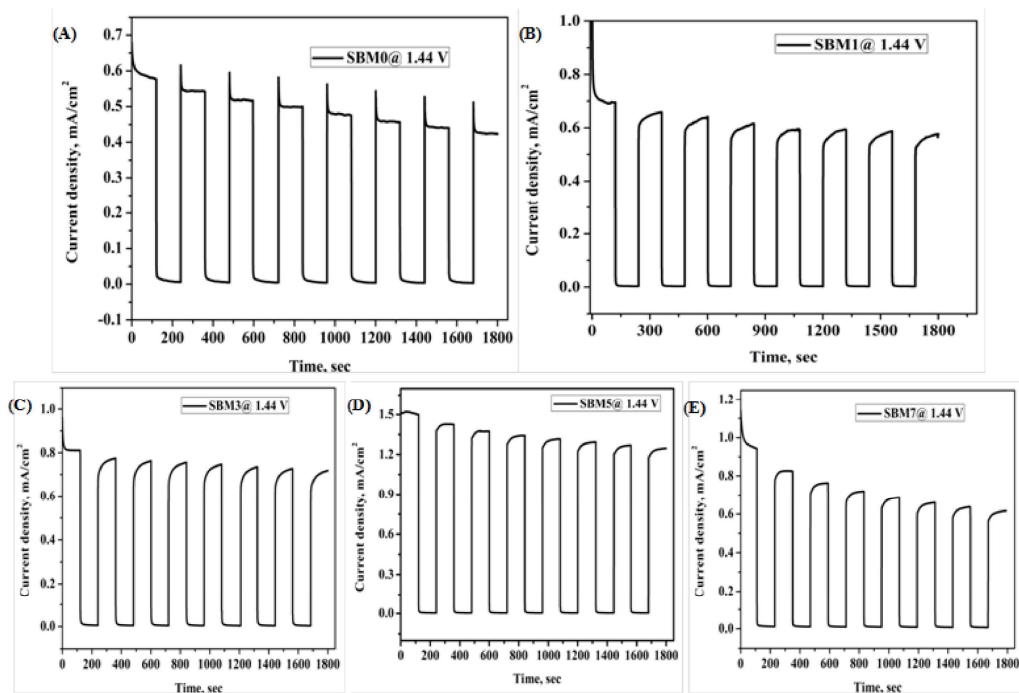


Figure 5.9 All BiVO₄ based photoanode was characterized for stability test by chopped light voltammetry at 0.8V vs. Ag/AgCl for 1800sec (A) SBM0, (B) SBM1, (C) SBM3, (D) SBM5 and (E) SBM7.

reasons behind the enhanced photocurrent due to photocharging. The photocharging effect is observed to be enhanced in the present case on the incorporation of Mo in the catalyst. The reduction potential of V (V) to V (IV) is more positive than the Mo (VI) to Mo (V) reduction; however, the redox kinetics in the latter case is significantly faster [316]. In view of this, during photocharging process, Mo (VI) will get reduced to Mo (V) first due to the kinetic effect; afterward Mo (V) would transfer the electron to V (V) and facilitate the reduction of V (V) to V (IV). As reported previously, this facilitated reduction of V(V) to V (IV) due to the presence of Mo would enhance the catalytic activity on photocharging [314]. The photocharging effect is also discussed to be due to the interfacial factor through the modification of band structure upon photocharging. The OCPV is measured in all the materials; its value is increased with the Mo

doping. The increase in the OCPV can be correlated with the relatively more significant bending of the conduction band than the valance band under photo-illumination. The increase in the OCPV indicates the lesser possibility of recombination and enhancement of the hole transfer property through the interface, which eventually would increase the PEC catalytic process in the material [287, 288].

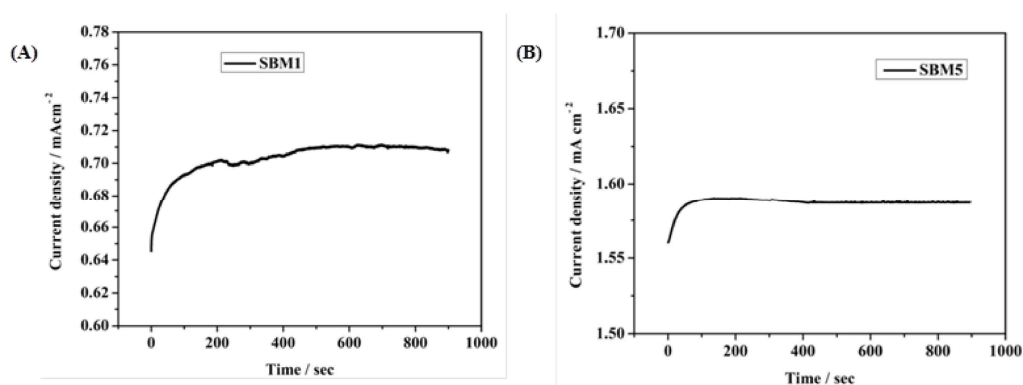


Figure 5.10 Stability test of (A) SBM1 and (B) SBM5 in 0.5M Na₂SO₄ in 0.1M PBS at 1.44V.

5.3.8 Interfacial charge transfer kinetics using SECM

The charger transfer at the semiconductor-electrolyte interface and quantification of the active sites in in-situ measurements have been performed by the SECM technique [317-322]. Investigation of the interface has been carried out by the tip feedback mode. When a tip is far from any surface, tip current, $i_{T,\infty}$ depends on the number of electrons transferred, concentration of electroactive species, diffusion coefficient and radius of ultra-microelectrode [317]. When the surface is an insulator, the tip current is $i_T < i_{T,\infty}$ which results negative feedback. When surface is conducting, redox active species is generated at the surface, tip current, $i_T > i_{T,\infty}$ as a result, positive feedback is observed.

In PEC water oxidation reaction, photogenerated holes at the BiVO₄ interface oxidize water to form oxygen. Since the direct investigation of the water oxidation intermediate or oxygen at the BiVO₄ surface in the feedback mode is technically difficult, the redox probe [Fe(CN)₆]³⁻/[Fe(CN)₆]⁴⁻ is used rather than the water oxidation intermediate or molecular oxygen [323]. It has been reported that redox mediator [Fe(CN)₆]⁴⁻ and [Fe(CN)₆]³⁻ can be used as the acceptor of the photogenerated holes and electrons to characterize the redox kinetics of the photo-catalyst for the PEC water-splitting reaction [324]. **Figure 5.11** (A) shows the schematics of the reaction at the BiVO₄ interface in the feedback approach. The photogenerated hole at the photoanode/electrolyte interface oxidizes the [Fe(CN)₆]⁴⁻ to the [Fe(CN)₆]³⁻. There is large driving force ($\Delta G \sim -2.0\text{eV}$) for transfer of the photogenerated hole from the valance band of BiVO₄ to [Fe(CN)₆]⁴⁻ for oxidation at the surface catalytic reaction. Therefore, the hole transfer from a valance band of BiVO₄ to [Fe(CN)₆]⁴⁻ is kinetically more favorable by $\Delta G \sim -0.4\text{ eV}$ than the water oxidation [33]. The cathodic potential at the probe is tuned to the reduction potential of [Fe(CN)₆]³⁻ to [Fe(CN)₆]⁴⁻ so that there is no side reaction such as oxygen reduction take place. Therefore, feedback current can be assumed mainly from the reduction of [Fe(CN)₆]³⁻. The hole transfer kinetics at BiVO₄/interface is measured by the feedback current of the reduction of [Fe(CN)₆]³⁻ in dark and illumination conditions. In the dark, photoanode behaves as an insulator because of the non-availability of the free electron or hole at the interface and hence negative feedback is observed, however on illumination, it behaves as conducting substrate because of photogenerated holes and electrons. The photogenerated holes at the interface oxidize [Fe(CN)₆]⁴⁻ to [Fe(CN)₆]³⁻, [Fe(CN)₆]³⁻ species diffuses to the probe and increases the mass transfer process, resulting in the positive feedback response. The normalized tip current (I_T) is calculated by using $I_T = i_T/i_{T,\infty}$ where, i_T is the real time tip current during the approach to the

substrate electrode and $i_{T,\infty}$ is steady current of the tip when the tip is far from the substrate. Prior to the approach of the probe to the substrate, the CV of ultra microelectrode was performed in 2 mM ferricyanide solution as shown in **Figure 5.12** shows a good response from the probe. The negative feedback response was fitted using equation 5.9 for the measurement of RG value. The positive feedback response under illumination was used for the hole kinetics measurements. The positive feedback response of all photoanodes are shown in **Figure 5.11**, the observation of positive feedback indicates the transfer of a hole from the illuminated electrode surface. The normalized apparent heterogeneous charge transfer rate constant (κ) and effective heterogeneous charge transfer rate constant κ_{eff} (in cm s^{-1}) at $\text{BiVO}_4/\text{electrolyte}$ interface is obtained from the fitting of experiment approach curve to the theoretical SECM kinetics model using equations 5.9- 5.14 [32].

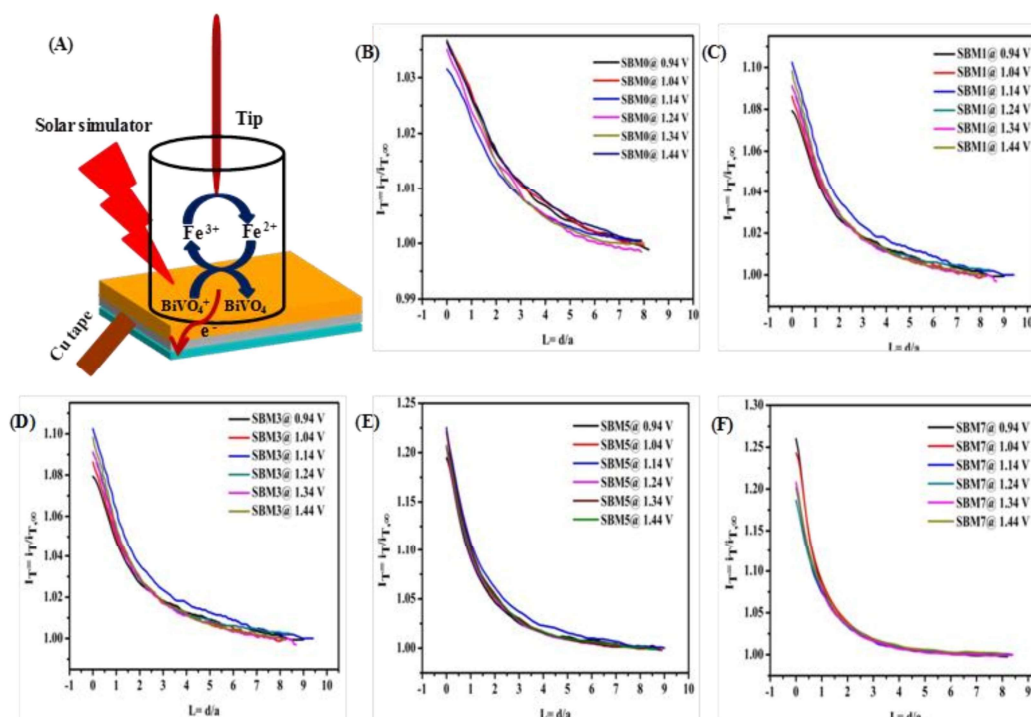


Figure 5.11 (A) The proposed mechanism of feedback mode of analysis of $\text{BiVO}_4/\text{electrolyte}$ interface by SECM analysis. In this technique, a 2mM ferricyanide solution was used as the

redox mediator. In illumination, photo-generated holes oxidizes the $[\text{Fe}(\text{CN})_6]^{4-}$ to $[\text{Fe}(\text{CN})_6]^{3-}$ at the interface and the cathodic potential applied at Probe reduces the photo-oxidized $[\text{Fe}(\text{CN})_6]^{3-}$ to $[\text{Fe}(\text{CN})_6]^{4-}$. This redox close loop gives positive feedback in illumination and negative feedback in dark conditions. SECM imaging of the surface is characterized by the measuring o probe current to measure the hole transfer from the interface to the $[\text{Fe}(\text{CN})_6]^{4-}$. Normalized SECM feedback approach curve of the BiVO_4 based photoanodes (B) SBM0, (C) SBM1, (D) SBM3, (E) SBM5 and (F) SBM7 in 2mM $[\text{Fe}(\text{CN})_6]^{3-}$ solution at different applied bias potential at substrate under illumination using Pt ultra-microelectrode having r_T value $4.5\mu\text{m}$.

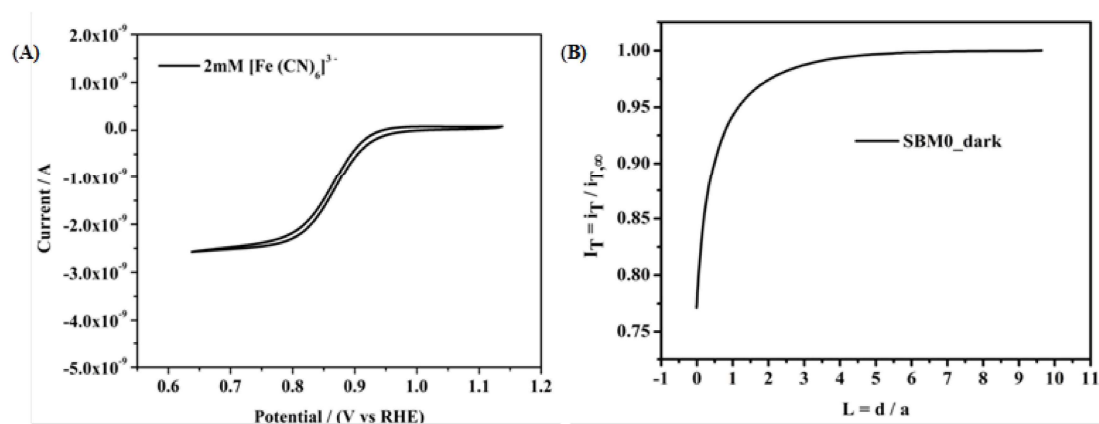


Figure 5.12 (A) CV of Pt ultra-microelectrode (UME) in 2 mM $[\text{Fe}(\text{CN})_6]^{3-}$ at 10mVs^{-1} scan rate and (B) probe approach curve (PAC) of Pt UME in 2mM $[\text{Fe}(\text{CN})_6]^{3-}$ solution at SBM0 photoanode in dark.

The normalized approach curves are fitted by using these equations [32]

$$I_T^{ins}(L, RG) = \frac{\frac{2.08}{RG^{0.358}} \left(L - \frac{0.145}{RG} \right) + 1.585}{\frac{2.08}{RG^{0.358}} (L + 0.0023RG) + 1.57 + \frac{LnRG}{L} + \frac{2}{\pi RG} Ln \left(1 + \frac{\pi RG}{2L} \right)} \quad (5.9)$$

$$\begin{aligned} I_T^{cond}(L + \kappa^{-1}, RG) \\ = \alpha(RG) + \frac{\pi}{4\beta(RG) \arctan(L + \kappa^{-1})} \\ + \left(1 - \alpha(RG) - \frac{1}{2\beta(RG)} \right) \frac{2}{\pi} \arctan(L + \kappa^{-1}) \quad (5.10) \end{aligned}$$

$$\begin{aligned} I_T(L, \kappa, RG) = I_T^{cond} \left(L + \frac{1}{\kappa}, RG \right) \\ + \frac{I_T^{ins}(L, RG) - 1}{(1 + 2.47RG^{0.31}L\kappa)(1 + L^{0.006RG^{-0.113}}\kappa^{-0.023RG+0.91})} \quad (5.11) \end{aligned}$$

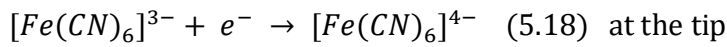
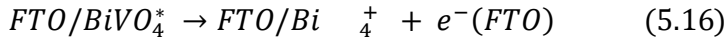
$$I_T = I_s \left(1 - \frac{I_T^{ins}}{I_T^{cond}} \right) + I_T^{ins} \quad (5.12)$$

$$\alpha(RG) = Ln2 + Ln2 \left(1 - \frac{2}{\pi} \arccos \left(\frac{1}{RG} \right) \right) - Ln2 \left(1 - \left(\frac{2}{\pi} \arccos \left(\frac{1}{RG} \right) \right)^2 \right) \quad (5.13)$$

$$\begin{aligned} \beta(RG) = 1 + 0.639 \left(1 - \frac{2}{\pi} \arccos \left(\frac{1}{RG} \right) \right) \\ - 0.186 \left(1 - \left(\frac{2}{\pi} \arccos \left(\frac{1}{RG} \right) \right)^2 \right) \quad (5.14) \end{aligned}$$

Where $RG = r_{\text{glass}}/r_T$ is the ratio of the radius of glass sheath (r_{glass}) to the radius of the active area of Pt UME (r_T), I_T^{cond} is diffusion control current for conducting substrate i.e. positive feedback, I_T^{ins} is diffusion control current for insulating substrate i.e. negative feedback.

The details reaction mechanism of PEC regeneration has been developed under the steady-state SECM using $[\text{Fe}(\text{CN})_6]^{4-} / [\text{Fe}(\text{CN})_6]^{3-}$ redox probe on the photoanode [33, 34].



On solving the above equations using steady-state approximation, the following result has been obtained as

$$\frac{1}{I_s} = \frac{1}{I_{T,cond}} + \frac{4D_{diffusion}[\text{Fe}^{3+}]^*}{\pi r_T l [\text{BiVO}_4^0] \phi_{hv} J_{hv}} + \frac{4D_{diffusion}}{\pi r_T l [\text{BiVO}_4^0] k'_{ox}} \quad (5.19)$$

For the first-order reaction at the BiVO_4 electrode surface, the following expression is in correlation with the feedback approach curve [30, 35].

$$\frac{1}{I_s} = \frac{1}{I_{T,cond}} + \frac{1}{\pi \kappa} \quad (5.20)$$

$$k_{eff} = \kappa \frac{D_{diffusion}}{r_T} \quad (5.21)$$

All approach curves have been numerically fitted using the equation 5.9 -5.14 and then kinetics parameters are calculated. Some of the fittings of the approach plots are shown in **Figure 5.13**.

The effective heterogeneous charge transfer rate constant k_{eff} is calculated using the relation $k_{eff} = \kappa D_{diffusion} / r_T$ where $D_{diffusion}$ is the diffusion coefficient of the redox probe $[\text{Fe}(\text{CN})_6]^{3-}$ and tabulated in Table 5.6. The low value of k_{eff} for SBM0 shows sluggish hole

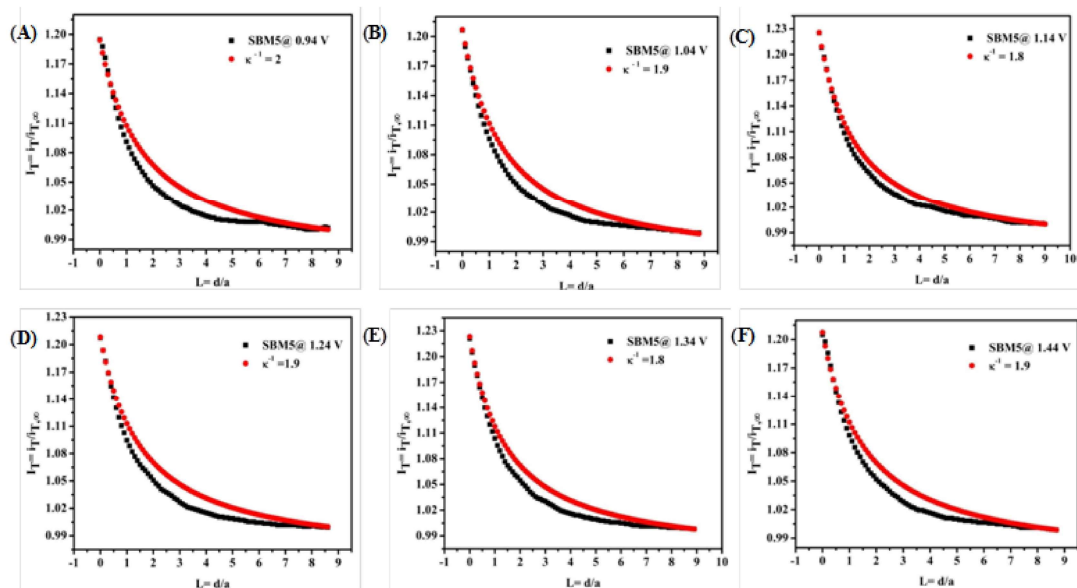


Figure 5.13 Normalized SECM feedback approach curve of the SBM5 at (A) 0.94V, (B)1.04V, (C) 1.14V, (D) 1.24V, (E) 1.34V and (F) 1.44V in 2mM $[\text{Fe}(\text{CN})_6]^{3-}$ solution at different applied potential at substrate under illumination using Pt ultra-microelectrode having r_T value $4.8\mu\text{m}$.

Table 5.6 The k_{eff} of hole transfer from the $\text{BiVO}_4/\text{electrolyte}$ interface to $[\text{Fe}(\text{CN})_6]^{3-}$

Potential, V	k_{eff} (in $10^{-3} \text{ cm s}^{-1}$)				
	SBM0	SBM1	SBM3	SBM5	SBM7
0.94	2.18	3.58	4.25	6.80	7.50
1.04	2.18	3.90	4.12	7.16	7.48
1.14	2.18	4.25	4.40	7.56	7.16
1.24	2.18	4.0	4.25	7.16	6.48
1.34	2.18	4.0	4.25	7.56	7.16
1.44	2.18	4.25	4.25	7.16	7.16

transfer process at the interface. When Mo was doped in to the BiVO_4 hole transfer rate constant is found to improve significantly. This improvement suggests that interfacial charge transfer is facilitated upon Mo doping. Further, the effect of applied bias on the hole transfer rate constant is investigated by approaching the probe at different applied potentials. The rate constant for all the materials remained unchanged with the applied potentials indicating its limiting value even at lowest applied potential.

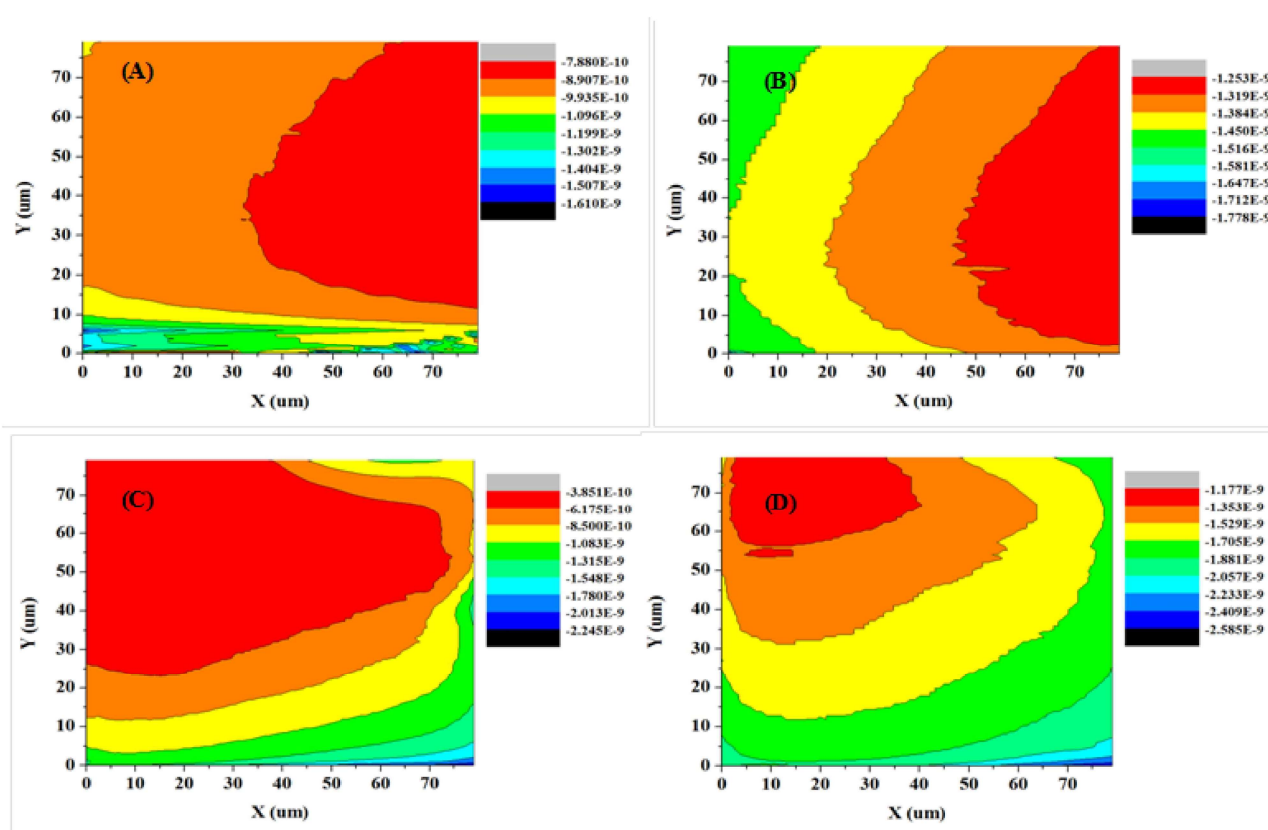


Figure 5.14 Scanning electrochemical microscopy (SECM) imaging of photoanodes SBM0 at (A) 0.94V and (B) 1.14V and SBM1 at (C) 0.94V and (D) 1.14V substrate potential in 2mM $[\text{Fe}(\text{CN})_6]^{3-}$ at constant height mode using Pt UME as probe and photoanodes as substrate.

The localized PEC activity of the BiVO₄ photoanodes was analyzed by imaging the surface in the constant height mode at the applied potentials of 0.94 V and 1.14 V to the substrate. A cathodic potential of 0.64 V was applied to the probe for the reduction of the [Fe(CN)₆]³⁻ to [Fe(CN)₆]⁴⁻. Therefore, during imaging of the substrate, feedback current at the probe was monitored. The catalyst substrate is mapped with various current regions, and the current response is increased marginally with more anodic applied potential to the substrate. The overall current response of the tip scanned over the substrate is increased with Mo doping in BiVO₄ up to 5% doping level. The images are further characterized with bigger current region at doping level up to 5%, originated from the overlapping diffusion layer across the catalyst substrate. At 7% doping, in place of overlapping region, the catalytic currents are characterized by small patches separated from each other. The observation can be correlated from the separated grains at 7% doping compared to the overlapped diffusion layer structure in all other samples. Catalytic current obtained from the overlapping diffusion layer is beneficial in catalyst design, as it provides a similar catalytic activity to that of the continuous films requiring fewer amounts of catalysts. The SECM imaging thus further indicates the betterment in the catalytic activity on Mo doping and reveals the regional distribution of the catalytic current over the catalyst substrates. Results thus indicate significant improvement in the catalytic activity of BiVO₄ through the inclusion of SnO₂ heterojunction and doping of Mo, which has been explained using some of the important interfacial measurements.

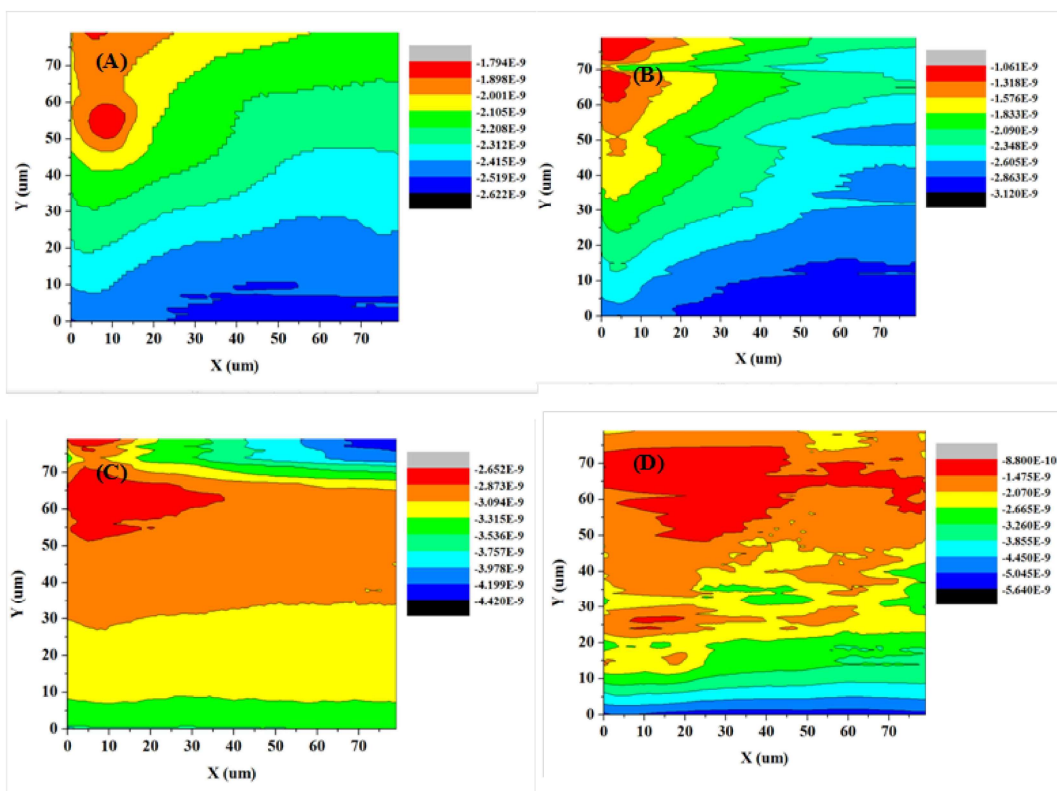


Figure 5.15 Scanning electrochemical microscopy (SECM) imaging of photoanodes SBM3 at (A) 0.94V and (B) 1.14V and SBM5 at (C) 0.94V and (D) 1.14V substrate potential in 2mM $[\text{Fe}(\text{CN})_6]^{3-}$ at constant height mode using Pt UME as probe and photoanodes as substrate.

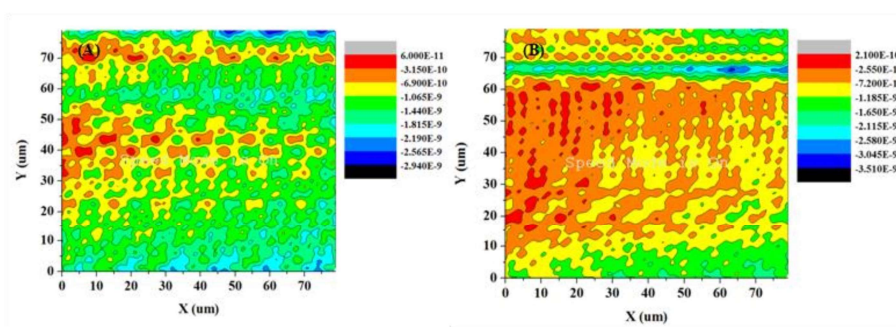


Figure 5.16 Scanning electrochemical microscopy (SECM) imaging of photoanodes SBM7 at (A) 0.94V and (B) 1.14V substrate potential in 2mM $[\text{Fe}(\text{CN})_6]^{3-}$ at constant height mode using Pt UME as probe and photoanodes as substrate.

5.4 Conclusion

Present investigation was aimed to improve the photo-electrocatalytic efficiency of BiVO₄ through the incorporation of SnO₂ interlayer and doping of Mo. The significant improvement (~154%) in the photocurrent was observed upon 5% Mo doping in SnO₂/BiVO₄. Strong correlation among the optical property of the material, the open circuit photovoltage (OCPV), and onset potential was observed in relation to the improvement in the PEC efficiency on Mo doping. The increase in the flat band potential and OCPV suggests the improvements in the charge separation upon the Mo doping which resulted in the enhancement in PEC efficiency. SECM investigation reveals significant improvement in effective hole transfer rate constant from 2.18 cm s⁻¹ to 7.56 cm s⁻¹ with the Mo doping in BiVO₄. The electrochemical impedance investigation supports the improvements in the charge transfer and transport efficiency by improvements in the bulk and surface properties of BiVO₄. The facilitated reduction of V (V) to V (IV) on Mo doping is also responsible for the improvement in the catalytic activity. The improvement in the catalytic activity has been evaluated from the improvement in the physicochemical at the bulk of the catalysts, its surface, and most importantly due to the improvement in its interfacial charge transfer processes. Mild expansion in the crystal lattice is also observed on replacement of V by Mo, the improvement in the catalytic activity however, related primarily to the electronic nature compared to any morphological changes.

Chapter 6. Insight into the PEC and interfacial charge transfer kinetics at the Co-Bi modified BiVO₄

6.1 Introduction

As has been mentioned in the previous chapters of the thesis hydrogen is the promising step toward the sustainable energy and zero carbon footprints [179, 275, 276]. The water-splitting reaction involves the oxygen evolution reaction (OER) and hydrogen evolution reaction (HER) at photoanodes and photocathode, respectively. However, the oxygen evolution reaction limits the overall water splitting due to sluggish kinetics. The development of an efficient photoanode is a key challenge in the PEC water splitting. A number of the photoanodes materials have been investigated over the years such as TiO₂, WO₃, α -Fe₂O₃ and BiVO₄ [78-85, 147]. Among the photoanodes, BiVO₄ is the promising photoanodes because of the narrow bandgap 2.4 eV, favorable band position, (photo) electrochemical stability in aqueous solution, earth-abundant and non-toxic and high theoretical efficiency 7.5 mAcm⁻² under AM 1.5 G illuminations [87-89]. The experimental solar to the hydrogen conversion efficiency of the bare BiVO₄ is 5.2 % [325, 326], which is much lower than the theoretical efficiency of ~ 9 % STH [90] due to the slow surface kinetics, poor hole diffusion, fast charge recombination. To overcome the limitations, a number of the strategies have been investigated, such as the heteroatom doping [107-110, 147], oxygen vacancy [94, 114-116], band engineering [99-103, 327], crystal facet engineering [328, 329], and nanostructure control [95-97] which lead to the improvements in the injection of the photogenerated holes to the interface. However, sluggish

surface OER kinetics and trapped surface state cause the significant electron-hole recombination [91, 118]. Surface modification of the BiVO_4 has been performed by oxygen evolution catalysts (OEC) to accelerate the OER kinetics and suppress the surface charge recombination. A number of the OEC such as CoPi [90, 94, 108, 110, 117, 120, 126], Co- B_i [83, 127-129], Ni-Bi [130], NiOOH/Ni-borate [130, 131], FeOOH [132, 133], Ni(Fe)OOH [134] and FeOOH/NiOOH [87] have been investigated to improve the onset potential and suppress the charge recombination for the PEC water oxidation. Among all, Co-based cocatalyst, especially CoPi has been extensively investigated because of low cost and excellent catalytic activity in PEC water oxidation [90, 94, 108, 110, 117, 119-121, 126]. CoPi is stabilized in the phosphate buffer, but the phosphate buffer solution is corrosive to the BiVO_4 photoanode [135]. The borate buffer solution is recently found relatively less corrosive to the BiVO_4 for the PEC water oxidation reaction [83, 134, 136]. Therefore, Co- B_i would be the promising materials for the PEC water oxidation reaction. However, Ding C et al. and Surendranath et al. have shown that there is low PEC activity of Co- B_i cocatalyst or insufficient charge transfer between Co- B_i cocatalyst and BiVO_4 photoanode [127, 330]. Dongqi et al. have shown the improved catalytic activity of the Co- B_i modified BiVO_4 [129]. In the previous chapter the Mo doped BiVO_4 anode material for the photoelectrochemical (PEC) splitting of water using solar light has been presented. In order to further improve the PEC efficiency, BiVO_4 is modified with cobalt borate (Co- B_i) as the electrocatalysts and presented in this chapter.

Photocharging (PC) effect is one of the unique techniques to improve the PEC of the photoanodes [92, 314, 315]. Smith et al. have reported for the first time that there are dramatic improvements in the photocurrent of the BiVO_4 under AM 1.5G illumination [314]. Wilson smith et al. have shown that the photocharging effect is a light-driven surface alteration and

preferential to the alkaline condition [92]. They have proposed that under illumination, the surface of the BiVO_4 is hydrogenated in the alkaline solution, and hence there is the formation of oxygen vacancy, which leads to the reduction of the vanadium +5 to +4 oxidation state on the surface of the photoanode which improves the surface charge transfer kinetics. The intensity-modulated photocurrent spectroscopy (IMPS) study reveals that there are improvements in the surface and bulk properties of the bare BiVO_4 upon the photocharging [315]. The qualitative and quantitative measurement of the photocharging effect has been reported; however, the in-situ study of the semiconductor-electrolyte interface (SEI) is missing. The lack of information gives the knowledge gap in understanding of the photocharging effect on the BiVO_4 and Co-Bi modified BiVO_4 . Therefore, we aim to fill this knowledge gap by providing the quantitative information of the Co-Bi modified BiVO_4 .

We have the first time demonstrated the performance of the Co-Bi modified BiVO_4 photoanode could be further improved by the prolonged exposure of the AM 1.5 G illumination at the applied potential under the aqueous solution. We have investigated the PEC, optical, structural, chemical, and electronic properties of the Co-Bi modified BiVO_4 upon the photocharging for further insight into the physical and chemical mechanism behind the photocharging. In this study, we have optimized the thickness of the Co-Bi loading on the BiVO_4 photoanode and studied the PEC, optical, structural, and electronic properties of the catalysts. After that, photocharging of the photoanodes under the applied bias has been performed. We observe that photocharging leads to the improvements in the PEC many folds. Secondly, we have used the impedance spectroscopy technique to investigate the effect of photocharging on the electronic properties of the photoanodes. Results show that there is a considerable change in the bulk electronic properties after and before the photocharging. Increase in the surface capacitance

shows the alteration surface properties. We further investigate the Mott-Schottky analysis to understand the electronic properties. These results suggest that there is a decrease in the donor density and an increase in the flat band potential due to the trapped photogenerated holes at surface.

Finally, scanning electrochemical microscopy (SECM) study has been employed to investigate localized interfacial charge transfer kinetics at the interface before and after the photocharging to quantify the effect of photocharging on photoanodes. In-situ interfacial photo-induced charge transfer reaction has been studied by scanning electron microscopy (SECM) in solid/liquid and liquid/liquid interface [35, 56, 283, 331-336]. Wittstock et.al have measured photogenerated charge transfer kinetic using BiVO₄ photoanode at interface between two immiscible electrolyte solution (ITIES) [334-336]. Bard group has used surface interrogation SECM to quantify photogenerated hydroxyl radical and dimerization rate constant of hydroxyl radical [284, 285]. Lopes group have investigated water splitting kinetics at SrTiO₃ [337, 338]. Markin and his group have used nanoscale photo-SECM to measure the water oxidation kinetics at Nb:TiO₂ [339]. The in-situ mapping in nanoscale resolution of photocatalytic activity of TiO₂ for Rhodamine decomposition has been investigated by Chen group [340]. The interfacial hole transfer kinetics at Mo:BiVO₄ photoanodes has been studied using redox couple. [33]. Recently, photocatalytic activity of BiVO₄/ FeOOH and CuWO₄/BiVO₄/FeOOH photoanode for water splitting reaction have been investigated using SECM [341]. It has been observed that, there are significant improvements in the hole transfer rates, indicating improvements in the interfacial charge transfer kinetics on incorporation of Co-Bi and by photocharging. In addition to the improvement in the PEC activity through the incorporation of Co-Bi, present investigation

demonstrates the photocharging as a noble approach to improve the PEC efficiency of the Co-Bi modified BiVO₄ photoanodes.

6.2 Experimental Section

6.2.1 Materials

Bismuth (III) Nitrate (Bi (NO₃)₃·5H₂O, 98%), Ammonium Vanadate (NH₄VO₄, >99%), Cobalt (II) nitrate (Co(NO₃)₂·6H₂O, 98%) and Sodium sulfite (Na₂SO₃, 98%) were purchased from Sigma Aldrich. Ammonium tetrathiomolybdate ((NH₄)₂ MoS₄, 99.95%) was purchased from Alfa Aesar. Sodium Sulphate (Na₂SO₄), sodium monohydrogen phosphate (Na₂HPO₄) and sodium dihydrogen phosphate (NaH₂PO₄) were obtained from Sarabhai M Chemicals. Boric acid, sodium hydroxide, ethylene glycol, and potassium ferricyanide were purchased from SDFCL.

6.2.2 Fabrication of Photoanode

BiVO₄ was prepared by the spin coating technique. In this typical synthesis procedure, BiVO₄ film was coated on FTO by the metal-organic decomposition method [147]. Before the deposition, the FTO glass was cleaned by ultrasonication in a soap solution, distilled water, ethanol, and acetone successively and then dried in an IR lamp. In this typical synthesis method, Bi(NO₃)₃·5H₂O (0.2 mmol) was dissolved in 5 mL of ethylene glycol-water mixture (8:2), and then NH₄VO₃ (0.2 mmol) was added slowly and then added 5 atom percentage of Mo using precursor ((NH₄)₂·MoS₄, 99.95%) and then sonicated for 30 minutes and kept on stirring for overnight at room temperature. The above solution was spin-coated on FTO substrate at 2000 rpm for 1 minute and then annealed at 350°C for 5 minutes on a hot plate. These coating was

repeated 10 times to achieve appropriate thickness for maximum efficiency and finally heated at 500°C for 3 h at a rate of 5°C per minute in the tube furnace.

After that, cobalt borate (Co-B_i) was deposited on the BiVO₄ by the photo-assisted electrochemical method [121, 126, 129, 342]. In this typical method, 2 mM cobalt (II) nitrate solution was prepared in 0.1 M borate buffer solution (BBS) of pH 8. The deposition was performed in three electrodes systems using FTO/BiVO₄ as a working electrode, Ag/AgCl (3 M KCl) as a reference electrode, and Pt wire as a counter electrode. Before the deposition of Co-B_i, LSV was performed from OCP to 0.5 V in 1 Sun illumination. Then, Co-B_i was photo - electrochemically deposited on FTO/BiVO₄ and the amount of deposition was varied by varying the deposition time. Thus, photoanodes were named as BV, BV/Co-B_i-1, BV/Co-B_i-2, BV/Co-B_i-3, and BV/Co-B_i-4. The details of sample abbreviations are written in supporting information. Prior to the deposition of Co-B_i, BiVO₄ surfaces were activated by performing LSV in 0.1 M Na₂SO₃ solution for 20 cycles assuming that in the presence of the sacrificial agent, oxidation kinetics would be very fast and hence photoanode would not be affected.

6.2.3 Photoelectrochemical (PEC) measurements

Photoelectrochemical measurements were carried out using CH Instrument (920 D model) in three electrodes systems, Ag/AgCl (3.0 M KCl) as a reference electrode, Pt rod as a counter, and BiVO₄ coated FTO as working electrode in 0.1 M BBS of pH 8 as an electrolyte. All PEC experiments were performed in the back illumination of photoanodes under 1 sunlight of Solar simulator fitted with AM 1.5G filter. The photocurrent was measured by linear sweep voltammetry (LSV) technique at 10 mVs⁻¹ scan rate, and chopped light voltammetry was recorded at a 5 mVs⁻¹ scan rate with the chopping of light at 5 s interval. Charge transfer and

transport efficiencies of photoanodes were measured at 0.8 V (vs Ag/AgCl) in 0.1 M Na₂SO₃ solution in 0.1 M BBS using following equations [311, 312].

$$\eta_{transfer} = \frac{J_{H_2O}}{J_{Na_2SO_3}} \times 100 \% \quad (6.1)$$

$$\eta_{transport} = \frac{J_{Na_2SO_3}}{J_{max.}} \times 100 \% \quad (6.2)$$

$$J_{max.} = \frac{\text{integration of light absorption}}{\text{integration of solar light spectrum}} \quad (6.3)$$

Where, $J_{max.}$ was calculated from the photocurrent obtained from the silicon detector. J_{H_2O} is photocurrent density of the water and $J_{Na_2SO_3}$ is the photocurrent of the oxidation of the sulfite.

Incident photon to current efficiency (IPCE) was measured at 1 V (vs. Ag/AgCl) in monochromatic light from 350 to 650 nm (xenon lamp) by using the following equation

$$IPCE \% = \left(\frac{J \left(\frac{A}{cm^2} \right)}{P_{in} \left(\frac{W}{cm^2} \right)} \times \frac{1240}{\lambda (nm)} \right) \times 100 \% \quad (6.4)$$

Where J is the photocurrent density, P_{in} is the power of the incident monochromatic light (measured by the silicon-based detector, Newport) and λ is the wavelength in nm.

Mott-Schottky experiments were performed in space charge region from -0.4 V to the 0.8 V with potential step 0.025 V at 100 Hz for measurements of donor density and flat band potential of photoanodes, which inherently affects PEC activity. The donor density and flat band potential of the catalysts are calculated from the following equation

$$\frac{1}{C^2} = \frac{2}{qA^2\epsilon\epsilon_0N_D} \left(V - V_{FB} - \frac{k_B T}{q} \right) \quad (6.5)$$

Where, C is the space charge capacitance, q is elementary charge, A is electrode surface area, ϵ_0 vacuum permittivity ($8.854 \times 10^{-12} \text{ Fm}^{-1}$), ϵ is relative permittivity of BiVO₄ (86) [310], N_D (cm^{-3}) is donor density, V is applied potential, V_{FB} is flat band potential, k_B is Boltzmann constant ($1.38 \times 10^{-23} \text{ J K}^{-1}$), and T is absolute temperature. From the above equation, N_D is calculated from the slope of $1/C^2$ vs. V plot.

Electrochemical Impedance Spectroscopy (EIS) was recorded at 0.8 V (vs. Ag/AgCl) by applying a sinusoidal wave of amplitude 10 mV in the frequency range from 10^5 to 10^{-1} Hz under 1 sun illumination. Further, Relaxation frequency and time constant of electron and hole were measured from EIS data to quantify the efficiency of photoanode materials.

The transient time constant (τ) is calculated as the time taken at $\ln D = -1$ where D is normalized transient current

$$D = \frac{I(t) - I(st)}{I(in) - I(st)} \quad (6.6)$$

Where I (t) is current at time t, I (st) is steady current, and I (in) is initial current at time t.

SECM study was performed on 920 D bipotentiostat (CH Instrument, Texas) using four electrodes system. Photoanode materials were used as the substrate, Ag/AgCl (3 M KCl) as a reference, Pt wire as a counter electrode, and Pt UME having RG value 5 and diameter $10 \mu\text{m}$ was used as a probe. Prior to the use of Pt UME, the electrode was polished with a micro polishing cloth with 1.0, 0.3, and $0.05 \mu\text{m}$ alumina powder successively and then cleaned in a 0.5 M H₂SO₄ solution by performing CV in the potential window from 0.8 V to -0.35 V for 20

cycles. 2mM $[\text{Fe}(\text{CN})_6]^{3-}$ the solution was used as a redox probe in 0.1 M phosphate buffer solution (PBS) of pH 7. The photoanodes were illuminated from the front side in the SECM setup. The potential of the probe during probe approach was chosen -0.1V in the region of steady diffusion current after recording CV in 2 mM $[\text{Fe}(\text{CN})_6]^{3-}$ as redox probe in 0.1 M PBS of pH 7 at 50 mVs^{-1} scan rate. Probe Approach Curve (PAC) technique was used to approach the curve to the substrate in dark and light to measure the kinetic parameter using four electrodes systems at different polarization potential to measure interfacial charge transfer kinetics. The normalized approach curves are fitted using following equations to calculate charge transfer rate constant at the electrode-electrolyte interface [32].

6.3 Result and discussion

6.3.1 Material characterization

BiVO_4 and Co- Bi modified BiVO_4 were characterized by the XRD technique, and results are shown in Figure 6.1 (A). XRD peaks at 2θ values of 18.46° , 28.48° , 30.10° , 34.95° , 39.80° , 42.17° , 46.45° and 52.93° correspond to (011), (121), (040), (002), (-112), (051), (042) and (161) plane of monoclinic phase of BiVO_4 (JCPDS 014-0688) respectively. The relatively strong peak at 28.48° is attributed to the preferential growth of BiVO_4 films along [121] direction. The impurity level doping of Mo in BiVO_4 is not detected in XRD. Upon Co- Bi modification, no change of XRD pattern shows the intact phase of BiVO_4 [127, 330]. The XRD peaks at 26.37° , 34.58° , 37.45° , 61.37° and 65.45° shows underneath FTO (JCPDS card 41-1445) substrate.

Investigation of the crystallization, local structure, and electronic properties of photoanodes was performed by Raman spectroscopy analysis. Figure 6.1 (B) shows the characteristic Raman spectra of the BiVO_4 at 826.80 , 713 , 367.53 , and 329.04 cm^{-1} . The

relatively strong band at 826.80 cm^{-1} and weak shoulder like a peak at 713 cm^{-1} are assigned to the $\nu_s(\text{VO}_4)$ (A_g) and $\nu_{as}(\text{VO}_4)$ (B_g) mode, respectively. The Raman band at 367.53 and 329.04 cm^{-1} are attributed to the $\delta_s(\text{VO}_4)$ (B_g) and $\delta_{as}(\text{VO}_4)$ (A_g), respectively. The rotational and translational modes (external modes) are observed at 213.23 cm^{-1} and 126.58 cm^{-1} , respectively, relatively at lower frequencies than the internal modes of VO_4^{3-} [292-297]. The weak band at 878.97 cm^{-1} is assigned to the $\nu_s(\text{MoO}_4)$. The Raman band at 516.30 cm^{-1} is due to the Co-Bi (E_g) mode of vibration and Raman band at 475.25 cm^{-1} due to Co_3O_4 (F_{2g}) mode. These results show the mixed phase of Co-Bi and Co_3O_4 are photo-electrodeposited on the BiVO_4 . The redshift in the most intense peak of $\nu_s(\text{VO}_4)$ (A_g) from 826.80 cm^{-1} to 824.79 cm^{-1} upon Co-Bi modification suggests the interaction of V-O bond to B^{3+} and Co^{3+} of Co-Bi. Similarly, redshift of bending vibrational modes $\delta_s(\text{VO}_4)$ (B_g) and $\delta_{as}(\text{VO}_4)$ (A_g) have also been observed. The V-O bond length were calculated for $\nu_s(\text{VO}_4)$ (A_g) vibration mode using the following equation [297].

$$\nu(\text{cm}^{-1}) = 21349 \exp(-1.9176R(A^\circ)) \quad (6.7)$$

Where ν is the Raman stretching frequency for V-O in cm^{-1} and R is the bond length in A° . V-O bond length has been increased from 169.55 pm to 169.67 pm after Co-Bi modification of BiVO_4 .

Morphology of BiVO_4 and Co-Bi modified BiVO_4 photoanodes were characterized by scanning electron microscopy (SEM), as shown in Figure 6.1 (C-G). Figure 6.1 (C) shows the uniform coating of BiVO_4 on FTO and the inset Figure shows the granular shape of BiVO_4 . The uniform and porous photo-electrodeposited Co-Bi with spherical shape is observed as shown in Figure 6.1 (D-G). The uniform deposition of spherical Co-Bi nanoparticles is obtained on the BiVO_4 , which supports the SEM analysis. Elemental analysis of BV and Co-Bi modified BV

photoanodes shows the atomic ratio of Bi and V is 1:1 as shown in Figure 6.2. The atomic percentage of Mo is 1.47%. This doping percentage Mo is decreased with the Co-B_i deposition. The atomic percentage of Co in BV/Co-B_i-1 is 2.33 % and is increased from 2.33% to 4.10% in BV/Co-B_i-4. The decrease in the Bi and V atomic percentage is expected due to the top layer of Co-B_i. The thickness of BiVO₄ and Co-B_i modified BiVO₄ are 750 nm and 775 nm, as shown in Figure 6.3.

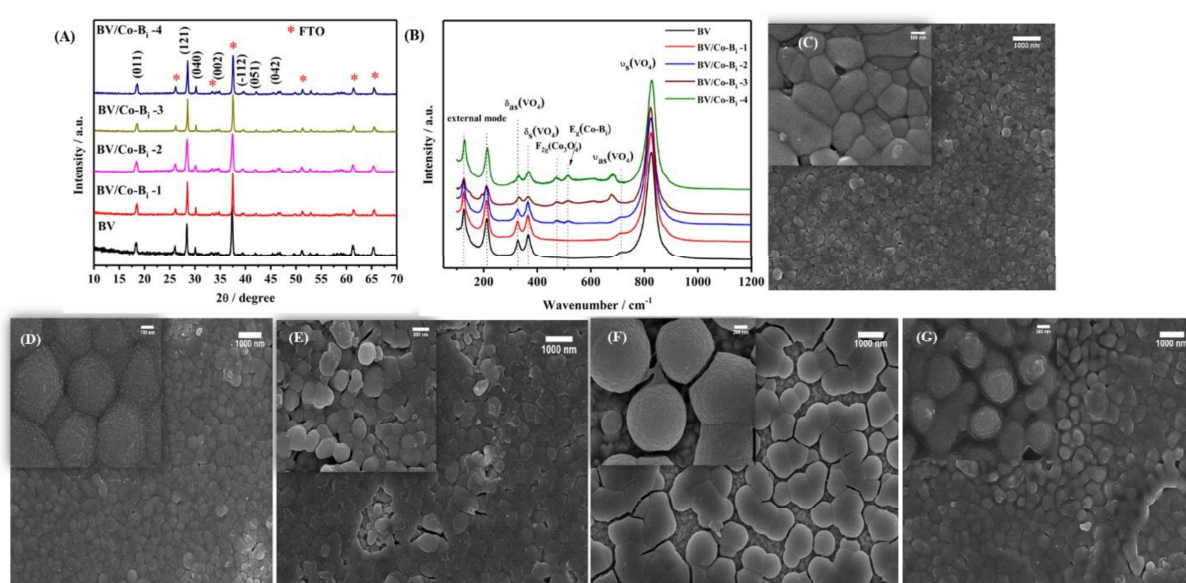


Figure 6.1 (A) XRD pattern of BV and Co-B_i modified BV, (B) Raman analysis of photoanodes. SEM images of (C) BV, (D) BV/Co-B_i-1, (E) BV/Co-B_i-2, (F) BV/Co-B_i-3 and (G) BV/Co-B_i-4.

The surface electronic properties of the photoanodes were investigated by using XPS as shown in Fig. 6.4. Fig. 6.4 (A) shows the spectra of 4f orbital of Bi, splits into the 4f_{5/2} and 4f_{7/2} components. Similarly, XPS spectra of V 2p orbital and Mo 3d orbital confirms the formation of the Mo doped BV. Upon Co-B_i modification, XPS spectra of Co 2p and B 1s orbital were

obtained which confirm the successful formation of heterojunction of BV and Co-B_i. The chemical states of constituent elements were determined from XPS measurements. The binding energy (BE) of Bi 4f_{5/2} and Bi 4f_{7/2} are 164.22 eV and 158.81 eV respectively with spin-orbit split energy of 5.41 eV reveals Bi in +3 oxidation state [110, 301, 343]. The BE of V 2p_{1/2} and V 2p_{3/2} are at 524.22 eV and 516.53 eV with spin-orbit split energy 7.69 eV, suggests that V is in +5 oxidation state. The BE of Mo 3d_{3/2} and Mo 3d_{5/2} were obtained at 235.22 eV and 232 eV respectively with spin-orbit energy 3.22 eV confirms the Mo is in +6 oxidation state [110, 301]. The BE at 780.30 eV and 795.27 eV are due to Co 2p_{3/2} and Co 2p_{1/2} which confirm the Co is in +3 oxidation state in Co-B_i [110, 343]. The BE at 191.80 eV further confirms the presence of B³⁺ in the photoanode matrix. The binding energy of Bi was increased upon the Co-B_i modification due to incorporation of the more electronegative B³⁺ and Co³⁺ as shown in Fig 6.4 (E & F).

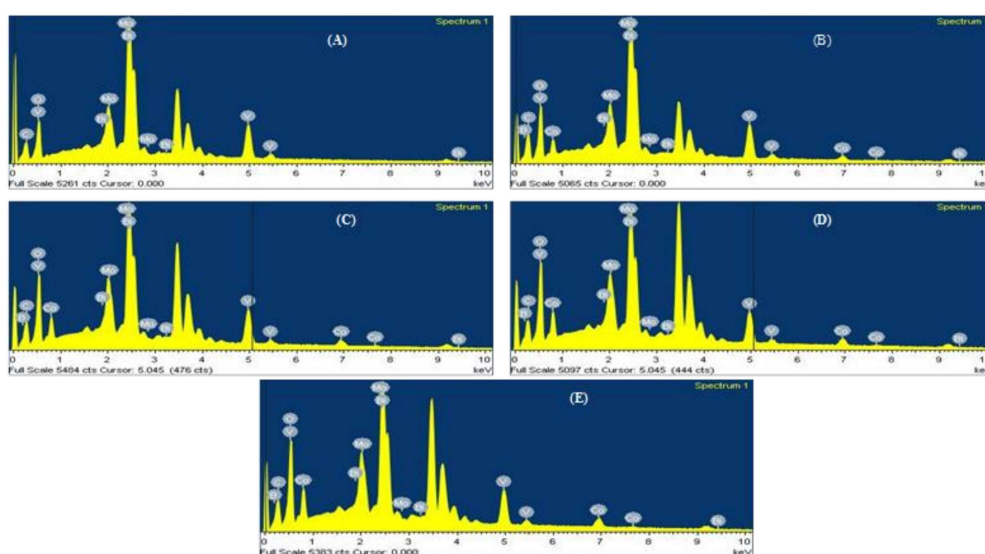


Figure 6.2 EDS elemental analysis of photoanodes (A) BV, (B) BV/Co-B_i-1, (C) BV/Co-B_i-2, (D) BV/Co-B_i-3 and (E) BV/Co-B_i-4.

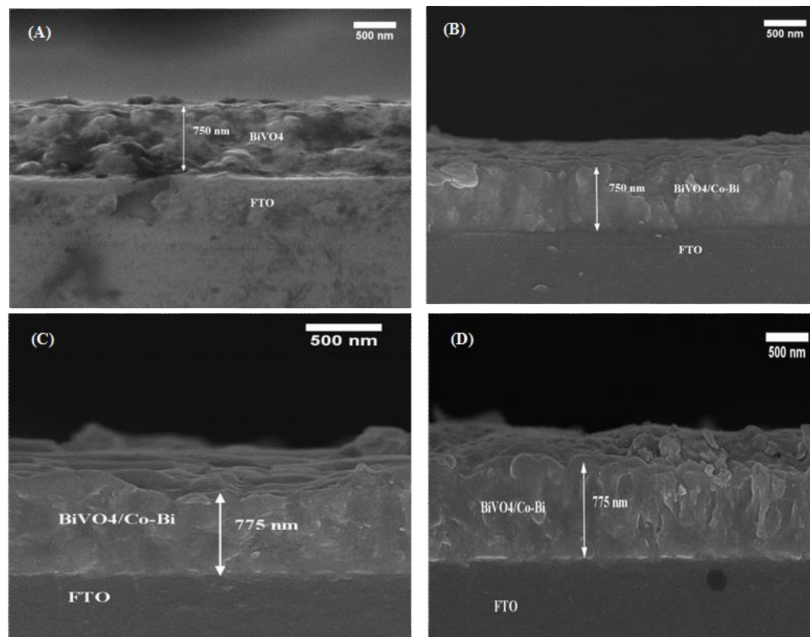


Figure 6.3 Cross-sectional thickness of photoanodes (A) BV, (B) BV/Co-Bi-1, (C) BV/Co-Bi-2 and (D) BV/Co-Bi-3.

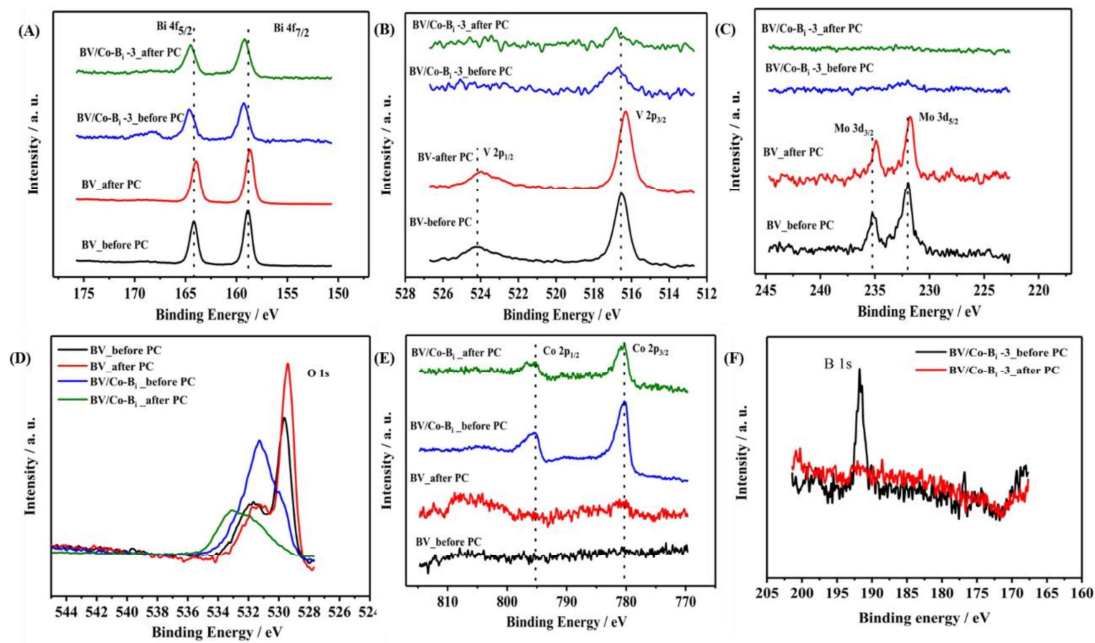


Figure 6.4 XPS analysis of (A) Bi 4f, (B) V 2p, (C) Mo 3d, (D) O 1s (E) Co 2p and (F) B 1s.

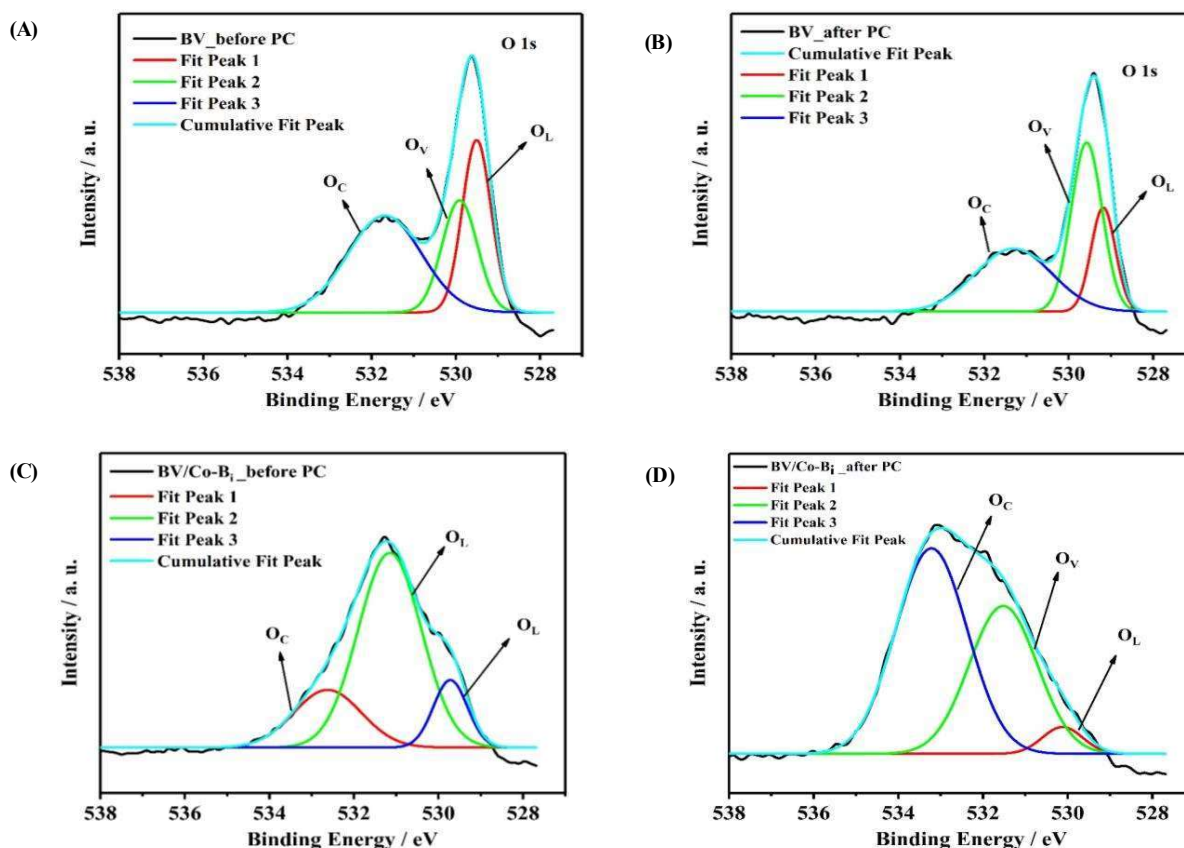


Figure 6.5. High resolution XPS analysis of O 1s for BV and BV/Co-Bi-3 before and after photocharging.

The BE of Bi 4f and V 2p in BV and BV/Co-Bi-3 photoanodes were decreased after photocharging. The decrease in BE can be due to reduction of V^{5+} to V^{4+} [92]. The high-resolution O 1s spectra of BV and BV/Co-Bi-3 were fitted into three components as lattice oxygen (O_L), oxygen vacancy region (O_V) and chemisorbed or dissociated oxidation species in water (O_C) as shown in Fig 6.5. The BE at 529.50 eV and 529.91 eV ascribed to O_L and O_V respectively in $BiVO_4$. Another BE at 531.68 eV is attributed to the chemisorbed oxygen or hydroxyl group. After the photocharging, BE of O_L is shifted towards the lower BE from 529.50

to 5.29.18 eV due to oxygen vacancy [92]. The oxygen vacancy is increased upon photocharging as O_V/O_L has been increase.

Upon Co-Bi incorporation in BiVO_4 , BE of O_L and O_C were observed at 529.72 eV and 532.62 eV respectively. The lattice oxygen peak is shifted to higher BE from 529.50 to 530.72 in the presence of more electronegative B^{3+} and Co^{3+} in Co-Bi. The oxygen vacancy has been increased upon CoBi modification as O_V/O_L increased with respect to BV. It has been reported that Co doping increase the oxygen vacancy in BiVO_4 [344]. After photocharging of BV/Co-Bi-3, BE of O_L is increased from 529.72 eV to 530.12 eV. The higher BE is expected due to photo-oxidation of Co^{3+} to Co^{4+} at electrode surface. Increment in O_V/O_L , further suggests increase of oxygen vacancy after photocharging. The chemisorbed oxygen is also increased suggests that water oxidation intermediates or hydroxide on the BV/Co-Bi-3 surface as Co(IV)-OH .

6.3.2 UV-Vis spectroscopy

The optical absorption property and bandgap of the photoanodes have been characterized by the UV-vis diffuse reflectance spectra, as shown in Figure. 6.6 (A). All photoanodes show strong absorption in the range of 500-330 nm. The absorption peak at 472 nm corresponds to the transition of the BiVO_4 from valence band to the conduction band. Improvement of light absorption was observed upon incorporation of the Co-Bi on the BiVO_4 . The enhancement of photo-absorption efficiency of photoanodes after CoBi modification can be explained in terms of light harvesting ability of Co-Bi in range of 550-350 nm as shown in Fig. 6.6 (A). This observation shows the synergic effect of Co-Bi electrocatalyst for light harvesting efficiency on the BV. [345]. Nature of the transition of band and the bandgap of the semiconductor were determined from the analysis of the plots of $(\alpha h\nu)^2$ vs $h\nu$ [152]. The bandgap of the BV is 2.0 eV, which is somewhat lower than the direct theoretical bandgap (~ 2.4 eV) of the BiVO_4 . Upon

incorporation of the Co-Bi, the bandgap of the photoanodes is increased from 2.0 eV to the 2.45 ± 0.12 eV. It has been reported that narrowing of the bandgap enhances the photon-absorption efficiency which ultimately improves the PEC activity of photoanodes [346]. CoBi modification enhances the light absorption efficiency and narrows the bandgap. Therefore, the synergistic effect of CoBi for light harvesting efficiency on BV has been observed.

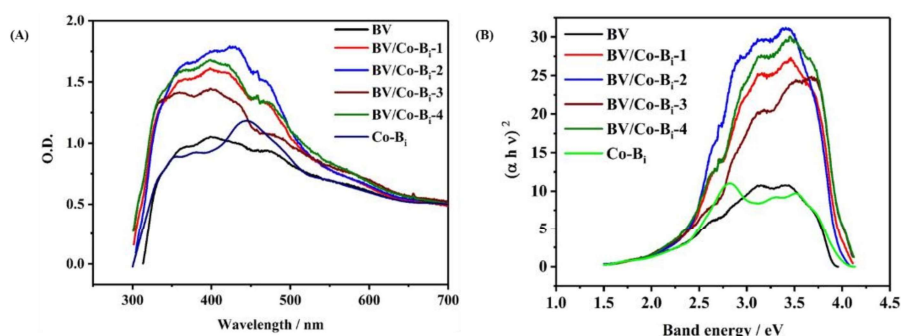


Figure 6.6 (A) Absorption spectra and (B) Tauc plot of photoanodes BV and BV/Co-Bi-3.

6.3.3 Photoelectrochemical study

The electrochemical and photo-electrochemical experiments were performed in the 0.1 M borate buffer solution (BBS, pH 8) using three electrodes systems under AM 1.5 G illuminations. It has been reported elsewhere that phosphate buffer solution (PBS) is somewhat corrosive to the BiVO_4 photoanode, and hence relatively less corrosive BBS is the alternative electrolyte for the water splitting [83]. The PEC activities of the photoanodes were performed by the chopped light voltammetry method. Figure 6.7 (A) shows a relatively low performance of BV with the high onset potential -0.30 V and low photocurrent density of 0.96 mAcm^{-2} at 0.8 V (vs. Ag/AgCl). The low photocurrent of BV could be caused by fast electron-hole recombination, low charge separation, and poor surface catalytic activity of BiVO_4 [87, 347]. The significant improvements

in photocurrents have been obtained from 0.96 mAcm^{-2} to 1.95 mAcm^{-2} , with 103 % improvements in Co-B_i modified BiVO₄. These results show optimum loading of the Co-B_i is $76 \mu\text{g cm}^{-2}$ for BV/Co-B_i-3. The improvements of the photocurrent of the Co-B_i modified BiVO₄ can be correlated with the enhancement of the photon absorption efficiency of the photoanode upon Co-B_i incorporation. The onset potential of Co-B_i modified BiVO₄ is cathodically shifted from -0.30 V to -0.40 V suggesting the thermodynamically favorable OER and improved surface kinetics. It has been reported that OEC on BiVO₄ significantly decrease the activation energy of PEC OER by changing the hole transfer mechanism from bulk to BiVO₄ to OEC and then OEC to water molecule [348]. The significant improvement in the photocurrent and onset potential suggest the synergistic effect of Co-B_i in light absorption efficiency of BV as shown in Fig. S4 (A). Co-B_i on the BiVO₄ acts as the hole collector, which improves photogenerated charge separation and bulk and surface charge transfer kinetics, therefore, overall interface OER kinetics enhanced significantly [87, 117, 126]. The increase in oxygen vacancy in CoB_i modified BV, as shown in Figure 6.3, increased the bulk and surface charge separation efficiency and hence overall PEC efficiency improved. There is no cathodic current transient observed in chopped light voltammetry of BV suggests no interfacial trapped hole available for the reduction reaction. However, chopped light voltammetry of Co-B_i modified photoanodes shows the cathodic transient current in the potential window from -0.15 V to 0.80 V when light was chopped off. This cathodic current is expected due to the reduction of photo-oxidized Co (IV) to Co (III) in the dark. It has been reported that photogenerated holes are stored in the form of Co (IV) in the presence of Co-B_i on BiVO₄, and when light is chopped off, Co (IV) gets reduced to Co (III) [277]. Collection and storage of photogenerated holes by Co (III) increases the lifetime and hence reduces the recombination process thus improving the catalytic activity. Photocharging

effect is an excellent technique to suppress the charge recombination and improve photocatalytic activity [92, 315, 346, 349, 350]. The details discussion of improvements in photocurrent upon photocharging is discussed in the subsequent section.

The overall efficiency of the photoanode depends on the two limiting parameters, the surface charge separation efficiency and the bulk charge separation efficiency. Therefore, these charge separation efficiencies were investigated by the hole scavenger method to quantify the catalytic activity of the photoanodes [312]. The surface charge separation efficiency of BV at 0.8 V (vs Ag/AgCl) was 57 % and increased to 81 % after incorporation of the Co-B_i. This result shows that co-catalyst facilitates the transfer kinetics of the hole at the interface, which supports the chopped light voltammetry result and light absorption efficiency. The bulk charge separation efficiency of BV was 30 % and increased to 47 % after modification of BV with Co-B_i. Co-B_i facilitates hole collection centre as Co (IV) on the interface, which improves photogenerated charge separation in the bulk. Increase in oxygen vacancy upon CoB_i modification, further improves the bulk charge separation efficiency. Therefore, the overall improvements in the photocurrents can be reason out from the improvements in the surface and bulk charge separation efficiencies.

PEC efficiency was measured by evaluating the incident photon to current efficiency (IPCE) as shown in Fig. 6.7 (B). The onset potential of the IPCE of photoanodes was observed at 500 nm, which is well supported by the absorption spectroscopy measurements. The onset wavelength of IPCE is ~ 500 nm which corresponds to the band gap of 2.48 eV. BV exhibits IPCE of 12 % at 400 nm. The IPCE value of Co-B_i modified BV was increased from 12 % to 34 %, with subsequent increase in Co-B_i thickness. The improvements in the IPCE of BV/Co-B_i-4 has been observed by ~ 183% increment with respect to BV. The improvements of the IPCE

upon Co-B_i modification are as accordance of the enhancement of the light absorption efficiency of BV. Further, PEC efficiency improvement is supported by enhancement in bulk and surface charge separation efficiency. The results also support the improvements of the photocurrent in the chopped light voltammetry study.

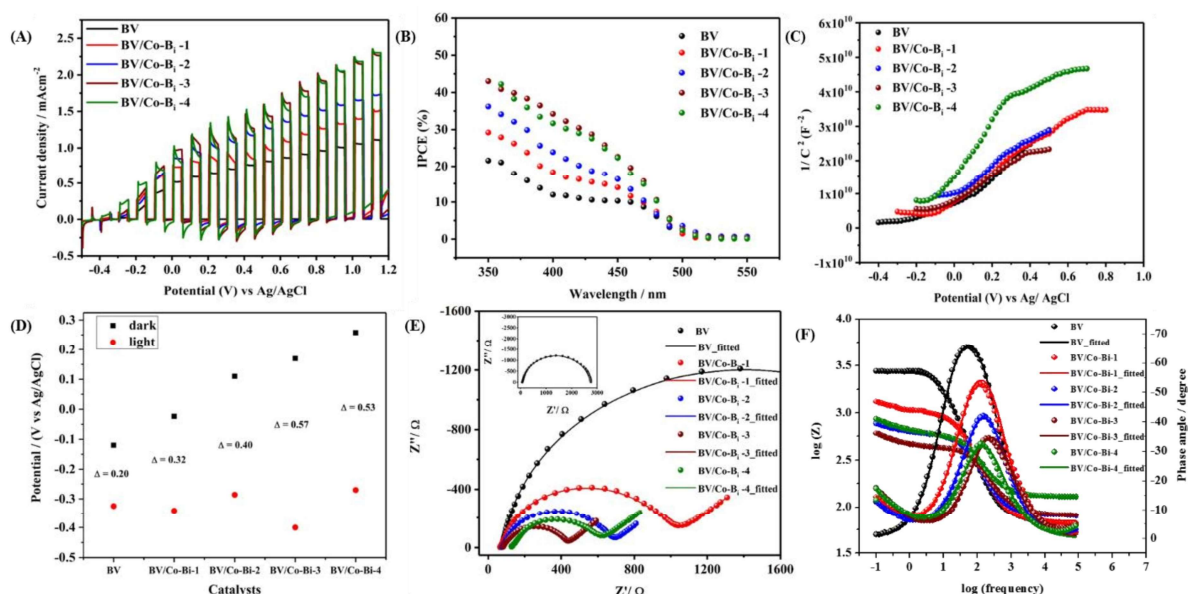


Figure 6.7 (A) Copped light voltammetry of photoanodes, (B) IPCE measurements, (C) Mott-Schottky plot, (D) open-circuit photovoltage, (E) Nyquist plot and (F) Bode plot.

Further, the insight into the improvements in surface and bulk charge separation efficiency of the photoanodes have been investigated by Mott-Schottky analysis. Donor density is the inherent property of the photoanode, and PEC activity is increased with the donor density. Donor density of the BV was $(5.10 \pm 0.24) \times 10^{20} \text{ cm}^{-3}$. After incorporation of Co-Bi, donor density was increased from $5.10 \times 10^{20} \text{ cm}^{-3}$ to $6.67 \times 10^{20} \text{ cm}^{-3}$. It has been reported that donor density increased upon Co-Pi incorporation in $\text{SnO}_2@\text{BiVO}_4$ [351]. The donor density of

BV/Co-B_i-2 is higher than the BV but the transport efficiency was same as that of BV. The photocurrent of BV/Co-B_i-2 is higher than BV is due to higher in surface charge separation efficiency and cathodic shift of flat band potential. The cathodic shift of flat band potential gives the favorable thermodynamics OER process. There is dramatic decrease of donor density in BV/Co-B_i-4 but the bulk charge separation efficiency is higher than the BV. Co-B_i incorporation on BV improves the photogenerated charge separation as OCPV (discussed in next section) of BV/Co-B_i-4 is 0.53 V as compared to the 0.20 V of BV. and more negative onset potential for OER. And, Co-B_i acts as the hole collector at the interface and facilitates the more thermodynamic favorable OER as onset potential is lower than that of BV. The enhancement in light absorption efficiency and oxygen vacancy upon CoB_i modification increase donor density. The increment in donor density improves bulk charge separation efficiency and bulk conductivity of photoanode. It is expected that OEC increase the quality of donor density as it collects hole at interface and facilitates the oxygen evolution reaction.

Flat band potential of the photoanode is a qualitative measurement of the band bending at the electrode-electrolyte interface, which mainly affects the photogenerated charge separation and recombination process at the interface and hence affects the overall PEC efficiency of the catalysts [161, 162, 286]. It has been reported that a high degree of band bending improves the charge separation and suppresses the electron-hole recombination process. Flat band potential was calculated from the Mott-Schottky plot (Fig. 6.7(C)) and tabulated in Table 6.1. The flat band potential of the BV was -0.15 V and shifted towards the cathodic side from -0.15 V to the -0.25 V with Co-B_i incorporation on the BiVO₄ surface. The increase in flat band potential suggests an increase in the degree of band bending which is as accordance with the enhancement of the donor density and hence, improvements in bulk charge separation efficiency observed.

The cathodic shift of flat band potential is consistent with the cathodic shift of onset potential of photocurrent. This result further supports the improvement in PEC efficiency of Co-B_i modified BV.

Table 6.1 Summary of characterization of PEC of photoanodes and impedance spectroscopy.

Photoanodes	Bandgap (eV)	Donor density (cm ⁻³)	Flat band potential, (V)	OCPV (V)	Charge transfer efficiency	Charge transport efficiency	R _{ct} (Ω)	C (F)	Relaxation frequency (Hz)	Relaxation time constant (ms)	L _D (nm)
BV	2.0±0.10	(5.10±0.24) ×10 ²⁰	-0.15±0.01	0.20±0.01	57 ± 3	30 ± 2	2677 ± 134	(5.22± 0.26) ×10 ⁻⁶	54 ± 3	2.95 ± 0.15	576 ± 28
BV/Co-B _i -1	2.41±0.12	(6.34±0.27) ×10 ²⁰	-0.20±0.01	0.32±0.02	59 ± 3	35 ± 2	980 ± 50	(5.77 ± 0.29) ×10 ⁻⁶	134 ± 7	1.18 ± 0.06	94 ± 5
BV/Co-B _i -2	2.45±0.12	(5.18±0.32) ×10 ²⁰	-0.19±0.02	0.40±0.02	70 ± 3	30 ± 1	610 ± 30	(5.97 ± 0.30) ×10 ⁻⁶	158 ± 8	1.00 ± 0.05	68 ± 3
BV/Co-B _i -3	2.20±0.11	(6.67±0.32) ×10 ²⁰	-0.25±0.01	0.57±0.03	73 ± 4	47 ± 2	354 ± 18	(4.58±0.23) ×10 ⁻⁶	229 ± 11	0.70 ± 0.04	33 ± 2
BV/Co-B _i -4	2.40±0.12	(3.25±0.30) ×10 ²⁰	-0.22±0.01	0.53±0.03	81 ± 4	44 ± 2	488 ± 24	(5.57±0.28) ×10 ⁻⁶	123 ± 6	1.29 ± 0.06	112 ± 6

The band position and the band bending are further investigated by the open circuit photovoltage (OCPV). The change in the OCPV is due to the change in the band bending and the charge recombination at the electrode-electrolyte interface. The extent of band bending at the electrode-electrolyte interface depends on the in-built potential and the charge recombination [287, 288]. The OCPV was calculated from the OCP difference in the dark and under illumination, as shown in Fig. 6.7(D). The OCPV of bare BV was 0.20 V and increased to 0.57 V with incorporation of the Co-B_i. It is assumed that the Fermi level of the photoanode is in equilibrium with the water oxidation band in the dark condition, and on illumination, the quasi-Fermi level of the hole is in equilibrium with the water oxidation band, and quasi-Fermi level of electron rises towards the conduction band [92, 314]. The Fermi level of BV is short of the water oxidation potential. When water oxidation co-catalyst Co-B_i is incorporated on the BiVO₄, there is a shifting of the Fermi level of photoanodes towards the water oxidation potential. These results show no surface states are available upon Co-B_i incorporation. This result supports the significant band bending

and improved charge separation upon Co-B_i incorporation, as observed from the flat band potential measurements.

6.3.4 Electrochemical Impedance Measurements

It is observed that the co-catalyst incorporation improves the overall PEC efficiency. This improvement in efficiency is a combined contribution of the surface and bulk phenomenon as the charge transfer is a surface phenomenon and charge transport is a bulk phenomenon. Further investigation has been carried out for the measurements of the bulk and surface characteristics of the materials. Electrochemical impedance spectroscopy (EIS) study has been performed to investigate the bulk and surface contribution in the PEC efficiency, as shown in Fig. 6.7(E and F). The Nyquist plot is used to investigate the charge transport and charge transfer resistance of the BV and BV/Co-B_i photoanodes. Two arcs at high and low frequency ascribed the bulk charge transport and electrode/electrolyte interfacial charge transfer respectively [352]. The low frequency resistance i.e. charge transfer resistance (R_{ct}) of the BV is 2677 Ω and is decreased to 354 Ω upon the incorporation of the Co-B_i. These results indicate significant improvements in the charge transfer kinetics. The increase in donor density due to oxygen vacancy improves the bulk charge separation efficiency and hence R_{ct} is decreased upon CoB_i modification. The incorporation of Warburg components in the Co-B_i modified BiVO₄ suggests the shift in the charge transfer kinetics at the interface from kinetic control to the diffusion control process. Jinhua Ye et. al. have reported that activation energy for PEC OER significantly decreased upon OEC incorporation, which indicates surface charge transfer reaction is fast enough and reaction transferred from kinetic control to diffusion control process [348]. The significant decrease in the R_{ct} value in Co-B_i modified BV in the present case suggests the fast charge transfer kinetics, and overall kinetics is limited by the diffusion process. The kinetics of the OER reaction over BiVO₄

is significantly improved due to the incorporation of the OER cocatalyst by lowering the activation energy of the process. This is achieved through the improvement in the hole capture property of the Co-B_i as supported from the significant decrease in the charge transfer resistance from the impedance measurements.

Charge transfer kinetics is further investigated by the Bode plot format of the impedance data and shown in Fig. 6.7 (F). The decrease in the phase angle upon the Co-B_i modification of BV as compared to BV shows improvements of the conductivity of the interface and hence charge transfer kinetics is improved. This result suggests the improvements in the surface catalytic activity as compared to the BV. Further, the kinetics is investigated in terms of the relaxation frequency and relaxation time constant (τ) of the photogenerated charge [147]. The relaxation frequency of the photogenerated charge is 54 ± 3 Hz for BV and increased from 54 Hz to 229 Hz upon Co-B_i modification. The increase in the relaxation frequency suggests the faster relaxation process of the photogenerated charge and hence, faster kinetics at the interface which further supports decrease in R_{ct} . The lifetime τ of photogenerated charge is calculated by using the relation $\tau = 1/2\pi f$ where f is the relaxation frequency. The τ of BV is 2.92 ms, and Co-B_i modification of the BiVO₄ leads to a decrease in the τ to 0.70 ms. This decrease in τ also supports the faster charge transfer at the interface and supports the improvements in the kinetics of water splitting upon the Co-B_i incorporation.

The overall PEC water oxidation efficiency and interfacial charge transfer depend on the diffusion of the hole in the BiVO₄ photoanodes. We have assumed that relaxation time constant is the time taken by the photogenerated hole to oxidize water molecules, including the diffusion of the hole in the bulk and interface to oxidize water molecules. Therefore, the diffusion length of holes is measured by using τ of holes from the Bode plots and calculated by using equation,

$L_D = (D \times \tau)^{1/2}$ where L_D is diffusion length, D is the diffusion coefficient of the photogenerated hole, taken as $2.60 \text{ cm}^2 \text{ s}^{-1}$ [313] and τ is the relaxation time of holes, the L_D values thus obtained are tabulated in Table 6.1. L_D of BV is 576 nm and is decreased with the Co-B_i incorporation on the BiVO₄. The significant decrease in the L_D shows the faster transfer of holes at the interface for water oxidation [147]. It is expected that holes are first stored in the Co-B_i co-catalyst in the form of Co (IV) and then transferred to the water molecules for oxidation. The drastic change of L_D from 576 nm to 33 nm shows the synergistic role of Co-B_i in PEC water oxidation. Since the thickness of films is ~ 750 nm, the diffusion of the hole in BV is essentially from bulk to electrochemical interface. However, in the presence of the Co-B_i, L_D is significantly lower compared to the thickness of the film, which suggests that the Co center acts as the reservoir of photogenerated holes and then transfers to the water molecules. This observation suggests the mechanism of transfer of holes from bulk to water molecule via the Co center. Photogenerated holes first collected by the Co (III) and then transferred to the water molecule for the oxidation process.

The stability test of the photoanodes was performed by the chronoamperometry method at the 0.8 V for the 2 h, the results are shown in Figure 6.8. BV and Co-B_i modified BV is quite stable for 2 h. The initial decrease in photocurrents is due to the capacitive loss, and then the increase of photocurrent is observed because of improvements in surface kinetics. Co-B_i modification of the BV enhances the stability of the photoanodes. The increase in photocurrent can be explained based on the photocharging effect. The photocharging of the BiVO₄ photoanode improved the photocurrents many folds due to the improvements in the surface and bulk properties of the photoanode materials. The detailed study of the photocharging effect on the BV and Co-B_i modified photoanodes is in the next sub-section. Photocurrent of BV and

BV/Co-B_i-3 after 2 h stability has been improved by ~ 35 %. The details explanation of improvement is discussed in next section.

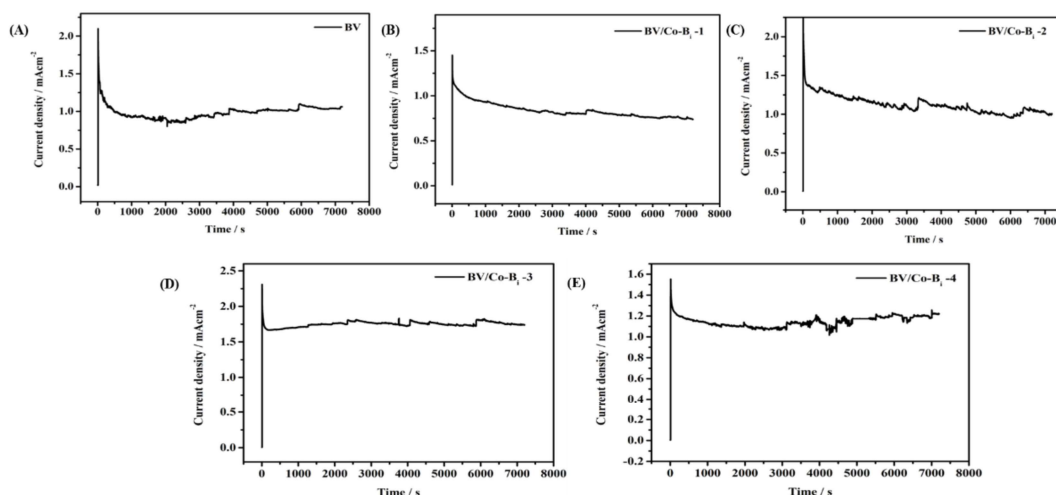


Figure 6.8 Stability test of the photoanodes (A) BV, (B) BV/Co-B_i-1, (C) BV/Co-B_i-2, (D) BV/Co-B_i-3 and (E) BV/Co-B_i-4 at 0.8V for 2 h.

6.3.5 Photocharging of the Photoanode

Photocharging of BiVO₄ has been carried out by continuous illumination, all the photoanodes have been exposed to 1 sun of solar simulator fitted with AM 1.5G filter for 2 h at 0.8 V in 0.1 M BBS (pH 8) and then the PEC catalytic activity has been investigated. The I-V characteristics of the treated and untreated photoanodes are shown in Figure 6.9. LSV and chopped light voltammetry results show significant improvements in the photocurrents of all photoanodes and tabulated in Table 6.2. The significant improvement in the photocurrent of BV (~ 36±2%) from 0.96 mA cm⁻² to 1.31 mAcm⁻² is observed at 0.8 V (vs. Ag/AgCl, 3M KCl). Similarly, 31%, 42%, 34% and 34% improvement of photocurrent of BV/Co-B_i-1, BV/Co-B_i-2, BV/Co-B_i-3, and BV/Co-B_i-4 respectively have been obtained upon photocharging. The significant improvement in photocurrents of BV and Co-B_i modified BiVO₄ is resulted due to the

improvement in the bulk and surface properties of the photoanodes upon photocharging. The photocurrent in BV is limited by poor surface and bulk charge separation efficiency and fast charge recombination process as given in Table 6.1. Improvement of surface and bulk charge separation efficiency of BV from 57 % to 71 % and 30 % to 37 % respectively upon photocharging result increase in photocurrent. BV/CoB_i has high surface and bulk charge separation efficiency with respect to the BV and as a result of that high photocurrent has been obtained as given in Table 6.1. Photocharging further improves surface and bulk charge separation efficiency. This improvement increases the photocurrent similar order of BV. The onset potential is cathodically shifted for BV, and Co-B_i modified BV from -0.30 V to -0.40 V and -0.35V to -0.50V respectively upon photocharging, which suggests the OER process is thermodynamically more favorable.

To find a correlation in improvements of photocurrents upon photocharging of BiVO₄ and Co-B_i modified BiVO₄, cyclic voltammetry (CV) was performed for photocharged and untreated photoanodes, as shown in Fig. 6.9. It has been reported that the presence of one or more cathodic peaks can be due to surface state of the photoanodes. This cathodic peak is due to the filling of the surface state from the transfer of an electron from the conduction band of the photoanodes during cathodic scan [353-355]. In the dark, the irreversible peak is observed due to the absence of photogenerated holes. This irreversible capacitive peak is attributed to the equilibration of the conduction band and surface state [355]. The redox peak is observed for BV in the dark suggests the absence of surface states. The reversible peak is due to reduction and re-oxidation of V(V) to V(IV) redox system. [92]. The significant improvements in the redox peak after PC is observed. Photogenerated charge contributes to the modification of the redox species which enhanced the redox peak. The new cathodic peak at 0.45 V (vs Ag/AgCl) shows the reduction of the

photogenerated surface state. The CV of BV/Co-B_i-3 in dark shows improved redox peak with the new cathodic peak similar to the photocharged BV suggests the surface state. The improvements in the redox peak are due to the presence of redox process of Co (III) and Co (IV). After photocharging, the redox peak of BV/Co-B_i-3 is further enhanced with significant improvements in the cathodic peak due to the reduction of photocharged product V⁵⁺ to V⁴⁺ and Co (IV) to Co (III). Improvements in the cathodic current suggests formation of more redox active centre during PC, which facilitates the OER and hence improves the photocurrent and PEC efficiency. The decrease in the cathodic peak in repeated CV cycles of BV/Co-B_i-3 photoanode after the PC has been observed as shown in Figure 6.9 (C). The decrease in cathodic current can be visualized for reduction of redox active centre Co(IV) to Co(III).. The formation

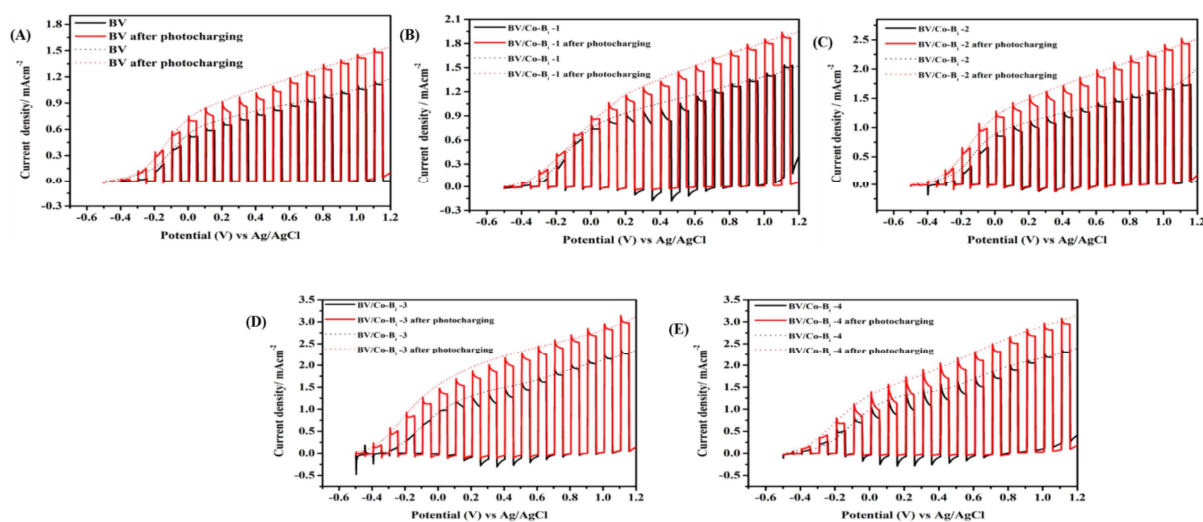


Figure 6.9 The effect of photocharging is characterized by chopped light voltammetry and LSV of (A) BV, (B) BV/Co-B_i-1, (C) BV/Co-B_i-2, (D) BV/Co-B_i-3 and (E) BV/Co-B_i-4. Chopped light voltammetry is shown in a solid line, and LSV is shown in the dotted line.

Table 6.2 Summary of characterization of PEC of photoanodes after photocharging treatment.

Photoanodes	Photocurrent increase (%)	Charge transfer efficiency	Charge transport efficiency	Rct (Ω)	C (F)	Relaxation frequency (Hz)	Relaxation time constant (ms)	L_D (nm)
BV	36 \pm 2	71 \pm 3	37 \pm 2	2560 \pm 120	(5.80 \pm 0.29) $\times 10^{-6}$	54 \pm 3	2.92 \pm 0.15	576 \pm 28
BV/Co-B _i -1	31 \pm 2	74 \pm 3	43 \pm	845 \pm 40	(5.67 \pm 0.28) $\times 10^{-6}$	134 \pm 7	1.18 \pm 0.06	94 \pm 5
BV/Co-B _i -2	42 \pm 2	87 \pm 4	39 \pm 2	500 \pm 25	(5.91 \pm 0.30) $\times 10^{-6}$	158 \pm 8	1.00 \pm 0.05	68 \pm 3
BV/Co-B _i -3	34 \pm 2	91 \pm 4	59 \pm 2	325 \pm 16	(6.49 \pm 0.32) $\times 10^{-6}$	263 \pm 13	0.61 \pm 0.03	25 \pm 1
BV/Co-B _i -4	34 \pm 2	94 \pm 5	55 \pm 2	430 \pm 20	(6.39 \pm 0.32) $\times 10^{-6}$	151 \pm 7	1.05 \pm 0.05	74 \pm 4

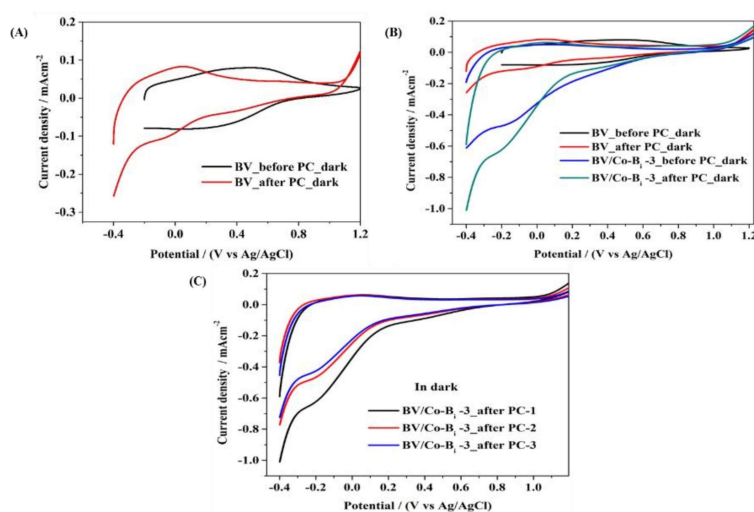


Figure 6.10 (A, B) CV of BV and BV/Co-B_i-3 before and after PC in the dark. (C) Multiple CV cycles of BV/Co-B_i-3 in the dark after PC

of the intermediate active sites during the photocharging process leads to the improvement of overall efficiency of the photoanodes. Photocharging, therefore enhances the number of low oxidation states in the catalytic system, and the effect is observed with BV and more pronounced in BV/Co-Bi catalysts. Under illumination, the holes are utilized for the oxidation of water and the electrons are utilized in lowering of the oxidation state of redox active species of the catalytic system. This reduction process significantly removes the electron and hole recombination process, thus improves the catalytic efficiency. It may further be recalled that during the chopped

light voltammetry experiments as shown in Figure 6.5(A), reduction current is observed at dark and the reduction current reduces to zero before the next illumination. This reduction current arises from the flow of charge from the lowered oxidation state of the catalytic system to the sink of the potentiostat. Observation of the reduction current supports our postulate of the mechanism of PEC process and its improvement due to Co-B_i incorporation and by photocharging. Photocharging is stable for the continuous process. It is reported that PEC activity of photocharged photoanodes can be achieved again by photocharging treatment. The XPS peak positions of Bi 4f, V 2p and Mo 3d shift ~ 0.20 eV towards the lower BE upon the photocharging as shown in the Figure 6.2. This decrease in the BE suggests the lowering of the oxidation states, which arises due to the partial reduction of the V⁵⁺ to V⁴⁺ oxidation state. After the photocharging, BE of O_L is shifted towards the lower BE from 529.50 to 529.18 eV due to partial reduction of the V⁵⁺ to V⁴⁺. The increment in O_V/O_L suggests increase in oxygen vacancy in BV after photocharging. BE of O_L is increased from 529.72 eV to 530.12 eV for BV/Co-B_i-3 after photocharging. The higher BE is expected due to photo-oxidation of Co³⁺ to Co⁴⁺ at electrode surface. Increment in O_V/O_L, with respect to untreated BV/Co-B_i-3 attributed to increase in oxygen vacancy after photocharging. The increase in oxygen vacancy after photocharging improves the bulk charge separation efficiency and conductivity of photoanodes. Therefore, photocurrent has been improved by ~ 35 % after photocharging. Increase in BE of chemisorbed oxygen suggests that water oxidation intermediates or hydroxide as Co(IV) -OH on BV/Co-B_i-3 surface

Further, the insight into the electronic properties of the photoanodes upon photocharging has been investigated by the EIS technique. Figure 6.11 shows the comparative study of the Nyquist plot before and after photocharging. It is reported that the conversion of V⁵⁺ to V⁴⁺ during

photocharging does not alter the bulk property [92]. The decrease in the R_{ct} value upon PC is observed for all the photoanodes. This decrease in R_{ct} from 2677 Ω to 2560 Ω for bare BV after PC suggests the improved bulk and surface conductivity. The improvement of conductivity of photoanodes can be attributed to the oxygen vacancy upon photocharging. Similarly, a significant decrease in the R_{ct} value of photocharged Co-B_i modified BiVO₄ is observed. These results show Co-B_i modification facilitates the fast charge transfer from bulk to the interface and improves interfacial charge transfer. The increase in capacitive current, as shown in Figure 6.10,

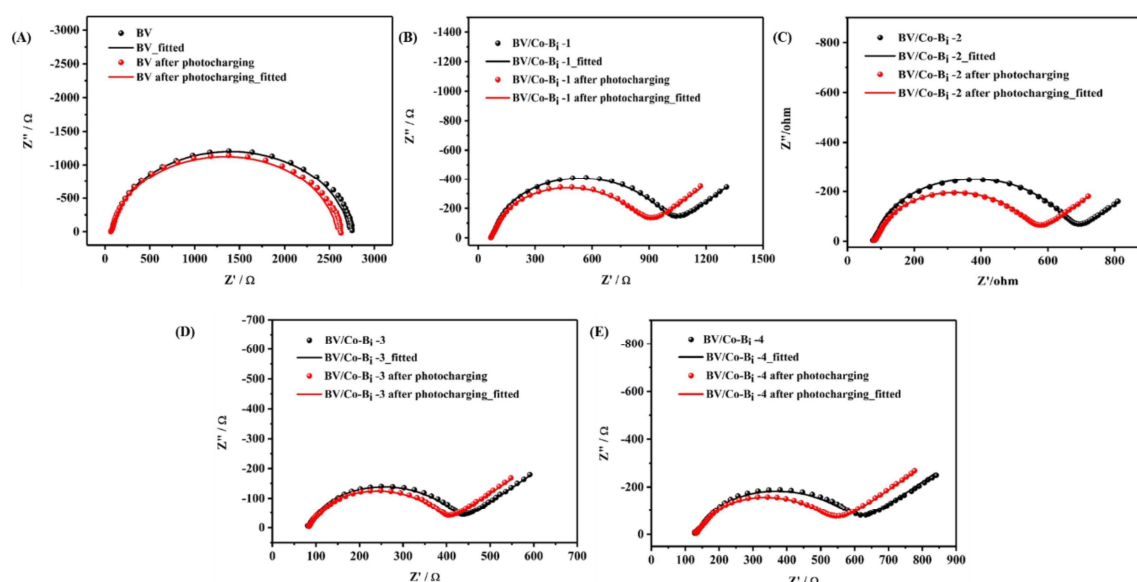


Figure 6.11 Electronic properties of the photoanodes are characterized by the measuring impedance at 0.8V under illumination in the frequency range from 10^5 to 10^{-1} Hz of (A) BV (B) BV/Co-B_i-1, (C) BV/Co-B_i-2, (D) BV/Co-B_i-3 and (E) BV/Co-B_i-4.

suggests surface modification on PC treatment. This improvement in capacitance is due to the formation of the surface layer of adsorption of oxy/hydroxyl intermediated rather than a localized surface trap during photocharging [92]. The surface capacitance acts as the hole reservoir, which improves interfacial charge transfer, and hence photocurrent is enhanced.

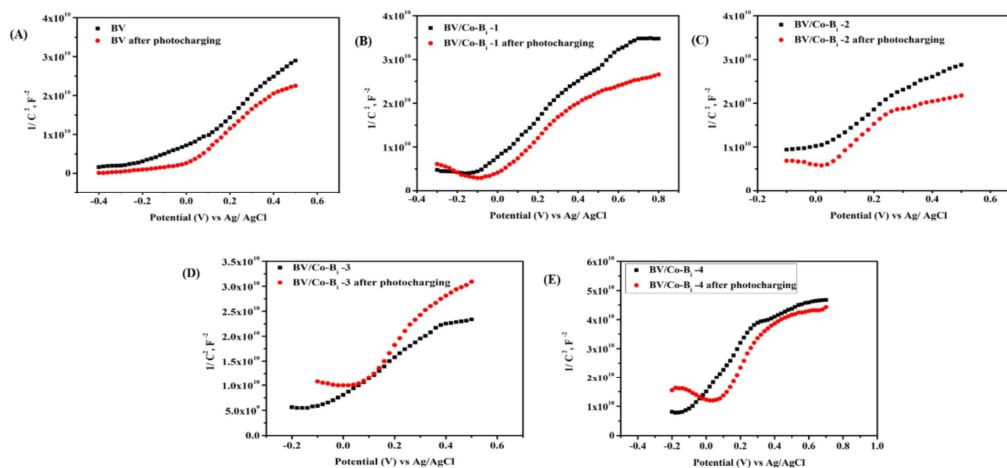


Figure 6.12 Mott-Schottky analysis of photoanodes (A) BV, (B) BV/Co-Bi-1, (C) BV/Co-Bi-2, (D) BV/Co-Bi-3 and (E) BV/Co-Bi-4 at 100Hz.

Relaxation frequency of photogenerated electron-hole is further increased upon photocharging, showing improvements in interfacial kinetics. The τ values is decreased after photocharging suggests improvements in hole transfer kinetics. Photocharging leads to a decrease in the diffusion length (L_D). It is previously stated that L_D calculation is based on the phase angle maxima, and a decrease of L_D reveals a shorter path of photogenerated holes as compared to untreated photoanodes. This observation is expected from the surface modification and storage of holes during the photocharging in the form of intermediate. Among several other factors, pinning of the electronic Fermi levels are also reported on photocharging [92], However, the enhancement of the redox intermediates at the BiVO_4 , which acts as a hole reservoir and minimization of the charge recombination is the reason for the enhancement of the PEC activity. It has also been reported that photocharged product V^{4+} induces the oxygen vacancy on the

surface of BiVO₄, and hence O²⁻ and OH⁻ species strongly absorb on the photoanode surface, which leads to the enhancement in the photocurrent [356].

6.3.6 Investigation of charge transfer by scanning electrochemical microscopy

Scanning electrochemical microscopy SECM has been employed to investigate localized interfacial charge transfer kinetics at the interface before and after the photocharging to quantify the effect of photocharging on photoanodes. Bingaman Zang et al. have demonstrated that photogenerated holes transfer from the valance band of BiVO₄ to the [Fe(CN)₆]⁴⁻ ($\Delta G \sim -2.0$ eV) is thermodynamically more favorable than water oxidation ($\Delta G \sim -1.6$ eV) [33]. Therefore, redox probe [Fe(CN)₆]⁴⁻/ [Fe(CN)₆]³⁻ is used instead of a water oxidation product to investigate the hole transfer kinetics at the interface. Before SECM experiment, UME was characterized in 2 mM ferricyanide solution as shown in Figure 6.13 (A). The UME of size 10 μm and RG 5 has been used for approach curve and SECM imaging. Negative approach curve has been obtained in the dark as shown in Fig. 6.13(B) suggests the insulating behavior of BiVO₄. Positive approach curves have been obtained (Figure 6.14) at different applied substrate potential under illumination, suggesting conducting behavior of BiVO₄ due to photogenerated electron-holes pairs. The photogenerated holes on the BiVO₄ interface oxidizes the ferrocyanide to ferricyanide which gives feedback loop to the probe for reduction of ferricyanide. The kinetic parameter i.e. normalized apparent heterogeneous charge transfer rate constant k has been obtained by fitting approach curves based on theoretical model as discussed in introduction and experimental chapter. The effective heterogeneous hole transfer rate constant ($k_{\text{eff.}}$) for oxidation of ferrocyanide to ferricyanide at the interface is calculated on the basis of normalized apparent heterogeneous charge transfer rate constant k with equation $k_{\text{eff}} = \kappa D_{\text{diffusion}}/r_T$ where $D_{\text{diffusion}}$ is the diffusion coefficient of redox probe and r_T is radius of UME. The k_{eff} is

tabulated in Table 6.3. The k_{eff} of BV at 0.4 V (vs Ag/AgCl) is $7.23 \times 10^{-3} \text{ cm s}^{-1}$ and increased with the applied potential at BiVO_4 substrate [147]. This result shows improvements in the interfacial charge transfer and charge separation efficiency with increase in applied potential. Shen et. al. have shown similar improvement in k_{eff} in BiVO_4 and Mo doped BiVO_4 with increase in applied potential [33]. The increase in applied potential at BiVO_4 change the activation energy by changing of fermi level of photoanodes. Sriram et. al observed similar trend of increment of k_{eff} with different doping concentration of Mo in BiVO_4 and at different applied potential [147]. It has been reported that improvement in interfacial hole transfer kinetics increases the charge separation and suppress the charge recombination process. Similarly, Wittstock and group have found that photoinduced charge transfer rates for water oxidation reaction (WOR) strongly depend on the polarization of BiVO_4 suspended ITIES and has been increased with increase in polarization, which ultimately improves the charge separation process in WOR [334, 335]. There are 33 % improvements in k_{eff} at 0.4 V (vs Ag/AgCl) upon Co- Bi incorporation on the BiVO_4 suggest the enhancement in the interfacial charge transfer. Co- Bi facilitates the hole transfer by capturing holes and transfer to the water molecule for oxidation. The improvements in k_{eff} are in good agreements with the surface charge separation efficiency and bulk charge separation efficiency as given in Table 6.1. Improvement in k_{eff} , further, can be supported by improvement in decrease in charge transfer resistance upon Co- Bi incorporation. The R_{ct} value was decreased from 2677 Ω to 354 Ω in BV/Co- Bi -3 as compared to BV. Enhancement in k_{eff} after Co- Bi modification can be correlated with the increase in the relaxation frequency of charge transfer from 54 Hz to 229 Hz. k_{eff} has been improved with increase in the polarization at the BV/Co- Bi -3 similar to the BV. Interfacial charge transfer kinetics is, further, investigated to quantify the improvements in the PEC efficiency in BV and Co- Bi modified BV

upon photocharging. The improvements in k_{eff} at 0.4 V (vs Ag/AgCl) have been observed from 7.23×10^{-3} to 9.05×10^{-3} cm s^{-1} and 9.61×10^{-3} to 11.76×10^{-3} cm s^{-1} after photocharging of BV and BV/Co-Bi-3 respectively. The improvement in charge transfer kinetics can be attributed to the improvement in surface charge transfer efficiency and bulk charge transfer efficiency upon photocharging as tabulated in Table 6.2. The decrease in R_{ct} of BV and BV/Co-Bi-3 photoanodes upon photocharging in further supports improvement in k_{eff} . The XPS results also support improvement of bulk and surface properties of photoanodes upon photocharging due to oxygen vacancy and hence ultimately improved k_{eff} . Further, k_{eff} has been improved with increase in substrate polarization after photocharging. Figure 6.14 shows the logarithm increase of k_{eff} with overpotential. According to Butler-Volmer equation, charge transfer rate constant is exponentially depended on the overpotential. Therefore, apparent standard hole transfer rate constant (k_{h+}^0) can be calculated using Butler-Volmer equation [332]. From the intercept of plot of Fig. 10, k_{h+}^0 has been calculated. The k_{h+}^0 of BV is found 6.30×10^{-3} cm s^{-1} and improved by 44 % upon Co-Bi incorporation. These results show BV/Co-Bi-3 has much large hole transfer rate as compared to BV. Further, k_{h+}^0 has been improved by 21 % and 13 % of BV and BV/Co-Bi-3 respectively upon photocharging. Similarly, Wittstock and his group have shown increase in apparent standard heterogeneous electron transfer rate constant (k_{e-}^0) with increase in polarization of the BiVO₄ dispersed ITIES [334, 335]. Shen et. al. have observed similar improvement of k_{h+}^0 in BiVO₄ upon Mo doping [33].

The localized PEC activity of the photoanodes have been investigated by SECM imaging in feedback mode [337-341, 357]. In-situ imaging of photocatalytic activity of BiVO₄ photoanode and effect of Co-Bi modification of BiVO₄ have been monitored using redox couple

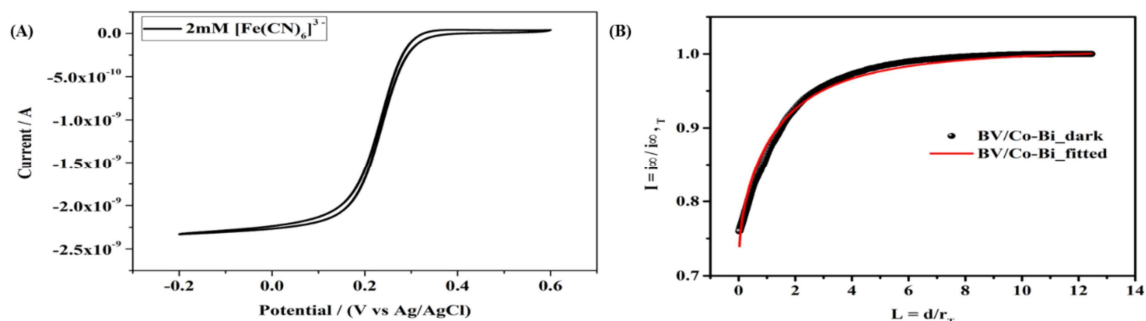


Figure 6.13 (A) CV of Pt UME in 2 mM $[\text{Fe}(\text{CN})_6]^{3-}$ solution at 50 mV s⁻¹ and (B) approach curve of Pt UME in 2 mM $[\text{Fe}(\text{CN})_6]^{3-}$ a solution towards BV/Co-Bi-3 in the dark.

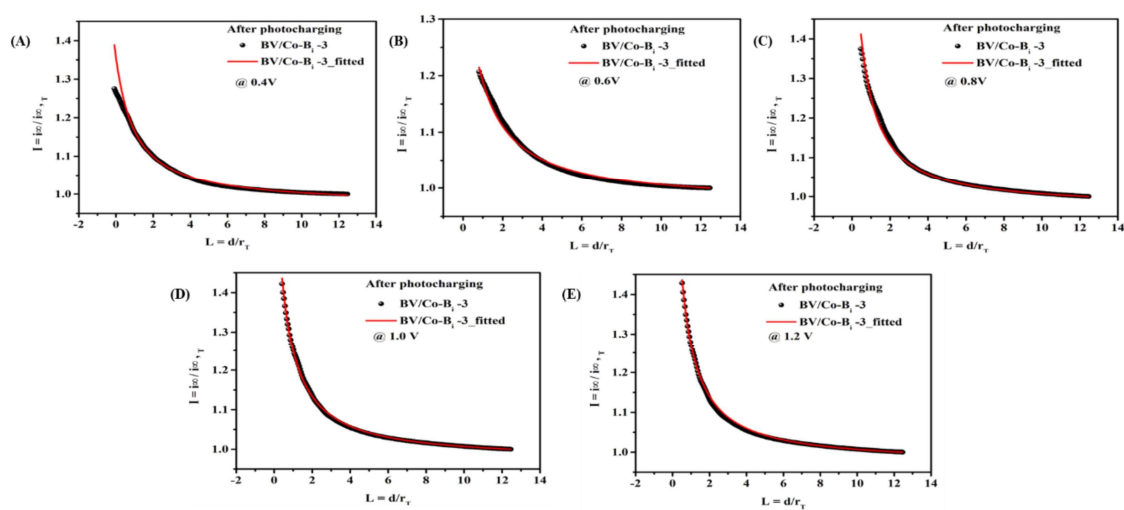


Figure. 6.14 Normalized feedback approach curves for Pt ultramicroelectrode (UME) towards BV/Co-Bi-3 under illumination using 2mM $[\text{Fe}(\text{CN})_6]^{3-}$ redox probe at various substrate potential with approach rate is 0.1 $\mu\text{m s}^{-1}$.

Table 6.3 Interfacial charge transfer kinetics is measured by the SECM feedback approach curve analysis

Potential, V	$K_{\text{eff}} (10^{-3} \text{ cm s}^{-1})$			
	BV	BV after photocharging	BV/Co-Bi-3	BV/Co-Bi-3 after photocharging
0.4	7.23 ± 0.55	9.05 ± 0.45	9.61 ± 0.48	11.76 ± 0.82
0.6	7.61 ± 0.53	9.98 ± 0.50	12.04 ± 0.60	13.95 ± 0.97
0.8	8.02 ± 0.56	11.70 ± 0.58	13.16 ± 0.66	21.85 ± 1.53
1.0	9.63 ± 0.67	15.31 ± 0.76	14.55 ± 0.73	21.87 ± 1.53
1.2	11.14 ± 0.78	16.92 ± 0.85	16.11 ± 0.81	25.50 ± 1.78

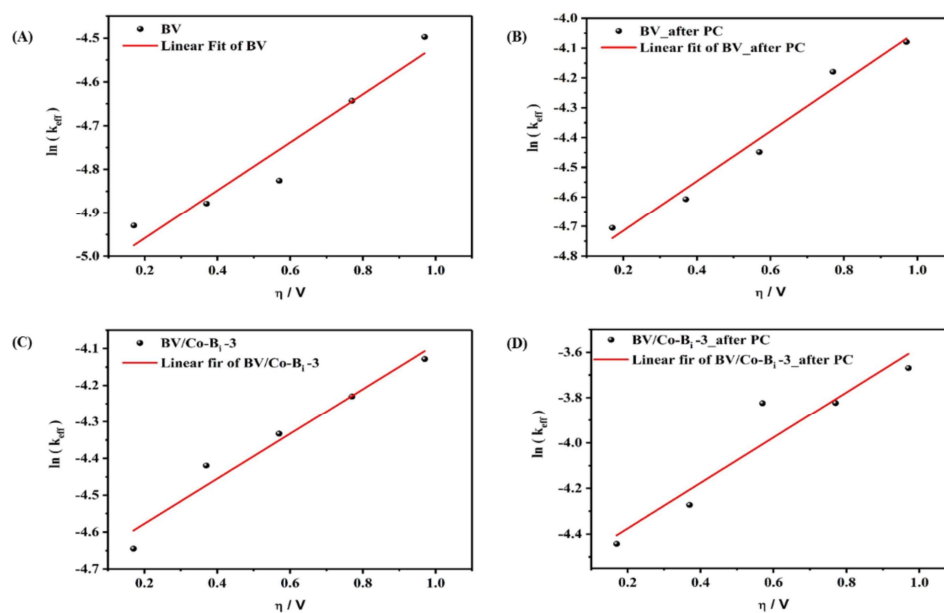


Figure 6.15 Plots of $\ln(k_{\text{eff}})$ vs. η of photoanodes (A) BV, (C) BV/Co-Bi-3 before photocharging, and (B) and (D) are after photocharging.

in feedback mode. The feedback current response of BV has been increased with the increase in applied substrate potential. The increase in photocurrent suggests improved interfacial hole transfer rate constant. Since RMS height of photoanodes surface BV and BV/Co-B_i-3 from AFM analysis was calculated as 41 ± 5 nm and SECM was performed at 50 μ m above the photoanode surface after the tilt correction. The average roughness distribution of photoanodes measured by approach curve was ± 5 μ m. Therefore, the localized high current response corresponds to the higher surface PEC activity of the photoanode. The increase in photocurrent with polarization supports the chopped light voltammetry experiment. At high polarization, there is improved charge separation and hence high feedback current has been observed. Similarly, Mo and W doped BiVO₄ has shown high feedback current for WOR, which corresponds to the high localized photocatalytic activity of photoanodes [357]. Lopes and his group have shown the high feedback current for WOR for pristine SrTiO₃ with respect to defected SrTiO₃ surface [338]. Markin et.al. have used nanoscale SECM probe for mapping of Nb:TiO₂ for OER. It has reported the uniform distribution of Nb over TiO₂ by measuring feedback current [339]. Similarly, Jiang group has mapped localized activity of TiO₂ for Rhodamine B (RhB) oxidation in terms of adsorbed oxidation product RhB 123 [340]. Further, after incorporation of Co-B_i on the BV, photocurrent has been increased with respect to BV as shown in Fig. 10. The increment in photocurrent can be attributed to the improvement of photocatalytic activity. This improvement can be due to increase in k_{h+}^0 after Co-B_i incorporation, which further supported with the chopped light voltammetry, EIS study, relaxation frequency of photogenerated charge and surface charge separation efficiency. Chen and his group have reported similar improvement in photocurrent upon BiVO₄ modification with OEC FeOOH [358]. It has been reported that localized photocatalytic activity of CuWO₄/BiVO₄/FeOOH reflects the local area.

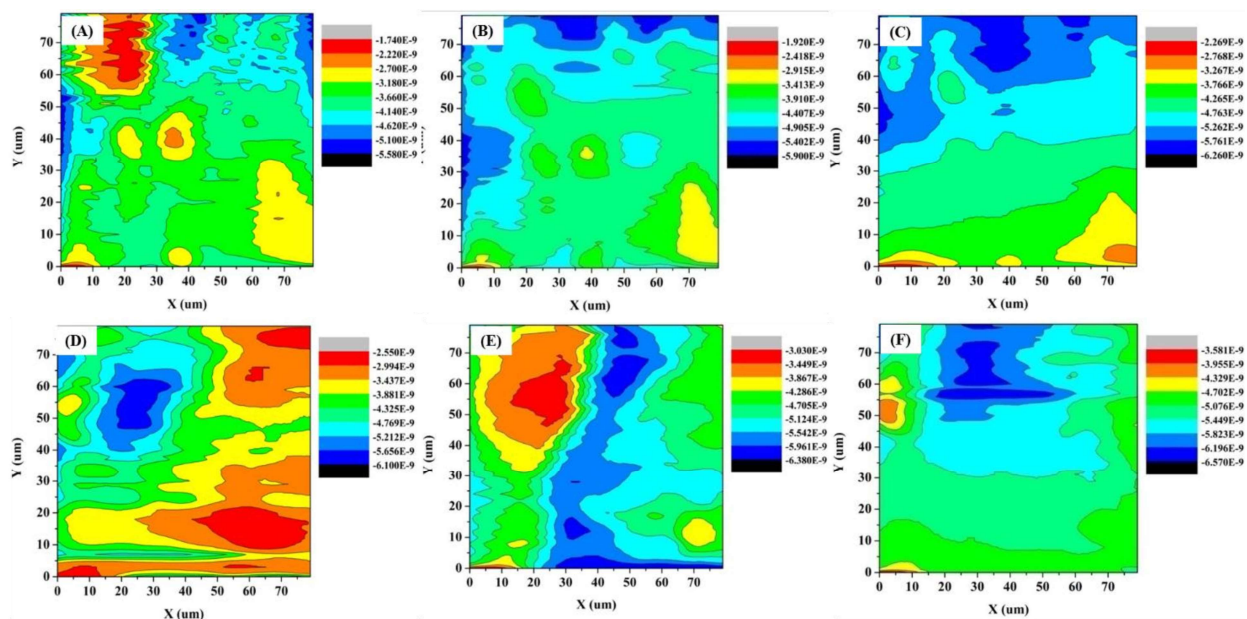


Figure 6.16 SECM imaging of photoanodes by measuring probe current in feedback mode at constant height using Pt UME in 2mM $[\text{Fe}(\text{CN})_6]^{3-}$ at various substrate potentials. SECM images of BV/Co-Bi-3 at (A) 0.4V, (B) 0.6V and (C) 0.8 V and BV/Co-Bi-3 after PC at (D) 0.4 V, (E) 0.6 V and (F) 0.8 V.

Further, photocharging effect on photocatalytic activity of BV and BV/Co-Bi-3 has been investigated by mapping of photoanodes as shown in Figure 6.15. The increased localized photocurrent of BV and BV/Co-Bi-3 after photocharging suggests improvement in the localized photocatalytic activity due to efficient hole transfer at the interface as k_{h+}^0 has been increased upon photocharging. Similarly, Lopes et. al. have reported the localized photoactivity of SrTiO_3 has been improved by 2.6 folds after electrochemical activation [337]. It has been reported that electrochemical activation causes the oxygen deficiency at the surface of SrTiO_3 . These results are further supported by improvement in surface and bulk charge separation efficiency, decrease in R_{ct} and oxygen vacancy in photoanodes as reported in previous section. The improvements in the feedback photocurrent upon the photocharging can be due to increase in the surface redox

state as shown in Figure 6.7. The redox surface state improves the surface catalytic activity and improves interfacial charge transfer kinetics.

6.4 Conclusion

In this chapter the significant improvements in the photocurrent upon the incorporation of the Co-B_i as an oxygen evolution catalyst on BiVO₄ has been demonstrated. The Co-B_i incorporation leads to an improvement of 103% photocurrent. The cathodically shifted onset potential shows the thermodynamically favorable OER. The increase in photovoltage suggests an absence of the surface state. The impedance data suggests the change in the kinetics of photogenerated charge upon Co-B_i incorporation from the kinetic control process to the diffusion control process. This result shows surface kinetics is no longer a limiting step. The decrease in the R_{ct} reveals the improvements in the bulk and surface conductivity, which leads to improvements in the photocurrent. The cathodic shift of the Fermi level is in agreement with the shift of onset potential.

The photocharging treatment of BV and Co-B_i modified BV enhances the photocurrent from 0.96 mAcm⁻² to 1.31 mAcm⁻² (36%) and from 1.95 mA cm⁻² to 2.63 mAcm⁻² (35%) for BV and BV/Co-B_i-3 respectively. The onset potential of PEC water oxidation is shifted cathodically further upon photocharging, suggesting favorable thermodynamic process. The increment in photovoltage reveals the improvements in the charge separation upon the photocharging. Impedance analysis shows improvement in the bulk and surface conductivity and enhanced the surface capacitance upon photocharging. The improvement in the interfacial hole transfer kinetics from 7.23×10⁻³ to 9.61×10⁻³ obtained for Co-B_i incorporation in BV. Further, the

interfacial hole transfer kinetics of BV and BV/Co-Bi₃ have been increased from 7.23×10^{-3} to 9.05×10^{-3} cm s⁻¹ and 9.61×10^{-3} to 11.76×10^{-3} cm s⁻¹ respectively upon photocharging. The SECM mapping of the interface reflects the localized photoelectrochemical activity of photoanodes.

Overall, our investigation in this chapter suggests that incorporation of Co-Bi₃ to the BiVO₄ enhances the photocurrent and improves the PEC efficiency due to the improvements in the bulk and surface improvements. Photocharging treatment further enhances the photocurrent and improves the PEC efficiency by alteration of bulk and surface electronic properties of the catalysts material. Therefore, this study shows the path of improvements of photoanode and OEC incorporated photoanode performance which is probed well using SECM measurements.

Chapter 7 Improvements in the photo-electrocatalysis of BiVO_4 by gamma irradiation and plasma treatment

7.1 Introduction

After the discussion about the development of the BiVO_4 based materials and its modification using the formation of interlayer and through various doping in the previous chapters, present chapter is focused on the modification of BiVO_4 using gamma radiation and plasma treatment to improve the catalytic performance of the material further. The gamma radiation has been used to alter the physical and chemical properties of materials such as optical, electrical, electronic and structural properties of the materials [137, 138]. The gamma radiation is used because of its high penetration power as compared to the other ionizing radiation and it does not induce the material to become radioactive. The alteration of chemical bonds due to the irradiation may improve the performance of materials. The grain size and bandgap of the ZnO thin film have been decreased upon the gamma irradiation [137]. The electron mobility of the In-ZnO based transistor has been improved upon exposure to the radiation [142]. Gamma radiation strongly affects the metal based oxide materials for the biosensor and gas sensor application [139-141]. The enhancement of the gas sensing sensitivity is due to the defect generation of the nanoparticles. The sensitivity of the SnO_2 based gas sensor for CO is improved upon the gamma irradiation [143]. There is red-shift of absorption of the InVO_4 with increase in the dose of gamma irradiation [144]. The sensitivity of InVO_4 based sensor for ammonia is improved significantly and is due to the defect introduction. The performance of TeO_2 has been linearly improved with the increase of γ

radiation dose. The gamma effect on the absorption spectra and energy bandgap of SeO_2 were reported to significantly increase the optical absorption due to change of chemical structure. The structural and optical properties of CdS, PbS, $\text{Fe}_{3-x}\text{O}_4$ thin film were also reported to improve the bandgap [145]. Gamma radiation has changed the bonding structure of g- C_3N_4 which reduces the optical bandgap energy. The PEC efficiency of irradiated g- C_3N_4 is enhanced two folds as compared to the non-irradiated g- C_3N_4 . The performance of irradiated g- C_3N_4 in the g- $\text{C}_3\text{N}_4/\text{BiVO}_4$ heterojunction has been improved by two folds [146]. Considering the previous reports present chapter is focused on the effect of the high dose of gamma radiation on the photo electrochemical performance of the BiVO_4 (BV) and cobalt borate (Co-Bi) modified BV. The significant improvement in photocurrent ($\sim 93\%$) at 0.8 V upon Co-Bi incorporation, which plays as a hole collector and facilitates as hole reservoir. The gamma radiation treatment leads to improve photocurrent of the BV and BV/Co-Bi. Mott-Schottky analysis and impedance analysis suggest a change in the bulk and surface properties upon gamma radiation treatment.

7.2 Experimental Section

7.2.1 Materials

Bismuth (III) Nitrate ($\text{Bi}(\text{NO}_3)_3 \cdot 5\text{H}_2\text{O}$, 98%), Ammonium Vanadate (NH_4VO_4 , >99%), Cobalt (II) nitrate ($\text{Co}(\text{NO}_3)_2 \cdot 6\text{H}_2\text{O}$, 98%) and Sodium sulfite (Na_2SO_3 , 98%) were purchased from Sigma Aldrich. Ammonium tetrathiomolybdate ($(\text{NH}_4)_2\text{MoS}_4$, 99.95%) was purchased from Alfa Aesar. Sodium Sulphate (Na_2SO_4), sodium monohydrogen phosphate (Na_2HPO_4) and sodium dihydrogen phosphate (NaH_2PO_4) were obtained from Sarabhai M Chemicals. Boric acid, sodium hydroxide, ethylene glycol and potassium ferricyanide were purchased from SDFCL.

7.2.2 *Fabrication of Photoanode*

BiVO₄ film was coated on cleaned FTO using spin coating technique. In this typical synthesis procedure, Bi (NO₃)₃·5H₂O (0.2 mmol) was dissolved in 5 mL of ethylene glycol-water mixture (8:2) and then NH₄VO₃ (0.2 mmol) was added slowly and then added 5 atom percentage of Mo using precursor ((NH₄)₂MoS₄, 99.95%) followed by sonication for 30 min and kept on stirring for overnight at room temperature. The reaction mixture (100 μL) was spin coated on FTO substrate at 2000 rpm for 1 min followed by annealing at 350 °C on hot plate for 5 min. The coating was repeated for 10 times to achieve desired thickness for maximum PEC efficiency followed by annealing at 500 °C in tube furnace for 3 h at ramp of 5 °C per min.

Cobalt borate (Co-B_i) was deposited on the BiVO₄ by photo-assisted electrochemical method [121, 126, 129, 342]. In this typical method, 2 mM cobalt (II) nitrate solution was prepared in 0.1 M borate buffer solution (BBS) of pH 8. Deposition of Co-B_i at FTO/BiVO₄ was performed in three electrodes system where substrate as working electrode, Ag/AgCl as reference electrode and Pt wire as counter electrode. Before deposition of Co-B_i, LSV was performed from OCP to 0.5V in 1 Sun illumination. Then, Co-B_i was photo-electrochemically deposited at 0.1V potential for same charge. Prior to the deposition of Co-B_i, BiVO₄ surface was activated by performing LSV in 0.1 M Na₂SO₃ solution for 20 cycles assuming that oxidation kinetics of sacrificial agent would be very fast and hence photoanode would not be affected.

After that, BiVO₄ and Co-B_i modified BiVO₄ were irradiated using gamma radiation for 50 kGy and 100 kGy dose. The samples are abbreviated as BV, BV-50 kGy, BV-100 kGy, BV/Co-B_i, BV/Co-B_i-50 kGy and BV/Co-B_i-100 kGy where BV is BiVO₄ and Co-B_i is cobalt borate and dose is in kGy.

7.2.3 Photoelectrochemical (PEC) measurements

Photoelectrochemical measurements were carried out with CH Instrument (920 D model) using a three electrode cell with an Ag/AgCl (3.0 M KCl) as reference electrode, Pt rod as counter and FTO/BiVO₄ and FTO/BiVO₄-Co-Bi as working electrode in 0.1 M BBS of pH 8 as electrolyte. All PEC experiments were performed in back illumination of photoanodes under 1 Sun light of Solar simulator fitted with AM 1.5G filter. Photocurrent was measured by linear sweep voltammetry (LSV) technique at 10 mVs⁻¹ scan rate and chopped light voltammetry was recorded at 5 mVs⁻¹ scan rate with chopping of light at 5 s interval.

Electrochemical Impedance Spectroscopy (EIS) was recorded at 0.8 V (vs Ag/AgCl) by applying sinusoidal wave of amplitude 10 mV in frequency range from 10⁵ to 10⁻¹ Hz under 1 sun illumination. Further, Relaxation frequency and time constant of electron and hole were measured from EIS data to quantify the efficiency of photoanode materials.

7.2.4 Characterization

XRD analysis of prepared samples were performed by using a Philips powder diffractometer (PW3040/60) with Cu K_α radiation ($\lambda = 1.5406 \text{ \AA}$). Raman spectra of photoanodes were recorded by using Lab RAM HR 800 Micro laser Raman system with an Ar⁺ laser of 516 nm. The morphology of photoanode materials was examined by field emission scanning electron microscopy (FE-SEM, JEOL model JSM-7600F). X-ray photoelectron spectroscopy (XPS, MULTILAB, VG Scientific, Al K_α radiation as monochromator) was used to investigate the binding energy of the photoanodes.

7.3 Result and discussion

7.3.1 Material characterization

All photoanodes were characterized by XRD technique and results are shown in Figure 7.1 (A). XRD peaks at 2θ values of 18.37° , 28.40° , 30.07° , 39.56° , 42.02° , 46.89° and 52.90° correspond to (011), (121), (040), (-112), (051), (042) and (161) respectively of monoclinic phase (JCPDS 014-0688) of BiVO_4 . The XRD peaks at 26.02° , 37.40° , 61.33° and 65.34° are due to FTO (JCPDS 41-1445). The relatively strong peak at 28.40° is attributed to the preferential growth of BiVO_4 films along (121) direction. There is positive shift ($\sim 0.35^\circ$) of peak position upon gamma irradiation of BV, suggests decrease in the grain size or lattice parameter upon gamma irradiation. The peak position at 34.50° , 35° , 47.21° , 50.07° , 54.42° and 59.25° have been observed for the gamma irradiated BiVO_4 . These new peaks suggest the defect of the BV lattice. Upon Co-Bi modification, small positive shift of XRD peak is observed for BV. However, a low intensity peak at 26.05° is observed due to the (210) of Co-Bi (JCPDS: 13-0305). On further, gamma irradiation of the Co-Bi modified BV leads to the shift of peak position towards the higher theta value, suggesting the decrease in the inner planer distance. Crystallinity of the BV and Co-Bi modified BV upon gamma irradiation is observed as suggested by the sharp XRD peak. It has been reported that gamma treatment improves the crystallinity which can be attributed to the densification due to localized heating during gamma irradiation. The crystallite size was calculated using Scherrer equation for BV at 28.40° of (121) plane as follows

$$D = \frac{k \lambda}{\beta \cos\theta} \quad (7.1)$$

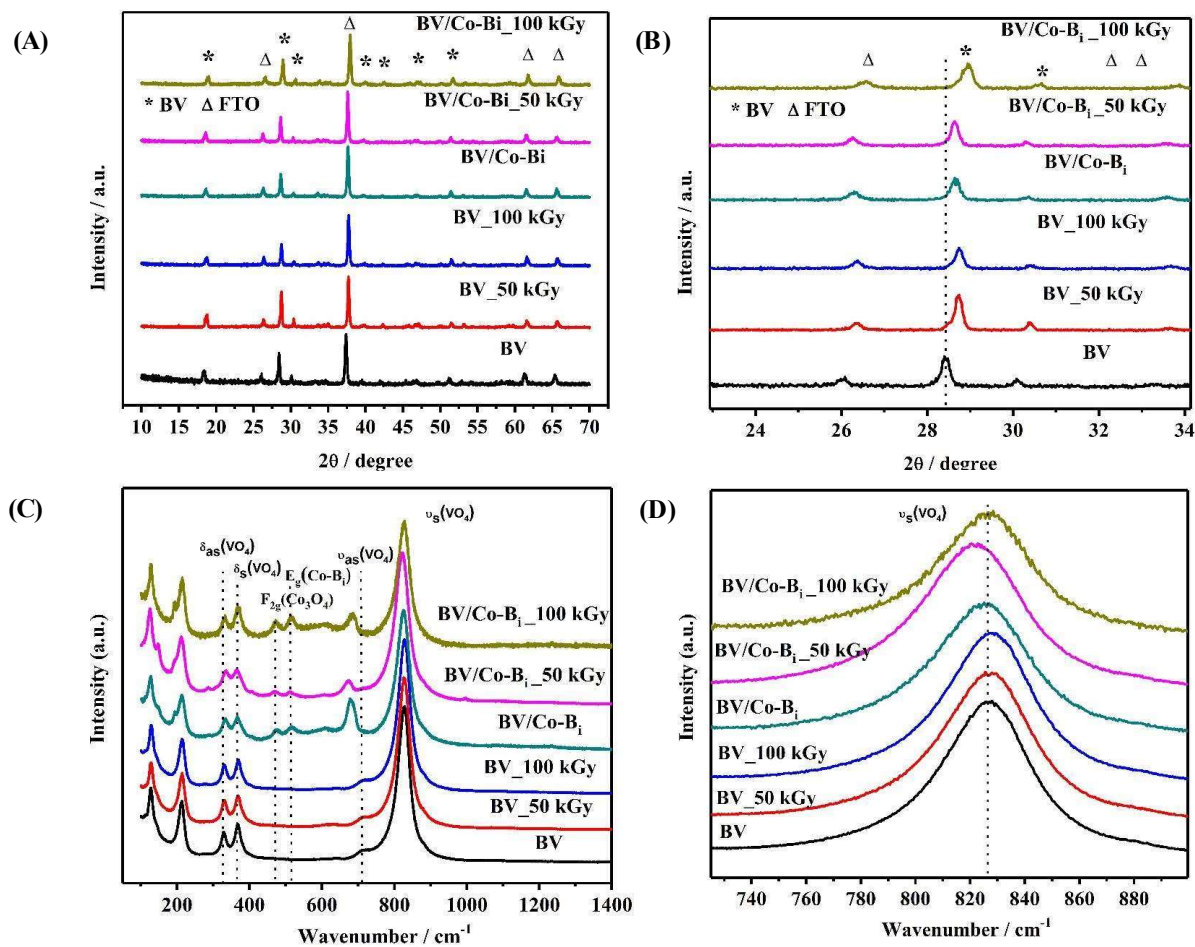


Figure 7.1 (A, B) XRD pattern and (C, D) Raman spectra of BV and Co-B_i modified BV with gamma irradiation.

Where D is the approximate size, which may be smaller or equal to the grain size, k (~ 0.94) is dimensionless shape factor, λ (1.54\AA) is wavelength of the X-ray radiation, β is the FWHM and θ is diffraction angle. The crystallite size of BV is obtained as 53.54 nm and decrease with the gamma irradiation from 53.54 nm to 45.16 nm. The crystallite size of Co-B_i modified BV is found as 38.96 nm which is smaller than BV. Gamma irradiation further leads to decrease of crystallite size of the Co-B_i modified BV.

Investigation of the crystallization, local structure and electronic properties of BV based photoanodes were performed by Raman spectroscopy analysis. Figure 7.1 (C, D) shows the characteristic Raman spectra of the photoanodes. The typical Raman bands of BV are observed at 826.34, 713.45, 367.14, 328.83, 212.64 and 126.94 cm^{-1} . The strong band at 826.34 cm^{-1} and weak shoulder like peak at 713.45 cm^{-1} are assigned to the $\nu_s(\text{VO}_4)$ (A_g) and $\nu_{as}(\text{VO}_4)$ (B_g) mode respectively of BV. The Raman band at 367.14 and 328.83 cm^{-1} are due to the $\delta_s(\text{VO}_4)$ (B_g) and $\delta_{as}(\text{VO}_4)$ (A_g) mode of vibration respectively. The rotational and translational modes (external modes) are observed at 212.64 cm^{-1} and 126.94 cm^{-1} respectively at lower frequencies than the internal modes of VO_4^{3-} [292-297]. The blue shift of vibrational frequency upon gamma irradiation suggests decrease in the crystallite size, which confirms by the XRD analysis. Co-B_i incorporation in BV leads to the decrease in the peak position of $\nu_s(\text{VO}_4)$ (A_g) mode of vibration from 826.34 to 826.05 cm^{-1} . There is abnormal shift of the peak position of Co-B_i modified BV at 50 kGy radiation dose suggesting the decrease in the lattice parameters. Further, treatment of the gamma irradiation, vibration frequency is obtained as BV/Co-B_i samples. The Raman bands at 518.46 and 613.08 cm^{-1} correspond to the vibration of Co-O-Co (E_g) and Co-O (A_{1g}) confirm Co-B_i deposition on the BV. Gamma irradiation of does 50 kGy leads to the decrease in the red shift of the vibrational frequency, however, 100 kGy leads to the blue shift of the vibration. The V-O bond length is calculated at the most intense peak of the BV using following equation [297].

$$\nu(\text{cm}^{-1}) = 21349 \exp(-1.9176R(A^\circ)) \quad (7.2)$$

Where, ν is the Raman stretching frequency for V-O in cm^{-1} and R is the bond length in A° . The V-O length of BV is 169.53 pm which decreased to 169.44 pm and 169.49 pm for BV-50 kGy and BV-100 kGy irradiation. These results suggest the decrease in the lattice parameters as

obtained from the XRD analysis. Further, Co-B_i incorporation leads to the increase in the V-O length from 169.53 pm to 169.62 pm. The gamma irradiation causes the increase in the V-O length from 169.62 pm to 169.87 pm for the 50 kGy dose and then decrease to the 169.52 pm for 100 kGy dose.

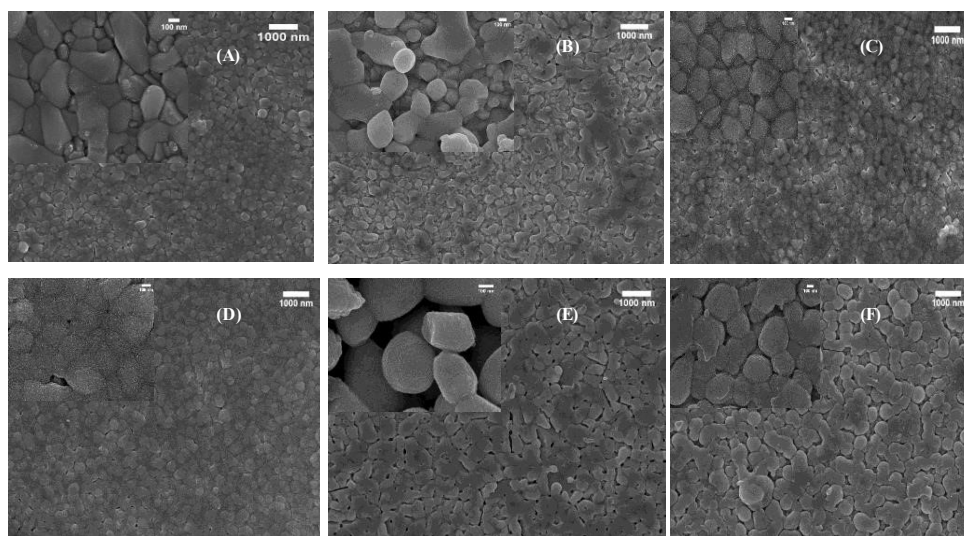


Figure 7.2 SEM images of (A) BV, (B) BV_50 kGy, (C) BV_100 kGy, (D) BV/Co-B_i, (E) BV/Co-B_i_50kGy and (F) BV/Co-B_i_100 kGy

Scanning electron microscopy is used to study effect of gamma irradiation on the morphology of BV and Co-B_i modified BV as shown in Figure 7.2. Figure 7.2 (A) shows the uniform coating of BiVO₄ on FTO and inset Figure shows granular shape of BiVO₄. Figure 7.2 (B) and (C) show the change of the morphology of BiVO₄ upon the gamma irradiation. Images reveal that there is microstructure change of the BiVO₄ and improvement of crystallinity upon the gamma irradiation. The spherical and uniform deposition of Co-B_i is observed on the BiVO₄ interface as shown in Figure 7.2 (D). There is significant change of surface morphology of the Co-B_i

modified BiVO_4 as shown in Figure 7.2 (E) and (F). The change of the microstructure and crystallinity of BiVO_4 and Co- Bi modified BiVO_4 have been observed as supported by the XRD data. Further, atomic force microscopy (AFM) is used to characterize the morphology of photoanodes. Figure 7.3 (A) shows the uniform coating of BiVO_4 on FTO. The gamma irradiation dose of 50 kGy and 100 kGy significantly changes the morphology of the BiVO_4 as shown in the Figure 7.3 (B) and (C). The granular deposition of Co- Bi is observed on the BiVO_4 as shown in the Figure 7.3 (D) which supports the SEM analysis.

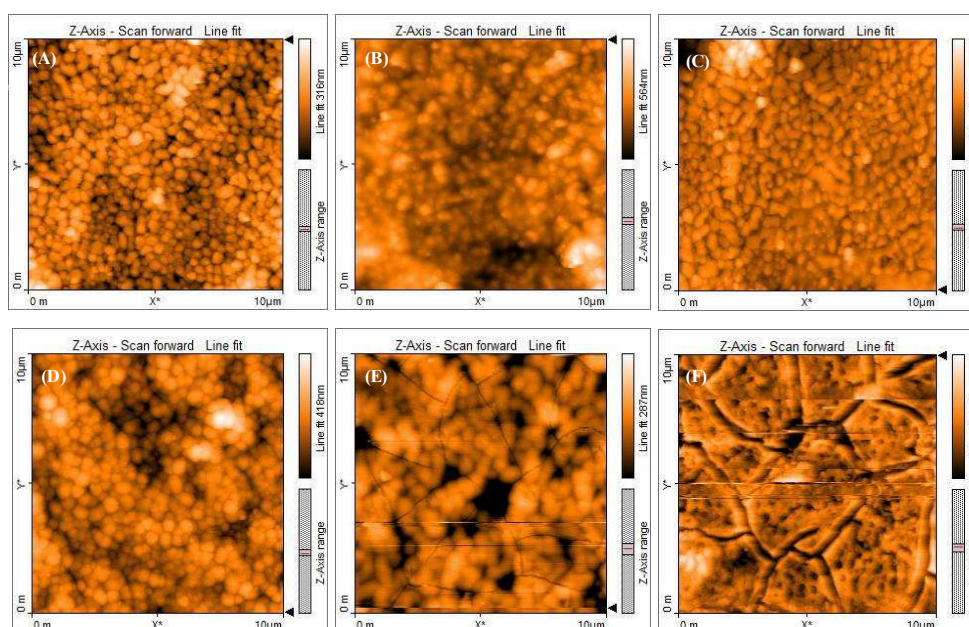


Figure 7.3 AFM images of (A) BV, (B) BV-50 kGy, (C) BV-100 kGy, (D) BV/Co- Bi , (E) BV/Co- Bi -50kGy and (F) BV/Co- Bi -100 kGy

The porosity of BV/Co- Bi is significantly improved upon the 50 kGy radiation dose. Further increase in the radiation dose results the cracking of the interfacial Co- Bi coating as shown in Figure 7.3 (F). Elemental analysis was carried out by Energy dispersive spectroscopy (EDS) as shown in **Figure 7.4** and. In BV, atomic ratio of Bi and V is found as 1:1. The decrease in the Bi,

V and Mo is due to top Co-B_i layer. The ~ 5% atomic percentage of Co shows the successful incorporation of Co-B_i heterojunction. The gamma irradiation reveals the decrease of the atomic constituent elements of the BiVO₄ and the Co-B_i modified BiVO₄. The thickness of BiVO₄ and Co-B_i modified BiVO₄ are obtained as 650 nm and 775 nm as shown in Figure 7.5.

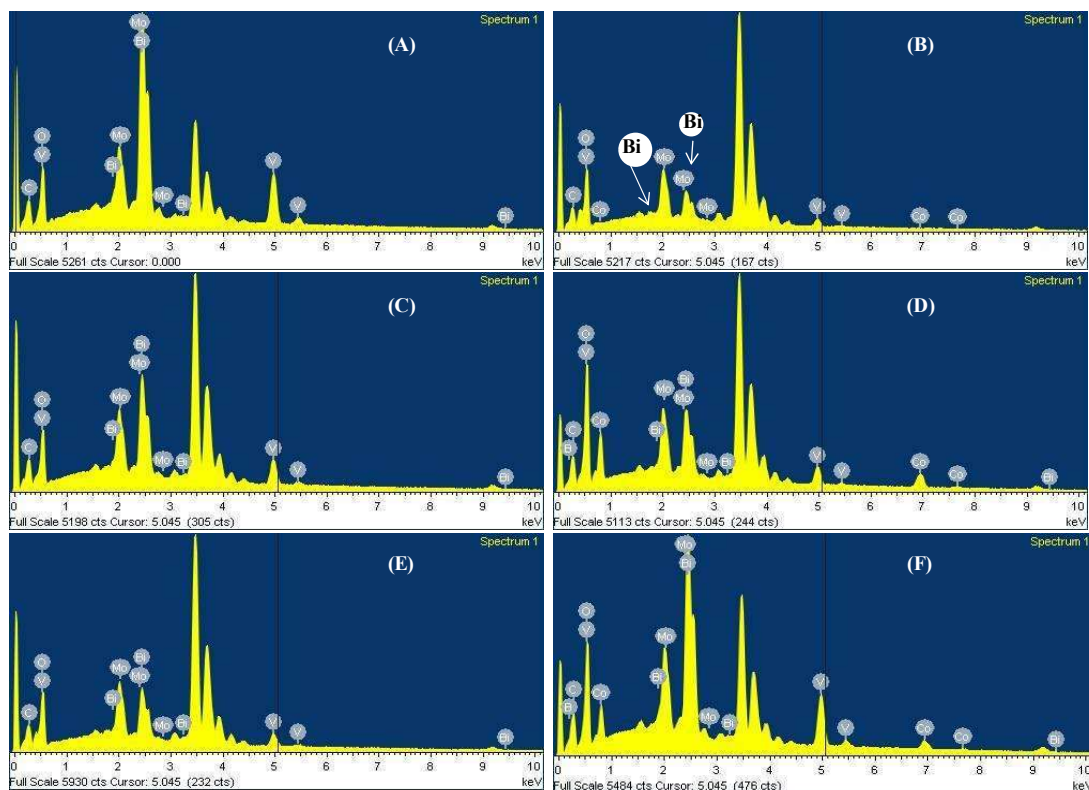


Figure 7.4 EDS images of (A) BV, (B) BV-50 kGy, (C) BV-100 kGy, (D) BV/Co-B_i, (E) BV/Co-B_i-50kGy and (F) BV/Co-B_i-100 kGy.

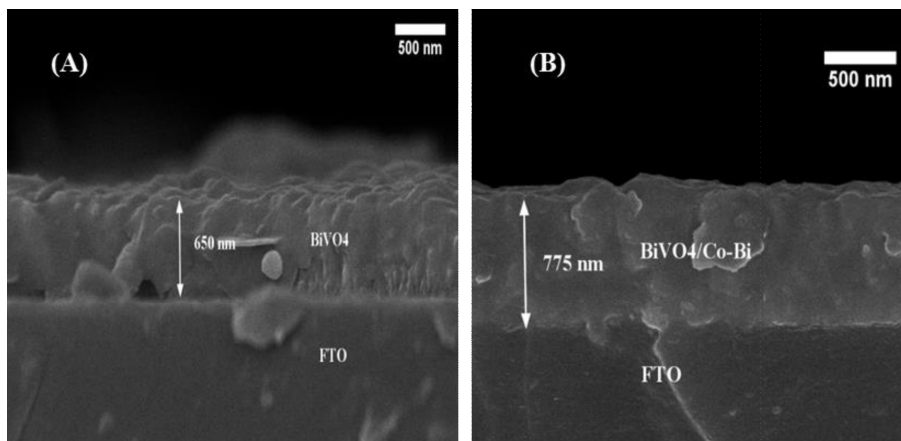


Figure 7.5 Cross-sectional view of the photoanodes (A) BV and (B) BV/Co-Bi.

7.3.2 UV-Vis spectroscopy

The electronic property of the BiVO_4 based photoanodes were characterized by the absorption spectroscopy measurements as shown in Figure 7.6 (A). UV-vis diffuse reflectance spectra were used to characterize the photoanodes. The BV shows the major absorption peaks at 474 nm due to transition in BiVO_4 . Gamma irradiation doses cause the red shift of absorption of BV. The new peak at 431 nm is due to the distortion of the BV lattice. The onset potential of the BV is at 696 nm which further shifts to the higher wavelength due to the gamma irradiation. Absorption is found to increase with the gamma irradiation which suggests improvement of the solar energy harvesting. Co-Bi incorporation leads to the improvement of the absorption and onset absorption in infrared region. The peaks position at 366 and 400 nm are due to the BV. The peak at 422 nm which is relatively at lower wavelength and 491 nm at the higher wavelength than BV are obtained for the Co-Bi modification. Upon gamma irradiation of the Co-Bi modified BV, the absorption peaks are blue shifted with respect to the BV/ Co-Bi . Co-Bi modification and gamma irradiation improve the absorption which enhances the photo-absorption efficiency and

hence efficiency of the PEC will increase. These observations show synergic effect of the Co-B_i and gamma irradiation on the PEC water splitting of the BV.

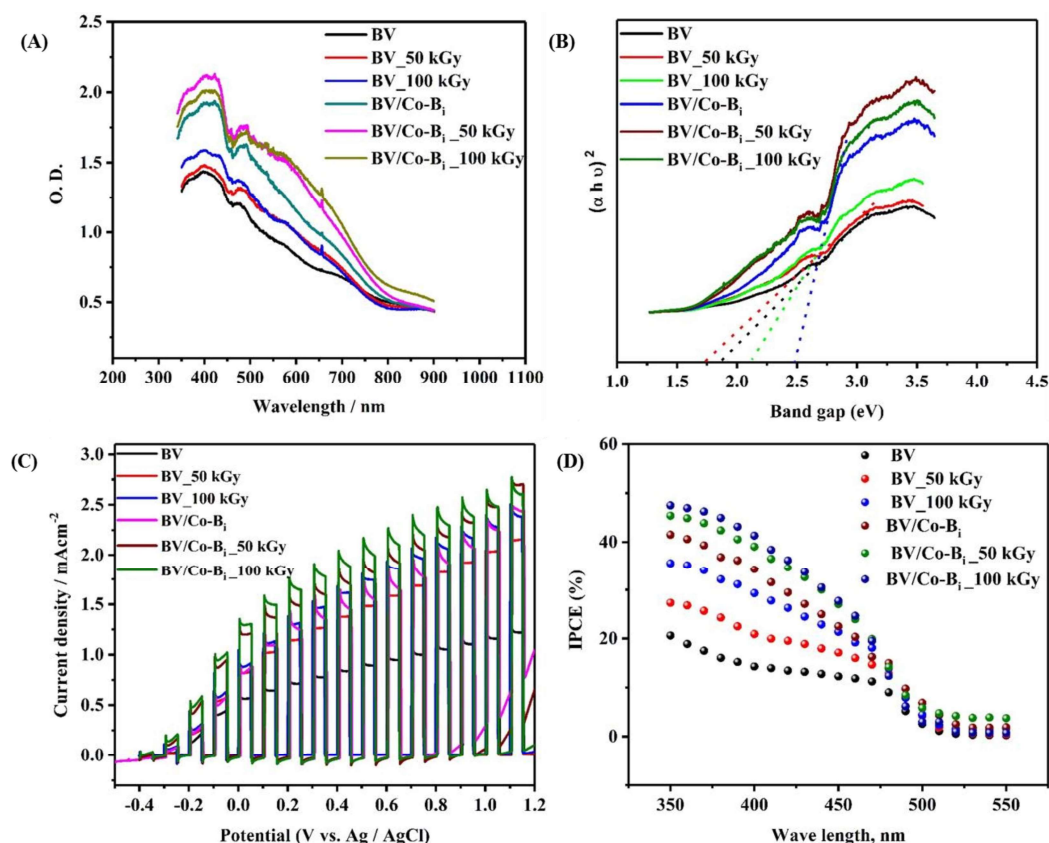


Figure 7.6 (A) UV-Vis spectroscopy measurements, (B) Tauc plot for bandgap measurement, (C) chopped light voltammetry of photoanodes and (D) IPCE measurements.

Nature of the band transition and the bandgap of the photoanodes are determined from the analysis of the Tauc plot. [152, 308]. The bandgap of the BV is 1.90 eV which is somewhat lower than the theoretical bandgap of the BiVO₄. Gamma irradiation causes the decrease in the bandgap from 1.90 eV to the 1.80 eV and increase to 2.1 eV for 50 kGy and 100 kGy radiation dose respectively as shown in Figure 7.6 (B). Co-B_i incorporation to the BV increases the

bandgap from 1.90 eV to 2.48 eV which further increased to 2.53 eV upon 50 kGy radiation dose. 100 kGy dose leads to the decrease in the bandgap of the Co-B_i modified BV.

7.3.3 Photoelectrochemical investigation

The photoelectrochemical investigation was performed in the 0.1 M BBS (pH ~8) due to less corrosive to the BiVO₄ than phosphate buffer solution [83, 134, 136]. The PEC activity of photoanodes was performed by chopped light voltammetry technique as shown in Figure 7.6 (C). The photocurrent of BV is obtained as 1.21 mAcm⁻² at 1.0 V vs. Ag/AgCl. The relatively low photocurrent is obtained due to the fast electron-hole recombination, low charge separation, and poor surface catalytic activity of BiVO₄ [87, 347, 359]. Upon the gamma irradiation, the photocurrent is increased from the 1.21 mAcm⁻² to 2.05 (~ 70%) and 2.40 mAcm⁻² (98 %) for the 50 kGy and 100 kGy radiation dose respectively. These results suggest that bulk and surface properties of the BV is improved for the PEC activity. The increase in the photo absorption efficiency as obtained from the absorption spectroscopy analysis supports the improvements in the photocurrent. Photocurrent is improved from 1.21 mAcm⁻² to 2.34 mAcm⁻² (~93 %) upon incorporation of co-catalyst shows the synergistic effect of Co-B_i in improvements of the charge transfer and transport kinetics at electrode-electrolyte interface. On gamma irradiation, photocurrent is increased from 2.34 mAcm⁻² to 2.57 (~ 10%) and 2.65 mAcm⁻² (13%) for 50 kGy and 100 kGy doses, which are 112% and 119% enhancement with respect to the BV. The significant improvements in the photocurrent suggesting the bulk and surface properties of gamma treated Co-B_i modified BV.

The onset potential of BV is -0.30 V vs. Ag/AgCl, which is cathodically shifted from -0.30 V to -0.32 V upon the gamma irradiation, suggesting the thermodynamically favorable OER. The significant improvements in the photocurrent and onset potential suggest the improvements in

the bulk and surface kinetics of the photoanodes. Co-B_i modification leads to the shift of onset potential from -0.30V to -0.34V due to facilitation of the OER kinetics at the interface. Co-B_i is reported as the hole collector which improves the charge transfer and transport efficiency and hence facilitates the faster kinetics at the interface as well as the thermodynamically favor OER as cathodic shift of onset potential suggested [87, 117, 126, 360]-. Further, gamma irradiation leads to the cathodic shift of the onset potential, which again suggest the surface and bulk properties of the photoanodes. The photocurrent and onset potential improvements could be due to the enhancement in the photo-absorption efficiency upon the gamma irradiation. The increase in the bandgap i.e. narrowing the bandgap improves the photocurrent. Gamma irradiation could change the micro-grain of the photoanodes and hence the bulk properties are changed. XRD and Raman analysis suggest the decrease in the grain size or crystallite size due to the gamma irradiation. V-O band is found to decrease significantly upon the gamma irradiation which could causes the crystallinity of the materials and hence the absorption efficiency is improved. Chopped light voltammetry of Co-B_i modified BV shows the cathodic transient current in the potential window from -0.35 V to 1.0 V vs. Ag/AgCl when light is chopped off. The cathodic transient current is due to the reduction of photo-oxidized Co (IV) to Co (III) when light is chopped off. The photogenerated holes are stored in the form of Co (IV) on the surface of the Co-B_i modified BiVO₄ under illumination and when light is chopped off, photo-oxidized Co (IV) gets reduced to Co (III) [277]. Collection and storage of the photogenerated holes in form of Co (IV) by Co (III) increase the lifetime and reduce the recombination process which leads to the improvements in the photocatalytic activity.

The PEC efficiency of photoanodes were investigated by the charge transfer and transport efficiency using hole scavenger method [311, 312]. The charge transfer efficiency of BV is

obtained as 55% and increased to 65% and 69% for 50 kGy and 100 kGy gamma irradiation, which suggest the improvements in the surface property and as results of photocurrent is enhanced. Co-B_i modification of the BV is further enhanced the charge transfer efficiency to 83%. Gamma irradiation improves the charge transfer efficiency to 93% for 50 kGy and then decrease to 76% for 100 kGy radiation dose. These results suggest that gamma irradiation causes the defects in the matrix by breaking the bond using high energy gamma radiation. Further, charge transport efficiency of the photoanodes was calculated for the investigation of the bulk properties. Charge transport efficiency is enhanced from 30% to the 53% upon the gamma irradiation. The improvements in the charge transfer and transport efficiency suggest the improvements in the bulk and surface properties upon gamma irradiation. These improvements could be due to the increase in the defects and breaking of same bonds in the material. Co-B_i further improves the transport efficiency due to the hole capture property of the co-catalyst. Further, gamma irradiation of Co-B_i modified BV leads to the increase in the charge transfer efficiency from 83% to 87% and then decreased to 76% for 50 kGy and 100 kGy radiation dose respectively. The overall photocurrent is increased due to the improvements in the charge transfer and transport efficiency.

Further, the PEC efficiency is measured in the term of IPCE as shown in Figure 7.6 (D). The onset potential of IPCE is 500 nm, which supports the bandgap of the photoanodes. However, absorption spectroscopy data reveals that absorption is the wavelength. IPCE of gamma irradiated BV is improved by 50% and 107% for 50 kGy and 100 kGy radiation dose. Co-B_i modification further improves the IPCE by 143%. The gamma irradiation enhanced the IPCE further by 178% and 200%. The improvements in the IPCE reflect the chopped light voltammetry and the absorption spectroscopy data.

7.3.4 Mott-Schottky analysis

Further, electronic properties of the photoanodes were investigated using Mott-Schottky analysis to insight into the improvements in charge transfer and transport efficiency. Donor density (N_d), the inherent property of the photoanode, is calculated from the Mott-Schottky plot as shown in Figure 7.7 (A). The N_d of BV is $4.6 \times 10^{20} \text{ cm}^{-3}$ and is decreased with the gamma irradiation from 4.6×10^{20} to 4×10^{20} and $3 \times 10^{20} \text{ cm}^{-3}$ for 50 kGy and 100 kGy radiation dose respectively. The decrease in the donor density suggests the breakage of the bonds. Co-B_i incorporation in the BV enhances the donor density from 4.6×10^{20} to $7.5 \times 10^{20} \text{ cm}^{-3}$ again supports the increase in the photocurrent. Further, gamma irradiation on the Co-B_i modified BV leads the first decrease and then increase in the donor density, causes the improvements in the photocurrent.

The flat band potential is the qualitative measurement of the band bending at the electrode-electrolyte interface, which significantly affects the photogenerated charge separation and recombination process [161, 162, 286]. It has been reported that high degree of band bending improves the charge separation and suppress the recombination process and hence overall PEC efficiency of the photoanodes improved. The flat band potential is calculated from the Mott-Schottky analysis as shown in the Figure 7.7 (A) and tabulated in Table 7.1. The flat band potential of BV is -85 mV and is shifted towards the anodic side from -85 mV to 54 mV and 77 mV for 50 kGy and 100 kGy radiation dose respectively. The anodic shift of the flat band potential suggests the hole trapped at the interface which causes the higher band bending and hence suppression of recombination process of photogenerated electron-hole which ultimately leads to the improvements in the photocurrent. The flat band potential of the Co-B_i modified BV is relatively more positive than the BV suggests the higher band bending and hence improved

charge separation at the interface. Gamma irradiation of the Co-B_i further improved the band bending at the interface due to the anodic shift of the flat band potential.

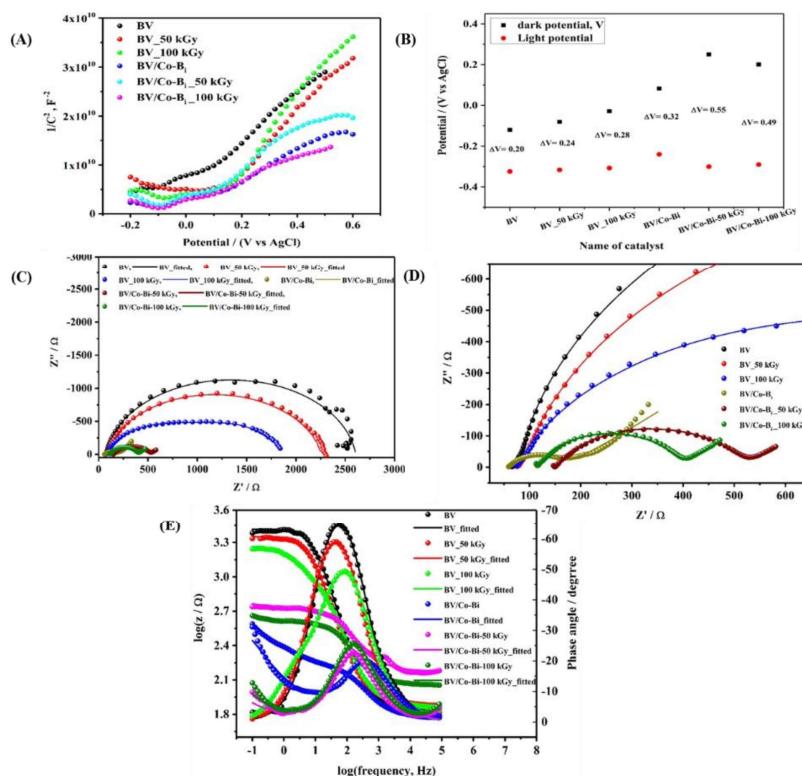


Figure 7.7 (A) Mott-Schottky plot, (B) open circuit photovoltage, (C) Nyquist plot, (D) zoomed Nyquist plot and (E) Bode plot of the photoanodes before and after gamma irradiation.

The band position and the band bending are further investigated by the open circuit photovoltage (OCPV). The change in the OCPV is due to the change in the band bending and the charge recombination at the electrode-electrolyte interface. The extent of band bending at the electrode-electrolyte depends on the in-built potential and the charge recombination [287, 288]. The OCPV is calculated from the OCP difference in the dark and illumination, as shown in Figure 7.7 (B). The OCPV of BV is 0.2 V and is increased from 0.2 V to the 0.32 V with the incorporation of the Co-B_i. The OCPV of the gamma irradiated photoanodes has been increased which shows that

the improvement of the band bending. The interesting observation is the change of OCP of photoanode in the dark. It is assumed that the Fermi level of the photoanode is in equilibrium with the water oxidation band in the dark condition, and in illumination, the quasi-Fermi level of the hole is in equilibrium with the water oxidation band, and quasi-Fermi level of electron rises towards the conduction band [92, 314]. The Fermi level of BV is short of the water oxidation potential. When water oxidation co-catalyst Co-Bi is incorporated on the BiVO₄, there is a shifting of the Fermi level of photoanodes towards the water oxidation potential. The OCPV is found to increase for irradiated photoanodes suggests the better separation of the charge, which ultimately improves the PEC efficiency. The result supports the significant band bending and better separation of charge upon Co-Bi incorporation, as observed from flat band potential.

Table 7.1 Summary of the PEC study of photoanodes.

Photoanodes	Band gap, eV	% increase @1.0 V	Donor density, (10 ²⁰ cm ⁻³)	Flat band potential, mV	OCP V (V)	Charge transfer efficiency	Charge transport efficiency	Transient time constant (in sec)	Rct (Ω)	C (μF)	Relaxation time constant (ms)
BV	1.90	-	4.6	-85	0.20	55	30	2.70	2472	6.97	3.10
BV-50 kGy	1.80	69	4	54	0.18	65	32	2.16	2150	8.58	3.69
BV-100 kGy	2.1	98	3	77	0.28	69	53	2.92	1820	15	1.98
BV/Co-Bi	2.48	93	7.5	-15	0.32	83	45	5.63	105	4.11	0.42
BV/Co-Bi-50 kGy	2.53	112	5	-12	0.59	87	42	5.26	391	7.39	1.03
BV/Co-Bi-100 kGy	2.47	119	8	-33	0.49	76	45	4.60	295	8.18	1.13

7.3.5 Impedance spectroscopy study

It is observed that co-catalyst incorporation improves the overall PEC efficiency. This improvement in efficiency is a combined contribution of the surface and bulk phenomenon as

charge transfers as a surface phenomenon and charge transport as a bulk phenomenon. For further investigation has been carried out for the measurements of the bulk and surface phenomenon. Electrochemical impedance spectroscopy (EIS) study has been performed to investigate the bulk and surface contribution in the PEC efficiency, as shown in Figure 7.7 (C) and (D). The Nyquist plot is used to study the photoelectrical conductivity of the bulk and surface of the BV and BV/Co-Bi photoanodes. The charge transfer resistance (R_{ct}) of the BV is 2472Ω and is decreased from 2472Ω to 105Ω upon the incorporation of the Co-Bi. This result shows significant improvements in the bulk and interfacial charge transfer kinetics, and hence photocurrent is increased with Co-Bi incorporation. The Warburg components in the Co-Bi modified BiVO_4 suggest the change in the charge transfer kinetics at the interface from kinetic control to the diffusion control process. The diffusion control process suggests surface kinetics is no longer a limiting factor for BiVO_4 photoanode for OER and hence overcome the photogenerated charge recombination. Gamma radiation treatment of the BV photoanodes leads to further decrease of the R_{ct} value from 2472Ω to 1820Ω and hence improved the conductivity of the photoanodes. This improvements of the conductivity of the photoanodes enhances the photocurrent as shown in the chopped light voltammetry experiment. The enhancement of the conductivity of the photoanodes is expected due to increase of the crystallinity of the photoanodes and microdefect generation as suggested by XRD and Raman spectra observation.

Charge transfer kinetics is further investigated by the Bode plot, as shown in Figure 7.7 (E). PEC kinetics is investigated in terms of the relaxation frequency and relaxation time constant (τ) of the photogenerated charge. The relaxation frequency of the photogenerated charge is 54.45 Hz for BV and increased from 54.45 Hz to 208.93 Hz upon Co-Bi modification. The relaxation frequency of the gamma radiation treated BV and BV/Co-Bi enhance significantly

which suggests the faster relaxation process of the photogenerated charge the faster kinetics at the interface. τ of photogenerated charge is calculated by using $\tau = 1/2\pi f$ where f is the relaxation frequency. The τ of BV is 3.10 ms, and Co-Bi modification of the BiVO₄ leads to a decrease in the τ from 3.10 ms to 0.42 ms. This decrease in τ also supports the faster charge transfer at the interface. Gamma radiation treatment of BV shows the decrease of the τ from 3.10 ms to 1.98 ms. This decrease of the relaxation time constant reveals the enhancement of the interfacial kinetics of the photogenerated holes. However, there is slightly increase of the τ of radiation treated BV/Co-Bi photoanodes. EIS result well supports the improvements in the kinetics of water splitting upon the Co-Bi incorporation.

The stability test of the photoanodes was performed by the chronoamperometry method at the 0.8 V for the 2 h, as shown in Figure 7.8. There is initial fast decay of photocurrent for BV and Co-Bi modified BV. The initial decrease in photocurrents is due to capacitive loss, and then the increase of photocurrent is observed because of improvements in surface kinetics. Co-Bi modification of the BV enhances the stability of the photoanodes. Gamma irradiation leads to stabilize the photocurrent and found to enhancement of the photocurrent with the time. The increase in photocurrent can be explained based on the photocharging effect. It has been reported elsewhere that photocharging of the BiVO₄ photoanode improved the photocurrents many folds due to improvements in the surface and bulk properties of the photoanode materials. Since the low conductivity of Co-Bi limits the PEC efficiency, photocharging is used as a tool to improve the surface, and bulk properties of the Co-Bi incorporated BiVO₄ to enhance the overall efficiency.

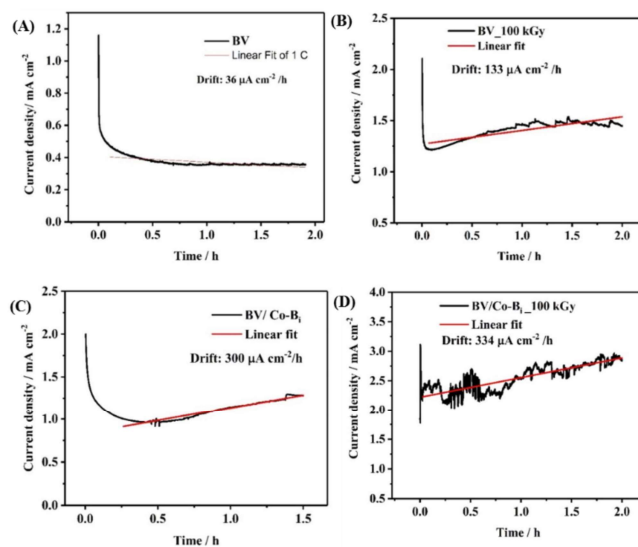


Figure 7.8 Stability test of the photoanodes (A) BV, (B) BV_100 kGy, (C) BV/Co-Bi and (D) BV/Co-Bi_100 kGy at 0.8 V for 2 h.

7.4 Conclusion

On gamma irradiation, the photocurrent is increased by 69% and 98 % on 50 kGy and 100 kGy dose of radiation of on BV photoanodes, the improvements are comparable with the incorporation of Co-Bi as oxygen evolution co-catalyst (93%). The cathodically shifted onset potential shows the thermodynamically favorable OER of irradiated photoanodes and Co-Bi modified BV. The increase in photovoltage suggests suppression of the surface state. The impedance data suggests the change in the kinetics of photogenerated charge upon Co-Bi incorporation from the kinetic control process to the diffusion control process. This result shows surface kinetics is no longer a limiting step. The decrease in the R_{ct} reveals the improvements in the bulk and surface conductivity, which leads to improvements in the photocurrent. The cathodic shift of the Fermi level is in agreement with the shift of onset potential. The decrease of

the R_{ct} value upon the gamma irradiation suggest the improvements of the conductivity of the photoanodes by incorporation of defect on the material and increase of the donor density.

Overall, our investigation suggests that incorporation of Co-Bi to the BiVO_4 enhances the photocurrent and improves the PEC efficiency due to the improvements in the bulk and surface improvements. The gamma radiation treatment further enhances the photocurrent and improves the PEC efficiency by alteration of bulk and surface properties. The surface and bulk conductivity are found to improve. Therefore, this study shows the path of improvements of photoanode and OEC incorporated photoanode performance.

Chapter 8: Conclusions and Future Scope

These research have been focused on the understanding of the fundamental mechanism of the water splitting process for the development of BiVO₄ based photoanodes and non-noble metal electrocatalyst. Electrical, electronics, optical properties of electrodes materials have been investigated and correlated with the photoelectrochemical water splitting process. The thermodynamics and kinetics processes are studied for HER process for noble and non-noble metal based electrocatalyst. In the first two chapters, the objective of the research and various instrumentations used during the course of the present thesis work is discussed. In Chapter 3 and 4 development of the cathode material is discussed. High conducting and porous network of three-dimensional graphene (3D-G) is synthesized via. The 3D-G provides the excellent charge transfer and diffusion of ions through highly porous network and improves the catalytic activity. We have synthesized the noble metal and 3D-G nanocomposites by the environmental friendly freeze drying method for reducing the loading of active material for the HER process. It has been observed that HER catalytic activity of Pt/3D-G is significantly better than the commercially available Pt/C catalysts due to the three-dimensional network of the 3D-G. The HER catalytic activity of the Pt, Pd, Au and Ag based catalyst have been compared with the pristine noble metal and found in the order of Pt > Pd > Au > Ag. The kinetic study of the HER process has been carried out by the Koutechy-Levich analysis for the understanding of the number of electrons transferred during the process and the rate constant of the electrons transferred. At 0V, number of electrons transferred is ~ 2 due to the one electrons for the Volmer mechanism and other for the Tafel or the Heyrovsky mechanism. The high rate constant of the Pt based catalyst

followed by the Pd, Au and Ag supports the performance of the catalysts. The temperature dependent catalytic activity of HER has been performed to calculate the activation energy of the process. Further, the temperature dependent HER process has been investigated and Tafel analysis has been carried out to understand the mechanism of the process. Temperature dependent transfer coefficient has calculation shows the dominance of enthalpy and entropy on the overall mechanism of the catalytic process. It has found that HER on Pt/3D-G and Pd/3D-G catalysts are enthalpy driven process and on Au/3D-G and Ag/3D-G is entropy driven process at the given potential window. Significant improvement of the 3D-G incorporated catalysts is expected to decrease in the use of expensive noble metals in the HER catalysis. Improvement in the catalytic activity through the incorporation of 3D-G generated positive indication in the utilization of less expensive Ag based catalysts without sacrificing the catalytic performance.

After the successful synthesis of the 3D-G and noble metal nanocomposites, we have tried to the replace the noble metal with the transition metal-based electro catalysts. In the line of the cost effectiveness and the high HER activity, MoS₂ based electrocatalysts have been investigated. MoS₂ and graphene based cathodic materials have been synthesized to replace the noble metals. Material characterization has revealed the 1T phase of MoS₂. Both the composite materials have shown very good catalytic activity for HER process and their catalytic activities are not so inferior to the commercially available Pt/C catalyst. Electrochemical investigations with Tafel analysis have indicated the Volmer-Heyrovsky mechanism for the HER process in MoS₂/GO catalytic system. LSV experiments were carried out in hydrodynamic mode and the results shown to have marginally higher electron transfer rate constant for MoS₂/rGO composite materials, where the current density and the onset potential for the HER process was comparatively favorable in the case of MoS₂/GO. Such anomaly in the observation has indicated

the enhanced mass transfer process for MoS₂/GO; such enhanced mass transfer has been ascertained from the exchange of proton at the functional group over the GO matrix and the bulk acidic solution. Electrochemical impedance measurements have shown to have high desorptive charge transfer resistance for MoS₂/rGO composite material responsible for the comparatively low HER. It has been observed that MoS₂/GO nanocomposites shows the higher HER catalytic activity than the MoS₂/rGO nanocomposites. SECM experiments were carried out using the catalyst modified substrate and the probe approach plot has shown the transformation of the composite modified electrode as the substrate from oxidation of proton to the efficient HER catalyst with the modulation of the applied potential. The SECM substrate scan has shown the enhanced oxidation current from the tip electrode at a cathodic applied potential to the MoS₂/GO composite modified substrate compared to the MoS₂/rGO composite modified substrate.

After the development of the cathodic materials, anodic materials have been developed for the oxygen evolution reaction (OER). The photoanodes such as the BiVO₄ has been used as the base material for the development of the photoanodes to improve the photo-electrocatalytic activity of the OER. The limitation of the BiVO₄ as photoanodes have been taken as research motivation. The fast charge recombination and the slow charge transfer have been rectified by using the Mo doping and SnO₂ heterojunction formation to enhance the charge transfer efficiency, charge transport efficiency and suppress the charge recombination process. The significant improvement (~154%) in the photocurrent was observed upon 5% Mo doping in SnO₂/BiVO₄. Strong correlation among the optical property of the material, the open circuit photovoltage (OCPV), and onset potential has been observed in relation to the improvement in the PEC efficiency on Mo doping. The increase in the flat band potential and OCPV suggests the improvements in the charge separation upon the Mo doping which resulted in the enhancement

in PEC efficiency. SECM investigation reveals significant improvement in effective hole transfer rate constant from 2.18 cm s^{-1} to 7.56 cm s^{-1} with the Mo doping in BiVO_4 . The electrochemical impedance investigation supports the improvements in the charge transfer and transport efficiency by improvements in the bulk and surface properties of BiVO_4 . The facilitated reduction of V (V) to V (IV) on Mo doping is also responsible for the improvement in the catalytic activity. The improvement in the catalytic activity has been evaluated from the improvement in the physicochemical at the bulk of the catalysts, its surface, and most importantly due to the improvement in its interfacial charge transfer processes. Mild expansion in the crystal lattice is also observed on replacement of V by Mo, the improvement in the catalytic activity however, related primarily to the electronic nature compared to any morphological changes.

After successful development of the BiVO_4 photoanodes and rectify the fast charge recombination process, slow surface catalytic activity of the BiVO_4 is taken as the motivation of work. The significant improvements in the photocurrent upon the incorporation of the Co-B_i as an oxygen evolution catalyst on BiVO_4 has been observed. The Co-B_i incorporation leads to an improvement of 103% photocurrent. The cathodically shifted onset potential shows the thermodynamically favorable OER. The increase in photovoltage suggests an absence of the surface state. The impedance data suggests the change in the kinetics of photogenerated charge upon Co-B_i incorporation from the kinetic control process to the diffusion control process. This result shows surface kinetics is no longer a limiting step. The decrease in the R_{ct} reveals the improvements in the bulk and surface conductivity, which leads to improvements in the photocurrent. The cathodic shift of the Fermi level is in agreement with the shift of onset potential. The photocharging treatment of BV and Co-B_i modified BV enhances the photocurrent

0.96 mAcm⁻² to 1.31 mAcm⁻² (36%) and 1.95 mA cm⁻² to 2.63 mAcm⁻² (35%) for BV and BV/Co-B_i-3 respectively. Onset potential is shifted cathodically, and photovoltage is increased upon the photocharging. Impedance analysis shows improvements in the bulk and surface conductivity and enhanced the surface capacitance upon photocharging. The anodic shift of flat band potential suggests trapped holes on the surface. This trapped hole is expected from the capacitive layer of water oxidation intermediate and hence, improvements in the photocurrent. The Co (III) plays a vital role in the storage of holes at the interface in the form of Co (IV), which facilitates the faster charge transfer for water oxidation. However, the growths of photocurrents are observed, suggesting the photogenerated surface hole and the V⁵⁺ to the V⁴⁺ on the interface. Overall, present investigation suggests that incorporation of Co-B_i to the BiVO₄ enhances the photocurrent and improves the PEC efficiency due to the improvements in the bulk and surface improvements. Photocharging treatment further enhances the photocurrent and improves the PEC efficiency by alteration of bulk and surface properties. The surface and bulk conductivity are found to improve. Therefore, this study shows the path of improvements of photoanode and OEC incorporated photoanode performance.

The BiVO₄ and Co-B_i modified BiVO₄ have been treated for the high dose of the gamma radiation. The effect of the gamma radiation on the chemical and physical properties of the photoanodes have been investigated. XRD data shows the increase of the crystallinity of the photoanodes. The SEM images shows the change of the morphology of the materials upon the gamma irradiation. The Co-B_i incorporation as oxygen evolution cocatalyst leads to an improvement of 93% of photocurrent than BV. There is increase of photocurrent by 69% and 98 % upon 50 kGy and 100 kGy dose of radiation of BV photoanodes. The cathodically shifted onset potential shows the thermodynamically favorable OER of irradiated photoanodes and Co-

Bi modified BV. The increase in photovoltage suggests suppression of the surface state. The impedance data suggests the change in the kinetics of photogenerated charge upon Co-Bi incorporation from the kinetic control process to the diffusion control process. The decrease in the R_{ct} reveals the improvements in the bulk and surface conductivity, which leads to improvements in the photocurrent. The decrease of the R_{ct} value upon the gamma irradiation suggest the improvements of the conductivity of the photoanodes by incorporation of defect on the material and increase of the donor density. The gamma radiation treatment further enhances the photocurrent and improves the PEC efficiency by alteration of bulk and surface properties. The surface and bulk conductivity are found to improve upon the gamma radiation. Therefore, this study shows the path of improvements of photoanode and OEC incorporated photoanode performance. Present investigation has developed and evaluated the performance of catalytic materials as cathode and anode for the electrochemical and photoelectrochemical generation of hydrogen and oxygen from water. The mechanistic information of the catalytic processes has been evaluated in the line to further improve their catalytic performance. It is encouraging to observed that the performance of the presently reported catalysts is comparable with respect to some of the benchmarked catalytic systems recently reported in the literature. Present thesis work opens a new direction in the characterization of the interfacial processes using SECM, of the catalytic materials investigated. The scope and objective of the present research work has been investigated satisfactorily, however there are enormous scope in improvements in the field of present research. Overall, the thesis work evolves out to provide directions for fabrication of evaluation of new cathode and anode materials for electrocatalytic and photo-electrocatalytic evolution of hydrogen and oxygen from water. Photocharging of photoanodes gives direction for the long-term stability of the photoanodes. It can be explored for the improvement of the

photoanodes for material stability. Additionally, the deposition of the passivating agents like, TiO₂ through the atomic layer deposition technique also to be incorporated for the improvement in the stability of such materials. The investigation will be extended further to evaluate the catalytic system in Z-scheme for sustainable generation of hydrogen and oxygen from water through photoelectrochemical routes. Present thesis has significant scope to extend its investigation in scaling up and designing the cells for sustainable catalytic performance. Investigation will also be carried to combine the photoelectrochemical catalytic system with redox flow battery system for simultaneous harvesting and storage of solar energy in sustainable mode.

References

- [1] J. Barber, Photosynthetic energy conversion: natural and artificial, *Chemical Society Reviews*, 38 (2009) 185-196.
- [2] N.S. Lewis, Toward cost-effective solar energy use, *science*, 315 (2007) 798-801.
- [3] M. Grätzel, Photoelectrochemical cells, *nature*, 414 (2001) 338-344.
- [4] X. Chen, C. Li, M. Grätzel, R. Kostecki, S.S. Mao, Nanomaterials for renewable energy production and storage, *Chemical Society Reviews*, 41 (2012) 7909-7937.
- [5] Z. Wang, C. Li, K. Domen, Recent developments in heterogeneous photocatalysts for solar-driven overall water splitting, *Chemical Society Reviews*, 48 (2019) 2109-2125.
- [6] D.M. Fabian, S. Hu, N. Singh, F.A. Houle, T. Hisatomi, K. Domen, F.E. Osterloh, S. Ardo, Particle suspension reactors and materials for solar-driven water splitting, *Energy & Environmental Science*, 8 (2015) 2825-2850.
- [7] A. Lasia, Hydrogen evolution reaction, *Handbook of fuel cells*, (2010).
- [8] Y. Yan, B.Y. Xia, B. Zhao, X. Wang, A review on noble-metal-free bifunctional heterogeneous catalysts for overall electrochemical water splitting, *Journal of Materials Chemistry A*, 4 (2016) 17587-17603.
- [9] T.R. Cook, D.K. Dogutan, S.Y. Reece, Y. Surendranath, T.S. Teets, D.G. Nocera, Solar energy supply and storage for the legacy and nonlegacy worlds, *Chemical reviews*, 110 (2010) 6474-6502.
- [10] L.R. Faulkner, A.J. Bard, *Electrochemical methods: fundamentals and applications*, John Wiley and Sons 2002.

- [11] J.M. Bockris, E. Potter, The mechanism of the cathodic hydrogen evolution reaction, *Journal of The Electrochemical Society*, 99 (1952) 169-186.
- [12] M. Zeng, Y. Li, Recent advances in heterogeneous electrocatalysts for the hydrogen evolution reaction, *Journal of Materials Chemistry A*, 3 (2015) 14942-14962.
- [13] G. Eliezer, *Physical Electrochemistry*, John Wiley, New York, 2011.
- [14] P. Sabatier, Hydrogénations et déshydrogénations par catalyse, *Berichte der deutschen chemischen Gesellschaft*, 44 (1911) 1984-2001.
- [15] R. Parsons, The rate of electrolytic hydrogen evolution and the heat of adsorption of hydrogen, *Transactions of the Faraday Society*, 54 (1958) 1053-1063.
- [16] S. Kumar, P.K. Sahoo, A.K. Satpati, Insight into the catalytic performance of HER catalysis of noble metal/3D-G nanocomposites, *Electrochimica Acta*, 333 (2020) 135467.
- [17] J.R. Swierk, S. Klaus, L. Trotochaud, A.T. Bell, T.D. Tilley, Electrochemical study of the energetics of the oxygen evolution reaction at nickel iron (oxy) hydroxide catalysts, *The Journal of Physical Chemistry C*, 119 (2015) 19022-19029.
- [18] G. Wu, N. Li, D.-R. Zhou, K. Mitsuo, B.-Q. Xu, Anodically electrodeposited Co+Ni mixed oxide electrode: preparation and electrocatalytic activity for oxygen evolution in alkaline media, *Journal of Solid State Chemistry*, 177 (2004) 3682-3692.
- [19] S. Holloway, K. Bennemann, Study of water adsorption on metal surfaces, *Surface Science*, 101 (1980) 327-333.
- [20] K.-i. Ataka, T. Yotsuyanagi, M. Osawa, Potential-dependent reorientation of water molecules at an electrode/electrolyte interface studied by surface-enhanced infrared absorption spectroscopy, *The Journal of Physical Chemistry*, 100 (1996) 10664-10672.

- [21] N. Garcia-Araez, V. Climent, J. Feliu, Potential-dependent water orientation on Pt (111), Pt (100), and Pt (110), as inferred from laser-pulsed experiments. Electrostatic and chemical effects, *The Journal of Physical Chemistry C*, 113 (2009) 9290-9304.
- [22] N. García-Araéz, V. Climent, J.M. Feliu, Evidence of water reorientation on model electrocatalytic surfaces from nanosecond-laser-pulsed experiments, *Journal of the American Chemical Society*, 130 (2008) 3824-3833.
- [23] I. Ledezma-Yanez, W.D.Z. Wallace, P. Sebastián-Pascual, V. Climent, J.M. Feliu, M.T. Koper, Interfacial water reorganization as a pH-dependent descriptor of the hydrogen evolution rate on platinum electrodes, *Nature Energy*, 2 (2017) 17031.
- [24] B. Conway, D. Wilkinson, Entropic and enthalpic components of the symmetry factor for electrochemical proton transfer from various proton donors over a wide temperature range, *Journal of electroanalytical chemistry and interfacial electrochemistry*, 214 (1986) 633-653.
- [25] H.A. Gasteiger, N.M. Markovic, P.N. Ross, H₂ and CO Electrooxidation on Well-Characterized Pt, Ru, and Pt-Ru. 1. Rotating Disk Electrode Studies of the Pure Gases Including Temperature Effects, *The Journal of Physical Chemistry*, 99 (1995) 8290-8301.
- [26] X.-Z. Yuan, H. Wang, PEM fuel cell fundamentals, *PEM Fuel Cell Electrocatalysts and Catalyst Layers*, Springer2008, pp. 1-87.
- [27] M.E. Lyons, L.D. Burke, Mechanism of oxygen reactions at porous oxide electrodes. Part 1.—Oxygen evolution at RuO₂ and Ru_xSn_{1-x}O₂ electrodes in alkaline solution under vigorous electrolysis conditions, *Journal of the Chemical Society, Faraday Transactions 1: Physical Chemistry in Condensed Phases*, 83 (1987) 299-321.

- [28] I. Man, H. Su, F. Calle-Vallejo, H. Hansen, J. Martinez, N. Inoglu, 506 Kitchin, J.; Jaramillo, TF; Norskov, JK; Rossmeisl, J. Universality in oxygen 507 evolution electrocatalysis on oxide surfaces, *ChemCatChem*, 2011.
- [29] T. Reier, M. Oezaslan, P. Strasser, Electrocatalytic oxygen evolution reaction (OER) on Ru, Ir, and Pt catalysts: a comparative study of nanoparticles and bulk materials, *Acs Catalysis*, 2 (2012) 1765-1772.
- [30] C. Lefrou, R. Cornut, Analytical expressions for quantitative scanning electrochemical microscopy (SECM), *ChemPhysChem*, 11 (2010) 547-556.
- [31] A.J. Bard, F.R.F. Fan, J. Kwak, O. Lev, Scanning electrochemical microscopy. Introduction and principles, *Analytical Chemistry*, 61 (1989) 132-138.
- [32] R. Cornut, C. Lefrou, New analytical approximation of feedback approach curves with a microdisk SECM tip and irreversible kinetic reaction at the substrate, *Journal of Electroanalytical Chemistry*, 621 (2008) 178-184.
- [33] B. Zhang, X. Zhang, X. Xiao, Y. Shen, Photoelectrochemical Water Splitting System □ A Study of Interfacial Charge Transfer with Scanning Electrochemical Microscopy, *ACS applied materials & interfaces*, 8 (2016) 1606-1614.
- [34] U. Mengesha Tefashe, K. Nonomura, N. Vlachopoulos, A. Hagfeldt, G. Wittstock, Effect of cation on dye regeneration kinetics of N719-sensitized TiO₂ films in acetonitrile-based and ionic-liquid-based electrolytes investigated by scanning electrochemical microscopy, *The Journal of Physical Chemistry C*, 116 (2012) 4316-4323.
- [35] C. Wei, A.J. Bard, M.V. Mirkin, Scanning electrochemical microscopy. 31. Application of SECM to the study of charge transfer processes at the liquid/liquid interface, *The Journal of Physical Chemistry*, 99 (1995) 16033-16042.

- [36] J.N. Tiwari, K. Nath, S. Kumar, R.N. Tiwari, K.C. Kemp, N.H. Le, D.H. Youn, J.S. Lee, K.S. Kim, Stable platinum nanoclusters on genomic DNA–graphene oxide with a high oxygen reduction reaction activity, *Nature communications*, 4 (2013) 2221.
- [37] Y.-J. Wang, N. Zhao, B. Fang, H. Li, X.T. Bi, H. Wang, Carbon-supported Pt-based alloy electrocatalysts for the oxygen reduction reaction in polymer electrolyte membrane fuel cells: particle size, shape, and composition manipulation and their impact to activity, *Chemical reviews*, 115 (2015) 3433-3467.
- [38] D. Koster, A.R. Zeradjanin, A. Battistel, F. La Mantia, Extracting the kinetic parameters of the hydrogen evolution reaction at Pt in acidic media by means of dynamic multi-frequency analysis, *Electrochimica Acta*, 308 (2019) 328-336.
- [39] S. Štrbac, M. Smiljanić, T. Wakelin, J. Potočnik, Z. Rakočević, Hydrogen evolution reaction on bimetallic Ir/Pt (poly) electrodes in alkaline solution, *Electrochimica Acta*, 306 (2019) 18-27.
- [40] F. Zheng, C. Zhang, X. Gao, C. Du, Z. Zhuang, W. Chen, Immobilizing Pd nanoclusters into electronically conductive metal-organic frameworks as bi-functional electrocatalysts for hydrogen evolution and oxygen reduction reactions, *Electrochimica Acta*, 306 (2019) 627-634.
- [41] Y.-Y. Liu, H.-P. Zhang, B. Zhu, H.-W. Zhang, L.-D. Fan, X.-Y. Chai, Q.-L. Zhang, J.-H. Liu, C.-X. He, C/N-co-doped Pd coated Ag nanowires as a high-performance electrocatalyst for hydrogen evolution reaction, *Electrochimica Acta*, 283 (2018) 221-227.
- [42] Y. Chen, X.-X. Zheng, X.-Y. Huang, A.-J. Wang, Q.-L. Zhang, H. Huang, J.-J. Feng, Trimetallic PtRhCo petal-assembled alloyed nanoflowers as efficient and stable bifunctional electrocatalyst for ethylene glycol oxidation and hydrogen evolution reactions, *Journal of Colloid and Interface Science*, 559 (2020) 206-214.

- [43] H.-Y. Chen, M.-X. Jin, L. Zhang, A.-J. Wang, J. Yuan, Q.-L. Zhang, J.-J. Feng, One-pot aqueous synthesis of two-dimensional porous bimetallic PtPd alloyed nanosheets as highly active and durable electrocatalyst for boosting oxygen reduction and hydrogen evolution, *Journal of colloid and interface science*, 543 (2019) 1-8.
- [44] D.-X. Yu, A.-J. Wang, L.-L. He, J. Yuan, L. Wu, J.-R. Chen, J.-J. Feng, Facile synthesis of uniform AuPd@ Pd nanocrystals supported on three-dimensional porous N-doped reduced graphene oxide hydrogels as highly active catalyst for methanol oxidation reaction, *Electrochimica Acta*, 213 (2016) 565-573.
- [45] X.-Y. Huang, L.-X. You, X.-F. Zhang, J.-J. Feng, L. Zhang, A.-J. Wang, L-proline assisted solvothermal preparation of Cu-rich rhombic dodecahedral PtCu nanoframes as advanced electrocatalysts for oxygen reduction and hydrogen evolution reactions, *Electrochimica Acta*, 299 (2019) 89-97.
- [46] M. Arenz, V. Stamenkovic, T.J. Schmidt, K. Wandelt, P.N. Ross, N.M. Markovic, CO adsorption and kinetics on well-characterized Pd films on Pt(111) in alkaline solutions, *Surface Science*, 506 (2002) 287-296.
- [47] N.R. Elezović, L. Gajić-Krstajić, V. Radmilović, L. Vračar, N.V. Krstajić, Effect of chemisorbed carbon monoxide on Pt/C electrode on the mechanism of the hydrogen oxidation reaction, *Electrochimica Acta*, 54 (2009) 1375-1382.
- [48] B. Fang, J.H. Kim, J.-S. Yu, Colloid-imprinted carbon with superb nanostructure as an efficient cathode electrocatalyst support in proton exchange membrane fuel cell, *Electrochemistry Communications*, 10 (2008) 659-662.

- [49] Z. Wu, B. Fang, A. Bonakdarpour, A. Sun, D. Wilkinson, WS₂ nanosheets as a highly efficient electrocatalyst for hydrogen evolution reaction., *Applied Catalysis B: Environmental*, 125 (2012) 59-66.
- [50] C. Hu, Y. Zhao, H. Cheng, Y. Hu, G. Shi, L. Dai, L. Qu, Ternary Pd₂/PtFe networks supported by 3D graphene for efficient and durable electrooxidation of formic acid, *Chemical Communications*, 48 (2012) 11865-11867.
- [51] C. Hu, H. Cheng, Y. Zhao, Y. Hu, Y. Liu, L. Dai, L. Qu, Newly-Designed Complex Ternary Pt/PdCu Nanoboxes Anchored on Three-Dimensional Graphene Framework for Highly Efficient Ethanol Oxidation, *Advanced Materials*, 24 (2012) 5493-5498.
- [52] P. Sahoo, R. Aepuru, H.S. Panda, D. Bahadur, Ice-templated synthesis of multifunctional three dimensional graphene/noble metal nanocomposites and their mechanical, electrical, catalytic, and electromagnetic shielding properties, *Scientific reports*, 5 (2015) 17726.
- [53] P.K. Sahoo, B. Panigrahy, D. Thakur, D. Bahadur, Ice-templating synthesis of macroporous noble metal/3D-graphene nanocomposites: their fluorescence lifetimes and catalytic study, *New Journal of Chemistry*, 41 (2017) 7861-7869.
- [54] P.K. Sahoo, N. Kumar, S. Thiyagarajan, D. Thakur, H.S. Panda, Freeze-Casting of multifunctional cellular 3D-graphene/Ag nanocomposites: synergistically affect supercapacitor, catalytic, and antibacterial properties, *ACS Sustainable Chemistry & Engineering*, 6 (2018) 7475-7487.
- [55] L.F. Pan, Y.H. Li, S. Yang, P.F. Liu, M.Q. Yu, H.G. Yang, Molybdenum carbide stabilized on graphene with high electrocatalytic activity for hydrogen evolution reaction, *Chemical Communications*, 50 (2014) 13135-13137.

- [56] S. Kumar, P.K. Sahoo, A.K. Satpati, Electrochemical and SECM investigation of MoS₂/GO and MoS₂/rGO nanocomposite materials for HER electrocatalysis, *ACS omega*, 2 (2017) 7532-7545.
- [57] D. Merki, X. Hu, Recent developments of molybdenum and tungsten sulfides as hydrogen evolution catalysts, *Energy & Environmental Science*, 4 (2011) 3878-3888.
- [58] Y. Yan, B. Xia, Z. Xu, X. Wang, Recent development of molybdenum sulfides as advanced electrocatalysts for hydrogen evolution reaction, *ACS Catalysis*, 4 (2014) 1693-1705.
- [59] X. Xu, X. Dong, Z. Bao, R. Wang, J. Hu, H. Zeng, Three electron channels toward two types of active sites in MoS₂@Pt nanosheets for hydrogen evolution, *Journal of Materials Chemistry A*, 5 (2017) 22654-22661.
- [60] Y. Wang, L. Zhang, X. Meng, L. Feng, T. Wang, W. Zhang, N. Yang, Scalable processing hollow tungsten carbide spherical superstructure as an enhanced electrocatalyst for hydrogen evolution reaction over a wide pH range, *Electrochimica Acta*, 319 (2019) 775-782.
- [61] M. Kozejova, V. Latyshev, V. Kavecansky, H. You, S. Vorobiov, A. Kovalcikova, V. Komanicky, Evaluation of hydrogen evolution reaction activity of molybdenum nitride thin films on their nitrogen content, *Electrochimica Acta*, 315 (2019) 9-16.
- [62] R. Lv, J.A. Robinson, R.E. Schaak, D. Sun, Y. Sun, T.E. Mallouk, M. Terrones, Transition metal dichalcogenides and beyond: synthesis, properties, and applications of single- and few-layer nanosheets, *Accounts of chemical research*, 48 (2014) 56-64.
- [63] Z. Li, X. Dai, K. Du, Y. Ma, M. Liu, H. Sun, X. Ma, X. Zhang, Reduced Graphene Oxide/O-MWCNT hybrids functionalized with p-Phenylenediamine as high-performance MoS₂ electrocatalyst support for hydrogen evolution reaction, *The Journal of Physical Chemistry C*, 120 (2016) 1478-1487.

- [64] C.-B. Ma, X. Qi, B. Chen, S. Bao, Z. Yin, X.-J. Wu, Z. Luo, J. Wei, H.-L. Zhang, H. Zhang, MoS₂ nanoflower-decorated reduced graphene oxide paper for high-performance hydrogen evolution reaction, *Nanoscale*, 6 (2014) 5624-5629.
- [65] K. Zhang, Y. Zhao, S. Zhang, H. Yu, Y. Chen, P. Gao, C. Zhu, MoS₂ nanosheet/Mo₂C-embedded N-doped carbon nanotubes: synthesis and electrocatalytic hydrogen evolution performance, *Journal of Materials Chemistry A*, 2 (2014) 18715-18719.
- [66] Y. Li, H. Wang, L. Xie, Y. Liang, G. Hong, H. Dai, MoS₂ nanoparticles grown on graphene: an advanced catalyst for hydrogen evolution reaction, arXiv preprint arXiv:1104.2966, (2011).
- [67] H.I. Karunadasa, E. Montalvo, Y. Sun, M. Majda, J.R. Long, C.J. Chang, A molecular MoS₂ edge site mimic for catalytic hydrogen generation, *Science*, 335 (2012) 698-702.
- [68] Y.H. Chang, C.T. Lin, T.Y. Chen, C.L. Hsu, Y.H. Lee, W. Zhang, K.H. Wei, L.J. Li, Highly Efficient Electrocatalytic Hydrogen Production by MoS_x Grown on Graphene-Protected 3D Ni Foams, *Advanced materials*, 25 (2013) 756-760.
- [69] J. Xie, H. Zhang, S. Li, R. Wang, X. Sun, M. Zhou, J. Zhou, X.W.D. Lou, Y. Xie, Defect-rich MoS₂ ultrathin nanosheets with additional active edge sites for enhanced electrocatalytic hydrogen evolution, *Advanced materials*, 25 (2013) 5807-5813.
- [70] C. Tsai, F. Abild-Pedersen, J.K. Nørskov, Tuning the MoS₂ edge-site activity for hydrogen evolution via support interactions, *Nano letters*, 14 (2014) 1381-1387.
- [71] C. Tsai, K. Chan, F. Abild-Pedersen, J.K. Nørskov, Active edge sites in MoSe₂ and WSe₂ catalysts for the hydrogen evolution reaction: a density functional study, *Physical Chemistry Chemical Physics*, 16 (2014) 13156-13164.

- [72] J. Benson, M. Li, S. Wang, P. Wang, P. Papakonstantinou, Electrocatalytic hydrogen evolution reaction on edges of a few layer molybdenum disulfide nanodots, arXiv preprint arXiv:1507.00061, (2015).
- [73] M.-R. Gao, J.-X. Liang, Y.-R. Zheng, Y.-F. Xu, J. Jiang, Q. Gao, J. Li, S.-H. Yu, An efficient molybdenum disulfide/cobalt diselenide hybrid catalyst for electrochemical hydrogen generation, *Nature communications*, 6 (2015).
- [74] M.A. Lukowski, A.S. Daniel, F. Meng, A. Forticaux, L. Li, S. Jin, Enhanced hydrogen evolution catalysis from chemically exfoliated metallic MoS₂ nanosheets, *Journal of the American Chemical Society*, 135 (2013) 10274-10277.
- [75] U. Maitra, U. Gupta, M. De, R. Datta, A. Govindaraj, C. Rao, Highly Effective Visible-Light-Induced H₂ Generation by Single-Layer 1T-MoS₂ and a Nanocomposite of Few-Layer 2H-MoS₂ with Heavily Nitrogenated Graphene, *Angewandte Chemie International Edition*, 52 (2013) 13057-13061.
- [76] D. Voiry, M. Salehi, R. Silva, T. Fujita, M. Chen, T. Asefa, V.B. Shenoy, G. Eda, M. Chhowalla, Conducting MoS₂ nanosheets as catalysts for hydrogen evolution reaction, *Nano letters*, 13 (2013) 6222-6227.
- [77] H. Li, K. Yu, C. Li, Z. Tang, B. Guo, X. Lei, H. Fu, Z. Zhu, Charge-Transfer Induced High Efficient Hydrogen Evolution of MoS₂/graphene Cocatalyst, *Scientific Reports*, 5 (2015) 18730.
- [78] M.D. Bhatt, J.S. Lee, Recent theoretical progress in the development of photoanode materials for solar water splitting photoelectrochemical cells, *Journal of Materials Chemistry A*, 3 (2015) 10632-10659.

- [79] S. Wang, H. Chen, G. Gao, T. Butburee, M. Lyu, S. Thaweesak, J.-H. Yun, A. Du, G. Liu, L. Wang, Synergistic crystal facet engineering and structural control of WO₃ films exhibiting unprecedented photoelectrochemical performance, *Nano Energy*, 24 (2016) 94-102.
- [80] P. Peerakiatkhajohn, J.H. Yun, H. Chen, M. Lyu, T. Butburee, L. Wang, Stable hematite nanosheet photoanodes for enhanced photoelectrochemical water splitting, *Advanced Materials*, 28 (2016) 6405-6410.
- [81] C. Zhen, R. Chen, L. Wang, G. Liu, H.-M. Cheng, Tantalum (oxy) nitride based photoanodes for solar-driven water oxidation, *Journal of Materials Chemistry A*, 4 (2016) 2783-2800.
- [82] S. Kment, F. Riboni, S. Pausova, L. Wang, L. Wang, H. Han, Z. Hubicka, J. Krysa, P. Schmuki, R. Zboril, Photoanodes based on TiO₂ and α -Fe₂O₃ for solar water splitting—superior role of 1D nanoarchitectures and of combined heterostructures, *Chemical Society Reviews*, 46 (2017) 3716-3769.
- [83] S. Wang, P. Chen, J.H. Yun, Y. Hu, L. Wang, An electrochemically treated BiVO₄ photoanode for efficient photoelectrochemical water splitting, *Angewandte Chemie International Edition*, 56 (2017) 8500-8504.
- [84] T. Butburee, Y. Bai, H. Wang, H. Chen, Z. Wang, G. Liu, J. Zou, P. Khemthong, G.Q.M. Lu, L. Wang, 2D porous TiO₂ single-crystalline nanostructure demonstrating high photo-electrochemical water splitting performance, *Advanced Materials*, 30 (2018) 1705666.
- [85] S.-C. Wang, F.-Q. Tang, L.-Z. Wang, Visible light responsive metal oxide photoanodes for photoelectrochemical water splitting: a comprehensive review on rational materials design, *Journal of Inorganic Materials*, 33 (2018) 173-196.

- [86] S.n. Murcia-López, C. Fàbrega, D.n. Monllor-Satoca, M.a.D. Hernández-Alonso, G.n. Penelas-Pérez, A. Morata, J.R. Morante, T. Andreu, Tailoring multilayered BiVO₄ photoanodes by pulsed laser deposition for water splitting, *ACS applied materials & interfaces*, 8 (2016) 4076-4085.
- [87] T.W. Kim, K.-S. Choi, Nanoporous BiVO₄ photoanodes with dual-layer oxygen evolution catalysts for solar water splitting, *Science*, 343 (2014) 990-994.
- [88] E.A. Mohamed, Z.N. Zahran, Y. Naruta, Simple preparation of highly active water splitting FTO/BiVO₄ photoanode modified with tri-layer water oxidation catalysts, *Journal of Materials Chemistry A*, 5 (2017) 6825-6831.
- [89] L. Zhou, C. Zhao, B. Giri, P. Allen, X. Xu, H. Joshi, Y. Fan, L.V. Titova, P.M. Rao, High light absorption and charge separation efficiency at low applied voltage from Sb-doped SnO₂/BiVO₄ core/shell nanorod-array photoanodes, *Nano letters*, 16 (2016) 3463-3474.
- [90] F.F. Abdi, N. Firet, R. van de Krol, Efficient BiVO₄ thin film photoanodes modified with Cobalt Phosphate catalyst and W-doping, *ChemCatChem*, 5 (2013) 490-496.
- [91] C. Zachäus, F.F. Abdi, L.M. Peter, R. Van De Krol, Photocurrent of BiVO₄ is limited by surface recombination, not surface catalysis, *Chemical science*, 8 (2017) 3712-3719.
- [92] B.J. Trzeźniewski, I.A. Digdaya, T. Nagaki, S. Ravishankar, I. Herraiz-Cardona, D.A. Vermaas, A. Longo, S. Gimenez, W.A. Smith, Near-complete suppression of surface losses and total internal quantum efficiency in BiVO₄ photoanodes, *Energy & Environmental Science*, 10 (2017) 1517-1529.
- [93] Y. Ma, S.R. Pendlebury, A. Reynal, F. Le Formal, J.R. Durrant, Dynamics of photogenerated holes in undoped BiVO₄ photoanodes for solar water oxidation, *Chemical Science*, 5 (2014) 2964-2973.

- [94] H.W. Jeong, T.H. Jeon, J.S. Jang, W. Choi, H. Park, Strategic modification of BiVO₄ for improving photoelectrochemical water oxidation performance, *The Journal of Physical Chemistry C*, 117 (2013) 9104-9112.
- [95] K.J. McDonald, K.-S. Choi, A new electrochemical synthesis route for a BiOI electrode and its conversion to a highly efficient porous BiVO₄ photoanode for solar water oxidation, *Energy & Environmental Science*, 5 (2012) 8553-8557.
- [96] V. Nair, C.L. Perkins, Q. Lin, M. Law, Textured nanoporous Mo: BiVO₄ photoanodes with high charge transport and charge transfer quantum efficiencies for oxygen evolution, *Energy & Environmental Science*, 9 (2016) 1412-1429.
- [97] Z.-F. Huang, L. Pan, J.-J. Zou, X. Zhang, L. Wang, Nanostructured bismuth vanadate-based materials for solar-energy-driven water oxidation: a review on recent progress, *Nanoscale*, 6 (2014) 14044-14063.
- [98] H.L. Tan, R. Amal, Y.H. Ng, Exploring the different roles of particle size in photoelectrochemical and photocatalytic water oxidation on BiVO₄, *ACS applied materials & interfaces*, 8 (2016) 28607-28614.
- [99] J. Su, L. Guo, N. Bao, C.A. Grimes, Nanostructured WO₃/BiVO₄ heterojunction films for efficient photoelectrochemical water splitting, *Nano letters*, 11 (2011) 1928-1933.
- [100] Y. Pihosh, I. Turkevych, K. Mawatari, J. Uemura, Y. Kazoe, S. Kosar, K. Makita, T. Sugaya, T. Matsui, D. Fujita, Photocatalytic generation of hydrogen by core-shell WO₃/BiVO₄ nanorods with ultimate water splitting efficiency, *Scientific reports*, 5 (2015) 11141.
- [101] J.-S. Yang, J.-J. Wu, Low-potential driven fully-depleted BiVO₄/ZnO heterojunction nanodendrite array photoanodes for photoelectrochemical water splitting, *Nano Energy*, 32 (2017) 232-240.

- [102] L.H. Hess, J.K. Cooper, A. Loiudice, C.-M. Jiang, R. Buonsanti, I.D. Sharp, Probing interfacial energetics and charge transfer kinetics in semiconductor nanocomposites: New insights into heterostructured TiO₂/BiVO₄ photoanodes, *Nano Energy*, 34 (2017) 375-384.
- [103] P.M. Rao, L. Cai, C. Liu, I.S. Cho, C.H. Lee, J.M. Weisse, P. Yang, X. Zheng, Simultaneously efficient light absorption and charge separation in WO₃/BiVO₄ core/shell nanowire photoanode for photoelectrochemical water oxidation, *Nano letters*, 14 (2014) 1099-1105.
- [104] Z. Zhang, B. Chen, M. Baek, K. Yong, Multichannel Charge Transport of a BiVO₄/(RGO/WO₃)/W₁₈O₄₉ Three-Storey Anode for Greatly Enhanced Photoelectrochemical Efficiency, *ACS applied materials & interfaces*, 10 (2018) 6218-6227.
- [105] L. Zhou, Y. Yang, J. Zhang, P.M. Rao, Photoanode with enhanced performance achieved by coating BiVO₄ onto ZnO-templated Sb-doped SnO₂ nanotube scaffold, *ACS applied materials & interfaces*, 9 (2017) 11356-11362.
- [106] H. Jung, S.Y. Chae, C. Shin, B.K. Min, O.-S. Joo, Y.J. Hwang, Effect of the Si/TiO₂/BiVO₄ heterojunction on the onset potential of photocurrents for solar water oxidation, *ACS applied materials & interfaces*, 7 (2015) 5788-5796.
- [107] S.P. Berglund, A.J. Rettie, S. Hoang, C.B. Mullins, Incorporation of Mo and W into nanostructured BiVO₄ films for efficient photoelectrochemical water oxidation, *Physical Chemistry Chemical Physics*, 14 (2012) 7065-7075.
- [108] F.F. Abdi, L. Han, A.H. Smets, M. Zeman, B. Dam, R. Van De Krol, Efficient solar water splitting by enhanced charge separation in a bismuth vanadate-silicon tandem photoelectrode, *Nature communications*, 4 (2013) 2195.

- [109] W. Luo, Z. Yang, Z. Li, J. Zhang, J. Liu, Z. Zhao, Z. Wang, S. Yan, T. Yu, Z. Zou, Solar hydrogen generation from seawater with a modified BiVO₄ photoanode, *Energy & Environmental Science*, 4 (2011) 4046-4051.
- [110] S.K. Pilli, T.E. Furtak, L.D. Brown, T.G. Deutsch, J.A. Turner, A.M. Herring, Cobalt-phosphate (Co-Pi) catalyst modified Mo-doped BiVO₄ photoelectrodes for solar water oxidation, *Energy & Environmental Science*, 4 (2011) 5028-5034.
- [111] M. Rohloff, B.r. Anke, O. Kasian, S. Zhang, M. Lerch, C. Scheu, A. Fischer, Enhanced Photoelectrochemical Water Oxidation Performance by Fluorine Incorporation in BiVO₄ and Mo: BiVO₄ Thin Film Photoanodes, *ACS applied materials & interfaces*, (2019).
- [112] S. Byun, G. Jung, S.-Y. Moon, B. Kim, J.Y. Park, S. Jeon, S.-W. Nam, B. Shin, Compositional engineering of solution-processed BiVO₄ photoanodes toward highly efficient photoelectrochemical water oxidation, *Nano energy*, 43 (2018) 244-252.
- [113] M. Huang, J. Bian, W. Xiong, C. Huang, R. Zhang, Low-dimensional Mo: BiVO₄ photoanodes for enhanced photoelectrochemical activity, *Journal of Materials Chemistry A*, 6 (2018) 3602-3609.
- [114] G. Wang, Y. Yang, Y. Ling, H. Wang, X. Lu, Y.-C. Pu, J.Z. Zhang, Y. Tong, Y. Li, An electrochemical method to enhance the performance of metal oxides for photoelectrochemical water oxidation, *Journal of Materials Chemistry A*, 4 (2016) 2849-2855.
- [115] J.-M. Wu, Y. Chen, L. Pan, P. Wang, Y. Cui, D. Kong, L. Wang, X. Zhang, J.-J. Zou, Multi-layer monoclinic BiVO₄ with oxygen vacancies and V⁴⁺ species for highly efficient visible-light photoelectrochemical applications, *Applied Catalysis B: Environmental*, 221 (2018) 187-195.

- [116] Y. Bu, J. Tian, Z. Chen, Q. Zhang, W. Li, F. Tian, J.P. Ao, Optimization of the Photo-Electrochemical Performance of Mo-Doped BiVO₄ Photoanode by Controlling the Metal–Oxygen Bond State on (020) Facet, *Advanced Materials Interfaces*, 4 (2017) 1601235.
- [117] M.R. Nellist, J. Qiu, F.A. Laskowski, F.M. Toma, S.W. Boettcher, Potential-sensing electrochemical AFM shows CoPi as a hole collector and oxygen evolution catalyst on BiVO₄ water-splitting photoanodes, *ACS Energy Letters*, 3 (2018) 2286-2291.
- [118] M. Zhong, T. Hisatomi, Y. Kuang, J. Zhao, M. Liu, A. Iwase, Q. Jia, H. Nishiyama, T. Minegishi, M. Nakabayashi, Surface Modification of CoO x Loaded BiVO₄ Photoanodes with Ultrathin p-Type NiO Layers for Improved Solar Water Oxidation, *Journal of the American Chemical Society*, 137 (2015) 5053-5060.
- [119] M. Liao, J. Feng, W. Luo, Z. Wang, J. Zhang, Z. Li, T. Yu, Z. Zou, Co₃O₄ nanoparticles as robust water oxidation catalysts towards remarkably enhanced photostability of a Ta₃N₅ photoanode, *Advanced Functional Materials*, 22 (2012) 3066-3074.
- [120] F.F. Abdi, R. van de Krol, Nature and light dependence of bulk recombination in Co-Pi-catalyzed BiVO₄ photoanodes, *The Journal of Physical Chemistry C*, 116 (2012) 9398-9404.
- [121] D.K. Zhong, M. Cornuz, K. Sivula, M. Grätzel, D.R. Gamelin, Photo-assisted electrodeposition of cobalt–phosphate (Co–Pi) catalyst on hematite photoanodes for solar water oxidation, *Energy & Environmental Science*, 4 (2011) 1759-1764.
- [122] F.S. Hegner, I. Herraiz-Cardona, D. Cardenas-Morcoso, N.r. López, J.-R.n. Galán-Mascarós, S. Gimenez, Cobalt hexacyanoferrate on BiVO₄ photoanodes for robust water splitting, *ACS applied materials & interfaces*, 9 (2017) 37671-37681.

- [123] M. Rohloff, B. Anke, S. Zhang, U. Gernert, C. Scheu, M. Lerch, A. Fischer, Mo-doped BiVO₄ thin films–high photoelectrochemical water splitting performance achieved by a tailored structure and morphology, *Sustainable Energy & Fuels*, 1 (2017) 1830-1846.
- [124] X. Cao, C. Xu, X. Liang, J. Ma, M. Yue, Y. Ding, Rationally designed/assembled hybrid BiVO₄-based photoanode for enhanced photoelectrochemical performance, *Applied Catalysis B: Environmental*, 260 (2020) 118136.
- [125] T. Tian, C. Dong, X. Liang, M. Yue, Y. Ding, Enhanced photoelectrochemical water oxidation activity of BiVO₄ by coating of Co-phenolic networks as hole-transfer and co-catalyst, *Journal of Catalysis*, 377 (2019) 684-691.
- [126] D.K. Zhong, S. Choi, D.R. Gamelin, Near-complete suppression of surface recombination in solar photoelectrolysis by “Co-Pi” catalyst-modified W: BiVO₄, *Journal of the American Chemical Society*, 133 (2011) 18370-18377.
- [127] C. Ding, J. Shi, D. Wang, Z. Wang, N. Wang, G. Liu, F. Xiong, C. Li, Visible light driven overall water splitting using cocatalyst/BiVO₄ photoanode with minimized bias, *Physical Chemistry Chemical Physics*, 15 (2013) 4589-4595.
- [128] Y. Ma, F. Le Formal, A. Kafizas, S.R. Pendlebury, J.R. Durrant, Efficient suppression of back electron/hole recombination in cobalt phosphate surface-modified undoped bismuth vanadate photoanodes, *Journal of Materials Chemistry A*, 3 (2015) 20649-20657.
- [129] D. Xue, M. Kan, X. Qian, Y. Zhao, A Tandem Water Splitting Cell Based on Nanoporous BiVO₄ Photoanode Cocatalyzed by Ultrasmall Cobalt Borate Sandwiched with Conformal TiO₂ Layers, *ACS Sustainable Chemistry & Engineering*, 6 (2018) 16228-16234.
- [130] S.K. Choi, W. Choi, H. Park, Solar water oxidation using nickel-borate coupled BiVO₄ photoelectrodes, *Physical Chemistry Chemical Physics*, 15 (2013) 6499-6507.

- [131] M.T. McDowell, M.F. Lichterman, J.M. Spurgeon, S. Hu, I.D. Sharp, B.S. Brunshwig, N.S. Lewis, Improved stability of polycrystalline bismuth vanadate photoanodes by use of dual-layer thin TiO₂/Ni coatings, *The Journal of Physical Chemistry C*, 118 (2014) 19618-19624.
- [132] J.A. Seabold, K.-S. Choi, Efficient and stable photo-oxidation of water by a bismuth vanadate photoanode coupled with an iron oxyhydroxide oxygen evolution catalyst, *Journal of the American Chemical Society*, 134 (2012) 2186-2192.
- [133] Y. Park, D. Kang, K.-S. Choi, Marked enhancement in electron-hole separation achieved in the low bias region using electrochemically prepared Mo-doped BiVO₄ photoanodes, *Physical Chemistry Chemical Physics*, 16 (2014) 1238-1246.
- [134] Y. Kuang, Q. Jia, H. Nishiyama, T. Yamada, A. Kudo, K. Domen, A Front-Illuminated Nanostructured Transparent BiVO₄ Photoanode for > 2% Efficient Water Splitting, *Advanced Energy Materials*, 6 (2016) 1501645.
- [135] F.M. Toma, J.K. Cooper, V. Kunzelmann, M.T. McDowell, J. Yu, D.M. Larson, N.J. Borys, C. Abelyan, J.W. Beeman, K.M. Yu, Mechanistic insights into chemical and photochemical transformations of bismuth vanadate photoanodes, *Nature communications*, 7 (2016) 12012.
- [136] Y. Kuang, Q. Jia, G. Ma, T. Hisatomi, T. Minegishi, H. Nishiyama, M. Nakabayashi, N. Shibata, T. Yamada, A. Kudo, Ultrastable low-bias water splitting photoanodes via photocorrosion inhibition and in situ catalyst regeneration, *Nature Energy*, 2 (2017) 16191.
- [137] S.M. Al-Sofiany, H. Hassan, A. Ashour, M.A. El-Raheem, Study of γ -rays enhanced changes of the ZnO: Al thin film structure and optical properties, *Int. J. Electrochem. Sci*, 9 (2014) 3209-3221.

- [138] A. Abu El-Fadl, E. El-Maghraby, G. Mohamad, Influence of gamma radiation on the absorption spectra and optical energy gap of Li-doped ZnO thin films, *Crystal Research and Technology: Journal of Experimental and Industrial Crystallography*, 39 (2004) 143-150.
- [139] N.D. Hoa, N. Van Quy, D. Kim, Nanowire structured SnO_x–SWNT composites: high performance sensor for NO_x detection, *Sensors and actuators B: Chemical*, 142 (2009) 253-259.
- [140] N. Van Duy, T.H. Toan, N.D. Hoa, N. Van Hieu, Effects of gamma irradiation on hydrogen gas-sensing characteristics of Pd–SnO₂ thin film sensors, *International Journal of Hydrogen Energy*, 40 (2015) 12572-12580.
- [141] N. Lavanya, A. Anithaa, C. Sekar, K. Asokan, A. Bonavita, N. Donato, S. Leonardi, G. Neri, Effect of gamma irradiation on structural, electrical and gas sensing properties of tungsten oxide nanoparticles, *Journal of Alloys and Compounds*, 693 (2017) 366-372.
- [142] A. Indluru, K. Holbert, T. Alford, Gamma radiation effects on indium-zinc oxide thin-film transistors, *Thin Solid Films*, 539 (2013) 342-344.
- [143] N. Lavanya, C. Sekar, A. Anithaa, N. Sudhan, K. Asokan, A. Bonavita, S. Leonardi, G. Neri, Investigations on the effect of gamma-ray irradiation on the gas sensing properties of SnO₂ nanoparticles, *Nanotechnology*, 27 (2016) 385502.
- [144] K. Yin, S. Liu, Q. Cai, A. Gao, S. Lu, M. Shao, The enhanced ammonia gas-sensing activity of gamma ray irradiated indium vanadate nanoribbons, *Journal of Materials Science: Materials in Electronics*, 25 (2014) 419-422.
- [145] Y. Ni, X. Ge, H. Liu, X. Xu, Z. Zhang, γ -Irradiation preparation of CdS nano-particles and their formation mechanism in non-water system, *Radiation Physics and Chemistry*, 61 (2001) 61-64.

- [146] N.A. Mohamed, H. Ullah, J. Safaei, A.F. Ismail, M.F. Mohamad Noh, M.F. Soh, M.A. Ibrahim, N.A. Ludin, M.A. Mat Teridi, Efficient Photoelectrochemical Performance of γ Irradiated g-C₃N₄ and Its g-C₃N₄@ BiVO₄ Heterojunction for Solar Water Splitting, *The Journal of Physical Chemistry C*, 123 (2019) 9013-9026.
- [147] S. Kumar, S. Ahirwar, A.K. Satpati, Insight into the PEC and interfacial charge transfer kinetics at the Mo doped BiVO₄ photoanodes, *RSC Advances*, 9 (2019) 41368-41382.
- [148] M. Noel, K. Vasu, Cyclic voltammetry and the frontiers of electrochemistry, *Aspect*1990.
- [149] Z. Chen, T.G. Deutsch, H.N. Dinh, K. Domen, K. Emery, A.J. Forman, N. Gaillard, R. Garland, C. Heske, T.F. Jaramillo, *UV-vis Spectroscopy, Photoelectrochemical Water Splitting*, Springer2013, pp. 49-62.
- [150] D. Wood, J. Tauc, Weak absorption tails in amorphous semiconductors, *Physical Review B*, 5 (1972) 3144.
- [151] E. Davis, N. Mott, Conduction in non-crystalline systems V. Conductivity, optical absorption and photoconductivity in amorphous semiconductors, *Philosophical Magazine*, 22 (1970) 0903-0922.
- [152] J. Tauc, R. Grigorovici, A. Vancu, Optical properties and electronic structure of amorphous germanium, *physica status solidi (b)*, 15 (1966) 627-637.
- [153] J. Tauc, A. Menth, D. Wood, Optical and magnetic investigations of the localized states in semiconducting glasses, *Physical Review Letters*, 25 (1970) 749.
- [154] Z. Chen, H.N. Dinh, E. Miller, *Photoelectrochemical water splitting*, Springer2013.
- [155] Z. Chen, T.F. Jaramillo, T.G. Deutsch, A. Kleiman-Shwarscstein, A.J. Forman, N. Gaillard, R. Garland, K. Takanabe, C. Heske, M. Sunkara, Accelerating materials development for

photoelectrochemical hydrogen production: Standards for methods, definitions, and reporting protocols, *Journal of Materials Research*, 25 (2010) 3-16.

[156] R. Van de Krol, M. Grätzel, *Photoelectrochemical hydrogen production*, Springer 2012.

[157] I.S. Cho, Z. Chen, A.J. Forman, D.R. Kim, P.M. Rao, T.F. Jaramillo, X. Zheng, Branched TiO₂ nanorods for photoelectrochemical hydrogen production, *Nano Letters*, 11 (2011) 4978-4984.

[158] X. Shi, L. Cai, M. Ma, X. Zheng, J.H. Park, General characterization methods for photoelectrochemical cells for solar water splitting, *ChemSusChem*, 8 (2015) 3192-3203.

[159] A. Hagfeldt, H. Lindström, S. Södergren, S.-E. Lindquist, Photoelectrochemical studies of colloidal TiO₂ films: the effect of oxygen studied by photocurrent transients, *Journal of Electroanalytical Chemistry*, 381 (1995) 39-46.

[160] C.-J. Lin, Y.-T. Lu, C.-H. Hsieh, S.-H. Chien, Surface modification of highly ordered TiO₂ nanotube arrays for efficient photoelectrocatalytic water splitting, *Applied Physics Letters*, 94 (2009) 113102.

[161] M. Etman, Flat-band and photocurrent onset potentials of layered WSe₂ anodes, *Electrochimica Acta*, 35 (1990) 1195-1199.

[162] K. Gelderman, L. Lee, S. Donne, Flat-band potential of a semiconductor: using the Mott–Schottky equation, *Journal of chemical education*, 84 (2007) 685.

[163] E. Barsoukov, J.R. Macdonald, *Impedance spectroscopy: theory, experiment, and applications*, John Wiley & Sons 2018.

[164] R.C. Engstrom, C.M. Pharr, Scanning electrochemical microscopy, *Analytical Chemistry*, 61 (1989) 1099A-1104A.

- [165] F. Zhou, P.R. Unwin, A.J. Bard, Scanning electrochemical microscopy. 16. Study of second-order homogeneous chemical reactions via the feedback and generation/collection modes, *The Journal of Physical Chemistry*, 96 (1992) 4917-4924.
- [166] K. Eckhard, X. Chen, F. Turcu, W. Schuhmann, Redox competition mode of scanning electrochemical microscopy (RC-SECM) for visualisation of local catalytic activity, *physical chemistry chemical physics*, 8 (2006) 5359-5365.
- [167] J. Santana, J. González-Guzmán, L. Fernández-Mérida, S. González, R. Souto, Visualization of local degradation processes in coated metals by means of scanning electrochemical microscopy in the redox competition mode, *Electrochimica Acta*, 55 (2010) 4488-4494.
- [168] G. Denuault, M.V. Mirkin, A.J. Bard, Direct determination of diffusion coefficients by chronoamperometry at microdisk electrodes, *Journal of electroanalytical chemistry and interfacial electrochemistry*, 308 (1991) 27-38.
- [169] A.J. Bard, G. Denuault, R.A. Friesner, B.C. Dornblaser, L.S. Tuckerman, Scanning electrochemical microscopy: theory and application of the transient (chronoamperometric) SECM response, *Analytical chemistry*, 63 (1991) 1282-1288.
- [170] A. Guinier, D. Sainte-Marie Lorrain, X-ray Crystallography.(Book Reviews: X-Ray Diffraction in Crystals, Imperfect Crystals, and Amorphous Bodies), *Science*, 142 (1963) 1564.
- [171] D.A. Skoog, F.J. Holler, S.R. Crouch, Principles of instrumental analysis, Cengage learning 2017.
- [172] R.L. McCreery, Raman spectroscopy for chemical analysis, John Wiley & Sons 2005.
- [173] S.J. Pennycook, B. David, C.B. Williams, Transmission electron microscopy: a textbook for materials science, *Microscopy and Microanalysis*, 16 (2010) 111.

- [174] J. Suntivich, H.A. Gasteiger, N. Yabuuchi, H. Nakanishi, J.B. Goodenough, Y. Shao-Horn, Design principles for oxygen-reduction activity on perovskite oxide catalysts for fuel cells and metal–air batteries, *Nature chemistry*, 3 (2011) 546.
- [175] M. Jahan, Z. Liu, K.P. Loh, A Graphene oxide and copper-centered metal organic framework composite as a tri-functional catalyst for HER, OER, and ORR, *Advanced Functional Materials*, 23 (2013) 5363-5372.
- [176] S. Dresp, F. Luo, R. Schmack, S. Kühl, M. Gliech, P. Strasser, An efficient bifunctional two-component catalyst for oxygen reduction and oxygen evolution in reversible fuel cells, electrolyzers and rechargeable air electrodes, *Energy & Environmental Science*, 9 (2016) 2020-2024.
- [177] Z.W. Seh, J. Kibsgaard, C.F. Dickens, I. Chorkendorff, J.K. Nørskov, T.F. Jaramillo, Combining theory and experiment in electrocatalysis: Insights into materials design, *Science*, 355 (2017) eaad4998.
- [178] J.N. Tiwari, W.G. Lee, S. Sultan, M. Yousuf, A.M. Harzandi, V. Vij, K.S. Kim, High-affinity-assisted nanoscale alloys as remarkable bifunctional catalyst for alcohol oxidation and oxygen reduction reactions, *ACS nano*, 11 (2017) 7729-7735.
- [179] M.G. Walter, E.L. Warren, J.R. McKone, S.W. Boettcher, Q. Mi, E.A. Santori, N.S. Lewis, Solar Water Splitting Cells, *Chemical Reviews*, 110 (2010) 6446-6473.
- [180] J. Li, S. Zhao, G. Zhang, Y. Gao, L. Deng, R. Sun, C.-P. Wong, A facile method to prepare highly compressible three-dimensional graphene-only sponge, *Journal of Materials Chemistry A*, 3 (2015) 15482-15488.
- [181] S. Mao, G. Lu, J. Chen, Three-dimensional graphene-based composites for energy applications, *Nanoscale*, 7 (2015) 6924-6943.

- [182] J. Niu, A. Domenech-Carbó, A. Primo, H. Garcia, Uniform nanoporous graphene sponge from natural polysaccharides as a metal-free electrocatalyst for hydrogen generation, *RSC Advances*, 9 (2019) 99-106.
- [183] Z. Chen, W. Ren, L. Gao, B. Liu, S. Pei, H.-M. Cheng, Three-dimensional flexible and conductive interconnected graphene networks grown by chemical vapour deposition, *Nature materials*, 10 (2011) 424.
- [184] Y. Xu, K. Sheng, C. Li, G. Shi, Self-assembled graphene hydrogel via a one-step hydrothermal process, *ACS nano*, 4 (2010) 4324-4330.
- [185] Z. Tang, S. Shen, J. Zhuang, X. Wang, Noble-metal-promoted three-dimensional macroassembly of single-layered graphene oxide, *Angewandte Chemie International Edition*, 49 (2010) 4603-4607.
- [186] Z.-S. Wu, S. Yang, Y. Sun, K. Parvez, X. Feng, K. Müllen, 3D nitrogen-doped graphene aerogel-supported Fe₃O₄ nanoparticles as efficient electrocatalysts for the oxygen reduction reaction, *Journal of the American Chemical Society*, 134 (2012) 9082-9085.
- [187] M.-Q. Yang, N. Zhang, Y. Wang, Y.-J. Xu, Metal-free, robust, and regenerable 3D graphene–organics aerogel with high and stable photosensitization efficiency, *Journal of catalysis*, 346 (2017) 21-29.
- [188] K. He, G. Chen, G. Zeng, A. Chen, Z. Huang, J. Shi, T. Huang, M. Peng, L. Hu, Three-dimensional graphene supported catalysts for organic dyes degradation, *Applied Catalysis B: Environmental*, 228 (2018) 19-28.
- [189] X. Xin, S.-H. Li, N. Zhang, Z.-R. Tang, Y.-J. Xu, 3D graphene/AgBr/Ag cascade aerogel for efficient photocatalytic disinfection, *Applied Catalysis B: Environmental*, 245 (2019) 343-350.

- [190] Q. Liu, J. Shen, X. Yang, T. Zhang, H. Tang, 3D reduced graphene oxide aerogel-mediated Z-scheme photocatalytic system for highly efficient solar-driven water oxidation and removal of antibiotics, *Applied Catalysis B: Environmental*, 232 (2018) 562-573.
- [191] R. Zhang, M. Ma, Q. Zhang, F. Dong, Y. Zhou, Multifunctional g-C₃N₄/graphene oxide wrapped sponge monoliths as highly efficient adsorbent and photocatalyst, *Applied Catalysis B: Environmental*, 235 (2018) 17-25.
- [192] H. Zou, G. Li, L. Duan, Z. Kou, J. Wang, In situ Coupled Amorphous Cobalt Nitride with Nitrogen-doped Graphene Aerogel as A Trifunctional Electrocatalyst towards Zn-air Battery Driven Full Water Splitting, *Applied Catalysis B: Environmental*, (2019) 118100.
- [193] Z. Sun, W. Fan, T. Liu, Graphene/graphene nanoribbon aerogels as tunable three-dimensional framework for efficient hydrogen evolution reaction, *Electrochimica Acta*, 250 (2017) 91-98.
- [194] Y.-C. Shi, J.-J. Feng, X.-X. Lin, L. Zhang, J. Yuan, Q.-L. Zhang, A.-J. Wang, One-step hydrothermal synthesis of three-dimensional nitrogen-doped reduced graphene oxide hydrogels anchored PtPd alloyed nanoparticles for ethylene glycol oxidation and hydrogen evolution reactions, *Electrochimica Acta*, 293 (2019) 504-513.
- [195] Q. Quan, X. Lin, N. Zhang, Y.-J. Xu, Graphene and its derivatives as versatile templates for materials synthesis and functional applications, *Nanoscale*, 9 (2017) 2398-2416.
- [196] X. Zhang, Z. Sui, B. Xu, S. Yue, Y. Luo, W. Zhan, B. Liu, Mechanically strong and highly conductive graphene aerogel and its use as electrodes for electrochemical power sources, *Journal of Materials Chemistry*, 21 (2011) 6494-6497.

- [197] H.-P. Cong, X.-C. Ren, P. Wang, S.-H. Yu, Macroscopic multifunctional graphene-based hydrogels and aerogels by a metal ion induced self-assembly process, *ACS nano*, 6 (2012) 2693-2703.
- [198] H. Zhang, I. Hussain, M. Brust, M.F. Butler, S.P. Rannard, A.I. Cooper, Aligned two- and three-dimensional structures by directional freezing of polymers and nanoparticles, *Nature materials*, 4 (2005) 787.
- [199] L. Qiu, J.Z. Liu, S.L. Chang, Y. Wu, D. Li, Biomimetic superelastic graphene-based cellular monoliths, *Nature communications*, 3 (2012) 1241.
- [200] J. Zheng, Y. Yan, B. Xu, Correcting the hydrogen diffusion limitation in rotating disk electrode measurements of hydrogen evolution reaction kinetics, *Journal of The Electrochemical Society*, 162 (2015) F1470-F1481.
- [201] H.A. Gasteiger, N.M. Markovic, P.N. Ross Jr, H₂ and CO electrooxidation on well-characterized Pt, Ru, and Pt-Ru. 1. Rotating disk electrode studies of the pure gases including temperature effects, *The Journal of Physical Chemistry*, 99 (1995) 8290-8301.
- [202] T. Schmidt, H. Gasteiger, G. Stäb, P. Urban, D. Kolb, R. Behm, Characterization of high-surface-area electrocatalysts using a rotating disk electrode configuration, *Journal of The Electrochemical Society*, 145 (1998) 2354-2358.
- [203] D.R. Lawson, L.D. Whiteley, C.R. Martin, M.N. Szentirmay, J.I. Song, Oxygen reduction at Nafion film-coated platinum electrodes: transport and kinetics, *Journal of The Electrochemical Society*, 135 (1988) 2247-2253.
- [204] Z. Galus, C. Olson, H. Lee, R. Adams, Rotating disk electrodes, *Analytical Chemistry*, 34 (1962) 164-166.

- [205] F. Gloaguen, F. Andolfatto, R. Durand, P. Ozil, Kinetic study of electrochemical reactions at catalyst-recast ionomer interfaces from thin active layer modelling, *Journal of Applied Electrochemistry*, 24 (1994) 863-869.
- [206] H.A. Gasteiger, S.S. Kocha, B. Sompalli, F.T. Wagner, Activity benchmarks and requirements for Pt, Pt-alloy, and non-Pt oxygen reduction catalysts for PEMFCs, *Applied Catalysis B: Environmental*, 56 (2005) 9-35.
- [207] M. Osawa, M. Tsushima, H. Mogami, G. Samjeske, A. Yamakata, Structure of water at the electrified platinum– water interface: A study by surface-enhanced infrared absorption spectroscopy, *The Journal of Physical Chemistry C*, 112 (2008) 4248-4256.
- [208] M.G. de Chialvo, A. Chialvo, Hydrogen evolution reaction: analysis of the Volmer-Heyrovsky-Tafel mechanism with a generalized adsorption model, *Journal of Electroanalytical Chemistry*, 372 (1994) 209-223.
- [209] M.G. de Chialvo, A. Chialvo, Kinetics of hydrogen evolution reaction with Frumkin adsorption: re-examination of the Volmer–Heyrovsky and Volmer–Tafel routes, *Electrochimica acta*, 44 (1998) 841-851.
- [210] P. Sahoo, R. Aepuru, H.S. Panda, D. Bahadur, Ice-templated synthesis of multifunctional three dimensional graphene/noble metal nanocomposites and their mechanical, electrical, catalytic, and electromagnetic shielding properties, *Scientific reports*, 5 (2015).
- [211] S. Fang, D. Huang, R. Lv, Y. Bai, Z.-H. Huang, J. Gu, F. Kang, Three-dimensional reduced graphene oxide powder for efficient microwave absorption in the S-band (2–4 GHz), *Rsc Advances*, 7 (2017) 25773-25779.
- [212] A.C. Ferrari, J. Robertson, Interpretation of Raman spectra of disordered and amorphous carbon, *Physical review B*, 61 (2000) 14095.

- [213] S. Stankovich, D.A. Dikin, R.D. Piner, K.A. Kohlhaas, A. Kleinhammes, Y. Jia, Y. Wu, S.T. Nguyen, R.S. Ruoff, Synthesis of graphene-based nanosheets via chemical reduction of exfoliated graphite oxide, *carbon*, 45 (2007) 1558-1565.
- [214] Q. Chen, L. Luo, H. Faraji, S.W. Feldberg, H.S. White, Electrochemical measurements of single H₂ nanobubble nucleation and stability at Pt nanoelectrodes, *The journal of physical chemistry letters*, 5 (2014) 3539-3544.
- [215] Q. Chen, L. Luo, H.S. White, Electrochemical generation of a hydrogen bubble at a recessed platinum nanopore electrode, *Langmuir*, 31 (2015) 4573-4581.
- [216] L.-l. Fang, Q. Tao, M.-f. Li, L.-w. Liao, D. Chen, Y.-x. Chen, Determination of the real surface area of palladium electrode, *Chinese Journal of Chemical Physics*, 23 (2010) 543.
- [217] B. Seger, P.V. Kamat, Electrocatalytically active graphene-platinum nanocomposites. Role of 2-D carbon support in PEM fuel cells, *The Journal of Physical Chemistry C*, 113 (2009) 7990-7995.
- [218] M. Łukaszewski, A. Czerwiński, Electrochemical preparation and characterization of thin deposits of Pd-noble metal alloys, *Thin Solid Films*, 518 (2010) 3680-3689.
- [219] M. Søgaaard, M. Odgaard, E.M. Skou, An improved method for the determination of the electrochemical active area of porous composite platinum electrodes, *Solid State Ionics*, 145 (2001) 31-35.
- [220] M. Łukaszewski, A. Czerwiński, Electrochemical behavior of palladium–gold alloys, *Electrochimica acta*, 48 (2003) 2435-2445.
- [221] R. Woods, Chemisorption at electrodes: hydrogen and oxygen on noble metals and their alloys, *Electroanalytical chemistry*, 9 (1976) 1-162.

- [222] M. Boudart, Turnover rates in heterogeneous catalysis, *Chemical reviews*, 95 (1995) 661-666.
- [223] B. Tilak, C.-P. Chen, Generalized analytical expressions for Tafel slope, reaction order and ac impedance for the hydrogen evolution reaction (HER): mechanism of HER on platinum in alkaline media, *Journal of Applied Electrochemistry*, 23 (1993) 631-640.
- [224] B. Conway, B. Tilak, Interfacial processes involving electrocatalytic evolution and oxidation of H₂, and the role of chemisorbed H, *Electrochimica Acta*, 47 (2002) 3571-3594.
- [225] W. Sheng, H.A. Gasteiger, Y. Shao-Horn, Hydrogen oxidation and evolution reaction kinetics on platinum: acid vs alkaline electrolytes, *Journal of The Electrochemical Society*, 157 (2010) B1529-B1536.
- [226] J. Durst, C. Simon, F. Hasché, H.A. Gasteiger, Hydrogen oxidation and evolution reaction kinetics on carbon supported Pt, Ir, Rh, and Pd electrocatalysts in acidic media, *Journal of The Electrochemical Society*, 162 (2015) F190-F203.
- [227] A.J. Bard, R. Parsons, J. Jordan, *Standard potentials in aqueous solution*, CRC press 1985.
- [228] R.A. Van Santen, M. Neurock, *Molecular heterogeneous catalysis: a conceptual and computational approach*, John Wiley & Sons 2009.
- [229] X.H. Xia, X.J. Zhao, W.C. Ye, C.M. Wang, Highly porous Ag-Ag₂S/MoS₂ with additional active sites synthesized by chemical etching method for enhanced electrocatalytic hydrogen evolution, *Electrochimica Acta*, 142 (2014) 173-181.
- [230] Y. Hou, B. Zhang, Z. Wen, S. Cui, X. Guo, Z. He, J. Chen, A 3D hybrid of layered MoS₂/nitrogen-doped graphene nanosheet aerogels: an effective catalyst for hydrogen evolution in microbial electrolysis cells, *Journal of Materials Chemistry A*, 2 (2014) 13795-13800.

- [231] Y. Yan, X. Ge, Z. Liu, J.-Y. Wang, J.-M. Lee, X. Wang, Facile synthesis of low crystalline MoS₂ nanosheet-coated CNTs for enhanced hydrogen evolution reaction, *Nanoscale*, 5 (2013) 7768-7771.
- [232] D. Merki, H. Vrubel, L. Rovelli, S. Fierro, X. Hu, Fe, Co, and Ni ions promote the catalytic activity of amorphous molybdenum sulfide films for hydrogen evolution, *Chemical Science*, 3 (2012) 2515-2525.
- [233] J. Shi, D. Ma, G.-F. Han, Y. Zhang, Q. Ji, T. Gao, J. Sun, X. Song, C. Li, Y. Zhang, X.-Y. Lang, Y. Zhang, Z. Liu, Controllable Growth and Transfer of Monolayer MoS₂ on Au Foils and Its Potential Application in Hydrogen Evolution Reaction, *ACS Nano*, 8 (2014) 10196-10204.
- [234] B. Hinnemann, P.G. Moses, J. Bonde, K.P. Jørgensen, J.H. Nielsen, S. Horch, I. Chorkendorff, J.K. Nørskov, Biomimetic Hydrogen Evolution: MoS₂ Nanoparticles as Catalyst for Hydrogen Evolution, *Journal of the American Chemical Society*, 127 (2005) 5308-5309.
- [235] J. Bonde, P.G. Moses, T.F. Jaramillo, J.K. Nørskov, I. Chorkendorff, Hydrogen evolution on nano-particulate transition metal sulfides, *Faraday Discuss*, 140 (2008) 219-231; discussion 297-317.
- [236] T.F. Jaramillo, J. Bonde, J. Zhang, B.-L. Ooi, K. Andersson, J. Ulstrup, I. Chorkendorff, Hydrogen evolution on supported incomplete cubane-type [Mo₃S₄] 4⁺ electrocatalysts, *The Journal of Physical Chemistry C*, 112 (2008) 17492-17498.
- [237] M.J. Allen, V.C. Tung, R.B. Kaner, Honeycomb Carbon: A Review of Graphene, *Chemical Reviews*, 110 (2010) 132-145.
- [238] K. Chang, W. Chen, L-Cysteine-Assisted Synthesis of Layered MoS₂/Graphene Composites with Excellent Electrochemical Performances for Lithium Ion Batteries, *ACS Nano*, 5 (2011) 4720-4728.

- [239] Q. Ma, X. Zhu, D. Zhang, S. Liu, Graphene oxide - a surprisingly good nucleation seed and adhesion promotion agent for one-step ZnO lithography and optoelectronic applications, *Journal of Materials Chemistry C*, 2 (2014) 8956-8961.
- [240] D. Zhang, Q. Ma, H. Fan, H. Yang, S.F. Liu, Millimeter-long multilayer graphene nanoribbons prepared by wet chemical processing, *Carbon*, 71 (2014) 120-126.
- [241] M. Acerce, D. Voiry, M. Chhowalla, Metallic 1T phase MoS₂ nanosheets as supercapacitor electrode materials, *Nature nanotechnology*, 10 (2015) 313-318.
- [242] S. Bai, L. Wang, X. Chen, J. Du, Y. Xiong, Chemically exfoliated metallic MoS₂ nanosheets: A promising supporting co-catalyst for enhancing the photocatalytic performance of TiO₂ nanocrystals, *Nano Research*, 8 (2015) 175-183.
- [243] R. Coehoorn, C. Haas, J. Dijkstra, C. Flipse, R. De Groot, A. Wold, Electronic structure of MoSe₂, MoS₂, and WSe₂. I. Band-structure calculations and photoelectron spectroscopy, *Physical Review B*, 35 (1987) 6195.
- [244] J.N. Coleman, M. Lotya, A. O'Neill, S.D. Bergin, P.J. King, U. Khan, K. Young, A. Gaucher, S. De, R.J. Smith, Two-dimensional nanosheets produced by liquid exfoliation of layered materials, *Science*, 331 (2011) 568-571.
- [245] K.F. Mak, C. Lee, J. Hone, J. Shan, T.F. Heinz, Atomically thin MoS₂: a new direct-gap semiconductor, *Physical Review Letters*, 105 (2010) 136805.
- [246] H. Li, Q. Zhang, C.C.R. Yap, B.K. Tay, T.H.T. Edwin, A. Olivier, D. Baillargeat, From bulk to monolayer MoS₂: evolution of Raman scattering, *Advanced Functional Materials*, 22 (2012) 1385-1390.
- [247] Á. Caballero, J. Morales, Can the performance of graphene nanosheets for lithium storage in Li-ion batteries be predicted?, *Nanoscale*, 4 (2012) 2083-2092.

- [248] J. Zhang, L. Zhao, A. Liu, X. Li, H. Wu, C. Lu, Three-dimensional MoS₂/rGO hydrogel with extremely high double-layer capacitance as active catalyst for hydrogen evolution reaction, *Electrochimica Acta*, 182 (2015) 652-658.
- [249] Y. Huang, R.J. Nielsen, W.A. Goddard III, M.P. Soriaga, The reaction mechanism with free energy barriers for electrochemical dihydrogen evolution on MoS₂, *Journal of the American Chemical Society*, 137 (2015) 6692-6698.
- [250] A.J. Bard, L.R. Faulkner, Fundamentals and applications, *Electrochemical Methods*, 2 (2001).
- [251] C.C. McCrory, S. Jung, I.M. Ferrer, S.M. Chatman, J.C. Peters, T.F. Jaramillo, Benchmarking hydrogen evolving reaction and oxygen evolving reaction electrocatalysts for solar water splitting devices, *Journal of the American Chemical Society*, 137 (2015) 4347-4357.
- [252] N. Pentland, J.M. Bockris, E. Sheldon, Hydrogen evolution reaction on copper, gold, molybdenum, palladium, rhodium, and iron mechanism and measurement technique under high purity conditions, *Journal of The Electrochemical Society*, 104 (1957) 182-194.
- [253] J. Benson, M. Li, S. Wang, P. Wang, P. Papakonstantinou, Electrocatalytic hydrogen evolution reaction on edges of a few layer molybdenum disulfide nanodots, *ACS applied materials & interfaces*, 7 (2015) 14113-14122.
- [254] Y. Li, H. Wang, L. Xie, Y. Liang, G. Hong, H. Dai, MoS₂ nanoparticles grown on graphene: an advanced catalyst for the hydrogen evolution reaction, *Journal of the American Chemical Society*, 133 (2011) 7296-7299.
- [255] M.A. Lukowski, A.S. Daniel, F. Meng, A. Forticaux, L. Li, S. Jin, Enhanced hydrogen evolution catalysis from chemically exfoliated metallic MoS₂ nanosheets, *J. Am. Chem. Soc.*, 135 (2013) 10274-10277.

- [256] D. Voiry, M. Salehi, R. Silva, T. Fujita, M. Chen, T. Asefa, V.B. Shenoy, G. Eda, M. Chhowalla, Conducting MoS₂ nanosheets as catalysts for hydrogen evolution reaction, *Nano Lett*, 13 (2013) 6222-6227.
- [257] D.R. Dreyer, S. Park, C.W. Bielawski, R.S. Ruoff, The chemistry of graphene oxide, *Chemical Society Reviews*, 39 (2010) 228-240.
- [258] W. Gao, G. Wu, M.T. Janicke, D.A. Cullen, R. Mukundan, J.K. Baldwin, E.L. Brosha, C. Galande, P.M. Ajayan, K.L. More, Ozonated graphene oxide film as a proton-exchange membrane, *Angewandte Chemie International Edition*, 53 (2014) 3588-3593.
- [259] T. Szabó, E. Tombácz, E. Illés, I. Dékány, Enhanced acidity and pH-dependent surface charge characterization of successively oxidized graphite oxides, *Carbon*, 44 (2006) 537-545.
- [260] M. Vinothkannan, R. Kannan, A.R. Kim, G.G. Kumar, K.S. Nahm, D.J. Yoo, Facile enhancement in proton conductivity of sulfonated poly (ether ether ketone) using functionalized graphene oxide—synthesis, characterization, and application towards proton exchange membrane fuel cells, *Colloid and Polymer Science*, 294 (2016) 1197-1207.
- [261] P. Thangasamy, N. Ilayaraja, D. Jeyakumar, M. Sathish, Electrochemical cycling and beyond: unrevealed activation of MoO₃ for electrochemical hydrogen evolution reactions, *Chemical Communications*, 53 (2017) 2245-2248.
- [262] X. Lu, Y. Lin, H. Dong, W. Dai, X. Chen, X. Qu, X. Zhang, One-Step Hydrothermal Fabrication of Three-dimensional MoS₂ Nanoflower using Polypyrrole as Template for Efficient Hydrogen Evolution Reaction, *Scientific Reports*, 7 (2017).
- [263] M. Metikoš-Huković, A. Jukić, Correlation of electronic structure and catalytic activity of Zr–Ni amorphous alloys for the hydrogen evolution reaction, *Electrochimica acta*, 45 (2000) 4159-4170.

- [264] Z. Zheng, N. Li, C.-Q. Wang, D.-Y. Li, Y.-M. Zhu, G. Wu, Ni–CeO₂ composite cathode material for hydrogen evolution reaction in alkaline electrolyte, *international journal of hydrogen energy*, 37 (2012) 13921-13932.
- [265] S. Morin, H. Dumont, B. Conway, Evaluation of the effect of two-dimensional geometry of Pt single-crystal faces on the kinetics of upd of H using impedance spectroscopy, *Journal of Electroanalytical Chemistry*, 412 (1996) 39-52.
- [266] M.E. Lyons, M.P. Brandon, The significance of electrochemical impedance spectra recorded during active oxygen evolution for oxide covered Ni, Co and Fe electrodes in alkaline solution, *Journal of Electroanalytical Chemistry*, 631 (2009) 62-70.
- [267] B. Conway, E. Gileadi, Kinetic theory of pseudo-capacitance and electrode reactions at appreciable surface coverage, *Transactions of the Faraday Society*, 58 (1962) 2493-2509.
- [268] A.J. Bard, *Scanning Electrochemical Microscopy*, New York, 2001.
- [269] H. Li, M. Du, M.J. Mleczko, A.L. Koh, Y. Nishi, E. Pop, A.J. Bard, X. Zheng, Kinetic study of hydrogen evolution reaction over strained MoS₂ with sulfur vacancies using scanning electrochemical microscopy, *Journal of the American Chemical Society*, 138 (2016) 5123-5129.
- [270] H.S. Ahn, A.J. Bard, Electrochemical Surface Interrogation of a MoS₂ Hydrogen-Evolving Catalyst: In Situ Determination of the Surface Hydride Coverage and the Hydrogen Evolution Kinetics, *The Journal of Physical Chemistry Letters*, 7 (2016) 2748-2752.
- [271] Q. Tang, D.-e. Jiang, Mechanism of hydrogen evolution reaction on 1T-MoS₂ from first principles, *ACS Catalysis*, 6 (2016) 4953-4961.
- [272] J. Yang, K. Wang, J. Zhu, C. Zhang, T. Liu, Self-Templated Growth of Vertically Aligned 2H-1T MoS₂ for Efficient Electrocatalytic Hydrogen Evolution, *ACS Applied Materials & Interfaces*, 8 (2016) 31702-31708.

- [273] J. Turner, Sverdrup g, Mann MK, Maness PC, Kroposki B, Ghirardi, Evans RJ, Blake D. Renewable hydrogen production, *International Journal of Energy Research*, 32 (2008) 379-407.
- [274] C. Du, J. Mo, H. Li, Renewable hydrogen production by alcohols reforming using plasma and plasma-catalytic technologies: challenges and opportunities, *Chemical reviews*, 115 (2014) 1503-1542.
- [275] T. Faunce, S. Styring, M.R. Wasielewski, G.W. Brudvig, A.W. Rutherford, J. Messinger, A.F. Lee, C.L. Hill, H. Degroot, M. Fontecave, Artificial photosynthesis as a frontier technology for energy sustainability, *Energy & Environmental Science*, 6 (2013) 1074-1076.
- [276] T. Hisatomi, J. Kubota, K. Domen, Recent advances in semiconductors for photocatalytic and photoelectrochemical water splitting, *Chemical Society Reviews*, 43 (2014) 7520-7535.
- [277] B. Klahr, S. Gimenez, F. Fabregat-Santiago, J. Bisquert, T.W. Hamann, Photoelectrochemical and impedance spectroscopic investigation of water oxidation with “Co–Pi”-coated hematite electrodes, *Journal of the American Chemical Society*, 134 (2012) 16693-16700.
- [278] J. Kwak, A.J. Bard, Scanning electrochemical microscopy. Theory of the feedback mode, *Analytical Chemistry*, 61 (1989) 1221-1227.
- [279] C.M. Sánchez-Sánchez, J. Rodríguez-López, A.J. Bard, Scanning electrochemical microscopy. 60. Quantitative calibration of the SECM substrate generation/tip collection mode and its use for the study of the oxygen reduction mechanism, *Analytical chemistry*, 80 (2008) 3254-3260.
- [280] F. Li, P.R. Unwin, Scanning electrochemical microscopy (SECM) of photoinduced electron transfer kinetics at liquid/liquid interfaces, *The Journal of Physical Chemistry C*, 119 (2015) 4031-4043.

- [281] P. Bertoncello, Advances on scanning electrochemical microscopy (SECM) for energy, *Energy & Environmental Science*, 3 (2010) 1620-1633.
- [282] B.C. Shah, A.C. Hillier, Imaging the Reactivity of Electro-oxidation Catalysts with the Scanning Electrochemical Microscope, *Journal of The Electrochemical Society*, 147 (2000) 3043-3048.
- [283] H. Ye, J. Lee, J.S. Jang, A.J. Bard, Rapid screening of BiVO₄-based photocatalysts by scanning electrochemical microscopy (SECM) and studies of their photoelectrochemical properties, *The Journal of Physical Chemistry C*, 114 (2010) 13322-13328.
- [284] D. Zigah, J. Rodríguez-López, A.J. Bard, Quantification of photoelectrogenerated hydroxyl radical on TiO₂ by surface interrogation scanning electrochemical microscopy, *Physical Chemistry Chemical Physics*, 14 (2012) 12764-12772.
- [285] H.S. Park, K.C. Leonard, A.J. Bard, Surface interrogation scanning electrochemical microscopy (SI-SECM) of photoelectrochemistry at a W/Mo-BiVO₄ semiconductor electrode: quantification of hydroxyl radicals during water oxidation, *The Journal of Physical Chemistry C*, 117 (2013) 12093-12102.
- [286] W.J. Albery, G.J. O'Shea, A.L. Smith, Interpretation and use of Mott–Schottky plots at the semiconductor/electrolyte interface, *Journal of the Chemical Society, Faraday Transactions*, 92 (1996) 4083-4085.
- [287] J.E. Thorne, S. Li, C. Du, G. Qin, D. Wang, Energetics at the surface of photoelectrodes and its influence on the photoelectrochemical properties, *The journal of physical chemistry letters*, 6 (2015) 4083-4088.

- [288] B. Iandolo, B. Wickman, I. Zorić, A. Hellman, The rise of hematite: origin and strategies to reduce the high onset potential for the oxygen evolution reaction, *Journal of Materials Chemistry A*, 3 (2015) 16896-16912.
- [289] J.H. Baek, B.J. Kim, G.S. Han, S.W. Hwang, D.R. Kim, I.S. Cho, H.S. Jung, BiVO₄/WO₃/SnO₂ double-heterojunction photoanode with enhanced charge separation and visible-transparency for bias-free solar water-splitting with a perovskite solar cell, *ACS applied materials & interfaces*, 9 (2017) 1479-1487.
- [290] K. Ding, B. Chen, Z. Fang, Y. Zhang, Z. Chen, Why the photocatalytic activity of Mo-doped BiVO₄ is enhanced: a comprehensive density functional study, *Physical Chemistry Chemical Physics*, 16 (2014) 13465-13476.
- [291] Z. Zhao, W. Luo, Z. Li, Z. Zou, Density functional theory study of doping effects in monoclinic clinobisvanite BiVO₄, *Physics Letters A*, 374 (2010) 4919-4927.
- [292] D. Zhou, L.-X. Pang, W.-G. Qu, C.A. Randall, J. Guo, Z.-M. Qi, T. Shao, X. Yao, Dielectric behavior, band gap, in situ X-ray diffraction, Raman and infrared study on (1-x) BiVO₄-x (Li_{0.5}Bi_{0.5})MoO₄ solid solution, *RSC Advances*, 3 (2013) 5009-5014.
- [293] S. Thalluri, C. Martinez-Suarez, A. Virga, N. Russo, G. Saracco, Insights from crystal size and band gap on the catalytic activity of monoclinic BiVO₄, *International Journal of Chemical Engineering and Applications*, 4 (2013) 305.
- [294] D. Zhou, W. Qu, C. Randall, L. Pang, H. Wang, X. Wu, J. Guo, G. Zhang, L. Shui, Q. Wang, Ferroelastic phase transition compositional dependence for solid-solution [(Li_{0.5}Bi_{0.5})_xBi_{1-x}][Mo_xV_{1-x}]O₄ scheelite-structured microwave dielectric ceramics, *Acta Materialia*, 59 (2011) 1502-1509.

- [295] J. Yu, A. Kudo, Effects of structural variation on the photocatalytic performance of hydrothermally synthesized BiVO₄, *Advanced Functional Materials*, 16 (2006) 2163-2169.
- [296] R.L. Frost, D.A. Henry, M.L. Weier, W. Martens, Raman spectroscopy of three polymorphs of BiVO₄: clinobisvanite, dreyerite and pucherite, with comparisons to (VO₄)³⁻-bearing minerals: namibite, pottsite and schumacherite, *Journal of Raman Spectroscopy: An International Journal for Original Work in all Aspects of Raman Spectroscopy, Including Higher Order Processes, and also Brillouin and Rayleigh Scattering*, 37 (2006) 722-732.
- [297] F.D. Hardcastle, I.E. Wachs, Determination of vanadium-oxygen bond distances and bond orders by Raman spectroscopy, *The Journal of Physical Chemistry*, 95 (1991) 5031-5041.
- [298] L. Chen, E. Alarcón-Lladó, M. Hettick, I.D. Sharp, Y. Lin, A. Javey, J.W. Ager, Reactive sputtering of bismuth vanadate photoanodes for solar water splitting, *The Journal of Physical Chemistry C*, 117 (2013) 21635-21642.
- [299] J. Su, X.-X. Zou, G.-D. Li, X. Wei, C. Yan, Y.-N. Wang, J. Zhao, L.-J. Zhou, J.-S. Chen, Macroporous V₂O₅-BiVO₄ composites: effect of heterojunction on the behavior of photogenerated charges, *The Journal of Physical Chemistry C*, 115 (2011) 8064-8071.
- [300] N. Myung, S. Ham, S. Choi, Y. Chae, W.-G. Kim, Y.J. Jeon, K.-J. Paeng, W. Chanmanee, N.R. de Tacconi, K. Rajeshwar, Tailoring interfaces for electrochemical synthesis of semiconductor films: BiVO₄, Bi₂O₃, or composites, *The Journal of Physical Chemistry C*, 115 (2011) 7793-7800.
- [301] C.D. Wagner, NIST X-ray photoelectron spectroscopy database, NIST Standard Reference Database 20, (2000).
- [302] J.-G. Choi, L. Thompson, XPS study of as-prepared and reduced molybdenum oxides, *Applied Surface Science*, 93 (1996) 143-149.

- [303] K.P.S. Parmar, H.J. Kang, A. Bist, P. Dua, J.S. Jang, J.S. Lee, Photocatalytic and photoelectrochemical water oxidation over metal-doped monoclinic BiVO₄ Photoanodes, *ChemSusChem*, 5 (2012) 1926-1934.
- [304] X. Wan, F. Niu, J. Su, L. Guo, Enhanced photoelectrochemical water oxidation of bismuth vanadate via a combined strategy of W doping and surface RGO modification, *Physical Chemistry Chemical Physics*, 18 (2016) 31803-31810.
- [305] J.H. Kim, Y.H. Jo, J.H. Kim, J.S. Lee, Ultrafast fabrication of highly active BiVO₄ photoanodes by hybrid microwave annealing for unbiased solar water splitting, *Nanoscale*, 8 (2016) 17623-17631.
- [306] L. Zhang, Z. Dai, G. Zheng, Z. Yao, J. Mu, Superior visible light photocatalytic performance of reticular BiVO₄ synthesized via a modified sol-gel method, *RSC advances*, 8 (2018) 10654-10664.
- [307] L. Shi, S. Zhuo, M. Abulikemu, G. Mettela, T. Palaniselvam, S. Rasul, B. Tang, B. Yan, N.B. Saleh, P. Wang, Annealing temperature effects on photoelectrochemical performance of bismuth vanadate thin film photoelectrodes, *RSC advances*, 8 (2018) 29179-29188.
- [308] H. Luo, A.H. Mueller, T.M. McCleskey, A.K. Burrell, E. Bauer, Q. Jia, Structural and photoelectrochemical properties of BiVO₄ thin films, *The Journal of Physical Chemistry C*, 112 (2008) 6099-6102.
- [309] W. Yao, H. Iwai, J. Ye, Effects of molybdenum substitution on the photocatalytic behavior of BiVO₄, *Dalton Transactions*, (2008) 1426-1430.
- [310] M. Valant, D. Suvorov, Chemical compatibility between silver electrodes and low-firing binary-oxide compounds: conceptual study, *Journal of the American Ceramic Society*, 83 (2000) 2721-2729.

- [311] I.S. Cho, C.H. Lee, Y. Feng, M. Logar, P.M. Rao, L. Cai, D.R. Kim, R. Sinclair, X. Zheng, Codoping titanium dioxide nanowires with tungsten and carbon for enhanced photoelectrochemical performance, *Nature communications*, 4 (2013) 1723.
- [312] H. Dotan, K. Sivula, M. Grätzel, A. Rothschild, S.C. Warren, Probing the photoelectrochemical properties of hematite ($\alpha\text{-Fe}_2\text{O}_3$) electrodes using hydrogen peroxide as a hole scavenger, *Energy & Environmental Science*, 4 (2011) 958-964.
- [313] H.S. Park, H.-W. Ha, R.S. Ruoff, A.J. Bard, On the improvement of photoelectrochemical performance and finite element analysis of reduced graphene oxide– BiVO_4 composite electrodes, *Journal of Electroanalytical Chemistry*, 716 (2014) 8-15.
- [314] B.J. Trzeźniewski, W.A. Smith, Photocharged BiVO_4 photoanodes for improved solar water splitting, *Journal of Materials Chemistry A*, 4 (2016) 2919-2926.
- [315] E.Y. Liu, J.E. Thorne, Y. He, D. Wang, Understanding photocharging effects on bismuth vanadate, *ACS applied materials & interfaces*, 9 (2017) 22083-22087.
- [316] R. Cammack, M.J. Barber, R.C. Bray, Oxidation-reduction potentials of molybdenum, flavin and iron-sulphur centres in milk xanthine oxidase, *Biochemical Journal*, 157 (1976) 469-478.
- [317] A.J. Bard, M.V. Mirkin, *Scanning electrochemical microscopy*, CRC Press 2012.
- [318] J.M. Barforoush, T.E. Seufferling, D.T. Jantz, K.R. Song, K.C. Leonard, Insights into the active electrocatalytic areas of layered double hydroxide and amorphous nickel–iron oxide oxygen evolution electrocatalysts, *ACS Applied Energy Materials*, 1 (2018) 1415-1423.
- [319] J.Y. Kim, H.S. Ahn, A.J. Bard, Surface interrogation scanning electrochemical microscopy for a photoelectrochemical reaction: water oxidation on a hematite surface, *Analytical chemistry*, 90 (2018) 3045-3049.

- [320] T. Sun, D. Wang, M.V. Mirkin, H. Cheng, J.-C. Zheng, R.M. Richards, F. Lin, H.L. Xin, Direct high-resolution mapping of electrocatalytic activity of semi-two-dimensional catalysts with single-edge sensitivity, *Proceedings of the National Academy of Sciences*, 116 (2019) 11618-11623.
- [321] P. Li, Z. Jin, Y. Qian, Z. Fang, D. Xiao, G. Yu, Probing Enhanced Site Activity of Co–Fe Bimetallic Subnanoclusters Derived from Dual Cross-Linked Hydrogels for Oxygen Electrocatalysis, *ACS Energy Letters*, 4 (2019) 1793-1802.
- [322] J.M. Barforoush, D.T. Jantz, T.E. Seufferling, K.R. Song, L.C. Cummings, K.C. Leonard, Microwave-assisted synthesis of a nanoamorphous (Ni_{0.8}, Fe_{0.2}) oxide oxygen-evolving electrocatalyst containing only “fast” sites, *Journal of Materials Chemistry A*, 5 (2017) 11661-11670.
- [323] N.L. Ritzert, J.n. Rodríguez-López, C. Tan, H.c.D. Abruña, Kinetics of interfacial electron transfer at single-layer graphene electrodes in aqueous and nonaqueous solutions, *Langmuir*, 29 (2013) 1683-1694.
- [324] J. Wang, J. Zhao, F. Osterloh, Photochemical charge transfer observed in nanoscale hydrogen evolving photocatalysts using surface photovoltage spectroscopy, *Energy & Environmental Science*, 8 (2015) 2970-2976.
- [325] J.W. Ager, M.R. Shaner, K.A. Walczak, I.D. Sharp, S. Ardo, Experimental demonstrations of spontaneous, solar-driven photoelectrochemical water splitting, *Energy & Environmental Science*, 8 (2015) 2811-2824.
- [326] L. Han, F.F. Abdi, R. van de Krol, R. Liu, Z. Huang, H.J. Lewerenz, B. Dam, M. Zeman, A.H. Smets, Efficient water-splitting device based on a bismuth vanadate photoanode and thin-film silicon solar cells, *ChemSusChem*, 7 (2014) 2832-2838.

- [327] Y. Zhou, L. Zhang, L. Lin, B.R. Wygant, Y. Liu, Y. Zhu, Y. Zheng, C.B. Mullins, Y. Zhao, X. Zhang, Highly efficient photoelectrochemical water splitting from hierarchical WO₃/BiVO₄ nanoporous sphere arrays, *Nano letters*, 17 (2017) 8012-8017.
- [328] G. Xi, J. Ye, Synthesis of bismuth vanadate nanoplates with exposed {001} facets and enhanced visible-light photocatalytic properties, *Chemical Communications*, 46 (2010) 1893-1895.
- [329] C.W. Kim, Y.S. Son, M.J. Kang, D.Y. Kim, Y.S. Kang, (040)-Crystal Facet Engineering of BiVO₄ Plate Photoanodes for Solar Fuel Production, *Advanced Energy Materials*, 6 (2016) 1501754.
- [330] Y. Surendranath, M. Dinca, D.G. Nocera, Electrolyte-dependent electrosynthesis and activity of cobalt-based water oxidation catalysts, *Journal of the American Chemical Society*, 131 (2009) 2615-2620.
- [331] J. Lee, H. Ye, S. Pan, A.J. Bard, Screening of photocatalysts by scanning electrochemical microscopy, *Analytical chemistry*, 80 (2008) 7445-7450.
- [332] A.J. Bard, L.R. Faulkner, Fundamentals and applications, *Electrochemical Methods*, 2 (2001) 580-632.
- [333] N.L. Ritzert, J. Rodriguez-Lopez, C. Tan, H.c.D. Abruña, Kinetics of interfacial electron transfer at single-layer graphene electrodes in aqueous and nonaqueous solutions, *Langmuir : the ACS journal of surfaces and colloids*, 29 (2013) 1683-1694.
- [334] S. Rastgar, G. Wittstock, Characterization of Photoactivity of Nanostructured BiVO₄ at Polarized Liquid-Liquid Interfaces by Scanning Electrochemical Microscopy, *The Journal of Physical Chemistry C*, 121 (2017) 25941-25948.

- [335] S. Rastgar, M. Pilarski, G. Wittstock, A polarized liquid–liquid interface meets visible light-driven catalytic water oxidation, *Chemical communications*, 52 (2016) 11382-11385.
- [336] G. Wittstock, M. Burchardt, S.E. Pust, Y. Shen, C. Zhao, Scanning electrochemical microscopy for direct imaging of reaction rates, *Angewandte Chemie International Edition*, 46 (2007) 1584-1617.
- [337] M. Plaza, X. Huang, J.P. Ko, M. Shen, B.H. Simpson, J. Rodríguez-López, N.L. Ritzert, K. Letchworth-Weaver, D. Gunceler, D.G. Schlom, Structure of the photo-catalytically active surface of SrTiO₃, *Journal of the American Chemical Society*, 138 (2016) 7816-7819.
- [338] B.H. Simpson, J.n. Rodríguez-López, Electrochemical imaging and redox interrogation of surface defects on operating SrTiO₃ photoelectrodes, *Journal of the American Chemical Society*, 137 (2015) 14865-14868.
- [339] J.H. Bae, A.B. Nepomnyashchii, X. Wang, D.V. Potapenko, M.V. Mirkin, Photo-Scanning Electrochemical Microscopy on the Nanoscale with Through-Tip Illumination, *Analytical chemistry*, 91 (2019) 12601-12605.
- [340] R. Jin, X. Ye, J. Fan, D. Jiang, H.-Y. Chen, In situ imaging of photocatalytic activity at titanium dioxide nanotubes using scanning ion conductance microscopy, *Analytical chemistry*, 91 (2019) 2605-2609.
- [341] S. Chen, S. Prins, A. Chen, Patterning of BiVO₄ Surfaces and Monitoring of Localized Catalytic Activity using Scanning Photoelectrochemical Microscopy, *ACS applied materials & interfaces*, (2020).
- [342] M.W. Kanan, D.G. Nocera, In situ formation of an oxygen-evolving catalyst in neutral water containing phosphate and Co²⁺, *Science*, 321 (2008) 1072-1075.

- [343] C. Ding, J. Shi, D. Wang, Z. Wang, N. Wang, G. Liu, F. Xiong, C. Li, Visible light driven overall water splitting using cocatalyst/BiVO₄ photoanode with minimized bias, *Physical chemistry chemical physics : PCCP*, 15 (2013) 4589-4595.
- [344] G. Liu, F. Li, Y. Zhu, J. Li, L. Sun, Cobalt doped BiVO₄ with rich oxygen vacancies for efficient photoelectrochemical water oxidation, *RSC Advances*, 10 (2020) 28523-28526.
- [345] W. Lv, Z. Liu, J. Lan, Z. Liu, W. Mi, J. Lei, L. Wang, Y. Liu, J. Zhang, Visible-light-induced reduction of hexavalent chromium utilizing cobalt phosphate (Co-Pi) sensitized inverse opal TiO₂ as a photocatalyst, *Catalysis Science & Technology*, 7 (2017) 5687-5693.
- [346] J. Villanueva-Cab, P. Olalde-Velasco, A. Romero-Contreras, Z. Zhuo, F. Pan, S.E. Rodil, W. Yang, U. Pal, Photocharging and Band Gap Narrowing Effects on the Performance of Plasmonic Photoelectrodes in Dye-Sensitized Solar Cells, *ACS applied materials & interfaces*, 10 (2018) 31374-31383.
- [347] X. Chang, T. Wang, P. Zhang, J. Zhang, A. Li, J. Gong, Enhanced surface reaction kinetics and charge separation of p-n heterojunction Co₃O₄/BiVO₄ photoanodes, *Journal of the American Chemical Society*, 137 (2015) 8356-8359.
- [348] G. Ge, M. Liu, C. Liu, W. Zhou, D. Wang, L. Liu, J. Ye, Ultrathin FeOOH nanosheets as an efficient cocatalyst for photocatalytic water oxidation, *Journal of materials chemistry A*, 7 (2019) 9222-9229.
- [349] J. Deng, X. Lv, J. Zhong, Photocharged Fe₂TiO₅/Fe₂O₃ Photoanode for Enhanced Photoelectrochemical Water Oxidation, *The Journal of Physical Chemistry C*, 122 (2018) 29268-29273.
- [350] W. Smith, Photocharged BiVO₄ photoanodes for improved solar water splitting, *J. Mater. Chem. A*, 2016, Advance Article, (2015).

- [351] J. Liu, J. Li, M. Shao, M. Wei, Directed synthesis of SnO₂@BiVO₄/Co-Pi photoanode for highly efficient photoelectrochemical water splitting and urea oxidation, *Journal of Materials Chemistry A*, 7 (2019) 6327-6336.
- [352] Y. Dai, J. Yu, C. Cheng, P. Tan, M. Ni, Engineering the interfaces in water-splitting photoelectrodes—an overview of the technique development, *Journal of Materials Chemistry A*, (2020).
- [353] B. Klahr, T. Hamann, Water oxidation on hematite photoelectrodes: insight into the nature of surface states through in situ spectroelectrochemistry, *The Journal of Physical Chemistry C*, 118 (2014) 10393-10399.
- [354] O. Zandi, T.W. Hamann, Enhanced water splitting efficiency through selective surface state removal, *The journal of physical chemistry letters*, 5 (2014) 1522-1526.
- [355] L. Bertoluzzi, L. Badia-Bou, F. Fabregat-Santiago, S. Gimenez, J. Bisquert, Interpretation of cyclic voltammetry measurements of thin semiconductor films for solar fuel applications, *The journal of physical chemistry letters*, 4 (2013) 1334-1339.
- [356] Y. Zhang, Y. Guo, H. Duan, H. Li, C. Sun, H. Liu, Facile synthesis of V⁴⁺ self-doped,[010] oriented BiVO₄ nanorods with highly efficient visible light-induced photocatalytic activity, *Physical Chemistry Chemical Physics*, 16 (2014) 24519-24526.
- [357] F. Conzuelo, K. Sliozberg, R. Gutkowski, S. Grütze, M. Nebel, W. Schuhmann, High-resolution analysis of photoanodes for water splitting by means of scanning photoelectrochemical microscopy, *Analytical chemistry*, 89 (2017) 1222-1228.
- [358] S. Chen, S. Prins, A. Chen, Patterning of BiVO₄ Surfaces and Monitoring of Localized Catalytic Activity Using Scanning Photoelectrochemical Microscopy, *ACS applied materials & interfaces*, 12 (2020) 18065-18073.

[359] A.J. Rettie, H.C. Lee, L.G. Marshall, J.-F. Lin, C. Capan, J. Lindemuth, J.S. McCloy, J. Zhou, A.J. Bard, C.B. Mullins, Combined charge carrier transport and photoelectrochemical characterization of BiVO₄ single crystals: intrinsic behavior of a complex metal oxide, *Journal of the American Chemical Society*, 135 (2013) 11389-11396.

[360] L. Xi, F. Wang, C. Schwanke, F.F. Abdi, R. Golnak, S. Fiechter, K. Ellmer, R. van de Krol, K.M. Lange, In situ structural study of MnPi-modified BiVO₄ photoanodes by soft X-ray absorption spectroscopy, *The Journal of Physical Chemistry C*, 121 (2017) 19668-19676.



Homi Bhabha National Institute

Report of Ph.D. Viva-Voce

Board of Studies in Chemical Sciences

A. General Details:

1. Name of the Constituent Institution: Bhabha Atomic Research Centre

2. Name of the Student: Sriram Kumar

3. Enrolment Number: CHEM01201404025

4. Date of Enrolment in HBNI: 1st August 2014

5. Date of Submission of Thesis: 26th October 2020

6. Title of the Thesis: Investigation of Bi-metallic Oxide Composites for electrochemical and Photoelectrochemical Splitting of Water

7. Number of Doctoral Committee Meetings held with respective dates:

Review Period	Date	Review Period	Date
1. OGC	28/06/2017	2. 01/07/2015-30/06/2017	10/07/2017
3. 01/07/2017-31/07/2018	03/08/2018	4. 01/08/2018-01/03/2019	01/03/2019
5. 02/03/2019-27/12/2019	27/12/2019	6.	

8. Name and Affiliation of the Thesis Examiner 1: Prof. Dipankar Koley, Associate Professor, Department of Chemistry, Oregon State University, Corvallis, Oregon 97331.

Recommendations of the Examiner 1 (Thesis Evaluation) ~~(i)~~ accepted, (ii) accepted after revisions, or (iii) rejected:

9. Name and Affiliation of the Thesis Examiner 2: Prof. Amartya Mukhopadhyay, Associate Professor, Department of Metallurgical Engineering and Materials Science, Indian Institute of Technology Bombay, Mumbai.

Recommendations of the Examiner 2 (Thesis Evaluation) (i) accepted, ~~(ii)~~ accepted after revisions, or (iii) rejected:

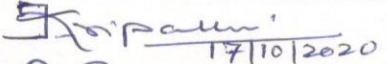
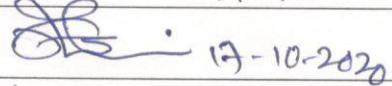
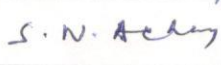
B. Record of the Viva-Voce Examination

1. **Date of Viva Voce Examination:** 17th October 2020
2. **Name and affiliation of External Examiner:** Prof. Amartya Mukhopadhyay, IIT-Bombay, Mumbai.

The Final PhD Viva Voce examination of Sriram Kumar, PhD student HBNI (Enrolment number CHEM01201404025) was held on 17-10-2020 for the PhD thesis entitled "Investigation of Bi-metallic Oxide Composites for electrochemical and Photoelectrochemical Splitting of Water". Sriram Kumar presented the PhD work on the cathode and anode materials developed for the water splitting experiment to generate photoelectrochemical generation of hydrogen and oxygen from water. The 3D graphene and noble metal composites are synthesised and 3D graphene Pt composite has shown superior performance compared to commercially available Pt/C catalytic system. MoS₂/graphene oxide and MoS₂/reduced graphene oxide composite materials are investigated as non-noble metal based catalyst, significant improvement has been observed in the composite materials, compared to the reported literature on similar material. The modified BiVO₄ photoanodes generated through several modification protocols have shown interesting electrochemical properties and the catalytic performances are improved significantly. The modifications strategies like, SnO₂, interlayer formation, Mo doping, effect of photocharging, effect of gamma radiation on the performance of the photoanode have been discussed. The interfacial charge transport properties are investigated using scanning electrochemical microscope in the line to explain the difference in the performance of the modified BiVO₄ photoanodes.

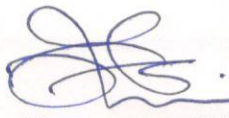
In addition to the doctoral committee members, the faculty members, students as listed in the attached sheet, attended the Viva Voce examination through online mode. Sriram Kumar presented the thesis well and explained to the questions asked during the thesis presentation. The external examiner, all the members of the doctoral committee and faculty members attended the Viva Voce examination unanimously recommended the acceptance of the thesis and awarding the PhD degree to Sriram Kumar.

3. **Attendance at Viva Voce (Doctoral Committee, External Examiner, others):**

Sr No	Composition	Name	Attended in person or through video; if in person, signature
1.	Chairman	Prof. A. K. Tripathi	 17/10/2020
2.	Convener (Guide)	Dr. A. K. Satpati	 17-10-2020
3.	External Examiner	Prof. Amartya Mukhopadhyay	
4.	Member	Prof. R. K. Singhal	 17.10.2020
5.	Member	Prof. S. N. Achary	 17-10-2020


17-10-2020
(Convener, Viva Voce Board)

Others attended the VIVA examination through video conferencing			
1	Faculty	Prof. P.D.Naik	
2	Faculty	Prof. T. K. Ghanty	
3	Faculty	Prof. D. K. Maity	
4	Faculty	Prof. H. Pal	
5	Faculty	Prof. K. K. Swain	K.K. Swain 17.10.2020
6	BARC, Scientist	Dr. Nicy Ajith	
7	BARC, Scientist	Mr. Srikant Sahoo	Srikant Sahoo
8	BARC, Scientist	Ms. Sudipa Manna	Sudipa Manna
9	BARC, Scientist	Mr. P. K. Mishra	P.K. Mishra
10	HBNI student	Abhishek Sharma	


 17-10-2020
 (Convener, Viva Voce Board)